RICE UNIVERSITY

Core Analysis and Core-Log Integration for Evaluation of Unconventional Formations

by

Zeliang Chen

A THESIS SUBMITTED
IN PARTIAL FULFILLMENT OF THE
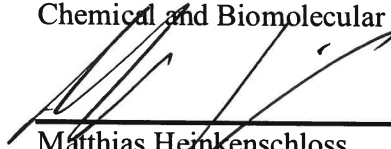REQUIREMENTS FOR THE DEGREE

Doctor of Philosophy

APPROVED, THESIS COMMITTEE

George J. Hirasaki, Chair,
A. J. Hartsook Professor Emeritus,
Chemical and Biomolecular Engineering

Walter G. Chapman,
William W. Akers Chair Professor,
Chemical and Biomolecular Engineering

Matthias Heinkenschloss,
Noah G. Harding Chair and Professor,
Computational and Applied Mathematics

HOUSTON, TEXAS
July 2019

ABSTRACT

Core Analysis and Core-Log Integration for Evaluation of Unconventional Formations

by

Zeliang Chen

Unconventional resources are of great importance in the global energy supply. This thesis develops new techniques and presents fundamental research serving unconventional formations evaluation for the petroleum industry.

First, hydrocarbon composition is a critical input to formation evaluation. In this thesis, a new technique using laboratory Nuclear Magnetic Resonance (NMR) core-analysis integrated with downhole NMR logging is developed to estimate the hydrocarbon composition in an organic-rich chalk prospect. More specifically, the contrasts in T_2 and T_1/T_2 distributions between fluids are used for fluid typing. Meanwhile, another technique based on the NMR laboratory-measured restricted diffusion of light hydrocarbons is proposed to estimate the mean pore size, heterogeneity length scale, and tortuosity of the hydrocarbon-filled porosity.

Second, it has been commonly observed that in organic-rich shale, the saturating hydrocarbons have higher NMR T_1/T_2 ratio than the saturating water. However, the origin of the high T_1/T_2 ratio was not clearly understood until now. In this thesis, the organic matter (i.e., kerogen) in the organic-rich shale is isolated for investigation. It is confirmed that the saturating heptane in kerogen has higher

T_1/T_2 ratio than water in kerogen and clays, which validates the fluid typing technique providing the wettability. This thesis also proves that the high T_1/T_2 ratio originates from dissolved heptane in kerogen and/or bitumen, where the dominant relaxation mechanism can be the [1]H-^{1}H dipole-dipole interaction, as a result of nanopore confinement.

Last but not least, permeability is an indicator of the producibility of reservoirs, and thereby a critical petrophysical property during formation evaluation. The existing ultralow-permeability measurement approaches for unconventional formations, including both steady-state and unsteady-state approaches, confronting various challenges. In this thesis, a novel unsteady-state method is proposed to determine the permeability by history matching, which consists of 1D transient-pressure experiments and numerical simulation incorporating real-gas pseudo pressure and table lookup. This novel method helps to improve the experimental efficiency, simplify the set-ups, reduce the complexity in data interpretation, and alleviate the pressure-limit constraint.

These new technologies and fundamental understandings could in principle be used to improve the evaluation of unconventional formations.

Acknowledgments

v

appreciate Dr. Janice Hewitt for her careful review of my thesis. She spent a whole semester to make me a better speaker and writer.

My sincere appreciation also goes to my colleagues: Maura Puerto, Dr. Dilipkumar Asthagiri, Dr. Peng He, Dr. Kun Ma, Dr. Aarthi Muthuswamy, Dr. Lei Ding, Dr. Yongchao Zeng, Dr. Luqing Qi, Dr. Le Wang, Dr. Pengfei Dong, Dr. Guoqing Jian, Dr. Jinlu Liu, Leilei Zhang, Arjun Parambathu, Jin Song, Eric Vavra, Reza Amirmoshiri, Xinglin Wang, Chutian Bai, and Yali Li, etc., for tremendous help throughout my research.

I would also like to thank all my friends: Qingxuan Kong, Shizheng Zhang, Siyang Xiao, Dr. Runmin Zhang, Yiyuan Yin, Dr. Jieyi Zhang, Dr. Yuchong Zhang, and all others, for making my Ph.D. journey full of happiness.

Most importantly, I wish to thank my parents, grandparents, and families for their constant love and encouragement. Their unconditional support allows me to pursue my dreams.

Contents

List of Figures

List of Tables

Nomenclature

Abbreviations

^{1}H	hydrogen nucleus (proton)
BET	Brunauer-Emmett-Teller gas-adsorption theory
BV	bulk volume
div	x-axis bin size (i.e., $\Delta \log_{10} T_2$)
HI	hydrogen index
NGLs	natural gas liquids
NMR	nuclear magnetic resonance
MSE	mean square error
pu	porosity units (1 pu = 1 %)
pu1	porosity units assuming HI = 1
pu/div	porosity units per division
pu1/div	porosity units per division assuming HI = 1
SEM	scanning electron microscopy
TOC	total organic carbon

Symbols

B_0	applied static magnetic field
B_1	disturbing magnetic field
c	isothermal compressibility
c_p	pore-volume compressibility
c_t	total compressibility
C	mass concentration
D	diffusivity of fluids
D_0	bulk diffusion coefficient
D_∞	diffusivity at the tortuosity limit

d	pore diameter
d_1	intergranular pore diameter according to T_1
d_2	intergranular pore diameter according to T_2
$d_{1\text{LM}}$	log-mean of d_1 distribution
$d_{2\text{LM}}$	log-mean of d_2 distribution
δ	gradient encoding time
Δ	diffusion evolution time
r_{ik}	separation between i'th and k'th nucleus
F_μ	formation factor of the microporosity
G	magnetic-field gradient
L_{D}	diffusion length
$L_{\text{D},1}$	diffusion length for T_1
$L_{\text{D},2}$	diffusion length for T_2
L_{M}	macroscopic heterogeneity length scale
m	Archie's cementation exponent
m	real-gas pseudo pressure (Chapter 5)
M	molar mass
k	permeability
k_∞	Klinkenberg-corrected permeability
r_{p}	pore radius
R	gas constant
R_{pore}	radius of intergranular pores
R_{g}	radius of kerogen or carbonate grain
S_{BET}	specific surface area from BET
S_{g}	surface area of kerogen granule
S_{o}	oil saturation
S	pore surface area
V	pore volume
S/V	surface-to-pore volume ratio

T	temperature
T_E	inter-echo spacing of T_2 measurement
T_d	dead time
T_1	longitudinal relaxation time
T_2	transverse relaxation time
T_{2app}	simulated downhole T_2
$T_{2,peak}$	T_2 value at mode (peak) of T_2 distribution
$(T_1/T_2)_{peak}$	T_1/T_2 ratio at the peak (Chapter 2)
$\left(T_1/T_{2app}\right)_{peak}$	T_1/T_{2app} ratio at the peak (Chapter 2)
$(T_1/T_2)_{peak}$	$(T_1/T_2)_{LM}$ value at $T_{2,peak}$ (Chapter 3)
$T_{2,cutoff}$	T_2 cutoff separating fluid signals
T_{1S}	surface component of T_1
T_{2S}	surface component of T_2
T_{1B}	bulk component of T_1
T_{2B}	bulk component of T_2
T_{2D}	diffusion component of T_2
T_{1LM}	log-mean of T_1 distribution
T_{2LM}	log-mean of T_2 distribution
$(T_1/T_2)_{LM}$	log-mean T_1/T_2 ratio as a function of T_2 (Chapter 3)
$\langle T_1/T_2 \rangle$	log-mean average of 1D T_1/T_2 distribution (Chapter 3)
$(T_1/T_2)_{LM}$	log-mean average of 1D T_1/T_2 distribution (Chapter 4)
V_g	volume of kerogen granule
V_B	bulk volume of kerogen pellets
z	gas-law deviation factors
$<$	subscript for intra-granular pores
$>$	subscript for inter-granular pores
γ_I	nuclear gyromagnetic ratio
μ	viscosity (Chapter 2 and Chapter 5)
ρ	density

ρ_B	bulk density of dry pellet
ρ_1	surface relaxivity for T_1
ρ_2	surface relaxivity for T_2
$\rho_{1,a}$	apparent surface relaxivity for T_1
$\rho_{2,a}$	apparent surface relaxivity for T_2
$\rho_{1,Dmol}$	molecular dipole component of ρ_1
$\rho_{2,Dmol}$	molecular dipole component of ρ_2
$\rho_{1,Dker}$	kerogen dipole component of ρ_1
$\rho_{2,Dker}$	kerogen dipole component of ρ_2
$\rho_{1,P}$	paramagnetic component of ρ_1
$\rho_{2,P}$	paramagnetic component of ρ_2
η	hydraulic diffusivity
τ	tortuosity
τ_s	surface-residence time of fluid molecule
τ_{se}	spin echo time
$\langle \Delta\omega^2 \rangle$	second moment of ^{1}H-^{1}H dipole-dipole
ϕ	porosity
ϕ_{gas}	gas porosity of organic-shale rock
ω	NMR resonance (i.e. Larmor) frequency
$\vec{\boldsymbol{\mu}}$	magnetic moment
$\vec{\boldsymbol{I}}$	spin angular momentum
t_p	duration of B_1 pulse

Chapter 1

Introduction

In the past decade, the oil and gas production from unconventional reservoirs increased dramatically around the world, especially in the U.S.. Unconventional reservoirs generally refer to the tight formations where resources, including oil and gas, cannot be produced at economic flow rates such that stimulation treatments for production are required. U.S. Energy Information Administration (EIA) has reported the history and projection to 2050 of the U.S. crude oil production (see Figure 1.1) (U.S. Energy Information Administration 2018). Figure 1.1 shows that unconventional oil production made up 54% of the U.S. total oil production in 2017, mainly from three major tight oil resources: Eagle Ford, Bakken, and Permian. The prediction in Figure 1.1 indicates that oil production from tight formations will keep increasing and dominate the U.S. domestic oil production in the next 30 years. As a result, the investigations into the unconventional formations have significantly been stimulated.
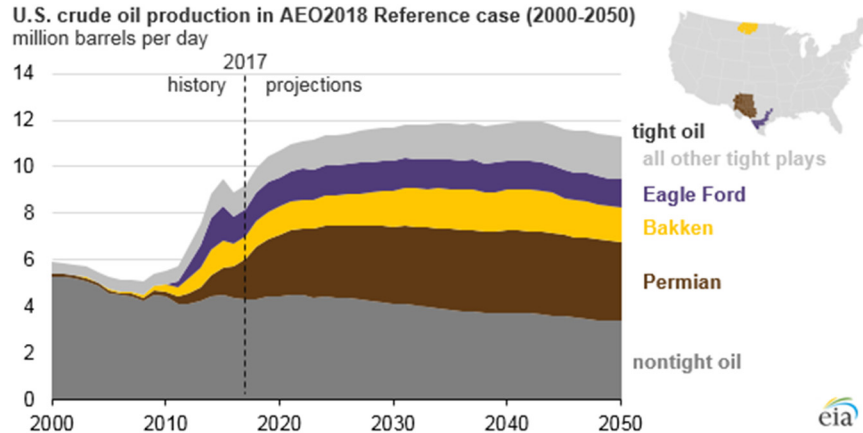
Figure 1.1 U.S. domestic crude oil production history and projection (U.S. Energy Information Administration 2018)

Formation evaluation is one of the most important subjects among the research interest. Formation evaluation refers to the acquisition of data and quantification of parameters needed for drilling, production, reservoir characterization, and reservoir engineering (Fanchi 2002).

This thesis focuses on the development and understanding of methodologies for determination of several critical petrophysical properties of unconventional formations, including total porosity, movable-fluid porosity, fluid saturation, fluid composition, pore-size distribution, tortuosity, permeability, etc.

Among the technologies for formation evaluation, NMR relaxometry, including laboratory NMR relaxometer and NMR downhole logging tool, has been proven as one of the most powerful techniques, which benefits from its non-destructive nature and the various measurable parameters. Therefore, in this thesis, NMR is used as the primary tool to estimate total fluid porosity, fluid type, fluid saturation, pore size, tortuosity, etc.

As for the permeability, the absolute permeability, which refers to the permeability to a single-phase fluid in a cleaned core, is measured in this thesis. The permeability measurement consists of fluid-flow experiments on cores and the solution to fit the data. This thesis aims at improving the permeability-estimation approach for ultra-low permeability cores.

This thesis is organized as follows:

Chapter 2 focuses on tight organic-rich chalk formations. This chapter develops an advanced technology using NMR core analysis and NMR core-log integration to estimate light-hydrocarbon composition utilizing the contrasts in T_2 and T_1/T_2 ratio between fluids. This chapter also presents a new approach to estimate the pore size and tortuosity of light-hydrocarbon filled porosity using laboratory-measured restricted diffusion and Padé approximation.

Chapter 3 focuses on organic-rich shale. This chapter shows the NMR responses of different fluids in organic-rich shale and its isolated components. It is observed that saturating hydrocarbons in organic matter (kerogen) yields larger T_1/T_2 ratio than water in both organic matter (kerogen) and inorganic matters (clays). This chapter validates T_1/T_2 ratio as a technique for fluid typing and saturation estimation.

Chapter 4 follows the research on organic-rich shale presented in Chapter 3. This chapter shows the NMR measurements on the heptane-saturated kerogen isolates with and without bitumen extraction. The relaxation mechanism between heptane and kerogen isolates is discussed in detail based on the experimental data.

It is found that the relaxation mechanism between kerogen and dissolved heptane is the same as bitumen and heptane, where the relaxation is dominated by ^{1}H-^{1}H dipole-dipole interaction.

Chapter 5 proposes a new core-analysis technique to estimate the ultra-low permeability of unconventional formation cores efficiently and accurately in the laboratory. This new technique combines unsteady-state transient-pressure experiments (i.e., 1D core flooding) and numerical simulation integrated with a fluid-property lookup table.

At last, Chapter 6 concludes this thesis, and Chapter 7 presents suggestions for future work.

It should be noted that this thesis is based on and slightly adapted from existing publications (Philip M. Singer, Chen, and Hirasaki 2016; Z. Chen et al. 2017; Z. Chen 2018; Philip M. Singer, Chen, et al. 2018; Z. Chen, Wang, et al. 2019; Z. Chen, Singer, et al. 2019).

Chapter 2

NMR Core-Log Integration for Evaluation of Organic-Rich Chalks

Note that this chapter is based on and slightly adapted from a published conference proceeding (Z. Chen, Singer, et al. 2019) and a master's thesis (Z. Chen 2018), where some portion is taken word-to-word. Also note that this work is submitted to the journal *Petrophysics* for consideration as a peer-reviewed article.

2.1. Introduction

The recent advances in horizontal drilling and hydraulic fracturing make gas (i.e., methane) and natural gas liquids (NGLs) production from tight reservoirs possible and economical. As a result, the fast-paced growth in the global gas and NGLs production stimulates research interests in this area. NMR was used as an irreplaceable tool for data acquisition because of the versatile and non-destructive

natures (Hürlimann et al. 2009; Kausik et al. 2011; Wang, Mutina, and Kausik 2014; Richard Frederick Sigal 2015; Marc Fleury and Romero-Sarmiento 2016; Valori et al. 2017; Ali Tinni, Sondergeld, and Rai 2018; Thern et al. 2018). NMR logging and laboratory NMR core analysis continue to contribute significantly to formation evaluation.

NMR measurements on methane-saturated tight rocks are valuable but challenging due to the lower hydrogen index (HI) compared to liquid-state hydrocarbons. Several recent NMR studies on methane demonstrate the capability of standard low-field NMR (2.3 MHz) bench-top relaxometer and logging tool to capture the signal from methane at achievable pressures. Kausik et al. (Kausik et al. 2011) investigate the dynamics of methane in kerogen and reports the T_2 and diffusivity of methane are greatly reduced in shale, while the HI is increased, compared to the bulk state. Valori et al. (Valori et al. 2017) develop a new methodology to estimate the permeability of gas-bearing shale rock using NMR-measured methane-saturated T_2. The research by Tinni et al. (Ali Tinni, Sondergeld, and Rai 2018) illustrates the effect of methane adsorption on gas production through laboratory NMR measurements.

NMR T_1/T_2 ratio has been proposed as a promising technique for fluid typing and composition estimation early on (Kausik et al. 2016; Philip M. Singer, Chen, and Hirasaki 2016; Philip M Singer et al. 2017; Philip M. Singer, Chen, et al. 2018; Z. Chen et al. 2017). The research on this technique has been extended to gas and NGLs recently. Thern et al. (Thern et al. 2018) study the responses of methane and

propane in activated carbon and shale. It is found that hydrocarbon (e.g., propane) is dissolved in kerogen within the shale rock and tends to yield higher T_1/T_2, which agrees with previous findings (Yang et al. 2012; Kausik et al. 2016; Philip M. Singer, Chen, and Hirasaki 2016; Z. Chen et al. 2017). Thern et al. (Thern et al. 2018) suggest hydrocarbons in nano-scale pores can be separated from hydrocarbons in inter-particle pores by either the T_2 cutoff or T_1/T_2 cutoff. The research conducted by Fleury et al. (Marc Fleury and Romero-Sarmiento 2016) using higher frequency (23 MHz) NMR also suggests exploiting T_1/T_2 for methane identification.

Besides T_1/T_2, diffusivity D measurement by NMR is widely implemented for composition estimation. Hürlimann et al. (Hürlimann et al. 2009) confirm that D-T_2 measurement contains detailed information about the composition of hydrocarbons. It is demonstrated that methane can be identified by high diffusivity values, even when dissolved in crude oil or kerogen (Hürlimann et al. 2009; Kausik et al. 2011).

The first topic of our research is the evaluation of hydrocarbon composition (i.e., methane and NGLs composition) by T_2, T_1/T_2, or D contrast. The composition is a critical input to formation evaluation because of the difference in value between methane, the NGLs (i.e., ethane, propane, butane, and pentane), and pentane plus. Note that ethane, propane, and butane are also known as condensates. Methane is a gas generally used for heating and electricity, with a relatively low value in the United States. However, propane, butane, and pentane (a component of natural gasoline) sell for approximately the same price as crude oil. Ethane is also highly

prized due to its utility as a petrochemical feedstock in ethylene manufacturing. Therefore, the prior knowledge of methane and NGLs composition contributes to reservoir valuation estimates. Our research proposes a new method of determining the volumetric composition and saturation of methane and NGLs in a petroleum reservoir using NMR logging integrated with NMR core analysis.

The second topic of our research is the evaluation of the mean pore size, heterogeneity length scale, and tortuosity of the light-hydrocarbon filled porosity using NMR restricted diffusion measurements. The mean pore size, heterogeneity length scale, and tortuosity are closely related to the permeability, which determines the producibility of a formation. Thereby these three petrophysical properties play critical roles in reservoir engineering. Our research proposes a new method of determining the mean pore size, as well as the tortuosity and the heterogeneity length scale, in a petroleum reservoir using NMR core analysis.

This chapter is organized as follows. The NMR background is introduced first. The NMR specifications and experimental details, including laboratory core saturation procedure and bulk fluid properties, are presented in the Experimental Details section. This is followed by the three types of NMR measurements associated with the analysis, which are divided into individual sections for T_2, T_1/T_2, and D. The section for T_2 includes simulations of downhole T_2 logs (namely T_{2app}) and a core-log calibration showcases how to estimate the composition. The section for T_1/T_2 incorporates simulations of downhole-measured T_1/T_{2app} and shows how T_1/T_2 and T_1/T_{2app} can be used for fluid typing and composition estimation. The section for D

shows how the Padé approximation is used to interpret the restricted diffusivity and determine the mean pore size, etc. The Conclusions section summarizes the findings.

2.2. Background: NMR Relaxation Times and Diffusivity

This part of research exploited the low-field ^{1}H pulsed-NMR relaxometer to measure the signal from the hydrogen nuclei in fluids, such as in water and hydrocarbons. The longitudinal and translational relaxation times, namely T_1 and T_2 respectively, are two fundamental NMR measurable parameters of the fluids. This sub-chapter focuses on the background of NMR technologies. At first, this sub-chapter discusses the basis of the NMR in terms of T_1 and T_2. Then, the discussion is extended to the relaxation times of fluids in porous media. Note that this sub-chapter has been presented before (Z. Chen 2018).

2.2.1. NMR Relaxation Times

2.2.1.1. Longitudinal and Transverse Relaxation Time

Hydrogen is the most abundant element in the universe. For example, hydrogen exists in the water molecule, and most of the organic matters, such as proteins and sugars. This feature is used by the petroleum engineers to determine the fluid amount in the reservoir by measuring the hydrogen quantities in the samples, because the typical fluids in the reservoirs are mainly water and hydrocarbons, such as methane and propane, where hydrogen is part of the molecules.

In the microscopic scale, hydrogen nuclei have one proton (i.e., ^{1}H) with a nuclear spin $I = ½$. This implies that the hydrogen nucleus has an intrinsic spin angular momentum. The spin angular momentum $\vec{I}$ and the magnetic moment $\vec{\mu}$ are proportional to each other (Levitt 2000):

$$\vec{\mu} = \gamma_I \vec{I}, \tag{2.1}$$

where γ_I is the gyromagnetic ratio of the proton.

In the macroscopic scale, a mole of water or hydrocarbons has millions of hydrogens, each of which contributes a small magnetic moment to bulk magnetization. Without external force, the directions of the small magnetic moments are isotropic. In this case, the magnetic moments are distributed with random directions, which leads to zero net bulk magnetization. However, once an external magnetic field is applied, the magnetic moments tend to align with the direction of the external field (as shown in Figure 2.1). This is because the energy of the magnetic moment in an external magnetic field is as follows:

$$E = -\vec{\mu} \cdot \vec{B}, \tag{2.2}$$

where $\vec{\mu}$ is the magnetic moment in the external field $\vec{B}$. Equation (2.2) implies that when the magnetic moment is in parallel to the external magnetic field, the total energy is the smallest. The total number of magnetic moment aligned with the magnetic field follows Boltzmann distribution.
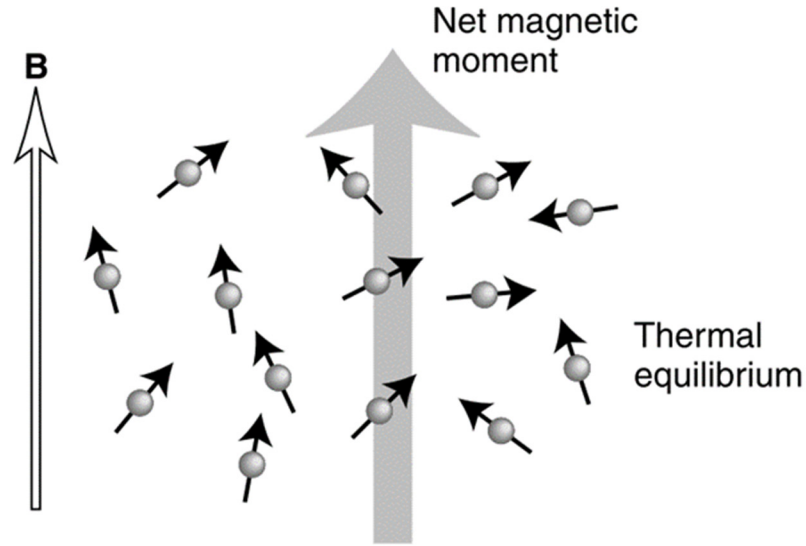
Figure 2.1 Induced bulk magnetization by an external magnetic field at thermal equilibrium (Levitt 2000).

Thus, in the presence of the external static magnetic field, the bulk magnetization of fluids will be induced, as shown in Figure 2.1. The net magnetization precesses around the static magnetic field at the Larmor frequency:

$$\omega = \gamma_I B, \tag{2.3}$$

where B is the strength of the static magnetic field; γ_I is the gyromagnetic ratio; and ω is the nuclear Larmor frequency. Equation (2.3) indicates that the Larmor frequency is proportional to the magnetic field. The relaxometor used in this research operates at 2.3 MHz.

Providing only the static magnetic field is not enough for measuring the relaxation times. It is necessary to disturb the magnetism from its steady state to exited state. Figure 2.2 shows the schematics of standard bench-top NMR spectrometers with parallel plate magnet (Mitchell et al. 2014). A static magnetic

field B_0 is applied onto the samples throughout the measurements. A coil

surrounding the sample applies a disturbing magnetic field B_1.
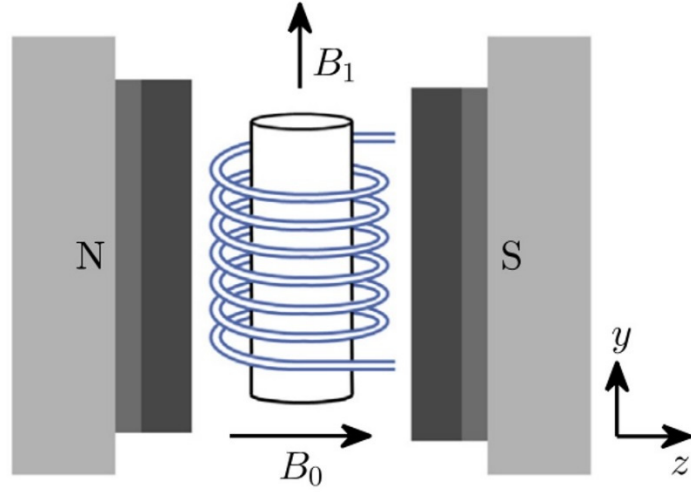
Figure 2.2 Schematics of standard bench-top (laboratory) permanent magnet configurations: parallel plate magnet. The B_0 magnetic field is generated on the z-axis between the pole pieces (light gray). Shim and gradient plates (medium/dark gray) can be included. The sample is placed in a solenoid rf coil (blue), which generates a B_1 field on the y-axis (Mitchell et al. 2014).

One can control the length of the applied B_1 pulse to flip the magnetization to

any angle θ with respect to the original direction (z-axis):

$$\theta = \gamma_I t_p B_1, \tag{2.4}$$

where t_p is the duration of B_1 pulse and θ is the angle that the magnetization has

been rotated. Figure 2.3 illustrates how the magnetization is rotated by 90º ($\pi/2$)

and 180º (π) pulse with B_1 in the direction of the x-axis. Note that by applying 180º

pulse, the magnetization is flipped from +z to -z direction.

After applying the B_1 pulse, the same solenoidal rf coil is used as the receiver,

which means the magnetization is measurable only when it is in the x-y plane. A

typical measurement of NMR named Free Induction Decay (FID) is conducted by

applying a 90º pulse and keeps measuring the intensity decay of the magnetization

in the *x-y* plane until the intensity decays to zero (see Figure 2.4).
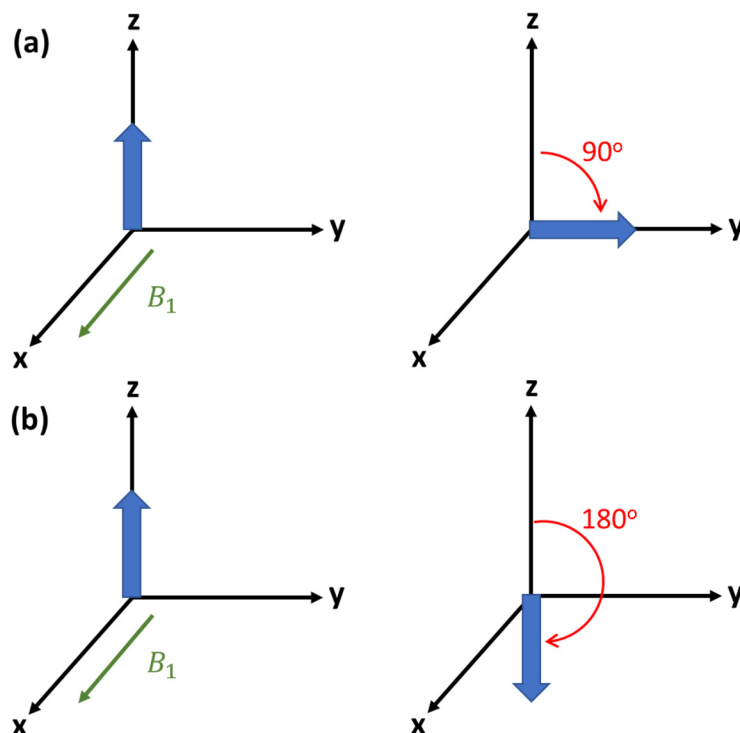
Figure 2.3 Schematics of magnetization flipping under (a) 90° ($\pi/2$) and (b) 180° (π) pulse by applying B_1 along the *x*-axis.
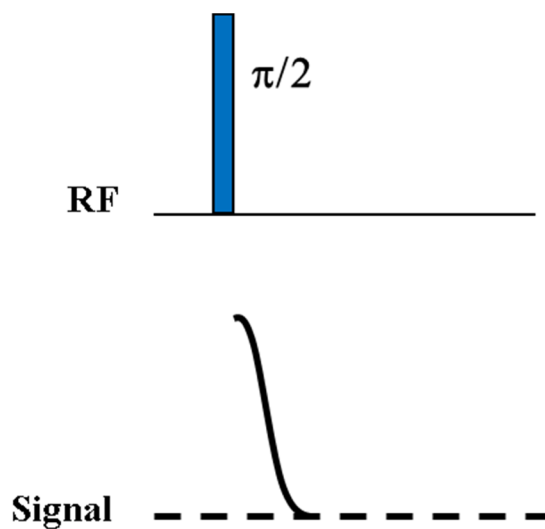
Figure 2.4 Free induction decay (FID) pulse sequence.

The longitudinal relaxation time is the characteristic time of the *z*-component of the disturbed magnetization returning to the equilibrated state. This measurement is usually done by implementing Inversion-Recovery pulse sequence (see Figure 2.5).
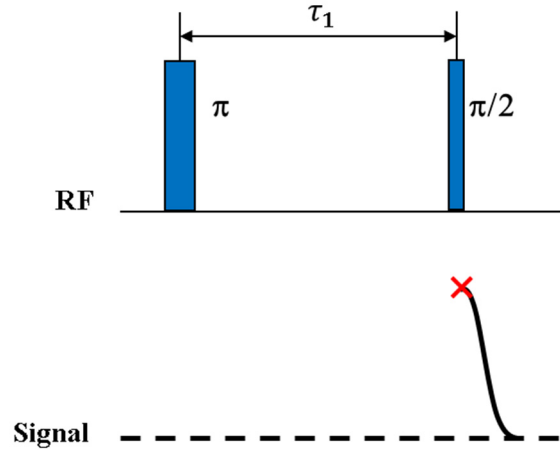
Figure 2.5 Inversion-recovery pulse sequence for longitudinal relaxation time measurement.

The Inversion-Recovery pulse sequence consists of a 180° pulse, followed by a 90° pulse. The first pulse is to flip the magnetization from +*z* to -*z*-direction. Moreover, the time gap τ_1 between those two pulses is called the wait time. After a certain wait time, the magnetization is flipped to the *x-y* plane by a 90º pulse for measurement, which is similar to the FID pulse. The maximum intensity of the following decay is picked up as the longitudinal magnetization decay for the wait time. The inversion-recovery curve of a single species (i.e., with single T_1 value) has this form:

$$M(\tau_1) = M_0 \left(1 - 2e^{-\frac{\tau_1}{T_1}} \right), \qquad\qquad (2.5)$$

where $M(\tau_1)$ is the maximum magnetization measured after the wait time of τ_1 and M_0 is the equilibrated magnetization. Note that as τ_1 goes to infinity, the measurement magnetization is relaxed back to its original state. By conducting the regularized inversion (Venkataramanan, Song, and Hürlimann 2002) on the acquired $M(\tau_1)$ at a series of τ_1's, the characterized time T_1 can be obtained.

The pulse sequence for measuring transverse relaxation time (i.e., T_2) is modified based on the FID pulse. The pulse sequence is named as CPMG pulse sequence (Figure 2.6) that is developed by Carr, Purcell, Meiboom and Gill.
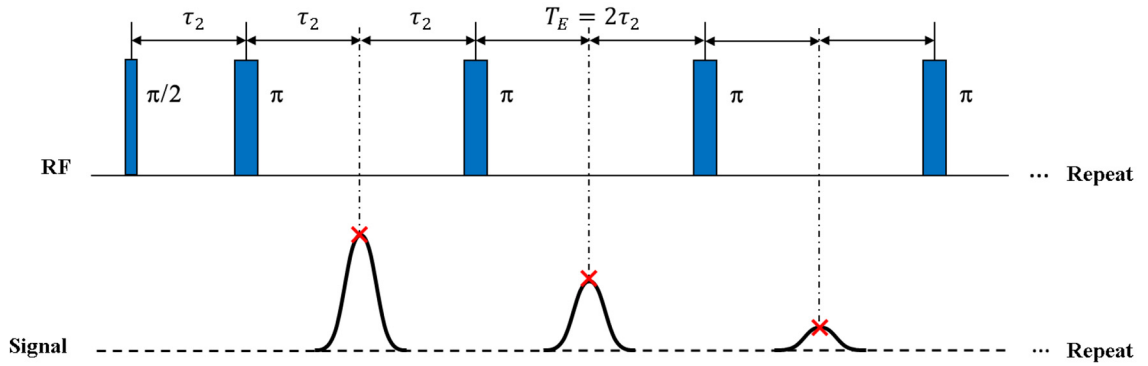
Figure 2.6 CPMG pulse sequence for transverse relaxation time measurement.

The difference between CPMG pulse sequence and FID pulse sequence is that CPMG has repeated 180° pulses following the first 90° pulse. The peaks that show up between the 180° pulses are named as the echo chain. This echo chain results from refocusing of magnetization that is de-phased by external magnetic inhomogeneity. The constant interval of those echoes, T_E, is called echo spacing. The decay caused by transverse relaxation has the following form:

$$M(nT_E) = M_0 e^{-\frac{nT_E}{T_2}},$$
(2.6)

where T_E is the echo spacing of the CPMG echo train, n is the number of the nth echo

and M_0 is the intensity of the original magnetization. By fitting the echo chain to

Equation (2.6), one can obtain the transverse relaxation time of the species.

The idea of the CPMG pulse sequence can also be applied to T_1

measurements, namely a series of 180° pulse can be added to the T_1 Inversion-

Recovery pulse sequence (Figure 2.5). With the Inversion-Recovery-CPMG pulse

sequence, one can obtain the signal including information from both longitudinal

and transverse relaxation. The decay of magnetization with multiple species, namely

various T_1's and T_2's, is as follows:

$$M(\tau_1, nT_E) = \sum_i M_i \left(1 - 2e^{-\frac{\tau_1}{T_{1,i}}}\right) e^{-\frac{nT_E}{T_{2,i}}}, \tag{2.7}$$

where M_i is the magnetization associated with $T_{1,i}$ and $T_{2,i}$. Then the T_1-T_2

correlation map can be generated by conducting 2D regularized inversion

(Venkataramanan, Song, and Hürlimann 2002).

2.2.1.2. NMR Relaxation in Porous Media

The longitudinal and transverse relaxation times of fluids behave differently

when they are in the bulk phase or porous media. The relaxation times of fluids in

porous media include additional information, such as wettability, pore size, and

surface relaxivity. These features provide the NMR the ability to characterize

petroleum systems.

The T_1 and T_2 of fluids in porous media can be broken down into various relaxation components as follows:

$$\frac{1}{T_1} = \frac{1}{T_{1B}} + \frac{1}{T_{1S}}, \tag{2.8}$$

$$\frac{1}{T_2} = \frac{1}{T_{2B}} + \frac{1}{T_{2S}} + \frac{1}{T_{2D}}, \tag{2.9}$$

where T_{1B} and T_{2B} are the bulk relaxation times of fluids not in porous media, while T_{1S} and T_{2S} are the surface relaxation times of fluids enhanced by the pore surface of porous media. In some of the cases, the T_{1S} and T_{2S} are much shorter than T_{1B} and T_{2B}. Typically, in unconventional porous media, the second term dominates. T_{2D} is the diffusion relaxation term resulting from molecular diffusion, internal magnetic gradient, and external magnetic gradient. The external magnetic gradient is typically generated by the logging tool in the downhole conditions, where the gradient has a significant impact of the T_2 of gas components. The external magnetic gradient is also applied in the laboratory measurements for diffusivities and profile imaging. This additional relaxation mechanism does not affect longitudinal relaxation. In terms of the usage of the CPMG pulse sequence, the T_{2D} can be expressed as (Kleinberg 1999):

$$\frac{1}{T_{2D}} = \frac{D(\gamma G T_E)^2}{12}, \tag{2.10}$$

where D is the molecular diffusion coefficient, G represents the summation of both internal and external magnetic gradient strength and the T_E is the echo spacing of the applied CPMG pulse sequence. In the case of low-field NMR, which yields a lower

internal gradient, the contribution of T_{2D} was significantly reduced if the external

gradient is not applied. The effect of the diffusion-relaxation term due to internal

gradients can be ruled out by comparing low-field and higher-field, or different

echo-spacing NMR data on the same sample (Singer et al., 2016).

In fast-diffusion regime (i.e., molecule diffuses many times across the pore

before being relaxed), which is valid in the case of water and light hydrocarbons in

tight formations, the surface relaxation enhanced by the porous media depends on

the chemical composition of the pore surface and the pore size of individual pores

(Kleinberg 1999):

$$\frac{1}{T_{1S}} = \rho_1 \left(\frac{S}{V}\right)_{pore}, \tag{2.11}$$

$$\frac{1}{T_{2S}} = \rho_2 \left(\frac{S}{V}\right)_{pore}, \tag{2.12}$$

where $\left(\frac{S}{V}\right)_{pore}$ is the surface-to-volume ratio of an individual pore, and ρ_1 and ρ_2 are

the surface relaxivity of the pore surface. The surface relaxivities are the parameters

reflecting the strength of the interactions between the magnetic moment of

hydrogen nuclei and the pore surface. If assuming the pores are spherical, the

surface-to-volume ratio is proportional to the pore diameter as:

$$\left(\frac{S}{V}\right)_{pore} = \frac{6}{d}, \tag{2.13}$$

where d is the pore diameter of individual pores. It means both T_1 and T_2

distributions have the pore size distribution encoded. Therefore, assuming the

surface relaxivities are known, the pore size distribution can be extracted from either T_1 or T_2 distributions.

2.2.2. NMR Measured Diffusivity

The NMR relaxometer can measure the diffusivity (i.e., self-diffusion coefficient) of fluids (in either bulk state or porous media). In this research, the pulsed gradient stimulated echo (PGSTE) pulse sequence (Mitchell et al. 2014) is implemented (see Figure 2.7).
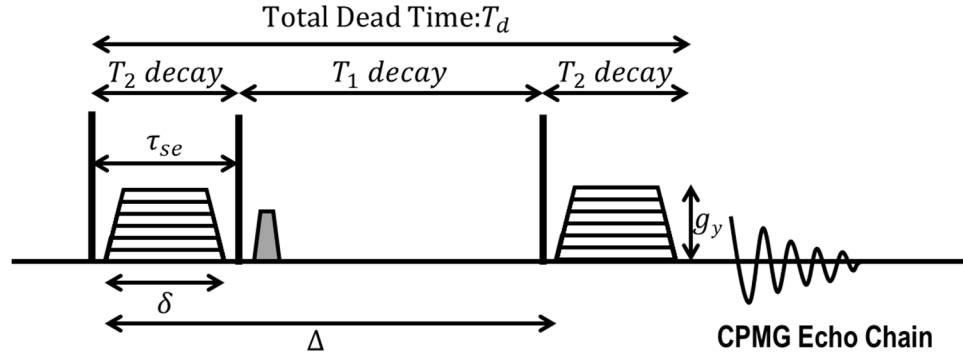
Figure 2.7 Pulsed gradient stimulated echo (PGSTE) pulse sequence (Mitchell et al. 2014). The vertical lines indicate 90° pulses. τ_{se} is the spin echo time. δ is the gradient encoding time, g_y is the magnetic-field gradient strength that is incremented during successive measurements. Δ is the diffusion evolution time. The gray trapezoid denotes the homospoil gradients.

The attenuation of the magnetization due to the diffusion of fluid molecules in the presence of PGSTE pulse sequence can be expressed by:

$$\frac{M(g_y)}{M(0)} = \exp\left(-D\gamma_I^2\delta^2 g_y^2\left(\Delta - \frac{\delta}{3}\right)\right) = \exp(-D\tau_D), \qquad (2.14)$$

where D is the diffusivity, γ_I is the gyromagnetic ratio of ^{1}H, δ is the gradient encoding time, g_y is the magnetic-field gradient strength and Δ is the diffusion

evolution time. The parameters besides the diffusivity can be combined into τ_D, of which the unit is ms/μm^2. τ_D varies with the applied magnetic-field gradient strength during measurements, which generates data points in analogous to the T_2 echo chain. By applying a multi-exponential inversion to the 1D data points, one can extract the diffusivity of fluids. In the actual measurements, the PGSTE includes the standard CPMG pulse sequence. Therefore, the 2D regularized inversion (Venkataramanan, Song, and Hürlimann 2002) can be implemented to construct the 2D D-T_2 correlation maps, similar to T_1-T_2 correlation maps.

It should be noted that the fluid molecules in porous media undergo restricted diffusion, which makes the measured diffusivity (a.k.a., restricted diffusivity) less than the bulk diffusivity. The degree of restriction has the pore size, and tortuosity encoded. This feature is used in the following context for pore size and tortuosity estimation.

2.3. Experimental Details

2.3.1. NMR Measurements

An Oxford Instruments GeoSpec2 rock-core analyzer with a resonance frequency of $\omega/2\pi$ = 2.3 MHz for ^{1}H (which is similar to downhole NMR logging tools) is used to acquire the NMR data. The measurements are conducted in an Oxford Instruments overburden core holder in either laboratory or reservoir conditions, which are discussed in the following subsection. The 2D T_1-T_2 data are acquired using 32 log-spaced points on an inversion-recovery curve ranging from

0.2 ms to 20,000 ms (typically). Each point on the inversion-recovery curve is followed by a series of CPMG echoes with an echo spacing of T_E = 0.2 ms. The 2D D-T_2 data are acquired using a unipolar stimulated-echo sequence (Mitchell et al. 2014) with 32 pulsed-field trapezoidal gradient steps ranging from zero to a maximum strength of g_y = 43 G/cm, a gradient encoding time of δ = 9 ms, a diffusion evolution time of Δ = 14.7 ms, and a dead time of T_d = 25 ms. The 2D correlation maps are processed using the fast inverse Laplace transform (analogous to Venkataramanan, Song and Hürlimann, 2002) with 120 (480 for higher resolution only for T_1/T_2 and T_1/T_{2app} analysis) log-spaced bins for T_1, T_2 and D. The units of the y-axis on the relaxation time distributions are in "pu/div", which means porosity units per x-axis bin-size. In the case of T_2 distribution, the bin size is "div = $\Delta \log_{10} T_2$ = ($\log_{10} T_{2,i+1} - \log_{10} T_{2,i}$)", which is independent of index "i" because of the log-spaced bin selection. This unit of the y-axis is also known as bin porosity.

2.3.2. Core Samples and Fluid Saturations

The core samples used in this work are from a reservoir of organic-rich bituminous chalks. These organic-rich chalks are tight rocks with a permeability of ~ 0.01 mD. The TOC (total organic carbon) of the organic-rich chalks is ~ 10 wt% (or ~ 20 vol%), and the kerogenous matter is early-stage mature Type II-S kerogen.

Petrophysically, the cores consist of water-wet micritic calcite and intergranular macropores containing kerogen, bitumen, light hydrocarbons, and small quantities of connate water.

The well was drilled with water-based mud. All downhole operations in the reservoir zone were underbalanced to prevent invasion and flushing. At the well site, the core was sealed in plastic wrap and aluminum foil and dip-coated in low melting paraffin to prevent evaporation. The core plugs used in this NMR study were drilled from the core with air mist to prevent adding water to the pore space. The core plugs are 25 mm in diameter and 48 mm in length, which are compatible with the Oxford Instrument NMR overburden core holder. A series of "twin" cores (No. 1 to No. 6) originating from the same depth of the formation are selected for laboratory core analysis. The pore space of the "as-received" core samples consists of bitumen, connate water (with unknown composition), and air, as detected by the laboratory NMR core-analyzer (shown in the following sub-chapter). The cores are then saturated with either water (i.e., brine with 8,000 ppm of NaCl), methane, ethane, propane, n-butane, n-pentane or n-decane for in-situ NMR measurements. Note that n-butane, n-pentane, and n-decane are hereafter shortened to butane, pentane, and decane, respectively.

The apparatus diagram for in-situ saturation is shown in Figure 2.8. The core samples are placed within the NMR overburden core holder for pressure saturation. A syringe pump is used to inject fluids while a hydraulic hand pump is used to maintain the confining pressure. All pressure saturations are conducted by injecting fluids at constant inlet-pressure with the outlet closed and connected to a pressure transducer. All of the laboratory NMR measurements are performed at a temperature of 30°C. The targeted pore pressure (1,200 psia) is adjusted such that the density of ethane at laboratory conditions would be the same as that at reservoir

temperature and pressure (68°C and 2,755 psia). The pressurization to the targeted

pore pressure takes two steps. The cores are initially pressurized from 14.7 psia

(ambient pressure) to 500 psia, and then from 500 psia to 1,200 psia. The step-wise

pressurization is meant to limit the pressure gradient and effective stress (a.k.a. net

pressure, namely the net stress between overburden stress and pore pressure) to

avoid irreversible change in the cores. The effective stress is kept constant at 1,000

psi during the NMR measurements.
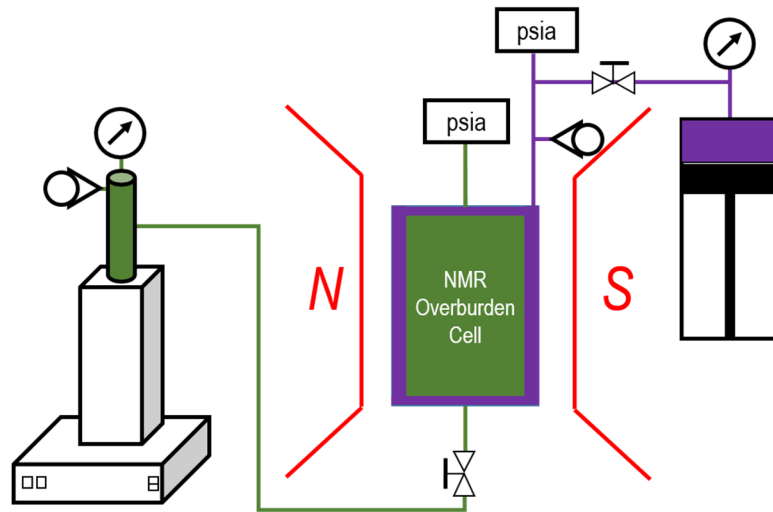
Figure 2.8 Schematic of the saturation apparatus for in-situ NMR measurements.

The details of saturations and measurements are tabulated as Table 2.1.

These series of "twin" cores are used in parallel for different saturating fluids

because the saturation alters the cores. More specifically, some connate water is

mobilized and expelled during pressurization and depressurization of light

hydrocarbons, as shown in Appendix II of this chapter. The NMR results on the as-

received cores reveal similar NMR responses (shown in the next section for T_2),

except for core No. 4. Core No. 4 has slightly less connate water saturation, but

similar total porosity as indicated by the T_2 measurements (as shown below).

Therefore, no distinction is made between these as-received "twin" cores. The order

of saturation listed in Table 2.1 for core No. 1 and No. 2 follows the order of actual

experiments. After each fluid saturation on core No.1 and No. 2, the cores are

depressurized and taken out of the overburden cell to remove excess fluid for the

next step. The deuterated core No. 1 (denoted as "D2O") is prepared by immersing

the core into fresh D_2O brine twice. Each deuteration step lasts for one week at

ambient conditions. It should be noted that the "C1(D2O)" is done by injecting

methane into core No. 1, which has been deuterated after propane saturation. The

purpose of "C1(D2O)" is to study the NMR responses of pure methane without the

interference from connate water so that the T_2, T_1/T_2, and diffusivity of the methane

can be readily observed.

Table 2.1 List of core number, saturating fluid, temperature, pore pressure, and confining pressure for NMR measurements on "twin" cores.

Core	Fluid	Label	T	P_{pore}	$P_{confining}$
			(°C)	(psia)	(psia)
1	Propane	C3	30	1,200	2,200
	D_2O	D2O	30	1,200	2,200
	Methane (D_2O)	C1(D2O)	30	1,200	2,200
2	Methane	C1	30	1,200	2,200
	Ethane	C2	30	1,200	2,200
3	H_2O	H2O	30	1,200	2,200
4	Pentane	C5	30	1,200	2,200
5	Decane	C10	30	1,200	2,200
6	Butane	C4	30	1,200	2,200

2.3.3. Bulk Properties of Saturating Fluids

The bulk properties of water and hydrocarbons at both laboratory conditions (30°C, 1,200 psia) and downhole conditions (68°C, 2,755 psia) are acquired and summarized in Table 2.2. The density and viscosity of fluids are inferred from the NIST REFPROP database with temperature and pressure as the inputs. The hydrogen indexes (HI) of fluids other than water are calculated by comparing the proton densities with that of water at the same temperature and pressure. Note that only methane shows significant differences in density and HI under different conditions. Also, note that methane under both conditions is a supercritical fluid instead of a gas.

The diffusivity of water measured at 25°C and ambient pressure is used for the laboratory conditions. For the reservoir conditions, Krynicki et al., (Krynicki, Green, and Sawyer 1978) measure the diffusivity of water at 70.05°C and at around 1,470 and 4,410 psia respectively, which are similar to the reservoir conditions in this work. These two measurements at different pressures both yield diffusivities around 5.6 μm^2/ms, which is adopted here as the bulk diffusivity of water at reservoir conditions.

The diffusivity of ethane, propane, butane, pentane, and decane are estimated by substituting the temperature and viscosity into Equation (2.15), which is an empirical correlation proposed by Lo et al. (Lo et al. 2002):

$$D_0 = 4.69 \times 10^{-3} \frac{T}{\mu},\qquad(2.15)$$

where D_0 is bulk diffusivity with a unit of $\mu m^2/ms$, T is temperature with a unit of K

and μ is viscosity with a unit of cP.

Table 2.2 Bulk properties of fluids on both laboratory and reservoir conditions.

Fluid	30°C, 1,200 psia (laboratory)				68 °C, 2,755 psia (reservoir)			
	Density	HI	Viscosity	Diffusivity	Density	HI	Viscosity	Diffusivity
	(g/cm^3)		(cP)	(μm^2/ms)	(g/cm^3)		(cP)	(μm^2/ms)
Water (H2O)	1.00	1.00	0.797	2.3	0.99	1.00	0.420	5.6
Methane (C1)	0.06	0.13	0.013	250.0	0.12	0.27	0.018	125.0
Ethane (C2)	0.36	0.65	0.047	30.1	0.35	0.64	0.046	34.5
Propane (C3)	0.50	0.83	0.106	13.4	0.48	0.80	0.092	17.4
Butane (C4)	0.58	0.90	0.168	8.5	0.56	0.88	0.141	11.3
Pentane (C5)	0.63	0.94	0.232	6.1	0.61	0.92	0.200	8.0
Decane (C10)	0.73	1.02	0.869	1.6	0.71	1.00	0.616	2.6

The diffusivity of methane is obtained differently. It is inferred from the

experimental data published by Oosting et al. (Oosting and Trappeniers 1971), who

measured the bulk diffusivity of methane as a function of bulk density and

temperature. The original data (Oosting et al., 1971) is re-organized and plotted in

Figure 2.9. The measured bulk diffusivities in different phases are clustered and

plotted against the predicted viscosity/temperature (μ/T). The predicted μ/T is

inferred from REFPROP based on the bulk density and temperature. It is obvious

that the bulk diffusivity of the vaporous and some of the supercritical methane does

not follow the Stokes-Einstein equation which predicts that D vs. μ/T is a straight

line on a log-log plot, similar to Equation (2.15). Therefore, the μ/T of methane on

both laboratory and reservoir conditions are used to estimate the bulk diffusivity

(shown as the two vertical dashed lines in Figure 2.9). The μ/T of methane under

laboratory conditions suggests a bulk diffusivity $\sim 250 \ \mu\text{m}^2/\text{ms}$, while methane

under downhole conditions yields a bulk diffusivity $\sim 125 \ \mu\text{m}^2/\text{ms}$. The mismatch in

the methane diffusivity between the laboratory and reservoir conditions is a

compromise of a better match in the ethane density.

The estimated diffusivities of bulk fluids at laboratory and reservoir

conditions are used later to simulate downhole logs and to interpret the restricted
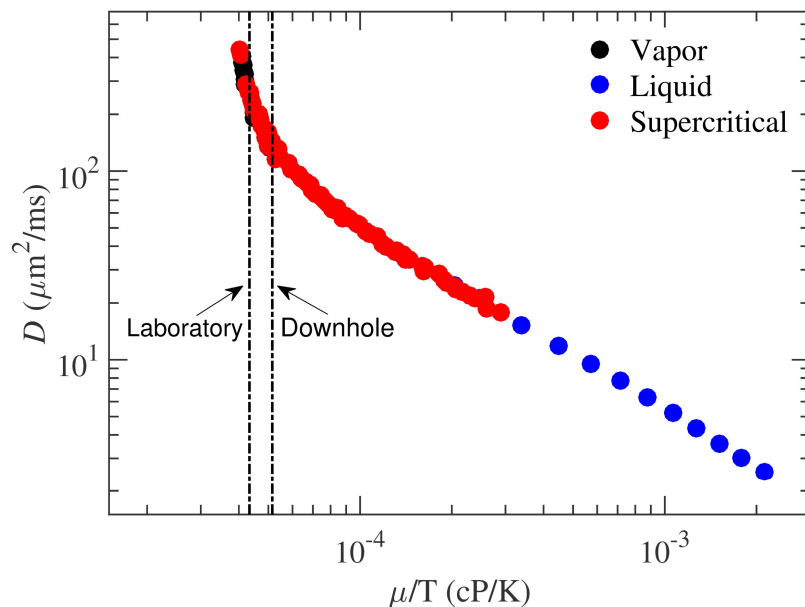
diffusion.

Figure 2.9 Bulk diffusivity D vs. viscosity/temperature (μ/T) of methane in different phases (Oosting and Trappeniers 1971). The μ/T's of methane under laboratory and downhole conditions are labeled by the vertical dash lines.

It should be noted that molecular dynamics (MD) simulation serves as a

more fundamental approach to estimate the bulk diffusivity, as well as NMR T_1 and

T_2 relaxation times, of water and alkanes (including methane). It has been

demonstrated that the MD simulation yields T_1, T_2 and diffusivity predictions in excellent agreements with experimental results (Philip M. Singer et al. 2017; P. M. Singer et al. 2018; Philip M. Singer, Asthagiri, et al. 2018).

2.4. Composition Estimation by T_2

This sub-chapter presents T_2 laboratory measurements on as-received and saturated cores. Note that the T_2 distributions are projected from 2D T_1-T_2 correlation maps. This sub-chapter also shows how the laboratory T_2 is used to calibrate the log to estimate the light-hydrocarbon composition.

2.4.1. T_2 Distributions of As-received Cores

Figure 2.10 shows the T_2 distributions of six as-received cores from the same depth. Obviously, the T_2 distributions can be divided into three regions by the vertical dashed lines, and are identified as: (A) bitumen and/or dissolved light hydrocarbon region (leftmost), which may contain light hydrocarbons dissolved in both bitumen and kerogen, as inferred from its high T_1/T_2 ratio revealed by the T_1-T_2 measurements (shown in the following section for T_1/T_2); (B) connate water region (middle), inferred from the fact that its signal intensity is decreased to almost zero by deuteration (i.e., exchange with D_2O, a.k.a. heavy water, shown in Appendix I of this chapter); (C) hydrocarbon region with small amount of connate water, where most of the connate signal can be eliminated by deuteration (also shown in Appendix I of this chapter).
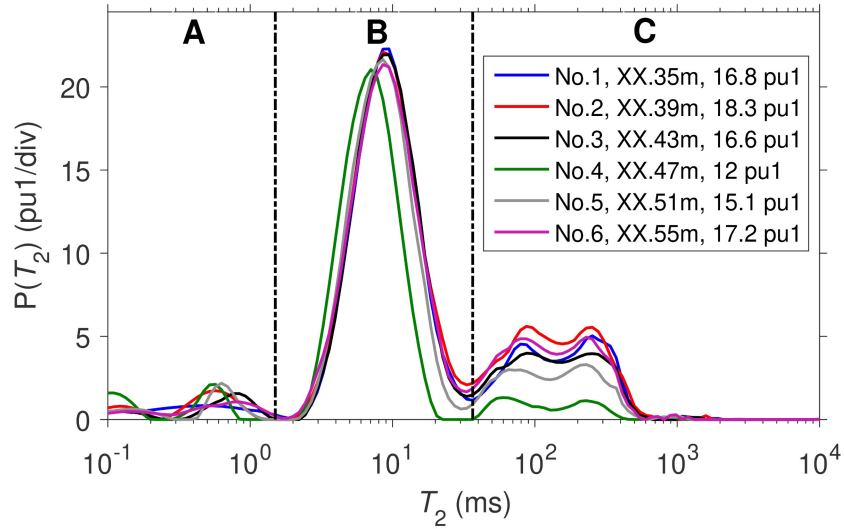
Figure 2.10 T_2 distributions of the as-received cores from the same depth. Dashed lines divide the T_2 distributions into three regions: (A) the leftmost region is the bitumen and/or dissolved hydrocarbon region; (B) the middle region is the connate-water region; (C) the rightmost region is the light hydrocarbon region (with small amounts of connate water). The legend indicates core number, concealed core depth, and NMR porosity. "pu1" refers to porosity units assuming HI = 1.

It should be noted that the reported "NMR porosity" of the as-received cores in Figure 2.10 and following plots is NMR liquid-filled porosity, while the "NMR porosity" of the saturated cores is the NMR total porosity. The reported porosity assumes that all the detected fluids have a hydrogen index of unity, i.e., HI = 1, which is the same as water. As such, the porosity values are listed in units of pu1, which is short for porosity units (pu) assuming HI = 1. The reported NMR liquid-filled porosity or NMR total porosity follows a relationship with the actual porosities as such:

$$\phi_l(\text{pu}) = \frac{\phi_l(\text{pu1})}{\text{HI}},$$
$$\phi(\text{pu}) = \frac{\phi(\text{pu1})}{\text{HI}},$$

(2.16)

where ϕ_l(pu) and ϕ(pu) are the actual liquid-filled and total porosity respectively, while ϕ_l(pu1) and ϕ(pu1) are the reported NMR liquid-filled porosity and NMR total porosity assuming HI = 1, respectively. It should be noted that a large fraction of the bitumen signal with short T_2 due to its high viscosity is not detectable by the low-field NMR relaxometer in this study. Therefore, the total porosity (i.e., NMR total porosity) reported in this study does not include the invisible portion of bitumen.

Figure 2.10 indicates that the cores from the same depth share very similar T_2 distributions, except that core No. 4 has less connate water in regions B and C, which also leads to a T_2 shift in region B.

2.4.2. T_2 Distributions of Saturated Cores

Saturating the as-received cores in the laboratory is critical to study the NMR responses of different fluids (see Table 2.1 for saturation details). In this study, we use the water and hydrocarbons respectively to saturate the core under the laboratory conditions. The T_2 distribution acquired on the 100% water-saturated core provides the total NMR porosity. Figure 2.11a presents the T_2 distribution of core No. 3 before and after water saturation. It is clear that there is around 8.1 pu of water introduced by water saturation. The fully water-saturated core (No. 3) suggests a total NMR porosity of ∼ 25 pu for all of the six "twin" cores.

Figure 2.11b, c, and d provide T_2 distributions of hydrocarbons in the cores. The measurements illustrate different NMR porosity, especially in region C, which is due to the differences in HI between the hydrocarbons. Under laboratory conditions,

methane is supercritical and yields a low HI of 0.13, while ethane, propane, butane,

pentane, and decane are all liquids and yield much higher HI's (see Table 2.2). It

should be noted that since the HI of methane at reservoir conditions is twice that at

laboratory conditions (also see Table 2.2), the simulated downhole T_2 response

(shown below) should be compensated.
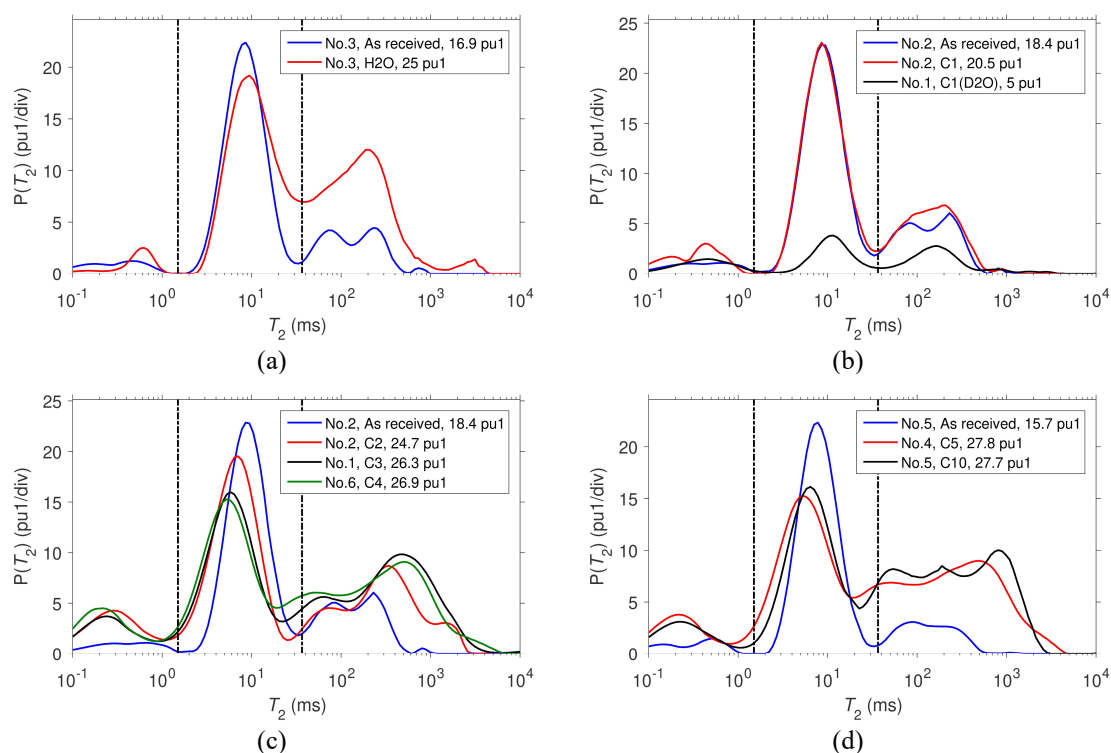
Figure 2.11 T_2 distributions of as-received and fully-saturated cores. Dashed lines divide the T_2 distributions into three regions, the same as in Figure 2.10. The legend indicates states of cores including core number, saturating fluid and NMR porosity. "pu1" refers to porosity units assuming HI = 1.

The total NMR porosity of water-saturated core in region A is slightly lower

than that of pentane- and decane-saturated cores, even though water, pentane, and

decane share similar HI (see Table 2.2). This is interpreted as the dissolution of

alkanes into either bitumen or kerogen, as suggested by the increase in signal

intensity of region A after pentane and decane saturation (see Figure 2.11d).

In addition to the NMR porosity, there are other noticeable changes in T_2 distributions of the saturated cores. For the water-saturated core (No. 3), a slight increase in T_2 of connate water in region B is observed. This is because the connate water in micropores in the micritic calcite (region B) is weakly diffusive-coupled with the water in the macropores that are between the large grains of co-precipitated kerogen and calcite (region C). The diffusive coupling is weak because some bitumen clogging up the pore throats limits the water exchange.

It is also observable that the T_2 of connate water (region B) is shifted to shorter values after saturation with longer alkanes, but not after methane. This indicates the connate water is mobilized by a gas-liquid drive of liquid hydrocarbons. The trend of T_2 shifting agrees with the mobility ratios of alkanes with respect to water (e.g., alkanes with longer carbon chain-lengths yields higher viscosities, which are closer to the viscosity of water). This also explains why the connate-water loss in cores after experiments increases with alkane carbon-number (see Appendix II of this chapter). Note that even though the T_2 of region B for connate water is shifted, the NMR porosity for this region is nearly unchanged for all the cases (except for "C1(D2O)"). This is because the invaded hydrocarbons occupy the pore-space originally for the expelled connate water. The invaded hydrocarbons have longer T_2 than connate water because the micritic calcite pores associated with region B are water-wet, such that hydrocarbons are relaxed by the water film coating the pore surface, and therefore have longer relaxation times compared to the connate water.

Since low-HI methane ("C1") only contributes a small amount of signal in region C indicated by Figure 2.11b, deuteration is useful when the methane response is analyzed. The T_2 of pure methane ("C1(D2O)") in region C is the same as methane in the saturated core ("C1"), confirming that the extra signal seen on "C1" is not an artifact. It should be noted that the signal in region B of "C1(D2O)" is due to water contamination because this part of the signal does not disappear after desaturation of methane, and can also be deuterated from the de-saturated core. The source of contamination may be from the moisture and remaining droplets of water (< 0.5 mL) in the tubing and valves of the apparatus.

The T_2 response of ethane and longer alkanes in region C is separated into several peaks. The wettability may account for the distinct peaks. The pores for region C are in-between the grains of co-precipitated kerogen and calcite. Therefore, the pores associated with region C are likely to be mixed wet. The longest T_2 of decane in region C is close to its bulk T_2 (about 3 s for deoxygenated decane). This may be because of a thin water film coating some surface of the mixed-wet pores, such that decane does not directly contact the pore walls. In such cases, the surface relaxation of decane is provided by the decane-water interface instead of the decane-solid interface. It can be expected that the surface relativity of the decane-water interface is much smaller compared to the decane-solid interface. On the other hand, decane in contact with the kerogen solid surface may yield shorter T_2 that is distinct from the bulk T_2. The same interpretation applies to other alkanes that have distinct peaks in region C.

2.4.3. T_{2app} Distributions and Composition Estimation

Due to magnetic-field gradients, NMR logging tools measure the "apparent" T_2 relaxation, defined as T_{2app} and given by:

$$\frac{1}{T_{2app}} = \frac{1}{T_2} + \frac{1}{T_{2D}}. \qquad (2.17)$$

T_2 is the transverse relaxation time without applied magnetic-field gradients, as reported in the previous subsections. T_{2D} is the additional term due to fluid diffusion in an applied magnetic-field gradient generated by the logging tool as such:

$$\frac{1}{T_{2D}} = \frac{\gamma^2 G^2 T_E^2 D}{12}. \qquad (2.18)$$

$\gamma/2\pi$ =42.58 MHz/T is the gyromagnetic ratio of the proton. The MREX NMR logging tool involved in this study has an echo spacing T_E of 0.4 ms. G is the magnetic-field gradient applied by the NMR logging tool. The NMR logging tool provides six shells of equal volume with G's of 17.0, 22.0, 23.4, 27.4, 32.7 and 38.7 G/cm respectively. D represents the diffusivity of hydrocarbons, where the restricted diffusivities under logging conditions (derived based on the following diffusivity measurement using Padé fit) are used. This is because the diffusion lengths of fluids, especially that of methane, are close to the pore diameter, which means the fluids experience restriction from the limited pore space. Note that in the cases where the restriction is negligible (i.e., the pore diameter is much greater than the diffusion length), bulk diffusivity of fluids can be used to calculate the magnetic-field gradient effect, which leads to simpler implementation.
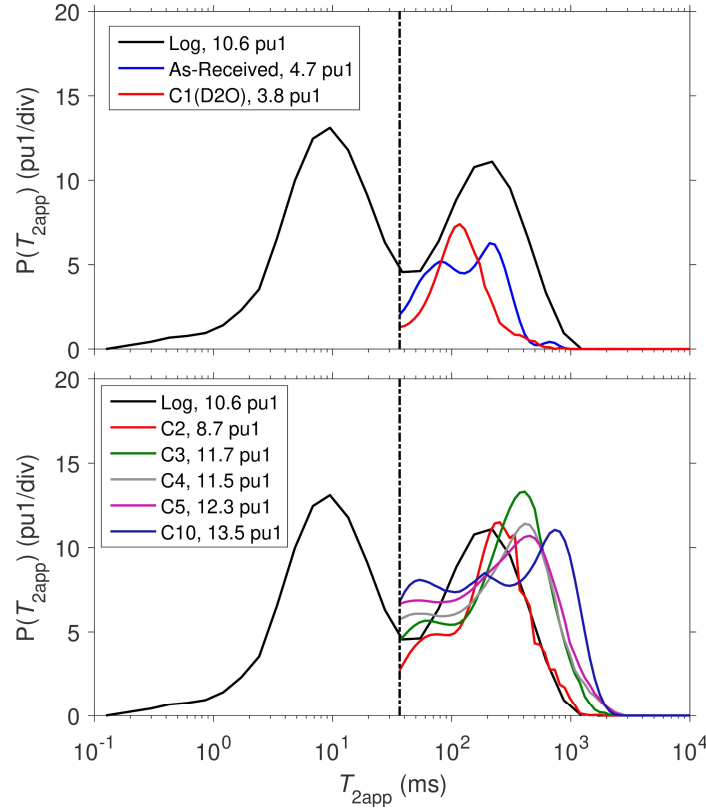
Figure 2.12 Comparison of incremental T_{2app} distribution from the downhole log and simulated T_{2app} distribution (region C only) based on laboratory-measured data. Note that the two subplots share the same log data. Also, note that the simulated T_{2app} distribution has the HI difference under different conditions compensated. The dashed vertical lines separate the region C from the other two regions. The legend indicates measurement name and the NMR porosity of region C. "pu1" refers to porosity units assuming HI = 1.

For a better core-log comparison, the extra T_{2D} term is added to the laboratory-measured T_2 distributions. In addition, the first echo (at 0.2 ms) of the time-domain raw data for the laboratory measurements is dropped to match the first echo time of the logging tool. Besides, the simulated T_{2app} is re-scaled by the HI of fluids, which means the bin porosity in the T_{2app} distribution of methane is boosted by a factor of two because of the difference in HI under reservoir and laboratory conditions (see Table 2.2). As for longer alkanes and water, the effect of re-scaling is insignificant because those fluids share similar HI at both conditions. Figure 2.12 presents the T_{2app} distribution from the downhole log and the T_{2app}

distributions from the as-received (i.e., connate-water saturated) and hydrocarbon-saturated cores simulated based on the laboratory measurements. Note that for simulated T_{2app} distributions, only region C is shown because region B is less informative due to the T_2 shift. The log data are acquired at the same depth where the as-received plugs were cored.

Introducing the T_{2D} term to laboratory-measured T_2 has no impact on regions A and B where T_2 is much shorter than T_{2D}. However, introducing the T_{2D} term leads to shorter relaxation time T_2 in region C, with narrower and higher peaks. It is found that methane has shorter T_{2app} than the log, while longer alkanes have higher T_{2app} than the log; therefore a combination of the hydrocarbons is expected to match with the log.

To determine the composition of light hydrocarbons in the reservoir, the T_{2app} distributions of light hydrocarbons in the core are numerically "mixed" in data post-processing by averaging their T_{2app} distributions according to different volume fractions. This analysis assumes that hydrocarbons yield the same T_{2app} distribution in the mixture as they would in single component form (i.e., the T_{2app} distributions are linearly additive). It is also assumed that, in the ethane- and higher alkane-saturated core, the signal of region C is from hydrocarbons with a negligible amount of connate water (i.e., only thin water films coating the water-wet portions of pores but not contributing to the signal intensity). This is suggested by the measurements shown in Appendix II of this chapter on de-saturated cores, of which the T_2 distributions provide nearly zero signal in region C, except for methane. In the case

of methane, "C1(D2O)" is used instead of "C1" for "numerical mixing" because "C1(D2O)" is measured after the propane experiment where the connate water in region C was expelled by propane (see Appendix II of this chapter). Hence, "C1(D2O)" presents the T_{2app} distribution when methane occupies the entire pore space of region C.

The "numerical mixing" of T_{2app} makes use of the T_{2app} of the "As-Received" as the baseline to represent the connate water in the reservoir. The T_{2app}'s of hydrocarbons are added to the "As-Received" after being multiplied by the total hydrocarbon saturation of region C and the volume fraction (i.e., composition) of individual hydrocarbon (see Appendix III of this chapter for the workflow). The total light hydrocarbon saturation in region C is about 65% since the connate-water saturation is 4.7 pu/ 13.5 pu ≈ 35%. Note that the NMR porosity of the fully decane-saturated (instead of water-saturated) core is adopted for the above saturation calculation because water in macropores (region C) is diffusively-coupled to water in micropores (region B), which leads to shorter T_{2app} and less NMR porosity for region C. A brute-force searching algorithm is implemented to determine the optimal volume fraction of hydrocarbons that minimizes the discrepancy (i.e., mean squared error) between "numerically mixed" T_{2app} distribution and the log for region C where $T_{2app} \geq 36.6$ ms. Note that the T_{2app} of region B is shifted due to loss of connate water, and is therefore not of interest.

The optimal volumetric fractions of hydrocarbons obtained by the brute-force search are listed in the legend of Figure 2.13. It is obvious that butane,

pentane, and decane do not contribute to the optimal "mixture". Methane

contributes around 27%, while ethane and propane contribute about the same

amounts, around 36% to the "mixture". By converting the volumetric fraction to the

porosity unit, one can derive that the total fluid-filled porosity of the three

hydrocarbons is 8.8 pu. Methane, ethane, and propane occupy approximately 2.4,

3.2, 3.2 pu, respectively.
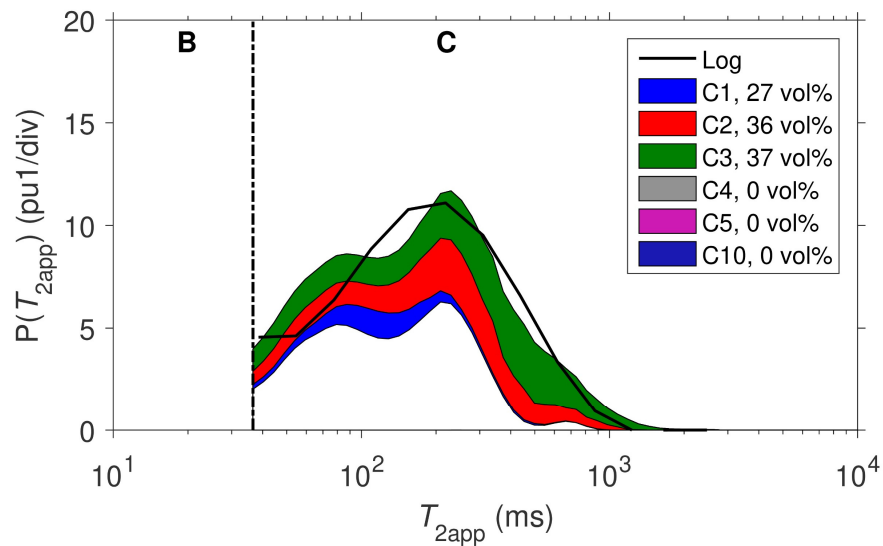
Figure 2.13 Comparison of incremental T_{2app} distributions from the downhole log and artificially "mixed" hydrocarbons saturated core (region C only). The T_{2app} distributions of hydrocarbons in the "mix" are broken down to single components with a color scheme to visualize the composition. The total colored area denotes the light hydrocarbon-filled porosity. The outline of the green area denotes the final T_{2app} distributions of the "mix". The white area under the blue area is associated with connate water. The optimal volumetric fraction of the "mix" is illustrated in the legend. The dashed vertical line indicates that the T_{2app} distributions above the region C cutoff are used to search for an optimal volumetric fraction. The "pu1" means NMR porosity shown in plots is assuming HI = 1.

2.5. Fluid Typing by T_1/T_2 and T_1/T_{2app}

This sub-chapter presents T_1-T_2 measurements conducted in the laboratory

on as-received and saturated cores. The contrasts in T_1/T_2 and T_1/T_{2app} are

discussed in detail and proposed as techniques for fluid typing and saturation estimation.

2.5.1. Laboratory-measured T_1/T_2

The laboratory-measured 2D T_1-T_2 correlation map can be transformed into a T_1/T_2 vs. T_2 correlation map. Figure 2.14 shows the T_1/T_2 vs. T_2 correlation maps of connate water and saturating fluids in the cores. It is found that the signal in region A has $T_1/T_2 \approx 10$ for both as-received and saturated states, indicating that the signal comes from viscous bitumen and/or hydrocarbons dissolved in kerogen (Philip M. Singer, Chen, and Hirasaki 2016; Z. Chen et al. 2017; Philip M Singer et al. 2017; Philip M. Singer, Chen, et al. 2018). Furthermore, the signal intensity in region A increases after hydrocarbon saturation, but not after water saturation. This results from lowering the viscosity of the bitumen after mixing with the saturating hydrocarbons, which leads to longer T_2 and thereby more detectable signal (Yang et al. 2012; Philip M Singer et al. 2017; Philip M. Singer, Chen, et al. 2018), as well as more signal from the saturating hydrocarbons dissolved in the kerogen grains (Philip M. Singer, Chen, and Hirasaki 2016; Z. Chen et al. 2017).

As for region B and C, Figure 2.14a indicates that saturating water has the same T_1/T_2 as connate water. The "C1" shown in Figure 2.14b overlays with the "As-received" 2D correlation map, which results from the low HI of methane. However, the pure methane signal shown in black suggests that methane in the core indeed has higher T_1/T_2 than connate water. As for the liquid hydrocarbons, Figure 2.14c

and Figure 2.14d also suggest that the saturating liquid-state hydrocarbons tend to yield broader T_1/T_2 distributions and higher T_1/T_2 ratios than connate water.
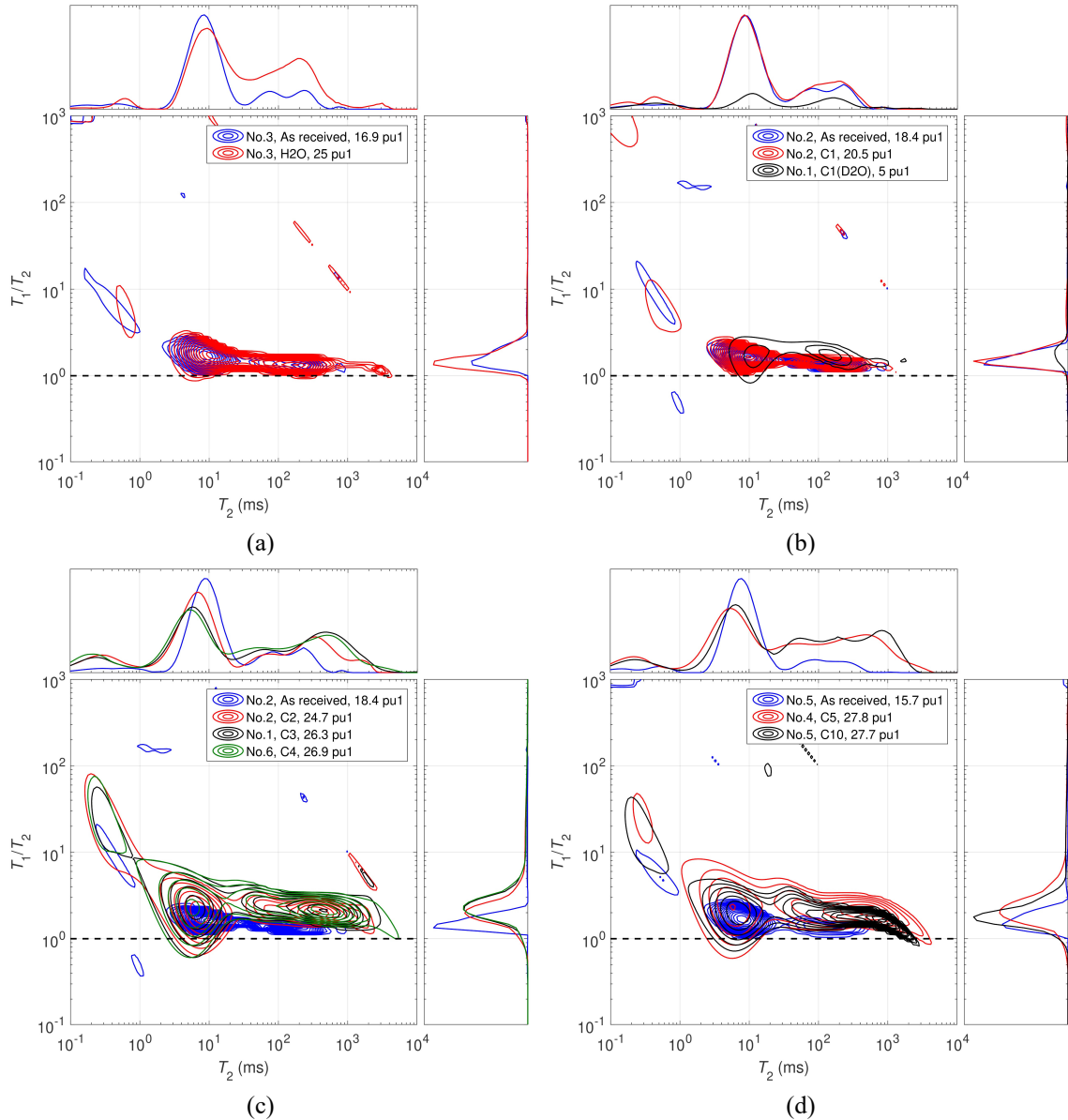
Figure 2.14 2D correlation maps of as-received and fully-saturated cores, with T_1/T_2 ratio on the y-axis, T_2 on the x-axis and porosity perpendicular to the page. For each subplot, the top subplot is the projected T_2 distribution. The right subplot is the projected T_1/T_2 ratio distribution. The legend indicates the states of the cores including core number, saturating fluid, and NMR porosity. "pu1" refers to porosity units assuming HI = 1. The dashed horizontal line is the T_1/T_2 = 1 line.

The T_1/T_2 ratio at the peak of region B and C in Figure 2.14 is plotted in Figure 2.15. The reason for choosing the peak values instead of the commonly chosen log-mean values is that the peak values are subject to less interference from the connate water, especially in region C. The T_1/T_2 of region A is with large scattering expected in this short-T_2 region (i.e., lower resolution) such that the T_1/T_2 of region A is not plotted in Figure 2.15.
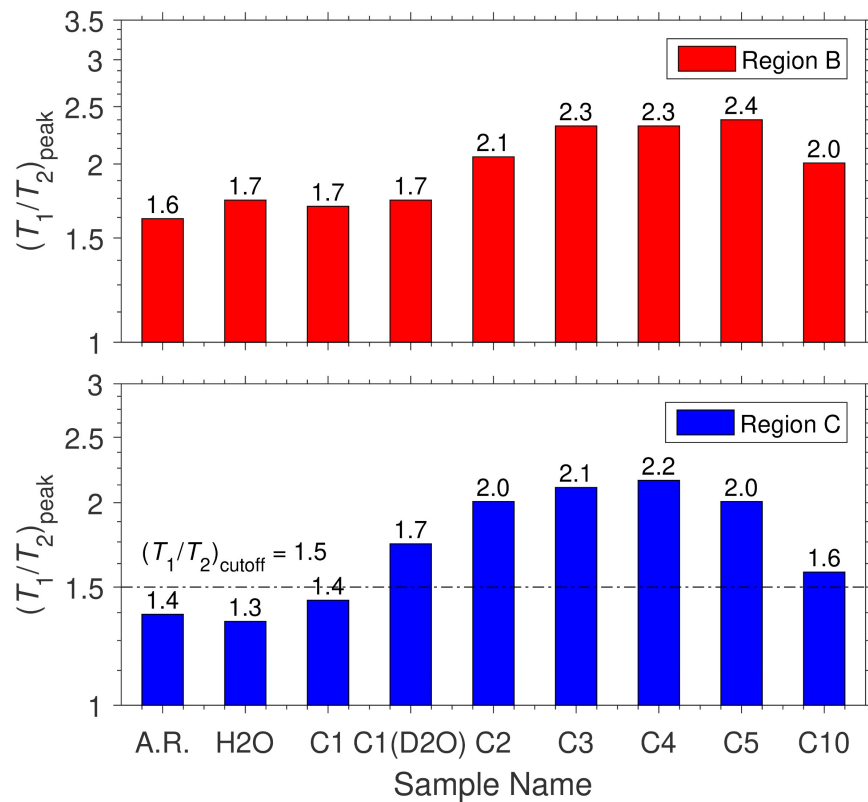
Figure 2.15 Comparison of T_1/T_2 ratio peak values in region B and C. The y-axis shows the T_1/T_2 at the peak of each region. The x-axis indicates connate water (as-received) or saturating fluids. The horizontal dashed line in the bottom subplot is the proposed T_1/T_2 cutoff separating hydrocarbons from water in region C.

The signal in region B is dominated by connate water, except for the case ("C1(D2O)") where the core is deuterated beforehand. The T_1/T_2's in region B are roughly 2. The scattering is due to the small amount of invasion of hydrocarbons into region B (see Appendix II of this chapter), which leads to more complexity and

less interest. Region C is most affected by the injecting fluids, since saturating hydrocarbons mainly exist in macropores. It is found that methane in the as-received yields the same T_1/T_2 as water due to interference from connate water. By contrast, methane in the deuterated core generates much higher T_1/T_2. It is readily observed that the T_1/T_2 of light hydrocarbons in region C peaks at butane. However, the mechanism that results in the peak should be further investigated, potentially by MD simulation.

The light hydrocarbons in region C have higher T_1/T_2 than water. As a result, a T_1/T_2 cutoff ~ 1.5 (indicated by the horizontal dashed line in the bottom subplot of Figure 2.15) can be applied to distinguish water from light hydrocarbons. This feature could be potentially exploited as a criterion for identifying water versus light hydrocarbons in core measurements.

2.5.2. Simulated Downhole-measured T_1/T_{2app}

The concept of calculating T_{2app} by introducing the effect of the magnetic-field gradient is then applied to 2D T_1-T_2 correlation maps for T_1-T_{2app} correlation maps (not shown). As a result, the T_1/T_{2app} acquired by logging tools is reproduced from the laboratory measurements. The projected 1D T_1/T_{2app} distributions of the signal in region C are isolated and plotted in Figure 2.16. This plot also indicates that hydrocarbons provide broader T_1/T_{2app} distributions compared to water.
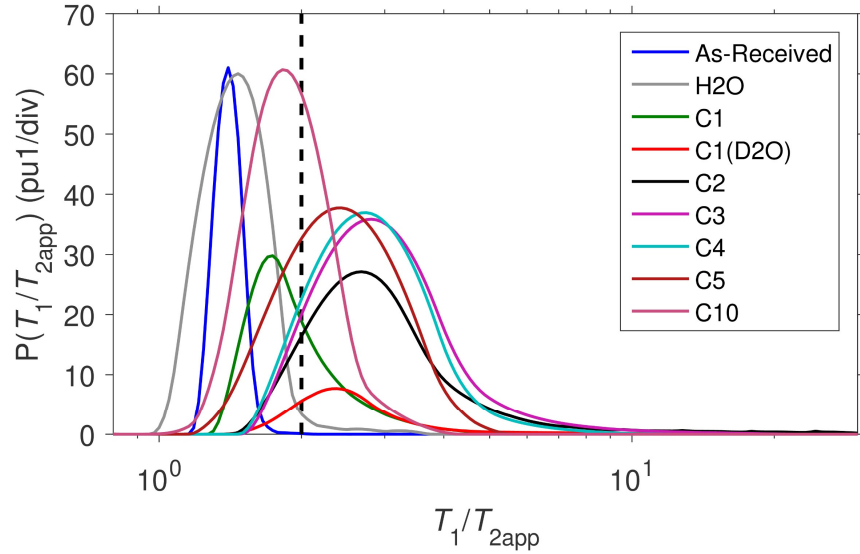
Figure 2.16 Projected 1D T_1/T_{2app} distributions of the signals in region C from 2D T_1/T_{2app}-T_{2app} correlation maps. The legend indicates the states of cores including saturating fluid. The vertical dashed line is the proposed T_1/T_{2app} cutoff separating lighter hydrocarbons from water and decane in region C.
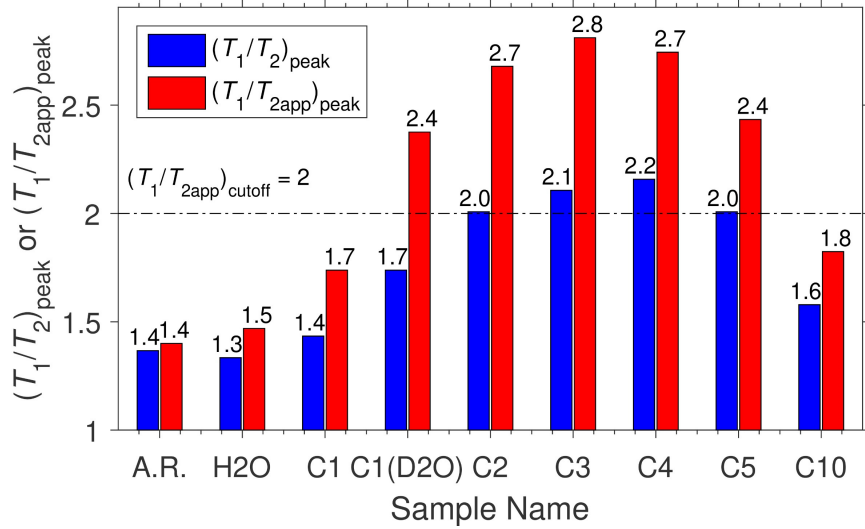
Figure 2.17 T_1/T_2 and T_1/T_{2app} at the peak of region C for the as-received state and different fluid saturations. Blue is for T_1/T_2. Red is for T_1/T_{2app} simulated using the logging tool magnetic-field gradients. The horizontal dashed line is the proposed T_1/T_{2app} cutoff separating lighter hydrocarbons from water and decane in region C.

It should be noted that unlike the numerical mixing of T_{2app}, the connate-water signal is not compensated here because only the peak values of the T_1/T_{2app}

distributions in Figure 2.16 are used as the representative T_1/T_{2app} for saturating fluids. It is because the peak value is less subjective to the interference of connate water. The comparison of T_1/T_{2app} is presented in Figure 2.17. It is obvious that the T_1/T_{2app} provides amplified contrast compared to T_1/T_2 (shown as the bottom plot in Figure 2.15). This finding suggests the downhole logs have a better chance of separating fluids with different diffusivity by T_1/T_{2app} contrast.

It is readily observed that the methane and NGLs (i.e., ethane, propane, butane, and pentane) yield higher values of T_1/T_{2app} due to higher diffusivities in contrary to water and decane. Hence, a T_1/T_{2app} cutoff, denoted by the dashed lines in Figure 2.16 and Figure 2.17, around 2 can be applied to distinguish methane and NGLs from other fluids, such as water and decane, in the downhole logs.
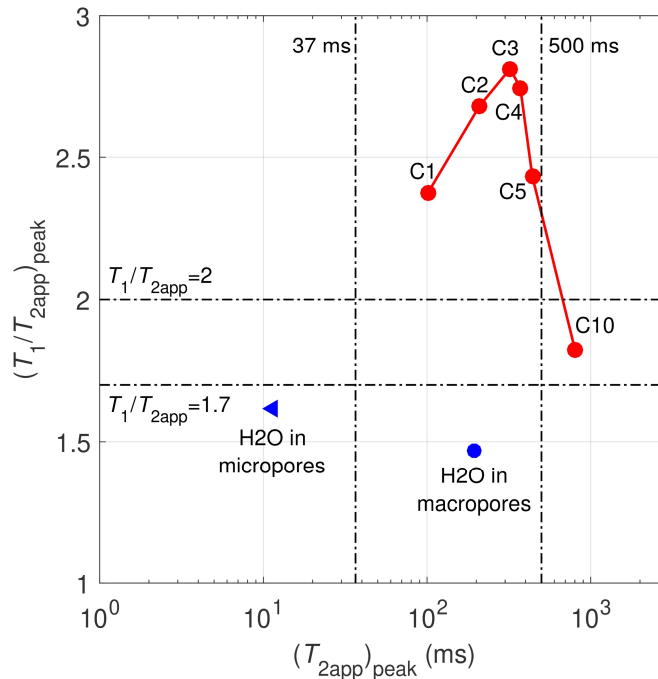
Figure 2.18 T_1/T_{2app} vs. T_{2app} of connate water at the peak of region B (blue triangle) and saturating fluids at the peak of region C (blue dot for macropore water and red dots for hydrocarbons). The horizontal and vertical dashed lines are cutoffs for fluid typing.

In addition to T_1/T_{2app} cutoff, T_{2app} can provide additional information for fluid typing. The peak values on the T_1/T_{2app} vs. T_{2app} correlation maps (not shown) are plotted in Figure 2.18. Figure 2.18 shows that NGLs have T_{2app} shorter than 500 ms. Therefore, one can apply a T_{2app} cutoff at 500 ms in addition to the T_1/T_{2app} cutoff to separate NGLs from water and decane. This can lead to a more robust result for fluid typing. By integrating T_1/T_{2app} cutoffs (e.g., 1.7 to separate connate water and 2 to separate methane and NGLs) and T_{2app} cutoff (500 ms) as suggested by Figure 2.18, one can also separate heavier alkanes, such as decane, from the others.

2.6. Restricted Diffusion and Pore Size

This sub-chapter presents $D\text{-}T_2$ measurements conducted in the laboratory on as-received and saturated cores. The diffusivities of light hydrocarbons are fitted to the Padé approximation to estimate the mean pore size, the heterogeneity length scale, and the tortuosity of the light hydrocarbon-filled porosity.

2.6.1. $D\text{-}T_2$ Measurements

Figure 2.19 shows the measurements of restricted diffusion on the cores at different states. Generally, the 2D $D\text{-}T_2$ measurements are challenging due to commonly short T_2 of tight rocks. For the unipolar stimulated-echo sequence (Mitchell et al. 2014) adopted here, the dead time $T_d = 25$ ms required to encode diffusion also acts as a dead time for T_2 measurements, which results in loss of

signal below $T_2 < 7$ ms (signal intensity attenuated to $\leq 5\%$, indicated by the dashed vertical line in Figure 2.19). The dead time T_d is composed of two parts as:

$$T_d = \Delta + \tau_{se},\qquad(2.19)$$

where Δ is the diffusion evolution time (a.k.a. observation time), and τ_{se} is the spin-echo time that consists of the gradient encoding time δ and some dead times. As mentioned in the Experimental Details sub-chapter, $\Delta = 14.7$ ms and $\tau_{se} = 10.3$ ms during the laboratory measurements. In this research, the T_2 from region A and B are mostly less than 7 ms where the diffusion measurement is limited, even though a small portion of region B can be seen. However, the signal from region C can be measured without significant loss. Hence, the restricted diffusivity at the peak of region C was picked for later analysis (see the following section).

The first thing to note from Figure 2.19 is that the measured diffusivities are all less than bulk values due to the restriction in the porous medium. Because of the interference from connate water, the 2D distributions in region C of liquid hydrocarbons are broad. Note that the bulk diffusivity of methane is around 250 $\mu m^2/ms$, which is out of range of y-axis in the 2D correlation map. Pure methane ("C1(D2O)") in Figure 2.19b generates a small peak with higher diffusivity which cannot be observed while the connate-water signal is present. It is also found that decane ("C10") follows the alkane correlation line (Lo et al. 2002).
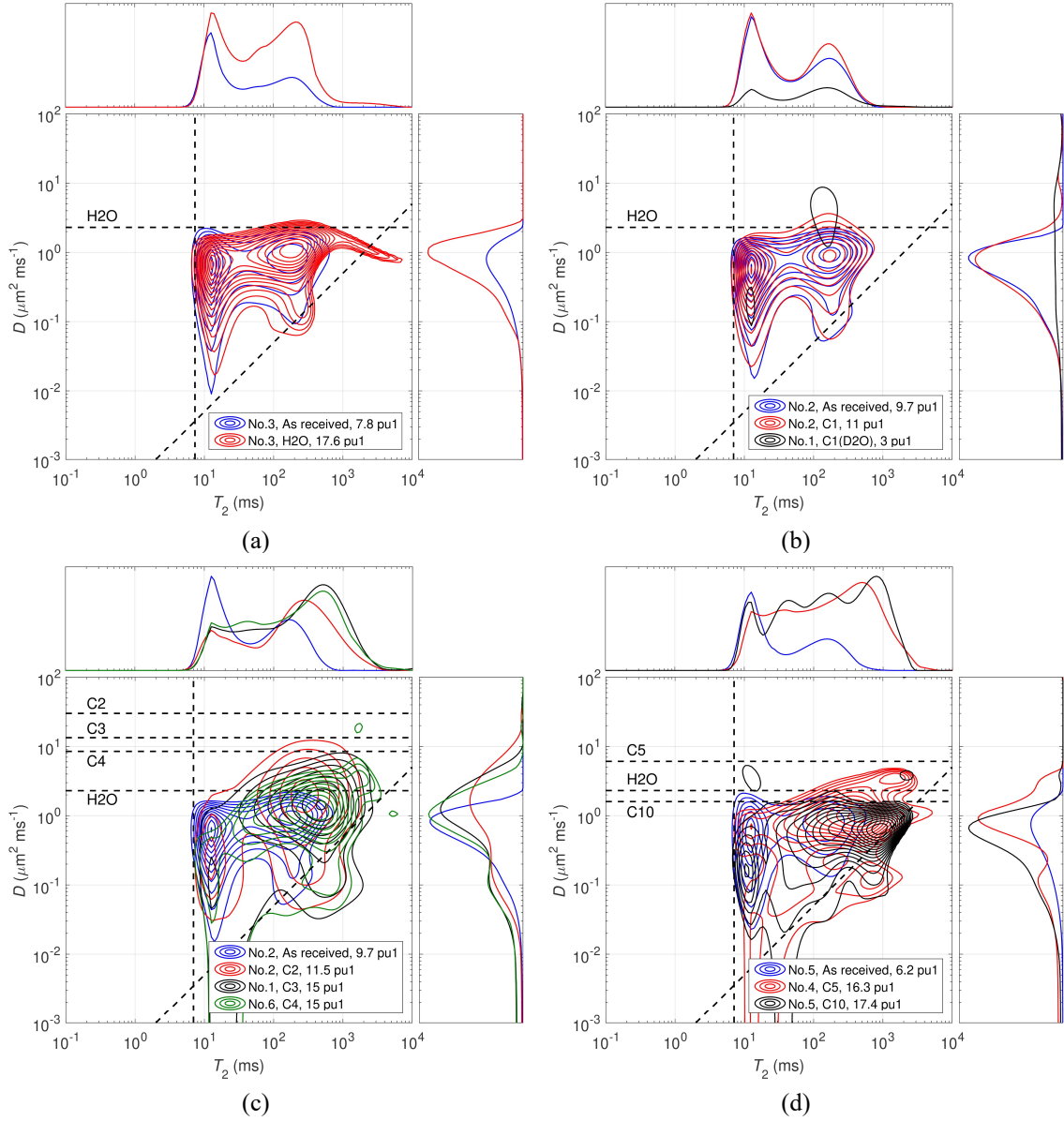
Figure 2.19 2D correlation maps of as-received and saturated cores, with D (diffusivity) on the y-axis, T_2 on the x-axis and porosity perpendicular to the page. For each subplot, the top subplot is the projected T_2 distribution. The right subplot is the projected D distribution. Dashed black horizontal lines are the bulk diffusivity of the fluids (labeled next to the lines) at laboratory conditions except for methane (which is out of range of the y-axis), dashed black diagonal line is the alkane correlation line (Lo et al. 2002), dashed black vertical line is to indicate the limitation from dead time (T_d=25 ms) inherent in the diffusion-encoding pulse sequence. The legend indicates the states of cores including core number, fluid name, and NMR porosity. "pu1" refers to porosity units assuming HI = 1.

2.6.2. Interpretation of Restricted Diffusion
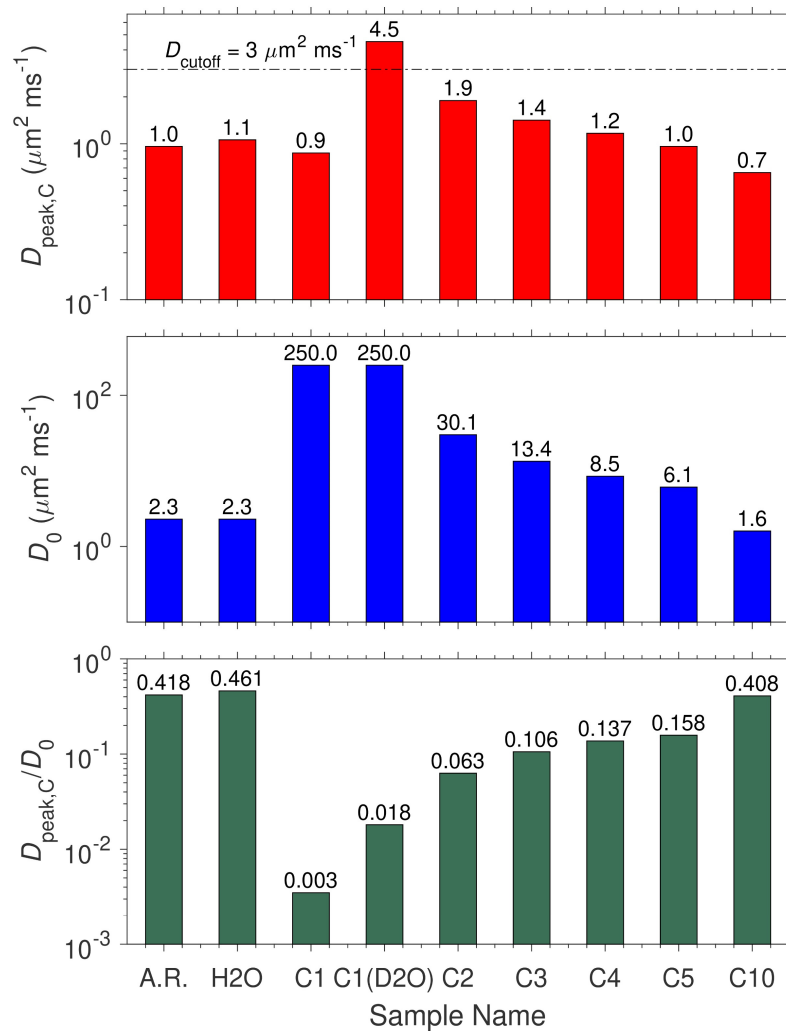
Figure 2.20 Comparison of restricted diffusivity, bulk diffusivity at laboratory conditions, and normalized restricted diffusivity of fluids at the peak of region C under laboratory conditions. The *y*-axis shows diffusivity. The *x*-axis indicates connate water (as-received) or saturating fluids. The horizontal dashed line in the top subplot is the proposed diffusivity *D* cutoff separating methane from the liquids in region C.

Figure 2.20 provides laboratory-measured restricted diffusivity at the peak

of region C, bulk diffusivity (under laboratory conditions) and normalized restricted

diffusivity with respect to the bulk diffusivity. The normalized restricted diffusivity

is a function of the restriction experienced during the diffusion evolution time.

Water and decane share similar bulk diffusivity, therefore almost the same amount

of restriction (i.e., the same normalized restricted diffusivity). Instead, methane and

NGLs have much higher bulk diffusivities, and therefore more restriction (i.e., lower

values of normalized restricted diffusivity compared with water or decane).

Furthermore, the restriction experienced by hydrocarbons becomes less as the

carbon number increases (e.g., as bulk diffusivity decreases). The measured

restricted diffusivity of methane suggests that a cutoff of 3 μm^2/ms (indicated by the

horizontal dashed line in the top subplot of Figure 2.20) can be implemented to

separate the methane, which is the only supercritical hydrocarbon, from the other

liquids in the laboratory diffusion measurements. Note that the extremely small

value of the normalized restricted diffusivity indicates methane is highly restricted

and approaching the tortuosity limit.
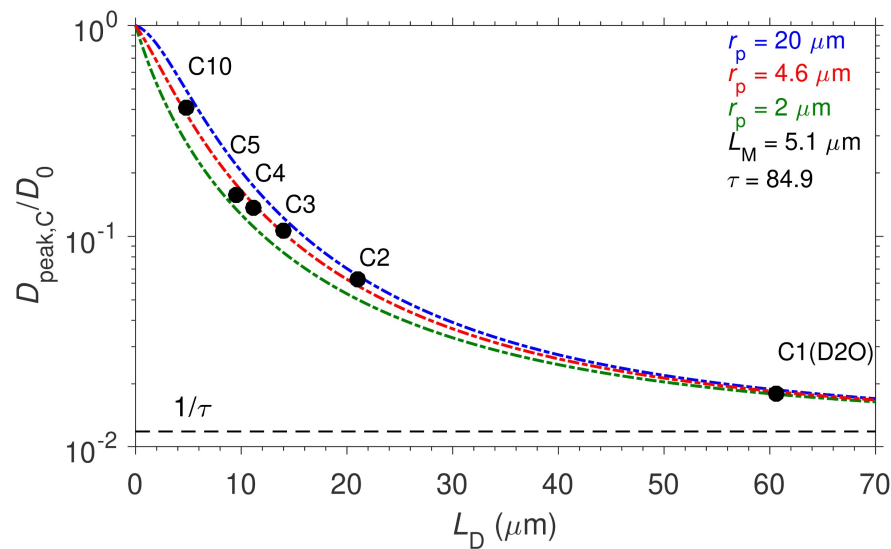
Figure 2.21 Normalized restricted diffusivity plotted against diffusion length L_D. The label indicates the source of each data point. Red dashed line is the model fit by Equation (2.21) (Hurlimann et al. 1994). The optimal three free-fitting parameters (r_p, L_M and τ) are listed in the top-right corner. Note that the blue and green dashed lines are generated by tuning the mean pore-radius r_p, while keeping the other two parameters the same as red, to visualize the sensitivity of the fit to the mean pore size. Also, note that the normalized restricted diffusivity of water is not included in the model fitting.

In Figure 2.21, the normalized restricted diffusivities of different hydrocarbons are plotted against diffusion length L_D calculated by:

$$L_D = \sqrt{D_0 \Delta}, \tag{2.20}$$

where D_0 is the bulk diffusivity at laboratory conditions and $\Delta = 14.7$ ms is the diffusion evolution time. Based on Padé approximation, Hürlimann et al. (Hurlimann et al. 1994) suggest that the normalized restricted diffusivity D/D_0 follows a relationship with diffusion length L_D:

$$\frac{D}{D_0} = 1 - \left(1 - \frac{1}{\tau}\right) \frac{\frac{4}{9\sqrt{\pi}} \frac{S}{V} L_D + \left(1 - \frac{1}{\tau}\right) \frac{L_D^2}{L_M^2}}{\frac{4}{9\sqrt{\pi}} \frac{S}{V} L_D + \left(1 - \frac{1}{\tau}\right) \frac{L_D^2}{L_M^2} + \left(1 - \frac{1}{\tau}\right)}, \tag{2.21}$$

where S is the pore surface area, and V is the pore volume, and we assume spherical pores that yield $S/V \approx 3/r_p$, where r_p stands for the pore radius of the hydrocarbon-filled space in region C. τ is the tortuosity of the hydrocarbon-filled space in region C, and can be expressed by:

$$\tau = \frac{D_0}{D_\infty}. \tag{2.22}$$

D_∞ is the diffusivity at the tortuosity limit. L_M is the macroscopic heterogeneity length scale. It should be noted that in the model suggested by Latour et al. (Latour et al. 1993), L_M is expressed by $(D_0\theta)^{1/2}$, where θ is the fitting parameter for a fluid. However, since there are different fluids with various D_0 involved in this work, the L_M is used as the fitting parameter as a whole, which means θ changes to accommodate different fluids.

Note that the data of saturating water is not plotted in Figure 2.21 because the water in macropores is diffusively coupled with the connate water in micropores, which affects the normalized restricted diffusivity.

According to the above model, there is a total of three free parameters: r_p, τ, and L_M. A least-square fit based on this model is applied to the $\log_{10}$-transformed restricted diffusivity shown in Figure 2.21. The final fit is presented in Figure 2.21 with r_p = 4.6 μm, L_M = 5.1 μm and τ = 84.9 as the optimized parameters. Another two curves are plotted by changing r_p to 20 μm and 2 μm, along with the final fit to demonstrate the sensitivity of this model to different pore size. The sensitivity analysis suggests this approach can be applied to estimate the pore size $r_p \leq 5$ μm with relatively high resolution.

It should be noted that the original model proposed by Hürlimann et al. (Hurlimann et al. 1994) is for the case of 100% saturation and 100% wetting. Minh et al. (Minh et al. 2015) suggest the equation should be changed accordingly if the investigated case is not 100% saturation nor 100% wetting. In this research, only the hydrocarbon-filled porosity (region C) is considered. Thereby the original model by Hürlimann et al. (Hurlimann et al. 1994) is still adopted in the present case.

The macroscopic heterogeneity length scale L_M is 5.1 μm, which is close to the pore radius of 4.6 μm. To our knowledge, there is no existing theory to interpret the L_M. Empirically the L_M should scale with pore-size as suggested by Latour et al. (Latour et al. 1993) and Hürlimann et al. (Hurlimann et al. 1994). More investigation into the physical meaning of L_M is required.
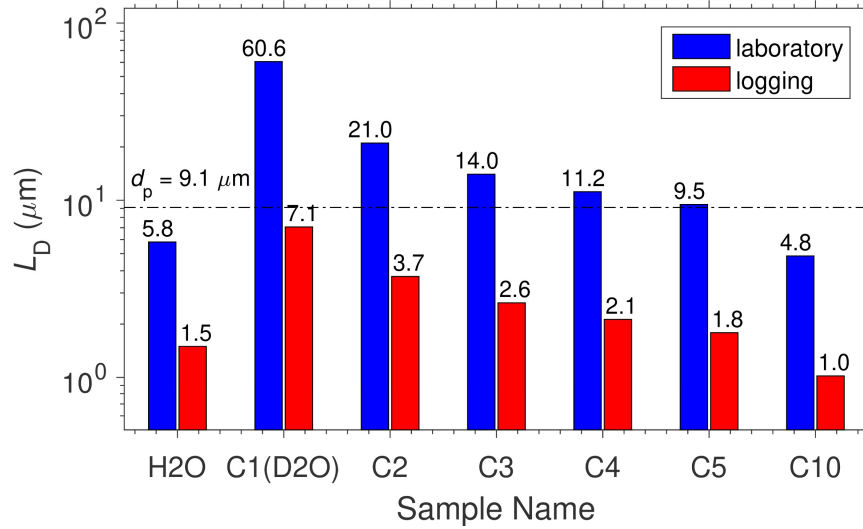
Figure 2.22 Comparison of diffusion length of saturating fluids during D-T_2 laboratory measurements (blue), and during T_{2app} measurements under logging conditions (red). The dashed horizontal line indicates the diameter of the pore space associated with region C estimated by the Padé fit as shown in Figure 2.21.

According to the above Padé fit acquired in the laboratory conditions, one can estimate the restricted diffusivities experienced by fluids during downhole logging by extrapolating the Padé fit to the downhole diffusion length L_D. To achieve this, the bulk diffusivity D_0 in laboratory conditions in Equation (2.20) is replaced by the bulk diffusivity in the reservoir conditions (as illustrated in the top subplot of Figure 2.23). Meanwhile, the diffusion evolution time in Equation (2.20) is changed to echo spacing T_E = 0.4 ms for the logging tool instead of Δ = 14.7 ms for the laboratory core analyzer.

The diffusion lengths on logging conditions are plotted in Figure 2.22 along with those at laboratory conditions for comparison. The pore diameter estimated by the Padé fit is also plotted as the dashed line. Note that the diffusion length of methane at logging conditions is close to the pore diameter, such that methane experiences restriction provided by the limited pore space in porous media. The

restriction is decreased as the diffusion length decreases. The restriction for fluids

other than methane is less significant, as suggested by the Padé fit. However, the

restriction is still not negligible. This is the reason why the restricted diffusivity is

applied in Equation (2.18) in place of the bulk diffusivity.
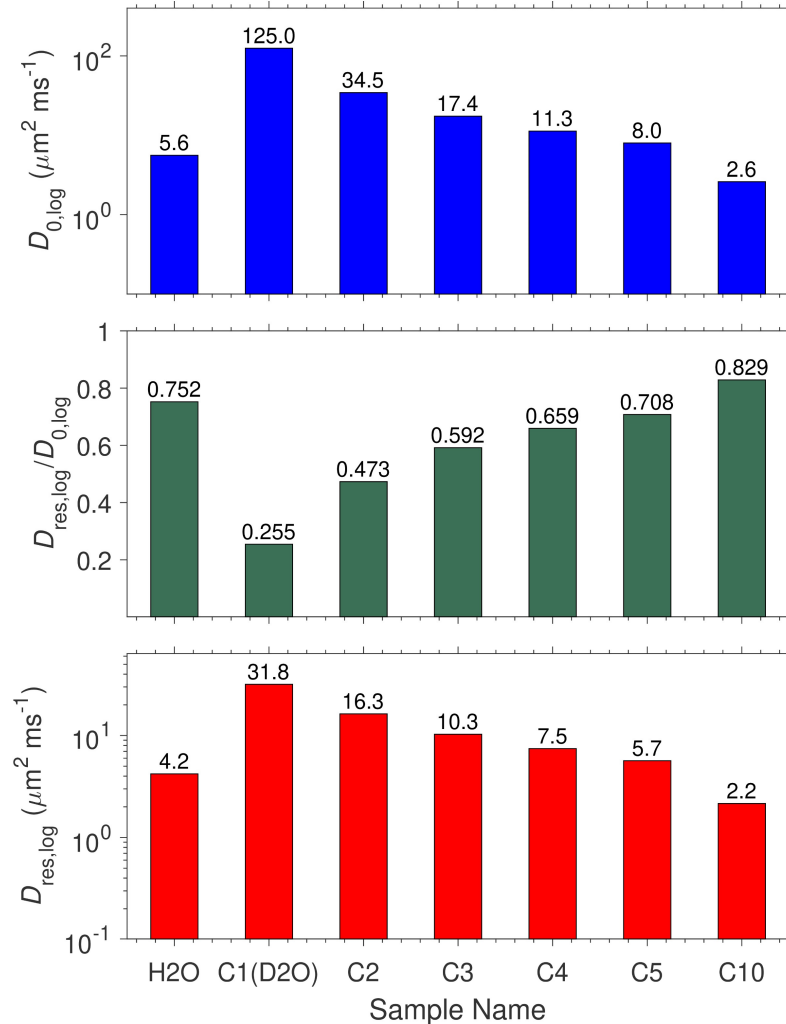
Figure 2.23 Bar chart of diffusivities during T_{2app} measurements under logging conditions. The top subplot is for the estimated bulk diffusivity of fluids in the reservoir as listed in Table 2.2. The middle subplot is of the extrapolated normalized restricted diffusivity based on the diffusion length L_D at logging conditions. The bottom subplot is the restricted diffusivity. For each subplot, the y-axis shows diffusivity. The x-axis indicates fluid types.

The middle subplot of Figure 2.23 illustrates the normalized restricted

diffusivity obtained by extrapolating the Padé fit to the diffusion length at logging

conditions. These values confirm that the diffusion of all fluids is restricted, to different extents. For example, methane is greatly restricted with a normalized restricted diffusivity of only 26%. The calculated restricted diffusivities are presented in the bottom subplot of Figure 2.23. The restricted diffusivities are implemented in the previous T_{2app} core-log calibration and T_1/T_{2app} subsections to simulate the NMR responses from the logging tool for composition estimation.

The pore radius derived by the Padé fit was then used to estimate the surface relaxivities, ρ_1 and ρ_2, of fluids in macropores (region C) under laboratory conditions by:

$$\begin{aligned} \rho_1 &= \frac{V}{ST_{1S}} = \frac{r_p}{3T_{1S}}, \\ \rho_2 &= \frac{V}{ST_{2S}} = \frac{r_p}{3T_{2S}}, \end{aligned}$$

(2.23)

where T_{1S} and T_{2S} are the surface relaxation components of T_1 and T_2, respectively. For water, methane, ethane, propane, and butane, T_{1S} and T_{2S} are approximated by T_1 and T_2 at the peak of region C where contributions from the bulk relaxation terms, T_{1B} and T_{2B}, are negligible. While for pentane and decane, the contributions from the bulk relaxation terms (i.e., $T_{1B} = T_{2B} = 3,754$ ms for pentane and $T_{1B} = T_{2B} = 1,350$ ms for decane by measurements with dissolved oxygen) are not negligible and thereby subtracted. The results are plotted in Figure 2.24. It is obvious that methane, including both "C1" and "C1(D2O)", undergoes higher surface relaxivities than the other liquid-state hydrocarbons. The longer alkanes experience lower surface relaxivities provided by the water-oil interface due to the mixed wettability.

It is remarkable that the surface relaxivity for T_1 of decane is nearly zero, which means T_1 is dominated by bulk relaxation. The surface relaxivities for water are close to methane. The high surface relaxivities of water in the macropores may be due to two reasons: 1) diffusive coupling exists between water in macro and micropores; 2) water is relaxed by the pore surface instead of a liquid-liquid interface, unlike hydrocarbons.
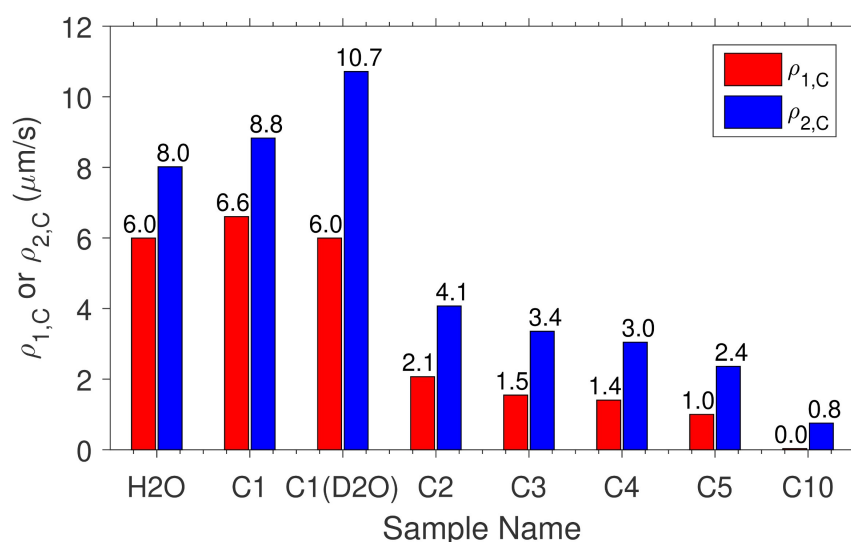
Figure 2.24 Comparison of surface relativities experienced by fluids in macropores (region C). The surface relaxivity of T_1 is plotted in red while the surface relaxivity of T_2 is plotted in blue.

2.7. Conclusions

In this work, tight rocks ($\sim$ 0.01 mD) from organic-rich chalk reservoir are saturated with various fluids, including water, methane, NGLs (ethane, propane, butane, and pentane) and decane. The laboratory NMR measurements provide T_2, T_1/T_2, and D for composition estimation, fluid typing and mean pore-size calculation.

The laboratory-measured T_2 distributions are transformed to downhole-measured T_{2app} distributions by simulating the magnetic-field gradient effect from the logging tools. The "numerically mixed" T_{2app} distribution successfully reproduces the downhole T_{2app} distribution from NMR logs, thereby yielding the downhole hydrocarbon composition. The core-log calibration indicates that methane, ethane, and propane are the main components in the reservoir, while butane and longer alkanes have negligible contributions.

The laboratory-measured T_1/T_2 ratio and simulated downhole-measured T_1/T_{2app} ratio both demonstrate a contrast between saturating fluids, which could in principle be exploited as a fluid-typing technique. The T_1/T_2 of hydrocarbons is higher than that of water, which suggests a $T_1/T_2 = 1.5$ cutoff to separate the hydrocarbons from water in core data. The magnetic-field gradient generated by logging tools amplifies the contrast in T_1/T_{2app} such that T_1/T_{2app} is more favorable for fluid typing. It is found that methane and NGLs yields $T_1/T_{2app} > 2$. As such, a $T_1/T_{2app} = 2$ cutoff for downhole logs is proposed to distinguish methane and NGLs from higher-order alkanes and water. T_{2app} cutoffs can also be used in addition to T_1/T_{2app} cutoffs for more robust fluid typing.

The laboratory-measured restricted diffusivity suggests that methane has higher diffusivity than all other liquids. The Padé approximation is used to fit restricted diffusivity as a function of diffusion length of the saturating hydrocarbons, all the way from C1 (with the highest degree of restriction) to C10 (with the lowest degree of restriction). According to the Padé fit, the mean pore-radius of the

hydrocarbon-filled porosity is estimated to be $r_p \approx 4.6$ μm. The heterogeneity length

scale $L_M \approx 5.1$ μm and the tortuosity $\tau \approx 84.9$ of the light hydrocarbon-filled porosity

are also estimated from the Padé fit.

2.8. Appendix I: Deuteration of Connate Water
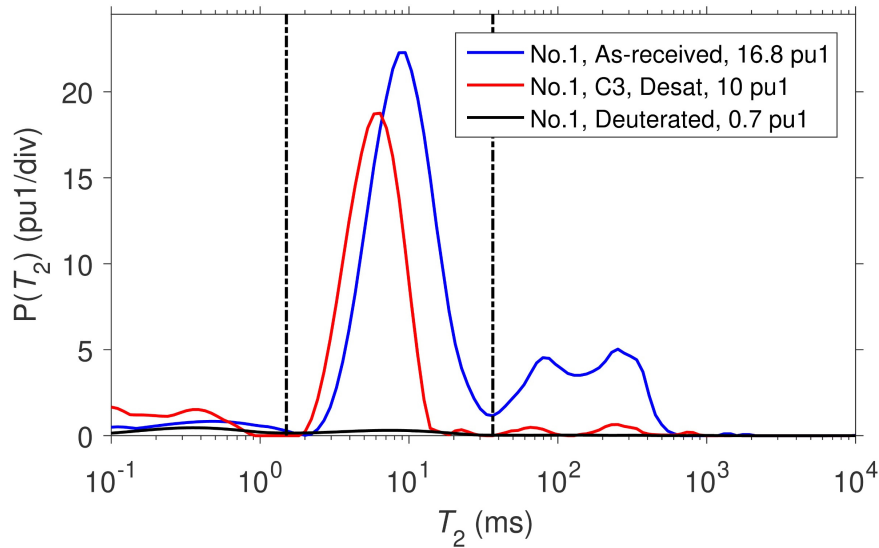
Figure 2.25 T_2 distributions of core No. 1 at three different states. The "As-received" is measured at the as-received state. The "C3, Desat" state is measured after propane desaturation. The "Deuterated" measured after "C3, Desat" is deuterated by D_2O. Dashed lines divide the T_2 distributions into three regions as in Figure 2.10. The legend indicates the core number, the state, and the NMR porosity. "pu1" refers to porosity units assuming HI = 1.

It has been mentioned in previous sections that the signals in region B and

region C in the as-received cores originate from connate water. This is confirmed by

the result of deuteration illustrated in Figure 2.25. Figure 2.25 focuses on the

measurements on core No. 1. The "As-received" is measured in the as-received state.

The "C3, Desat" is the state after desaturation of propane following the NMR

measurements. The NMR porosity dropping by $\sim$ 7 pu1 from "As-received" to "C3,

Desat" indicates that propane saturation and desaturation removes connate water,

which is discussed in detail in the following Appendix II. The "Deuterated" state

measured after "C3, Desat" is prepared by immersing core No. 1 in D_2O brine. The

"Deuterated" state shows nearly zero signal, which confirms that the signal in region

B and region C are both from connate water.

2.9. Appendix II: Expulsion of Connate Water

The loss of connate water and the shift of T_2 are results of connate water

mobilization and expulsion by the hydrocarbon saturation and desaturation, which

is confirmed by Figure 2.26. The comparison between T_2 distributions of the as-

received and de-saturated cores was shown in Figure 2.26. It is known that these

"twin" cores (No. 1 to No. 6) share similar T_2 distributions as indicated by Figure

2.10. Therefore, only the as-received No. 2 core is plotted as the baseline.
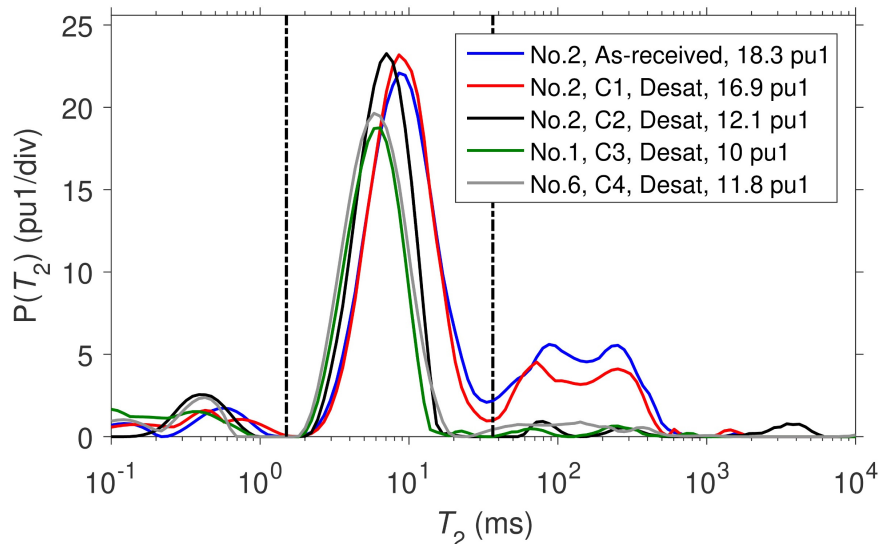
Figure 2.26 T_2 distributions of as-received and de-saturated cores. The "As-received" is measured at the as-received state. The "Desat"s states are measured after the desaturation of hydrocarbons. Dashed lines divide the T_2 distributions into three regions as in Figure 2.10. The legend indicates the core number, the state, and the NMR porosity. "pu1" refers to porosity units assuming HI = 1.

Figure 2.26 indicates the connate water is removed after hydrocarbon desaturation. As noticed, methane barely removes the connate water from the core. The amount of connate water expelled by hydrocarbons increases with the carbon-chain length. The connate water in region C is nearly zero after desaturation of ethane, propane, and butane. The trend of the amount of water-expulsion can be explained by the difference in mobility ratios of hydrocarbons, as proposed in the sub-chapter on T_2 distributions. Meanwhile, the shift of T_2 in region B can be explained by Equation (2.23). In the current case, S stays constant while V is reduced as a result of less connate water. This shift of T_2 after desaturation agrees with the T_2 shift observed in Figure 2.11 in saturated cores.

Figure 2.27 presents additional clear evidence of connate water expulsion. Figure 2.27a and Figure 2.27b are the 2D profile-T_2 correlation maps of water-saturated core No. 3 and decane-saturated core No. 5 with a resolution of 1.5 mm along the core plug axis. Note the T_2 distributions are homogeneous along the axial direction in the water-saturated core. In contrast, heterogeneity is found in the decane-saturated core, where the inlet has less fluid in region B at the expense of more fluids in region C. This is interpreted as connate water in micropores being displaced by decane near the inlet. The connate-water expulsion results from the very high pressure-gradient during the early stage of pressurization or depressurization, because the fluids are injected at constant pressure.

Based on the measurements on the de-saturated cores shown in Figure 2.26, the fluid saturations in region C are visualized in Figure 2.28. As indicated in Table

2.1, the hydrocarbon saturation of ethane and higher carbon-number alkanes (i.e.

"C2" to "C10") is conducted on the as-received cores, where the connate water in

region C is expelled by the alkanes during saturation. The C2-C10 alkanes occupy

nearly the entire pore space of region C, except for a water-film coating the pore

surface.

(a)   (b)
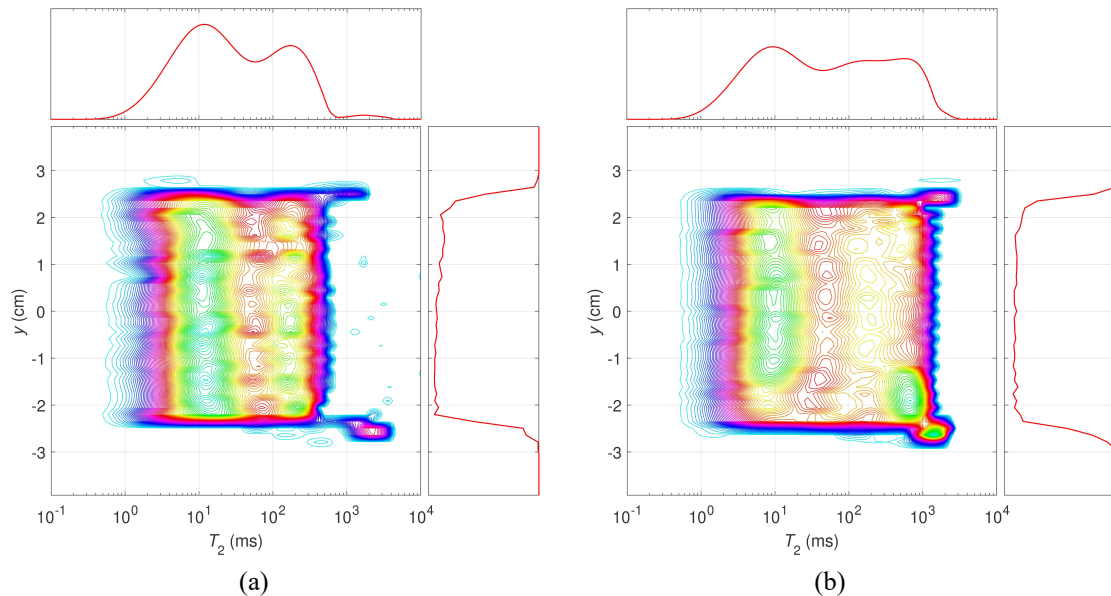
Figure 2.27 2D correlation maps of (a) water- and (b) decane-saturated cores, No. 3 and No. 5, with y (position in the axial direction) on the y-axis, T_2 on the x-axis and porosity perpendicular to the page. The top subplot is the projected T_2 distribution. The right subplot is the projected porosity profile.

However, in the case of methane saturation on the as-received core (i.e.,

"C1"), the connate water is not removed, such that the methane only partially

occupies the pore space of region C, and the NMR measurement on "C1" has

interference from the water signal. The "C1(D2O)" is conducted on the C3-

desaturated core, where the connate water has already been expelled by the

saturation and desaturation of propane, furthermore, the remaining water film in

the core is deuterated. Under these conditions, the methane takes up the entire pore

space, similar to the NGLs and decane. Therefore, the NMR distributions in region C for "C1(D2O)" and "C2" to "C10" are dominated by pure alkanes. This is the reason why "C1(D2O)" is used in the saturation estimation instead of "C1".
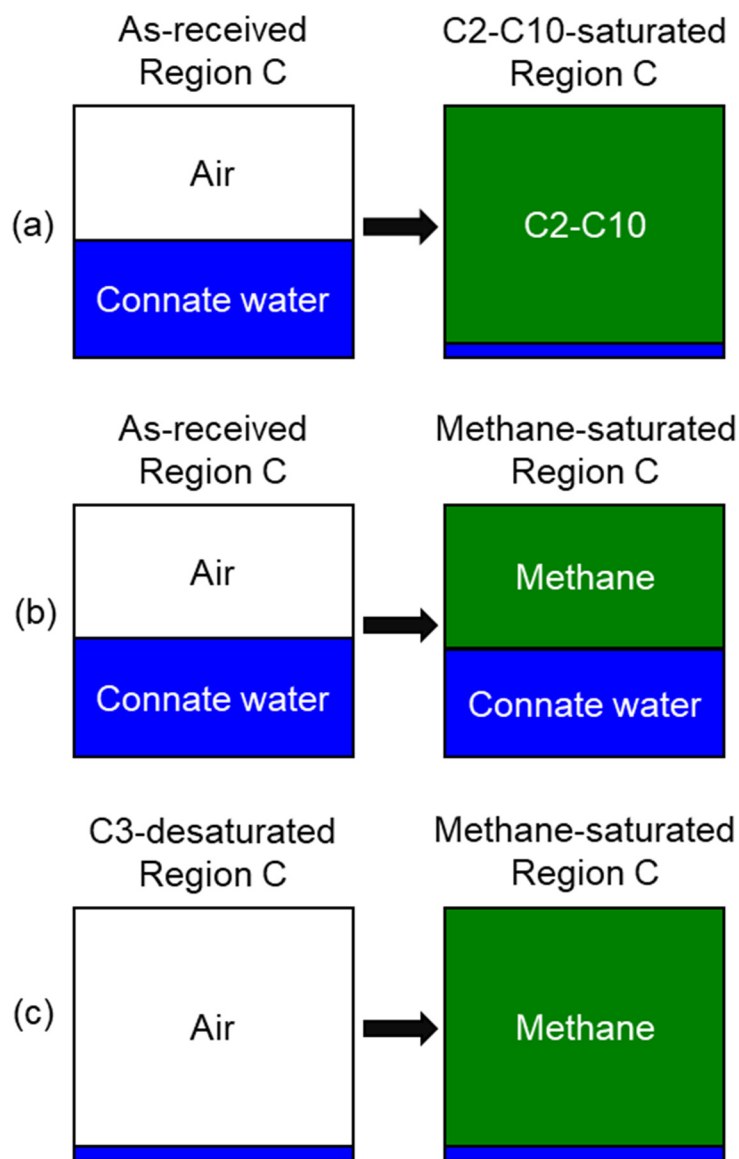
Figure 2.28 A visualization of fluid saturation in the pore space of region C before and after each hydrocarbon-saturation: (a) for NGLs and "C10"; (b) for "C1"; and (c) for "C1(D2O)". Note that the residual water of the "C3-desaturated" in subplot (C) is deuterated.

2.10. Appendix III: Saturation Estimation Workflow
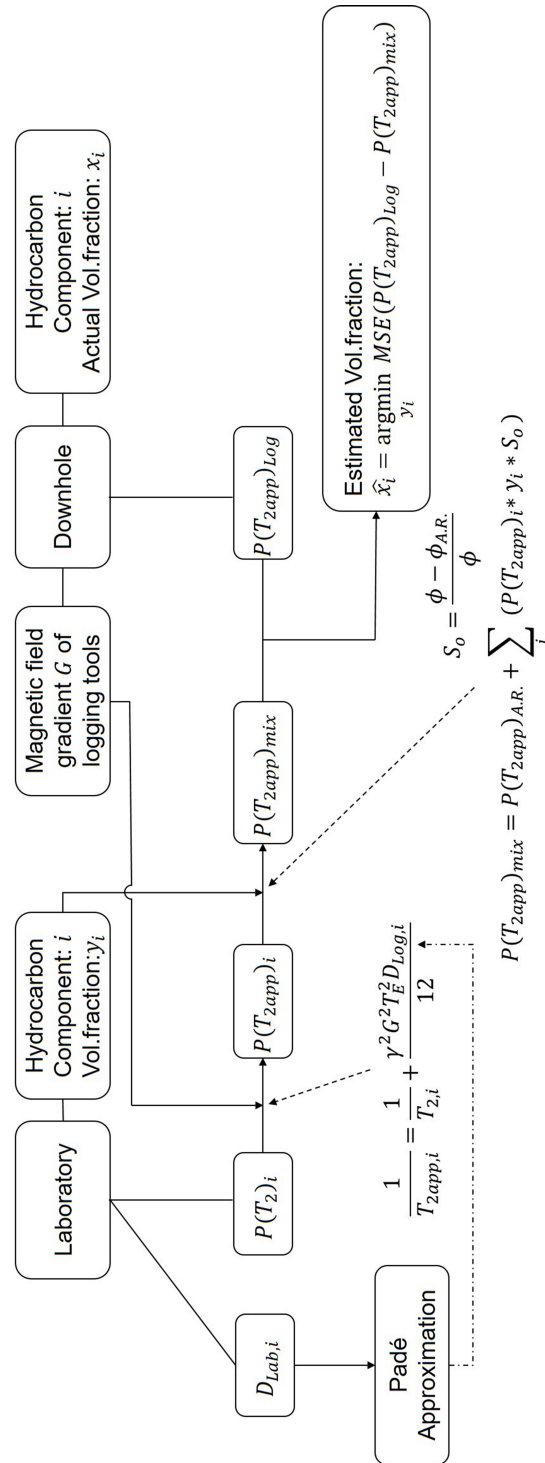
Figure 2.29 The workflow for the hydrocarbon-saturation estimation based on the T_{2app} distributions simulated using laboratory-measured T_2 distributions and the Padé approximation.

Figure 2.29 illustrates the workflow for the hydrocarbon-saturation estimation, the results of which are presented in Figure 2.12 and Figure 2.13. This estimation is based on the comparison between the simulated T_{2app} distributions from laboratory measurements and the downhole-logged T_{2app} distribution.

As mentioned in the previous section, the laboratory-measured T_2 distributions were converted to the T_{2app} distributions by considering the effect of magnetic gradients from the logging tool. It should be noted that the restricted diffusivities in the downhole conditions used in the simulation of T_{2app} distributions are different from the laboratory-measured restricted diffusivities, due to the difference in diffusion length (see Equation (2.20)). Therefore, the downhole restricted diffusivity is calculated by extrapolating the Padé approximation to the diffusion length for the logging tool.

As shown in Figure 2.29, the numerically mixed T_{2app} distribution from laboratory measurements is compared to the T_{2app} logging data. The difference in the T_{2app} distribution between the laboratory "mix" and the log is quantified by the mean squared error (i.e., MSE). The optimal volume fraction of each hydrocarbon is estimated by minimizing the MSE using a grid-search algorithm.

Chapter 3

NMR Characterization of Fluids in Organic-Rich Shale Part 1: Fluid Typing

Note that this chapter is based on and slightly adapted from a published journal article (Philip M. Singer, Chen, and Hirasaki 2016) and a master's thesis (Z. Chen 2018), where some portion is taken word-to-word.

3.1. Introduction

Over the past five years, low-field NMR has proven to be an evermore powerful technique for characterizing unconventional reservoirs such as gas shale and tight oil. In particular, case studies have shown that log interpretation in unconventional reservoirs is significantly enhanced by integrating NMR log data with NMR core-analysis data from the same well (Ramirez et al. 2011; Cao Minh et

al. 2012; Rylander et al. 2013; Jiang et al. 2013; Philip M. Singer et al. 2013; Lessenger et al. 2015). Important petrophysical quantities derived from such NMR core-log integration studies in organic shales include: total porosity, movable-fluid porosity, bound-fluid porosity, pore-size distribution, fluid typing, and saturation. Other NMR-derived petrophysical quantities such as viscosity, wettability, and permeability are more complex in organic shale, in part because of the low "nanodarcy" permeability of the organic-shale matrix, and also because of the associated difficulties with sampling live fluids downhole.

Of particular interest recently in unconventional reservoir characterization is an NMR log of the movable-hydrocarbon porosity. Such measurements and interpretation are challenging due to potentially overlapping signal in the 1D T_2 domain between bound water and bound hydrocarbon, i.e., bitumen, and movable water and movable hydrocarbons. A log of the movable-hydrocarbon porosity has a direct impact on calculating hydrocarbon reserves, and furthermore, can help identify sweet spots in the reservoir to optimize horizontal well placement for hydraulic fracturing and production. In response to this challenge, laboratory low-field NMR core-analysis in organic shale has proven that 2D T_1-T_2 correlation maps and the T_1/T_2 ratio can be a powerful tool for fluid typing and saturation (Jiang et al. 2013; Ozen and Sigal 2013; Rylander et al. 2013; Philip M. Singer et al. 2013; Kausik et al. 2015; Lessenger et al. 2015; Nicot et al. 2016; Marc Fleury and Romero-Sarmiento 2016), as well as for characterizing the kerogen itself (Birdwell and Washburn 2015). In response to these advances in laboratory interpretation, NMR logging tools have focused on improving the T_1-T_2 measurement (Anand et al. 2015;

Xiao et al. 2015). Of equal importance to laboratory studies is the use of simulations (Kathryn E. Washburn 2014; Chi, Heidari, and Garcia 2015) to better understand the NMR response in organic shale and the nature of the NMR surface-relaxation mechanism.

Laboratory studies of organic-shale core typically involve resaturating the as-received core with laboratory fluids, such as water, i.e., brine, light hydrocarbon-liquids (Odusina, Sondergeld, and Rai 2011; J. Chen et al. 2012) or even methane (R.F. Sigal and Odusina 2011; Kausik et al. 2011; A. Tinni et al. 2014; Richard Frederick Sigal 2015), without solvent extraction or cleaning the organic shale beforehand. Solvent extraction is generally only effective on crushed shale samples, and furthermore it has been shown to significantly alter the organic matter (Reeder et al. 2016). Laboratory resaturation studies can provide key insight into the NMR response of the various fluid types in the various pore types, provided some a-priori knowledge exists about the location of the resaturating fluid in the pore network. More specifically, the resaturating fiuid can potentially access the kerogen-hosted organic-matter (OM) pores and the inorganic inter-/ intraparticle (IP) pores (Loucks et al. 2012), since both are in general intimately mixed. As such, restoring the organic-shale core with the same saturation conditions as the undisturbed reservoir can be a challenge. In addition to the potentially complex saturation history of the organic-shale core, it is also known that there is potential for wettability alteration during hydraulic fracturing due to the presence of functionalized groups on the kerogen surface (Hu et al. 2015). These complexities can, in certain situations, present challenges to the interpretation of low-field NMR

measurements in organic shale; however, a deeper, more fundamental understanding could significantly improve the interpretation of NMR log and core data.

In light of these challenges, this chapter presents a fundamental study into the 2D low-field NMR response of fluids in the organic-matter pores of saturated kerogen isolates. Experimenting with isolates ensures complete control and knowledge of the fluid type and pore type, without complications from saturation history or wettability alteration. This study is to validate the use of 2D T_1-T_2 correlation maps and the T_1/T_2 ratio for fluid typing in organic shale by comparing the response of hydrocarbons in kerogen isolates with water in clay isolates. This laboratory scenario is a similar fluid arrangement to what a downhole NMR log would measure in the undisturbed organic-shale reservoir.

3.2. Experiment

The NMR data were acquired on an Oxford Instruments GeoSpec2 rock-core analyzer at a resonance frequency of $\omega/2\pi = 2.3$ MHz, which is similar to wireline NMR logging tools. All measurements were made at 30 °C and ambient pressure. The 2D T_1-T_2 data were acquired with 32 log-spaced inversion-recovery steps ranging from 0.1 to 1,000 ms (typically), followed by a CPMG train with an echo spacing of $T_E = 0.1$ ms. The 2D maps were processed using the fast inverse-Laplace transform (Venkataramanan, Song, and Hürlimann 2002) with 120 log-spaced bins for T_1, and T_2. The units of the relaxation distributions are in p.u./div, i.e., porosity

units per division, where for instance, for T_2, div $= \log_{10}\left(T_{2,i+1}\right) - \log_{10}(T_{2,i})$ is independent of the bin index i.

The organic shale used in this study was an outcrop Kimmeridge oil shale from the coast of Dorset, UK. This quarry rock is known for its high total organic carbon (TOC), and has been used in low-field NMR and SEM experimental studies (Curtis et al. 2010), as well as for molecular dynamics simulations (Ungerer, Collell, and Yiannourakou 2015). The Kimmeridge oil shale is from the Late Jurassic Period, and it is the primary source rock for the North Sea oil. RockEval (pyrolysis) data on the as-received shale yield: hydrogen Index $= 684$ mg-HC/g-TOC, oxygen Index $= 12$ mg-CO_2/g-TOC, $T_{max} = 424$ °C, Leco TOC $= 10.1$ wt%, thereby indicating an immature Type II kerogen. XRD data on the as-received shale yield: 57 wt% clays, 19 wt% quartz, 16 wt% carbonates, and 5 wt% pyrite. The grain density is $\rho_g = 2.16$ g/cm^3 and gas porosity is $\phi_{gas} = 7.1$ p.u..

The kerogen was then isolated by HCl/HF acid digestion, followed by the sink-float separation technique. Inductively coupled plasma indicated 11.7 wt% pyrite in the isolated kerogen (3.1 vol% in the matrix, equivalently), similar to what was previously observed in isolated kerogen from the Kimmeridge oil shale (Acholla and Orr 1993). SEM images of the pyrite indicated large, ~3 µm, crystals of pyrite localized in clusters, i.e., not on the kerogen surface. Further kerogen isolation from pyrite with a chromous solution was not attempted due to the uncertainty in coating the kerogen surfaces with paramagnetic chromium ions.

The isolated kerogen powder was then dried at 110 ℃, then pelletized in a pellet press at 60,000 psi with a pellet diameter of 25 mm, a height of ~4 mm, and a mass of ~2.5 g. The kerogen pellet was then placed in a pressure saturator, exposed to vacuum, and pressure saturated with high-purity n-heptane at 5,000 psi hydrostatic pressure for 16 hours. Similar saturations were obtained by vacuum followed by n-heptane saturation at ambient pressure.

A significant amount of swelling in the pellet's bulk volume occurred ~55% after n-heptane saturation, possibly as a result of disjoining pressure effects similar to n-heptane on carbon (Hirasaki 1993). An alternative explanation for the swelling is that kerogen, as organic matter, behaves like a polymer when being mixed with small molecules like water or heptane. Similar swelling effects can often be observed in polymer and proteins. Such mixing process can often be described by the Flory-Huggins theory (Flory 1942; Huggins 1942).

Using the total NMR porosity of the heptane-saturated pellet, the bulk volume of the swollen pellet, and the dry pellet mass before saturation, a grain density for pure kerogen of $\rho_{\text{ker}} = 1.21$ g/cm^3 was determined (with the pyrite contribution removed). This kerogen density is consistent with previous experiments and simulation (Ungerer, Collell, and Yiannourakou 2015).

A twin kerogen pellet was saturated with DI-water, using vacuum followed by 5,000 psi hydrostatic pressure for 16 hours. The same pellet was then used for pressure saturating with partially deuterated water (named "D$_2$O" fluid for short), consisting of a 90% D$_2$O:10% H$_2$O mix with an NMR hydrogen index of 0.10. All

other fluids were processed with an NMR hydrogen index of 1.00, since the heptane,
DI water and low-salinity brine used in this research all yield NMR hydrogen
indexes very close to unity. The NMR porosity of the kerogen pellets was computed
using the swollen bulk volume. The NMR measurements were made soon after
saturation (within hours), then the pellets were crushed and taken for BET surface-
area and SEM imaging. The BET adsorption isotherm data were acquired using N_2
after vacuum drying at 110 °C for 16 hours.

NMR relaxation and diffusion of the bulk fluids were also measured. In all
cases, the relaxation times T_{1B} and T_{2B} were reduced from their pure-component
values due to the effects of dissolved oxygen (Lo et al. 2002). In the case of *n*-
heptane, $T_{1B} = T_{2B} = 1,910$ ms and $D_0 = 3.43$ μm^2/ms. In the case of DI-water,
$T_{1B} = T_{2B} = 2,750$ ms and $D_0 = 2.31$ μm^2/ms. In the case of D_2O, $T_{1B} = T_{2B} =$
5,460 ms and $D_0 = 2.31$ μm^2/ms. The NMR bulk-properties of water and heptane
are very similar, which stems from the fact that their bulk viscosities are also similar
~1 cP at ambient conditions. The D_2O data will be discussed in the following
chapter.

Clay isolates of kaolinite, Ca-montmorillonite, and Na-montmorillonite were
obtained from the Clay Minerals Society. The clays were saturated by pelletizing the
clay powder with 3 wt% NaCl brine in the pellet press (Matteson et al. 2000), at a
pressure of 40,000 psi.

The organic-shale rock was re-saturated by crushing the rock in a mortar and pestle, pulling a vacuum, then pressure saturating with n-heptane at 5,000 psi or with 6 wt% brine (equal parts NaCl:KCl:CaCl₂) at 5,000 psi.

3.3. Fluid Typing

3.3.1. Heptane in Kerogen vs. Water in Kerogen

The results for heptane in kerogen are shown in Figure 3.1. It should be noted that there was negligible signal from dry kerogen or probe background on the scale of any plots in this manuscript. The data in Figure 3.1 indicate a two-peak structure in T_2. As shown in the T_2 projection, the two-peak structure has a minimum in amplitude at 1.5 ms, which is used to define the cutoff between the two peaks at $T_{2,\text{cutoff}} = 1.5$ ms (dashed vertical line). The slow-relaxing pores with $T_2 > T_{2,\text{cutoff}}$ are interpreted as fluid in intergranular kerogen pores created during pelletization, and given the symbol (>). The fast-relaxing pores with $T_2 < T_{2,\text{cutoff}}$ are interpreted as intragranular pores or "dissolved" fluid in kerogen and given the symbol (<). As indicated in Table 3.1, the porosity for the heptane-saturated intergranular pores is $\phi_> \sim 36$ p. u., which is consistent with a random bead-pack, while the porosity for dissolved heptane ($\phi_< \sim 8$ p. u.) is ~ 4 times less. Also indicated in Table 3.1 are the $T_{2,\text{peak}}$ values at the peak, i.e., mode, of the two distributions, where $T_{2,\text{peak},<}$ is ~ 84 times shorter than $T_{2,\text{peak},>}$.

The data for heptane in kerogen in Figure 3.1 indicates a large variation in T_1/T_2 ratio across the T_2 spectrum. This variation can be quantified by the $(T_1/T_2)_{\text{LM}}$

line, defined as the log-mean average along the T_1/T_2 direction at a specific T_2 location, repeated across the entire T_2 spectrum. Figure 3.2 shows the $(T_1/T_2)_{\mathrm{LM}}$ line (upper) across the T_2 spectrum (lower) for heptane in kerogen.
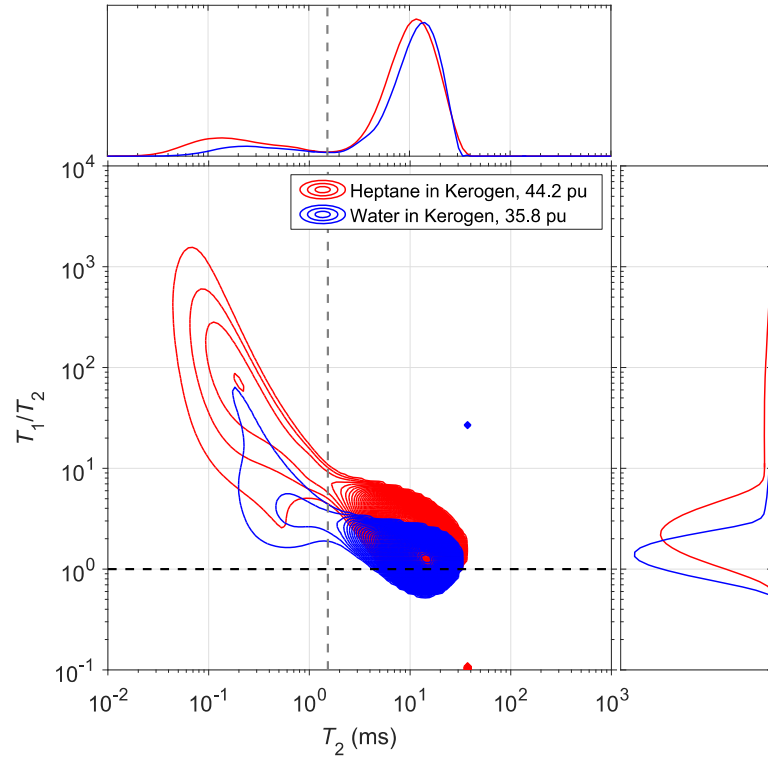
Figure 3.1 2D correlation map with T_1/T_2 ratio on the y-axis, T_2 on the x-axis and porosity coming out of the page. The top subplot is the projected T_2 data; the right subplot is the projected T_1/T_2 ratio data. The legend indicates fluid name, matrix name, and total fluid-porosity. The dashed black horizontal line is the T_1/T_2 = 1 line. The dashed grey vertical line is $T_{2,\mathrm{cutoff}}$ = 1.5 ms separating dissolved fluid(<) from intergranular pores (>). Dry kerogen showed negligible signal on the scale of this plot.

What is readily clear from the data in Figure 3.1 and Figure 3.2 is the pronounced heterogeneity in the spin dynamics of heptane in the kerogen pore-network. This finding is different to previously reported data in the re-saturated organic-shale core, where the light/movable hydrocarbon is generally observed as a single peak in the T_1-T_2 map, usually in the vicinity of $T_1/T_2 \sim 4$ (Ozen and Sigal 2013). The single-peak observation opposed to the two-peak feature may result

from two possibilities: (1) the T_2 of the fast relaxing peak is too short to be detectable; (2) the intergranular fluid signal is dominating in the T_2 distribution because of the high intergranualr porosity as a result of ground-up samples (i.e., kerogen slurry when being saturated) in use.
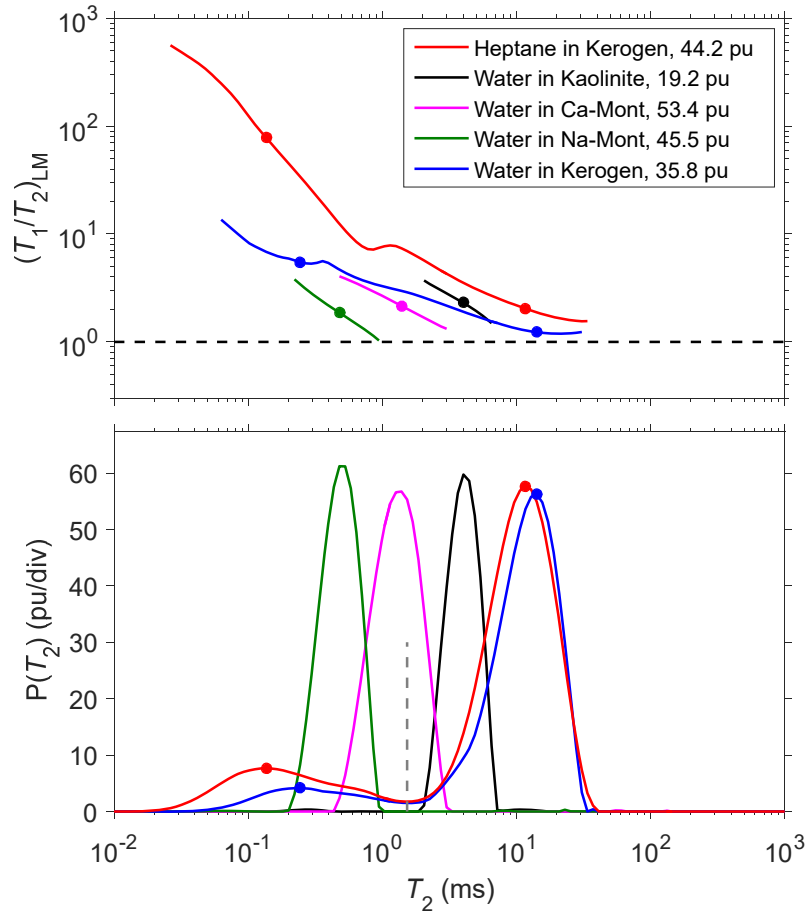
Figure 3.2 The upper figure is the log-mean $(T_1/T_2)_{LM}$ curve vs. T_2 obtained from the 2D correlation maps, and dashed horizontal line is the $T_1/T_2 = 1$ line. The lower figure is the projected T_2 data from the 2D correlation maps. The legend indicates fluid name, matrix name, and total fluid porosity. For kerogen data (red and blue), the dots in the upper and lower figures correspond to $T_{2,peak}$ and $(T_1/T_2)_{peak}$ listed in Table 3.1, and the dashed grey vertical line is $T_{2,cutoff} = 1.5$ ms separating dissolved fluid ($<$) from intergranular pores ($>$). For the clay data, the dots in the upper figure are the T_{2LM} and $<T_1/T_2>$ listed in Table 3.2. Ca-mont and Na-mont T_2 distribution amplitudes have been reduced by a factor of 1/2 for better comparison.

As shown in Figure 3.2 and indicated in Table 3.1, the data indicate that $(T_1/T_2)_{LM}$ at the peak for dissolved heptane signal, defined as $(T_1/T_2)_{peak,<} \sim 78$, is

~39 times greater than $(T_1/T_2)_{\text{peak,>}}$ ~2 at the peak for intergranular pore signal. As discussed in the next chapter, the larger T_1/T_2 ratio can be explained by the dissolution of heptane into the kerogen granule.

Also shown in Figure 3.1 and Figure 3.2 are data for water in kerogen. The motivation for studying water in kerogen is twofold: (1) water has less affinity to organic-matter surfaces than heptane, which makes it a good tool for probing the NMR response as a function of surface affinity; (2) it is generally believed that hydraulic fracturing may cause water uptake in the organic-matter pores as a result of wettability alterations in the presence of surface functionalized-groups (Hu et al. 2015). If an NMR log were to be measured before and after fracturing, NMR fluid typing could potentially determine the uptake of fracture water in the organic shale.

What is readily clear from the water data in Figure 3.1 is that the T_2 distribution of the intergranular pores (>) is similar to that of heptane. As shown in Figure 3.2 and indicated in Table 3.1, the $T_{2,\text{peak,>}}$ value at the peak of the water distribution is comparable to that of heptane, and with comparable porosity $\phi_>$. The dissolved-fluid peak (<) on the other hand, indicates that $\phi_<$ for water ($\phi_< = 4$ p. u.) is ~2 times lower than heptane ($\phi_< = 8$ p. u.), and the $T_{2,\text{peak,<}}$ value at the peak of the water distribution is ~2 times longer than for heptane. The lower porosity $\phi_<$ for water compared with heptane is expected since water may not be dissolved in kerogen. The kerogen pellet is dried, vacuumed and pressure saturated with water, however, it should be noted that the kerogen pellet has been saturated with pentane before drying. Therefore, it is most likely that the dissolved-fluid

signal is from the remaining pentane that is not completely dried before water

saturation. The higher heptane uptake in the dissolved-fluid region compared to

water is also consistent with the mixing process described by the Flory-Huggins

theory (Flory 1942; Huggins 1942).

Figure 3.2 shows that there is a significant contrast in $(T_1/T_2)_{LM}$ between

heptane and water, especially towards shorter T_2 where they are increasingly

separated. As indicated in Table 3.1, the dissolved-fluid peak ($<$) indicates that

$(T_1/T_2)_{peak,<}$ for heptane is ~14 times greater than water, which makes for a clear

contrast mechanism for fluid typing at short T_2. The intergranular peak ($>$)

indicates that $(T_1/T_2)_{peak,>}$ for heptane is only ~2 times greater than water,

however, the $(T_1/T_2)_{LM}$ is clearly separated between heptane and water across the

entire T_2 spectrum.

Table 3.1 Summary of porosity ϕ, $T_{2,peak}$, and $(T_1/T_2)_{peak}$ ratio for absorbed (or dissolved) fluid ($T_2 < 1.5$ ms) and intergranular pores ($T_2 > 1.5$ ms), for heptane, water, or D_2O in kerogen.

Fluid	Heptane	Water	D_2O
Matrix	Kerogen	Kerogen	Kerogen
$\phi_< (\mathbf{p.u.})$	8.3	4.0	3.2
$\phi_> (\mathbf{p.u.})$	35.9	31.8	31.7
$T_{2,peak,<}$	0.14	0.24	0.48
$T_{2,peak,>}$	11.7	14.2	18.9
$(T_1/T_2)_{peak,<}$	78.1	5.5	6.5
$(T_1/T_2)_{peak,>}$	2.0	1.2	1.0

3.3.2. Heptane in Kerogen vs. Water in Clays

The results for water in a selection of clays are shown in Figure 3.3, including kaolinite, Ca-montmorillonite, and Na-montmorillonite. The data agree well with previous NMR findings at higher magnetic-field (M. Fleury et al. 2013), except for the signal from hydroxyls, which are not detectable in the present case due to the longer echo spacing at the lower magnetic field. Note that in both datasets, the water in kaolinite has longer T_2 relaxation than the commonly accepted ~3 ms cutoff for clay-bound water in (shaly) sandstones, while the montmorillonites lie < 3 ms.

In contrast to the data for heptane in kerogen, the data for water in clay in Figure 3.3 clearly indicate a narrow single-peak T_2 distribution, in conjunction with a narrow single-peak T_1/T_2 distribution. The average values $\langle T_1/T_2 \rangle$, computed from the log-mean average of the projected T_1/T_2 data in Figure 3.3, show a narrow range $\langle T_1/T_2 \rangle = 1.9$ to 2.3 for the clays, as listed in Table 3.2. Figure 3.2 shows the $(T_1/T_2)_{\mathrm{LM}}$ vs. T_2 for a better comparison of the 2D correlations. What is remarkable in Figure 3.2 is that $(T_1/T_2)_{\mathrm{LM}}$ for heptane in kerogen is consistently greater than for water in clays, across the entire T_2 spectrum. This indicates that fluid typing by T_1/T_2 contrast is possible with NMR logs, which measures reservoir fluids in their undisturbed state, i.e., hydrocarbons in organic-matter pores and water in the inorganic-matter pores, provided no invasion has occurred. What is required to interpret the NMR log are NMR core-data on saturated isolates, such as in Figure 3.2, from which an optimal cutoff line in T_1/T_2 vs. T_2 can be determined which separates hydrocarbons from water. The optimal cutoff for the particular reservoir in question

could then be implemented on the 2D NMR logs to yield an NMR saturation log. For the present case, according to Figure 3.2, the same cutoff could be used to separate wetting water in kerogen originating from water-based-mud invasion or hydraulic-fracture water.
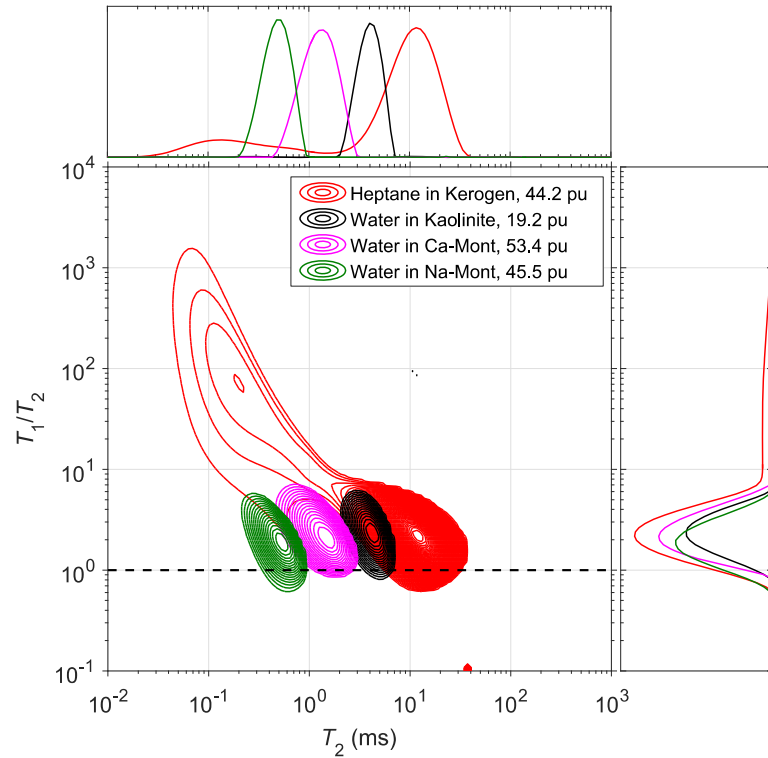
Figure 3.3 2D correlation map with T_1/T_2 ratio on the y-axis, T_2 on the x-axis, and porosity coming out of the page. The top subplot is the projected T_2 data; the right subplot is the projected T_1/T_2 ratio data. The legend indicates fluid name, matrix name, and total fluid porosity. Ca-mont and Na-mont projected amplitudes have been reduced by a factor of 1/2 for better comparison. The dashed horizontal line is the $T_1/T_2 = 1$ line.

It should be noted that the minimum detectable T_2 in NMR logging tools is typically 0.3 ms, which implies that the dissolved heptane in kerogen ($T_{2,\text{peak},<} = 0.14$ ms) is not fully detectable downhole. However, downhole logging is acquired at reservoir temperatures, which will typically increase the relaxation times from their ambient values by a factor 2 to 3 (Philip M. Singer et al. 2013). This implies that dissolved heptane in kerogen is potentially measurable downhole and that the

aforementioned log calibration study with core should be conducted at reservoir temperatures in the laboratory.

3.3.3. Re-saturated Organic Shale
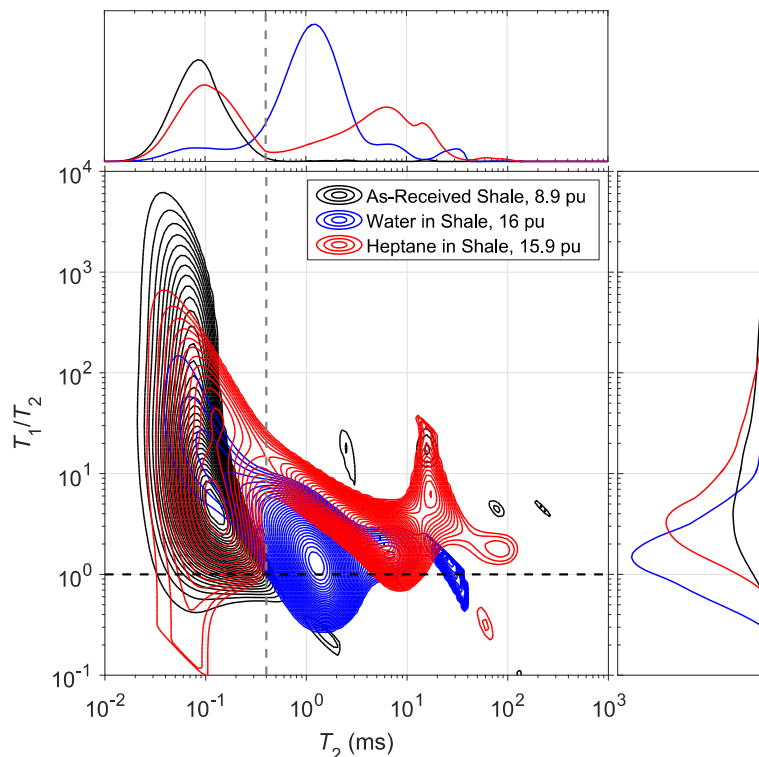
Figure 3.4 2D correlation map with T_1/T_2 ratio on the y-axis, T_2 on the x-axis and porosity coming out of the page. The top subplot is the projected T_2 data; the right subplot is the projected T_1/T_2 ratio data. The legend indicates fluid name, matrix name, and total fluid porosity. The dashed horizontal line is the $T_1/T_2 = 1$ line. The dashed grey vertical line is the cutoff separating water ($T_2 < 0.4$ ms) from re-saturated heptane ($T_2 > 0.4$ ms) in the case of "heptane in shale" data.

Further insight into the isolates results can be gained by re-saturating the original organic shale with heptane and water. Figure 3.4 shows the 2D correlation map of as-received shale, water re-saturated shale, and heptane re-saturated shale. The as-received data show an extended peak along the T_1/T_2, with a short $T_2 \sim 0.1$ ms. The as-received signal is reminiscent of partially water-saturated clays, which have their external, i.e., interparticle, clay-water gone, but their internal, i.e.,

interlayer, clay-water in place. This is corroborated by the water re-saturated data which shift the entire spectrum to longer $T_{2LM} = 1.1$ ms, and increases the fluid porosity by an amount comparable to $\phi_{gas} = 7.1$ p. u.. The re-saturated water fills in the external pores, and fast exchange between internal and external waters results in a single peak at longer relaxation times.

Re-saturating the shale with heptane has a completely different effect, namely the internal clay-water signal remains, while the resaturated heptane fills in the empty external clay pores. This is corroborated by the fact that the re-saturated heptane porosity is comparable to $\phi_{gas} = 7.1$ p. u.. Since the two fluids are immiscible, the internal-water peak remains largely undisturbed. Using this hypothesis of fluid distribution, a T_2 cutoff of 0.4 ms is used to separate internal clay-water ($T_2 < 0.4$ ms) from resaturated heptane ($T_2 > 0.4$ ms), shown as the dashed vertical line in Figure 3.4. Once the heptane signal has been isolated, the resulting map yields the log-mean values for heptane in shale listed in Table 3.2. Since the fluid separation is approximate, Table 3.2 lists approximation signs by the heptane in shale data, and the $\langle T_1/T_2 \rangle$ is a lower bound given that there could be heptane signal below $T_2 < 0.4$ ms, which would tend to increase the heptane $\langle T_1/T_2 \rangle$.

The projected T_1/T_2 for heptane in shale (cut using $T_2 > 0.4$ ms) is shown in the upper plot in Figure 3.5, alongside the projected T_1/T_2 data for water in shale. As listed in Table 3.2, the heptane in shale clearly shows a larger average $\langle T_1/T_2 \rangle$ compared to water in shale. In the lower plot of Figure 3.5 are the heptane in

kerogen and the water in clay (Na-montmorillonite) for comparison. The same trend

is found between upper and lower plots, namely $\langle T_1/T_2 \rangle \sim 4$ for heptane is a factor of

~ 2 times larger than $\langle T_1/T_2 \rangle \sim 2$ for water. These findings corroborate with those

found previously in re-saturated organic shale (Ozen and Sigal 2013), which

validates T_1/T_2 as a contrast tool for fluid typing in organic shale.
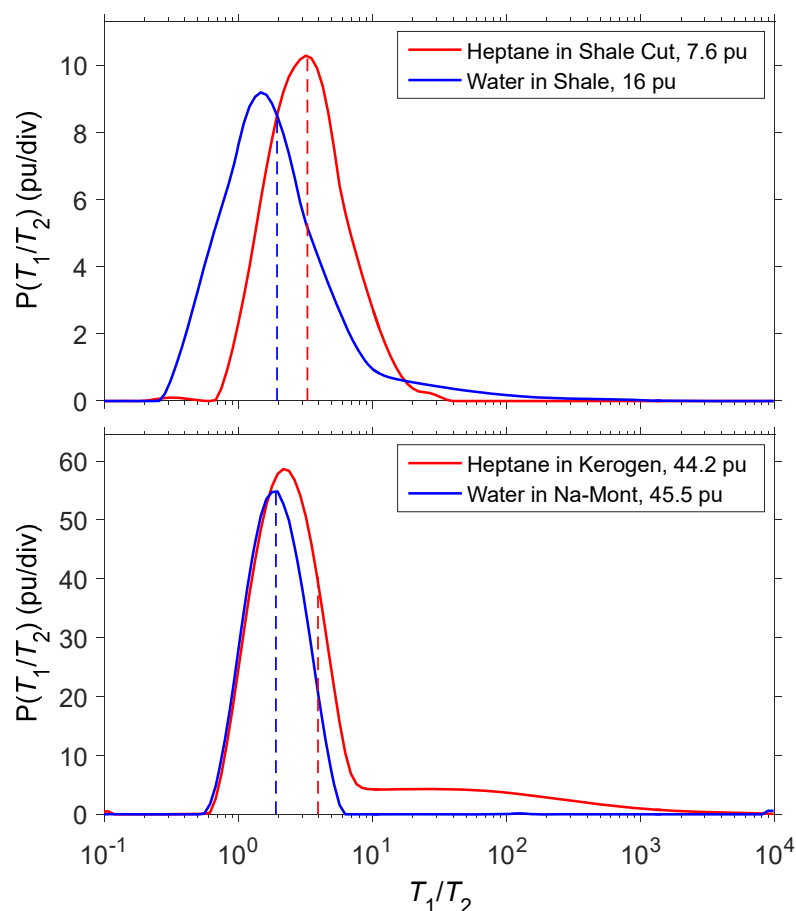
Figure 3.5 1D distributions of the projected T_1/T_2 ratio data from the 2D correlation maps. The legend indicates fluid name, matrix name, and total fluid porosity. Water in shale (water in Na-mont) amplitude has been reduced by a factor of 1/2 (2/3) for better comparison, respectively. Dashed vertical lines indicate log-mean averages <T_1/T_2> of the 1D distributions. "Heptane in Shale Cut" in the upper figure indicates that only $T_2 > 0.4$ ms data are used from Figure 3.4.

The results for heptane in shale suggest that the re-saturated heptane fills

the empty external clay-water pores in the shale, i.e., the inorganic pores. The data

in Figure 3.5 would therefore suggest that the T_1/T_2 contrast depends more on the fluid type than on the pore type, at least where nanopore confinement is concerned. This hypothesis is plausible if the primary surface-relaxation mechanism is hydrogen-hydrogen dipole-dipole interactions enhanced by nanopore confinement, rather than surface para-magnetism (see kerogen surface-relaxation section). In other words, the confinement of the nanopores has more influence on the surface relaxation than the nature of the pore surface itself, and the T_1/T_2 contrast depends more on fluid type than pore type. An important consequence is that while NMR logging can measure fluid typing and saturation in organic-shale reservoirs, it may be less sensitive to what nanopore type the fluid is in. As such, integrating NMR logs with other petrophysical logs would invariably improve the identification of sweet spots for optimizing lateral well placement and increasing production.

Table 3.2 Summary of total porosity, log-mean T_{1LM}, log-mean T_{2LM}, and log-mean average $<T_1/T_2>$ ratio for various fluids and samples.

Fluid	Matrix	ϕ (p. u.)	T_{1LM} (ms)	T_{2LM} (ms)	$\langle T_1/T_2 \rangle$
Heptane	Kerogen	44.2	17.3	4.7	3.9
Heptane	Shale	~7.7	~16.7	~5.0	>3.3
Water	Kerogen	35.8	11.3	7.5	1.5
Water	Shale	16.0	2.1	1.1	1.9
Water	Kaolinite	19.2	8.5	3.9	2.3
Water	Ca-Mont	53.4	2.8	1.3	2.2
Water	Na-Mont	45.5	0.8	0.5	1.9
D_2O	Kerogen	34.9	15.3	10.2	1.5

Heptane in shale values are approximate since heptane signal is assumed to only lie $T_2 >$ 0.4 ms (see Figure 3.4).

3.4. Conclusions

2D NMR data of heptane-saturated kerogen isolates show two distinct peaks in the T_2 spectrum. The slow-relaxing peak has a porosity ~36 p.u. (similar to a random bead-pack), and is interpreted as intergranular pores created, i.e., manufactured, during the pelletization process. The fast-relaxing peak has a porosity ~8 p.u. and a large T_1/T_2 ~78, and is interpreted as dissolved fluid in kerogen.

The data for heptane-saturated kerogen isolates show larger values of T_1/T_2 compared to water-saturated kerogen isolates and water-saturated clay isolates, across the entire T_2 spectrum. This validates T_1/T_2 as a contrast tool for fluid typing and saturation in downhole NMR logs. The resaturated organic shale (the same source rock used for the kerogen isolates) shows higher average $<T_1/T_2>$ ~4 for resaturated heptane versus resaturated water $<T_1/T_2>$ ~2, consistent with both the saturated isolates data and previously reported findings in re-saturated organic-shale cores.

Chapter 4

NMR Characterization of Fluids in Organic-Rich Shale Part 2: Relaxation Mechanism of Kerogen

Note that this chapter is based on and slightly adapted from three published journal articles (Philip M. Singer, Chen, and Hirasaki 2016; Z. Chen et al. 2017; Philip M. Singer, Chen, et al. 2018) and a master's thesis (Z. Chen 2018), where some portion is taken word-to-word. Also note that the data, especially porosity values, in one of the articles (Z. Chen et al. 2017) is re-processed by eliminating inaccuracy from calibration samples (Z. Chen 2018).

4.1. Introduction

In the past decade, as the oil and gas production from unconventional reservoirs increased dramatically, the investigations into organic shale have greatly

stimulated both NMR log data interpretation and NMR core analysis (Jiang et al. 2013; Kausik et al. 2016; Reeder et al. 2016; Anand et al. 2017; Tandon, Heidari, and Daigle 2017; Kathryn E. Washburn and Cheng 2017). Among them, studies focused on kerogen have become more and more popular (Ertas, Kelemen, and Halsey 2006; J. Chen et al. 2012; Philip M. Singer, Chen, and Hirasaki 2016; Philip M Singer et al. 2017; Philip M. Singer, Chen, et al. 2018; B. Zhang and Daigle 2017). Kerogen, which is defined as solid, insoluble and immobile organic matter, constitutes most of the total organic content (TOC) of organic shale (Durand 1980), which makes characterizing kerogen essential for formation evaluation.

Low-field NMR relaxometry has proved to be a key technique for evaluating both organic shale and kerogen (Kausik et al. 2016; Philip M. Singer, Chen, and Hirasaki 2016; B. Zhang and Daigle 2017; Kathryn E. Washburn and Cheng 2017). Fluid typing by traditional 1D T_2 distribution faces challenges due to overlapping signal. For example, bitumen, clay-bound water, and hydrocarbon in organic pores may have similar T_2 relaxation times, which results in ambiguity in the interpretation of T_2 distribution. Therefore, introducing an additional dimension, T_1, is necessary to resolve the complex signal. T_1-T_2 correlation maps (see Figure 4.2) and associated T_1/T_2 ratios have demonstrated to be successful tools in identifying different fluids in various pores types (Marc Fleury and Romero-Sarmiento 2016; Kausik et al. 2016; Philip M. Singer, Chen, and Hirasaki 2016). However, the NMR response of fluids in shale is not yet fully understood, such as the cause of the high T_1/T_2 ratio of heptane in kerogen isolates at short T_2 (Nicot et al. 2016). Previous

studies have shown the possibility of the existence of bitumen in kerogen, even in

the case of immature Type II kerogen (Philip M. Singer, Chen, and Hirasaki 2016).
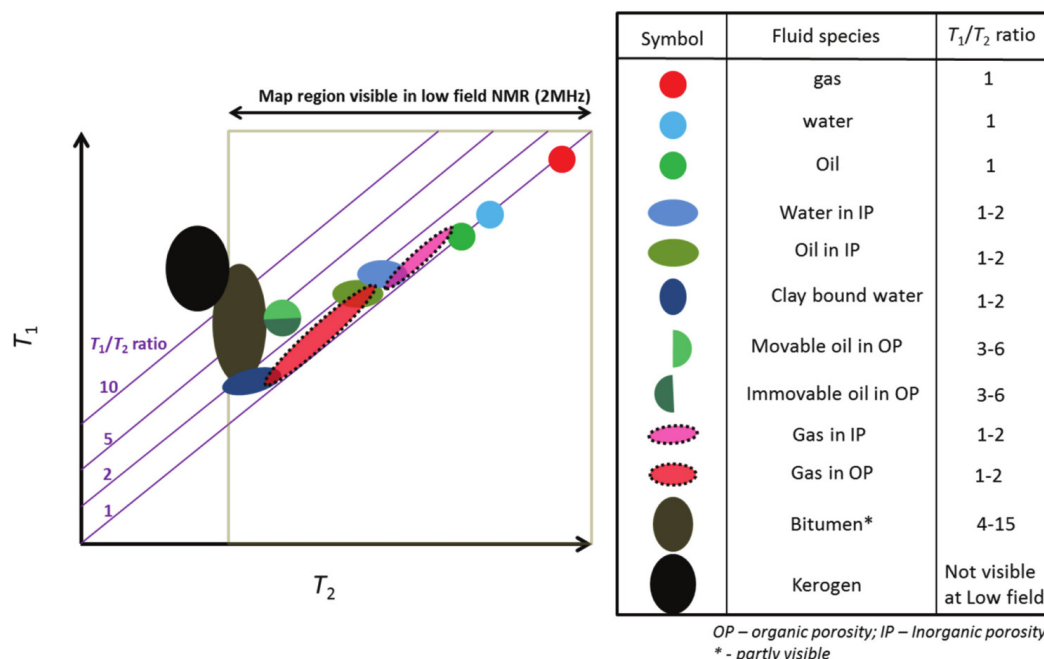
Figure 4.1 The low-field NMR (2 MHz) T_1-T_2 map for all the components in unconventional shales in a homogenous magnetic field (Kausik et al. 2016).

This chapter presents a comprehensive study into the origins of the high

T_1/T_2 ratio of heptane in kerogen isolates using 2D NMR correlation maps

integrated with nitrogen gas-adsorption BET and UV-VIS absorption spectroscopy.

This chapter has four sub-chapters to show the details of the research after the

"Background" sub-chapter. The first sub-chapter provides details of experiments,

including BET surface area and UV-VIS analysis that confirms the existence of

bitumen in immature Type II kerogen, and the bitumen-extraction effects on the

swelling of kerogen. The second part shows how bitumen extraction affects the 2D

NMR response, particularly for the dissolved heptane peak. The third part presents

the interpretation of the NMR results before and after bitumen extraction. The last

part is to elucidate the NMR surface-relaxation mechanism in kerogen and organic nano-pores in general.

4.2. Background: Diffusive Coupling and T_2-T_2 exchange

4.2.1. Diffusive Coupling

This section explores the diffusive-coupling effect on fluids in porous media. The discussion in Section 2.2.1 is based on individual pores. Once the pore structure of porous media gets more complex with multiple pores connected, the analysis of surface relaxation becomes much more complicated. The connected pores can behave like a larger single pore or still like multiple pores depending on the strength of the connectivity. This effect is called diffusive coupling.

Ramakrishnan *et al.*, 1999 and Dunn, Bergman and Latorraca, 2002 studied the diffusive coupling effect in the carbonate rock system. Concretely, the carbonate system is made up of carbonate grains. The void space between grains is called intergranular porosity, or macro-porosity, of which the symbol is ϕ_m. The grains are porous by itself with a intragranular porosity, or micro-porosity, of which the symbol is ϕ_μ. Intuitively, the micro-pores have much smaller pore diameters. The fluid molecule in carbonate rocks can travel between intragranular and intergranular pore space and get relaxed when it hits either the outer or inner grain surface.

Ramakrishnan *et al.*, 1999 and Anand and Hirasaki, 2007 suggested that the transverse magnetization decay of a single type of fluid (i.e., water) in the carbonate system can be expressed as:

$$M(t) = \phi_{\mathrm{m}} e^{-\frac{\rho_{2,\mathrm{a}}t}{V_{\mathrm{sm}}}} + \phi_{\mu} e^{-\frac{t}{T_{2,\mu}}}, \qquad (4.1)$$

where $\rho_{2,\mathrm{a}}$ is the apparent transverse surface relaxivity of intergranular pores; V_{sm} is the surface-to-volume ratio of intergranular pores; and $T_{2,\mu}$ is the transverse relaxation time of fluids in intragranular pores. If intragranular and intergranular pore spaces are completely isolated (i.e. $\frac{\rho_{2,\mathrm{a}}}{V_{\mathrm{sm}}} \ll \frac{1}{T_{2,\mu}}$), the T_2 distribution has two main peaks, i.e., intragranular molecules have shorter T_2 than the intergranular molecules due to smaller pore space. If two pore spaces are strongly diffusively coupled, the T_2 distribution can have only one main peak. The intermediate state can possibly exist when the two pores are weakly diffusively coupled. In summary, The diffusion coupling tends to average the relaxation time between those two pores (Kathryn E. Washburn 2014).

A quantitative way to interpret the diffusive coupling effect is to derive the expression of the apparent surface relaxivity (Ramakrishnan et al. 1999; Dunn, Bergman, and Latorraca 2002). The apparent surface relaxivity $\rho_{2,\mathrm{a}}$ for the intergranular pore is:

$$\rho_{2,\mathrm{a}} = \rho_{2,\mu}(1 - \phi_{\mu}) + \sqrt{\frac{\phi_{\mu} D_0}{F_{\mu} T_{2,\mu}}}, \qquad (4.2)$$

where D_0 is the bulk diffusivity of the fluids; $\rho_{2,\mu}$ is the "intrinsic" transverse surface

relaxivity of intragranular pores; and F_μ is the formation factor of the porous grain.

The formation factor is a function of porosity and Archie's cementation exponent m:

$$F_\mu = \phi_\mu^{-m}. \tag{4.3}$$

The Archie's cementation factor m is close to 2 for most of the conventional

sedimentary rocks, including carbonates. An analogy can be made for calculating the

apparent longitudinal surface relaxivity by simply replacing $\rho_{2,\mu}$ and $T_{2,\mu}$ in Equation

(4.2) by $\rho_{1,\mu}$ and $T_{1,\mu}$:

$$\rho_{1,a} = \rho_{1,\mu}(1 - \phi_\mu) + \sqrt{\frac{\phi_\mu D_0}{F_\mu T_{1,\mu}}}, \tag{4.4}$$

where $\rho_{1,\mu}$ is the "intrinsic" longitudinal surface relaxivity. Substituting Equation

(4.3) into Equations (4.2) and (4.4) yields:

$$\rho_{1,a} = \rho_{1,\mu}(1 - \phi_\mu) + \sqrt{\frac{D_0}{T_{1,\mu}}} \phi_\mu^{\frac{m+1}{2}}, \tag{4.5}$$

$$\rho_{2,a} = \rho_{2,\mu}(1 - \phi_\mu) + \sqrt{\frac{D_0}{T_{2,\mu}}} \phi_\mu^{\frac{m+1}{2}}. \tag{4.6}$$

Suppose the intergranular porosity $\phi_\mu = 0$, namely the grain is not porous,

the apparent surface relaxivities are equal to their "intrinsic" values. However, if ϕ_μ

gets close to 1, the apparent surface relaxivities approach to very large values. In the

latter case, the T_1 and T_2 of the water in intergranular pores are shifted to the

shorter range and merge with the T_1 and T_2 of water in intragranular pores. This results in the disappearing of the bi-modal feature. Equations (4.5) and (4.6) are the analytical explanation of the diffusive coupling effect.

Anand and Hirasaki, 2007 also introduce the diffusion length to characterize the strength of diffusive coupling. The diffusion length of molecules into the carbonate grain for transverse relaxation is written in the following form:

$$L_{2,D} = \sqrt{\frac{D_0 T_{2,\mu}}{\phi_\mu F_\mu}}, \tag{4.7}$$

where the definition of parameters is the same as Equation (4.2). The same analogy is made for Equation (4.7) for the case of T_1:

$$L_{1,D} = \sqrt{\frac{D_0 T_{1,\mu}}{\phi_\mu F_\mu}}. \tag{4.8}$$

By substituting Equation (4.3) into Equations (4.7) and (4.8), one can derive:

$$L_{1,D} = \sqrt{D_0 T_{1,\mu}} \; \phi_\mu^{\frac{m-1}{2}}, \tag{4.9}$$

$$L_{2,D} = \sqrt{D_0 T_{2,\mu}} \; \phi_\mu^{\frac{m-1}{2}}. \tag{4.10}$$

To satisfy the condition of $\frac{\rho_{2,a}}{V_{sm}} \ll \frac{1}{T_{2,\mu}}$ for bi-modal feature, by assuming small $\rho_{2,\mu}$ and $1/V_{sm} = 3/R_{pore} \approx 3/R_g$, the Equation (4.2) can be re-written as:

$$\frac{3}{R_g}\sqrt{\frac{\phi_\mu D_0}{F_\mu T_{2,\mu}}} \ll \frac{1}{T_{2,\mu}}. \tag{4.11}$$

where R_{pore} is the pore radius and R_g is the grain radius. Here we only illustrate the analysis for the transverse relaxation, because the analysis for longitudinal relaxation is the same. Then, by combining Equation (4.7) and (4.11), one would have:

$$L_{2,D} \ll \frac{R_g}{3\phi_\mu}. \tag{4.12}$$

Since $3\phi_\mu$ is in the order of 1, one can conclude that the validity of the bi-modal feature of T_1 and T_2 distributions requires the diffusion length much smaller than the grain size (Anand and Hirasaki 2007):

$$L_{1\ or\ 2,D} \ll R_g. \tag{4.13}$$

Note that all the above derivation is based on the carbonate system. However, in terms of kerogen isolates, this model is still valid, i.e., the kerogen isolates also have both intragranular and intergranular pore spaces. Thus, the analysis discussed in this section is adapted to explain the experimental results in sub-chapter 4.5 quantitatively.

4.2.2. T_2-T_2 Exchange
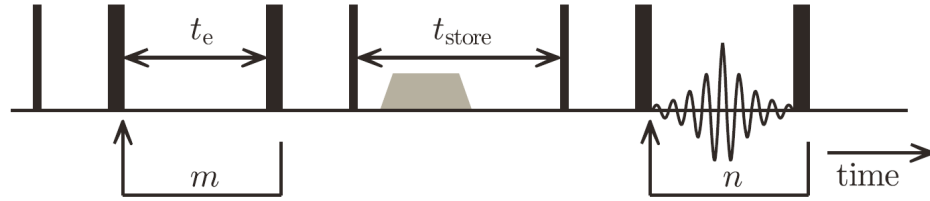
Figure 4.2 A schematic of the pulse sequence for the T_2-T_2 exchange experiment. This sequence consists of two CPMG echo trains separated by a z-storage delay (stimulated echo) of duration t_{store} (or Δ). The first CPMG echo train has a total duration mt_e; the number of echoes m is incremented over sequential experiments to construct a 2D data array. The second CPMG train has a total duration of nt_e. To determine an exchange rate, the storage time t_{store} is incremented in separate experiments (Mitchell et al. 2014).

T_2-T_2 exchange measurements can be implemented to monitor diffusive exchange processes in the porous media (K. E. Washburn and Callaghan 2006; Monteilhet et al. 2006; Mitchell et al. 2007, 2014). In terms of the pulse sequence, T_2-T_2 exchange measurements require a pair of CPMG echo trains. These two echo trains are separated by a z-storage interval with a duration (i.e., t_{store} or Δ) (Mitchell et al. 2014). The details of the pulse sequence are illustrated in Figure 4.2. The first echo train is named direct echo chain (i.e., T_{2a}) while the second one is named indirect echo train (i.e., T_{2b}). Note that the data are obtained only from the indirect CPMG echo train. The experimental data have the following form:

$$\frac{M(mt_e, nt_e)}{M(0,0)} = \exp\left(-\frac{mt_e}{T_{2a}}\right)\exp\left(-\frac{nt_e}{T_{2b}}\right). \tag{4.14}$$

It should be noted that the T_1 relaxation happens during the storage interval should be compensated when analyzing the data. By applying the 2D inversion (Venkataramanan, Song, and Hürlimann 2002), the T_2-T_2 exchange correlation maps, namely T_{2a} vs. T_{2b} correlation maps, can be generated.

4.3. Experiment

4.3.1. Sample Preparation

4.3.1.1. Origin of Kerogen and Isolation

The isolated kerogen used in this study was originally from a well-studied outcrop Kimmeridge oil shale from the coast of Dorset, UK (Curtis et al. 2010; Restuccia, Ptak, and Rein 2017). This type of shale has high TOC (total organic carbon) ~10 wt%. RockEval (pyrolysis) data showed that this shale contains immature type II kerogen (i.e., same as in sub-chapter 3.2).
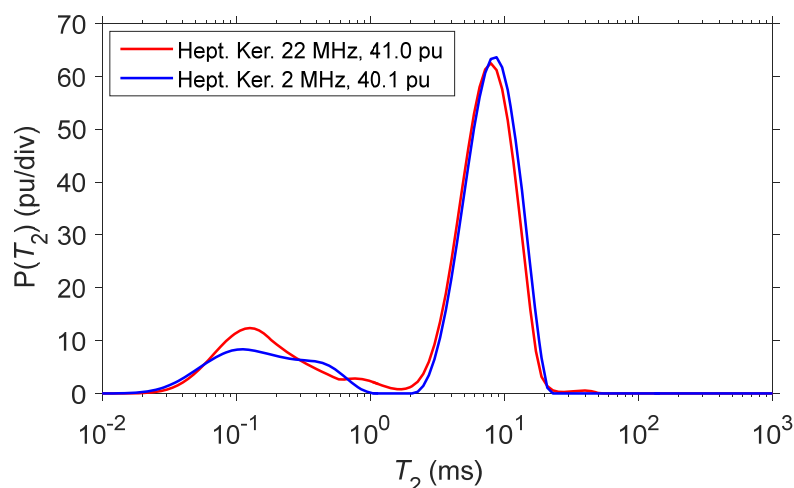
Figure 4.3 1D distributions of the T_2 data for heptane in kerogen at 22 MHz (red) and 2 MHz (blue). The legend indicates fluid name, matrix name, resonance frequency, and total fluid porosity.

The shale was demineralized by HCl/HF acid to remove inorganic content, followed by the sink-float separation technique for isolating kerogen. Inductively coupled plasma (ICP) data indicated 8.2 wt% pyrite in the isolated kerogen. One of the previous studies (shown in Chapter 3) on the same kerogen (isolated from the same piece of shale rock) indicated a higher pyrite concentration of 11.7 wt% due to

a different kerogen isolation procedure. The T_2 distributions are found to be almost identical between the two different kerogen batches, i.e., T_2 is independent of pyrite concentration. It indicates that pyrite does not result in internal gradient effects, namely T_{2D} is negligible. The absence of the internal gradient effects was also confirmed by showing that T_2 of heptane in kerogen was independent of magnetic field strength and echo spacing (see Figure 4.3). The internal-gradient contribution on T_2 distribution is expected to scale as:

$$\frac{1}{T_{2D}} \propto B_0^2 = \omega^2/\gamma_I^2, \qquad (4.15)$$

where B_0 is the static magnetic field strength, and ω is the Larmar frequency.
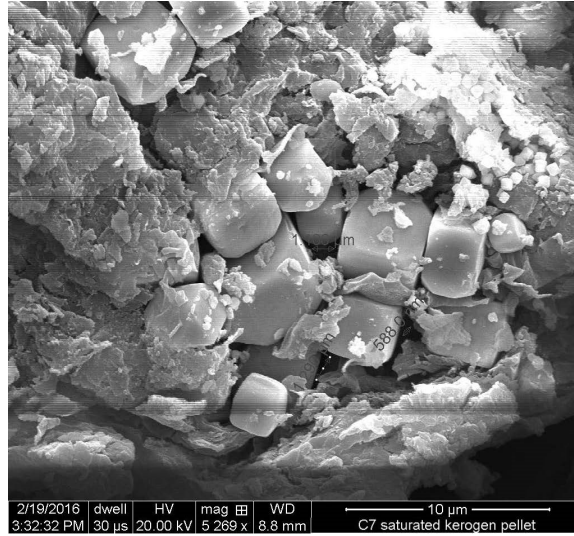
Figure 4.4 SEM image of localized pyrite crystals in isolated kerogen pellet.

The negligible internal-gradient contribution is because the pyrite is highly localized and clustered in the kerogen as shown in the SEM image (Figure 4.4). The signal from liquids near localized pyrite most likely suffers from very large internal-gradient effects and is therefore not observable due to short $T_{2D} \ll T_E$.

4.3.1.2. Bitumen Extraction, Pelletization and Saturation

In this part of the research, three samples were prepared following the procedure shown in Figure 4.5. They are: (1) "With Bitu", indicating that the bitumen was not extracted; (2) "Extracted A", indicating that it underwent Soxhlet extraction; and (3) "Extracted B", indicating that it had the bitumen extracted by so-called "static extraction", which means immersing kerogen in toluene for prolonged times.

With Bitu.	Extracted A	Extracted B
Vacuum dried	Vacuum dried	Vacuum dried
-	Soxhlet extraction: 15 days (110°C)	Static extraction: 24 days (80°C: 2 days)
-	Vacuum dried	Vacuum dried
Pelletized at 77 kpsi	Pelletized at 77 kpsi	Pelletized at 77 kpsi
Saturated with heptane at 5 kpsi	Saturated with heptane at 5 kpsi	Saturated with heptane at 5 kpsi
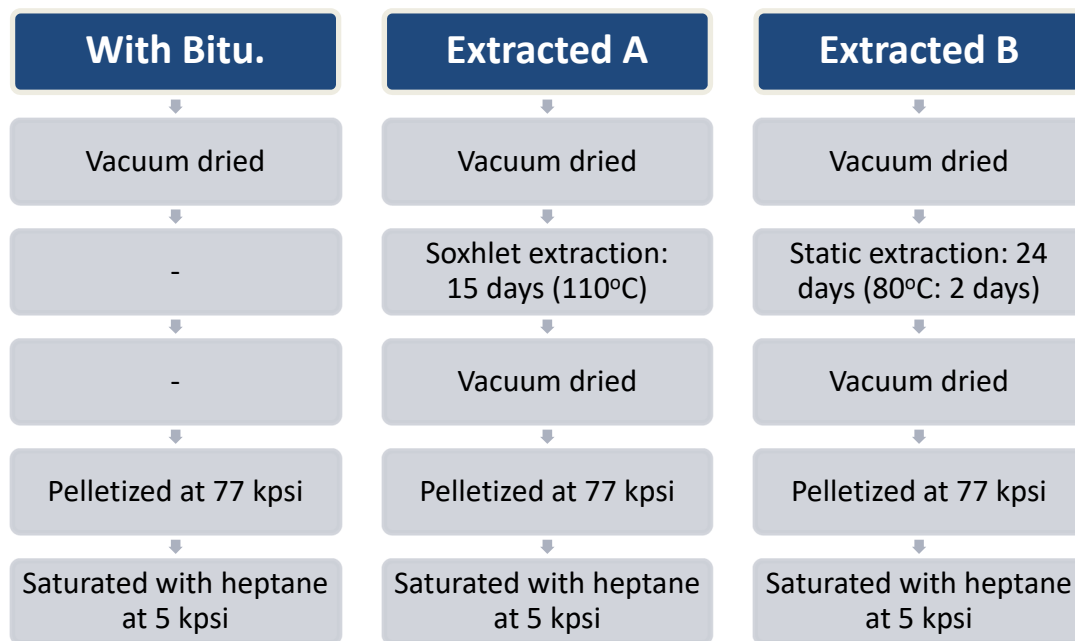
Figure 4.5 Summary of the preparation history of three samples. The sample labeled "With Bitu." (left column) did not undergo bitumen extraction before pelletization. The other samples, labeled as "Extracted A" and "Extracted B", underwent bitumen extraction by toluene using different procedures.

For all the three samples, the isolated kerogen powder was first vacuum-dried at 110 ℃ for three days to remove humidity on the kerogen particles surface from the sink-float separation. The drying temperature was then increased to 140 ℃ for one day to make a better comparison between "With Bitu." and "Extracted A"

and "Extracted B" (which were both vacuum-dried at 140 ℃ after toluene treatment). That way all the samples were exposed to 140 ℃.

For the Soxhlet extraction, ~1.5 g of kerogen powder was extracted by boiled toluene (~110 ℃ under ambient pressure). For "static extraction", ~1.5 g of kerogen powder was immersed in ~300 mL pure toluene at room temperature for a total of 24 days, followed by heating up to 80 ℃ in a water bath for a total of two days.

After extraction, the kerogen powder of both "Extracted A" and "Extracted B" was separated from the toluene, and then vacuum-dried again at 140 ℃ for four days to remove the toluene. Meanwhile, the bitumen extract was collected and concentrated by a rotary evaporator, and then analyzed by a UV-3600 Plus UV-VIS-NIR Spectrophotometer. At the same time, a series of calibration samples were prepared for concentration analysis. The calibration samples were made by dissolving different amounts of Athabasca bitumen in pure toluene. By comparing the absorbance of concentrated extract and the calibration samples, the concentration of extract expressed by Athabasca bitumen equivalent could be determined (Z. Chen et al. 2017). It is found that approximately the same amount, 0.6 wt% - 0.8 wt%, of Athabasca bitumen equivalent was removed from the kerogen powder of "Extracted A" and "Extracted B". The UV-VIS analysis confirmed the existence of bitumen in isolated kerogen, even though the weight percentage is low. By definition, the bitumen was removed from "Extracted A" and "Extracted B" since bitumen is solvent-extractible, while kerogen is not.

Roughly ~1 g of powder from each sample was then pelletized in a die press at 77,000 psi. The compressed pellet was cylindrical in shape. Each sample consisted of four pellets (~ 0.25 g each) with an average diameter of ~ 8 mm and an average thickness of approximately ~4.9 mm per pellet. The kerogen pellets were then vacuum-saturated with high-purity *n*-heptane at 5,000 psig hydrostatic pressure for ~16 hours. Different amounts of swelling in the pellet's bulk-volume after heptane saturation was observed among the three samples, as reported in the following subsection. NMR measurements were taken at various stages of this process.

After all NMR measurements were complete, the pellets were taken for measuring specific surface-area by nitrogen-gas adsorption using Autosorb AS-3B from Quantachrome Instruments. The gas-adsorption isotherms were acquired on intact pellets after being vacuum-dried at 110 ℃ for ~12 hours to remove heptane. The specific surface area was then calculated by analyzing the adsorption isotherm using Brunauer–Emmett–Teller (BET) theory (Brunauer, Emmett, and Teller 1938), which is a commonly accepted technique for pore-size analysis (Foley, Farooqui, and Kleinberg 1996). A similar specific surface area of $S_{\mathrm{BET}} \sim 14 \ \mathrm{m}^2/\mathrm{g}$ was found for all three samples.

4.3.2. Kerogen Swelling

4.3.2.1. Swelling Direction

The size of pellets, including thickness and diameter, was measured by caliper for the dried, saturated, and de-saturated samples. The average values of the four pellets of each sample were calculated (see Figure 4.6).
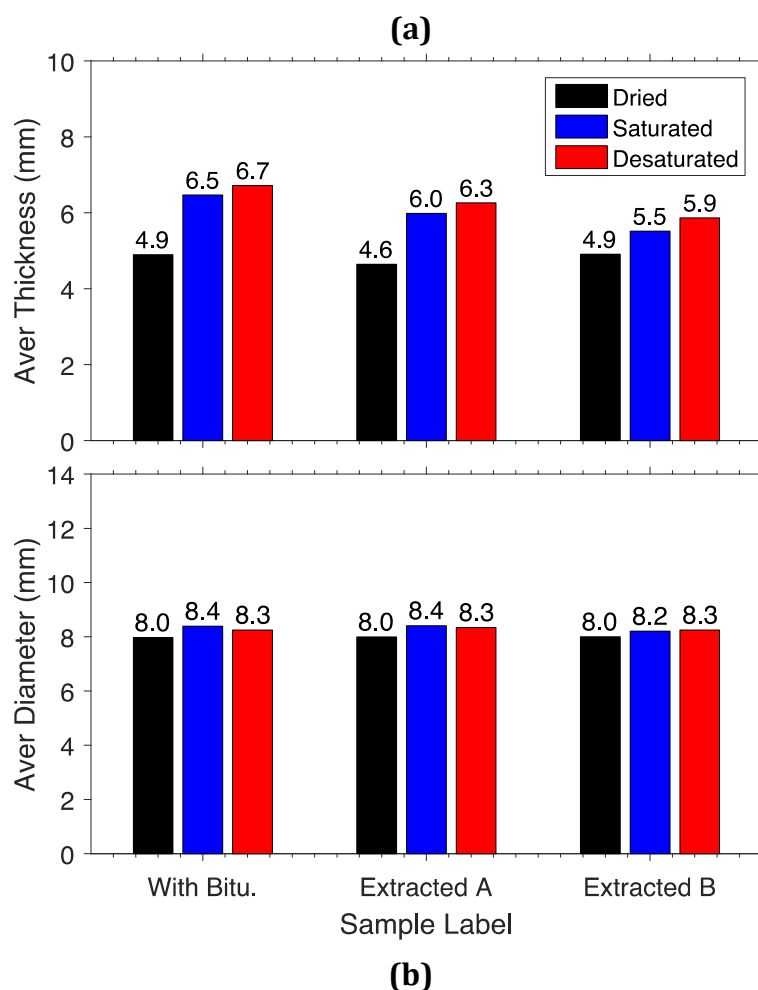
Figure 4.6 (a) The average thickness of the four pellets for each sample. The black bar shows the average thickness of the pellets before heptane saturation (dried); the blue bar shows the average thickness measured right after heptane saturation (saturated); and the red bar shows the average thickness measured after heptane was fully evaporated (desaturated). (b) shows the average diameter of four pellets of each sample; the color scheme is the same as in (a).

Figure 4.6 shows that before saturation with heptane, the average thickness for all samples was ~4.9 mm and the average diameter was ~8.0 mm. However, after saturation with heptane, the average thickness of the three samples increased dramatically. The thickness of "With Bitu." increased by 33% after saturation and 37% after desaturation compared to the original thickness before saturation. The increase in thickness for "Extracted A" was 30% and 37% after saturation and desaturation, respectively. However, for "Extracted B", the thickness only increased by 12% and 20%, respectively. It is therefore found that "static extraction" reduces the swelling of the pellets in the axial direction, more so than for Soxhlet extraction. On the other hand, the average diameter of all samples only increased by a small amount, < 5%, for either saturated or desaturated. This observation indicates anisotropy in the pellet structure, which was caused by the higher axial stress compared to radial stress during pelletization. As a result, the pellets tended to relax and swell more in axial direction compared to the radial direction. This explains the unexpected anisotropy in the swelling direction.

4.3.2.2. Bulk Swelling Percentage

Based on the thickness and diameter of single pellets, the total volume of each sample (consisting of four pellets) is calculated as follows:

$$BV = \sum_{i=1}^{4} \pi \frac{D_i{}^2}{4} H_i, \tag{4.16}$$

where BV is the total bulk volume of each sample, and H_i and D_i represent the thickness and diameter of each individual pellet. Then a normalized parameter, called the swelling percentage, is introduced:

$$\text{Swelling}_{\text{sat/desat}} = \frac{\text{BV}_{\text{sat/desat}} - \text{BV}_{\text{dried}}}{\text{BV}_{\text{dried}}}, \tag{4.17}$$

where BV_{dried} is the bulk volume of the dry pellets before saturation, BV_{sat} is the bulk volume of saturated pellets, and BV_{desat} is the bulk volume of desaturated pellets. The swelling is defined as the percentage of bulk volume change of saturated or desaturated sample compared with the dried sample.
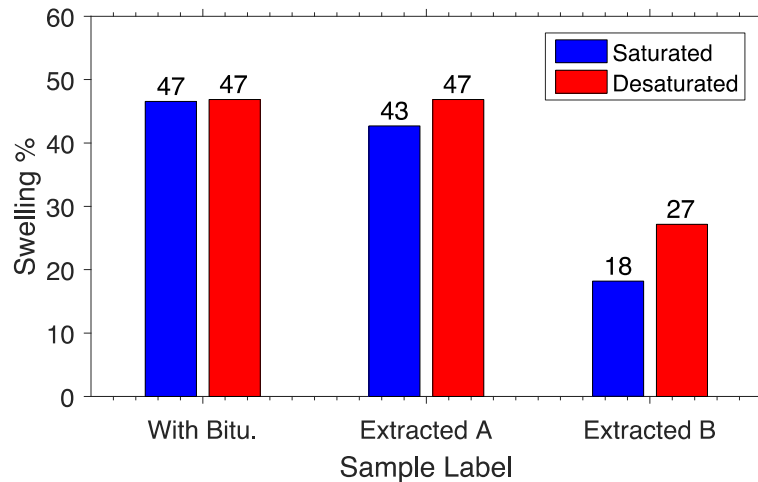
Figure 4.7 Swelling percentage of the bulk volume of samples. The blue bar shows the swelling of saturated pellets, and the red bar shows the swelling of desaturated pellets.

Figure 4.7 shows a bar chart of swelling percentage determined by Equation (4.17). The bulk volume for "With Bitu." increased by 47 % after exposure to heptane, and this value is nearly a constant after heptane desaturation. "Extracted A" caused the bulk volume to increase by 43 % after exposure to heptane, which is slightly less than "With Bitu.", and 47 % after desaturation. In contrast, the swelling

percentage for "Extracted B" is much smaller, only ~18 %; after heptane

desaturation, the swelling slightly increased to ~27 % compared to dried. The

swelling of 18 % is close to the reported swelling of heptane-saturated Type II

kerogen (Ertas, Kelemen, and Halsey 2006), even though different procedures for

sample preparation were adopted. Both Soxhlet and static extraction reduced the

swelling percentage, however, the reduction from static extraction was more

significant, indicating that static extraction was more efficient in reducing the

swelling than Soxhlet extraction.

A possible explanation for the reduction in swelling for bitumen-extracted

kerogen is the following: although kerogen and bitumen are both crosslinked

polymers that are capable of absorbing suitable liquids, which cause swelling (Ertas,

Kelemen, and Halsey 2006; Kelemen et al. 2006), their swelling capability might not

be the same. Kerogen is believed to have more crosslinkage compared to bitumen,

even though their chemical composition is similar. One would therefore expect

bitumen to have more capacity to swell because of less crosslinkage. Therefore, in

the presence of bitumen, more swelling could be expected after introducing

heptane. In fact, Reeder *et al.* (Reeder et al. 2016) observed using SEM that kerogen

collapses after bitumen extraction.

In terms of the swelling behavior, an analogy can be made from kerogen to

coal (Jin and Firoozabadi 2016). Swelling behavior of coal is attributed to surface

adsorption and absorption into the coal matrix (Ottiger et al. 2008). Thus, the same

swelling behavior can be expected on kerogen isolates. The heptane can be

adsorbed onto kerogen particle surface or dissolved into kerogen particle. The

dissolution leads to the swelling of the kerogen particle and then the kerogen

pellets. The phenomenon that the particles swell after introducing light

hydrocarbons is captured by Pathak et al. 2017 using dynamic light scattering (DLS).

However, further study is needed into the reason why Soxhlet and static

extraction result in different swelling percentages. It is also possible that the higher

temperature for Soxhlet changes the geomechanical properties of kerogen, and/or

that static extraction removes slightly more bitumen than Soxhlet extraction.

4.4. NMR Measurement

This sub-chapter concentrates on the NMR measurements on the heptane-

saturated kerogen isolates. In the first section, the specifications of NMR

measurements are discussed in detail. In the second section, the results of the NMR

measurements are shown and summarized.

4.4.1. Specifications of NMR Measurements

The kerogen isolates were measured at 30 °C and ambient pressure using an

Oxford Instruments GeoSpec2 rock-core analyzer, with a resonance frequency of

$\omega/2\pi = 2.3$ MHz for ^{1}H. The 2D T_1-T_2 data were acquired using 32 log-spaced

points on inversion-recovery curve ranging from 0.1 to 1,000 ms. Each point was

followed by a series of CPMG echoes with an echo spacing of $T_E = 0.1$ ms. These 2D

raw data were processed using a fast 2D Laplace Inversion analogous to

Venkataramanan *et al* 2002, with 120 log-spaced bins for T_1, and T_2. The units of the

y-axis on the relaxation time, T_1 and T_2, distributions are in "p.u./div", which means

porosity units per x-axis bin-size. In the case of T_2 distribution, "div $= \Delta \log_{10} T_2 =$

$(\log_{10} T_{2,i+1} - \log_{10} T_{2,i})$", which is independent of index "i" because of the log-

spaced bin selection. This unit is also known as bin porosity.

(a)

(b)
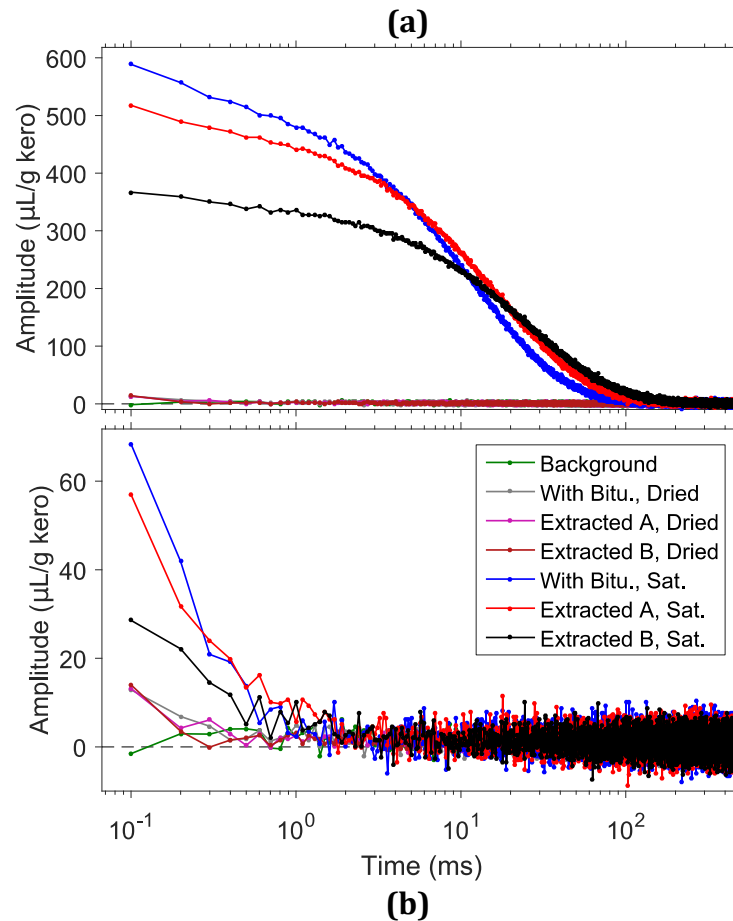
Figure 4.8 CPMG echo trains acquired on various samples. "Background" is acquired on an empty container. "Dried" is the dried kerogen isolate of each sample before pelletization. "Sat." is the heptane-saturated kerogen pellets of each sample. The name before "Dried" and "Sat." indicates the sample name. Echo trains of "Background" and "Dried" are the same for both (a) and (b). (a) Shows the full CPMG echoes for the saturated samples. (b) Shows the CPMG echoes for the saturated samples, but with the slow-relaxing T_2 components subtracted for a better comparison at short echo times. Except for "Background", the amplitudes of the others are normalized by kerogen mass. The y-axis is in units of µL per gram of kerogen, assuming HI = 1.

Figure 4.8 shows the CPMG echo trains acquired on dried and heptane-saturated kerogen samples, as well as the empty sample container. The background signal measured on the empty glass sample containers, named "Background", is found to be within random noise. The vacuum-dried kerogen powder before pelletization labeled as "Dried" was measured as well.

"Extracted A, Dried" and "Extracted B, Dried" are vacuum-dried after bitumen extraction. The unit of the y-axis is defined as μL/g of kerogen, which means the signal intensity is normalized by the kerogen mass of samples.

The CPMG echoes of fully heptane-saturated samples are plotted in Figure 4.8(a). They are labeled with the sample name followed by "Sat.". It is challenging to compare the "Dried" signal with the signal from saturated samples; therefore, Figure 4.8(b) shows the raw echoes of saturated kerogen with the slow-relaxing T_2 peak subtracted (i.e., applying a $T_{2,\text{cutoff}} = 1.69$ ms in T_2 distributions shown in the next sub-chapter) followed by a conversion from the T_2 domain back to the time domain. Then the only remaining saturated signal shown in Figure 4.8(b) is from dissolved heptane in kerogen.

From Figure 4.8(b) one can tell that three decays of "Dried" demonstrate an observable amount of signal compared with "Background". This signal is unlikely from kerogen because kerogen is solid and thus not detectable by traditional low-field NMR with a relative "long" echo spacing of $T_E = 0.1$ ms. Furthermore, toluene treatment does not make a noticeable change in signal intensity. Therefore, the signal is also unlikely from bitumen. This tiny amount of signal is most likely from

the remaining humidity on the kerogen surface. As reported in the previous subsection, the kerogen has a specific surface area around 14 m²/g. By converting the y-axis units from μL/g to μL/m² with this specific surface area, the humidity on kerogen indicated by the first echo is determined to be ~1 μL/m², which is reasonable. Therefore, the data shown in the following sub-chapter was processed with the "Dried" signal subtracted in the time domain, i.e., before the inverse Laplace inversion. It is also noted that for saturated samples, "Sat.", the signal intensity of the fast-relaxing components increased dramatically from "Dried", implying the fast-relaxing peak on T_1-T_2 correlation maps are from heptane and not from potential inversion artifacts.

NMR measurements were then made continuously during controlled evaporation until all heptane was "desaturated" from the kerogen pellets, where controlled evaporation refers to briefly opening the sample container to evaporate the volatile heptane. NMR relaxation of pure n-heptane was also measured at ambient conditions to be $T_{1B} = T_{2B} = 1,918$ ms, which are reduced from their pure-component values due to dissolved oxygen (Lo et al. 2002). The bulk diffusivity of heptane at room temperature was measured to be 3.43 μm^2/ms. Meanwhile, a hydrogen index of HI = 0.98 for n-heptane was derived using the molecular weight and density at ambient condition. Since this HI was close to unity, all the NMR porosity reported below were processed assuming HI = 1, thereby avoiding rescaling.

4.4.2. NMR on Saturated Kerogen Isolates

4.4.2.1. T_2 Distribution

The NMR responses shown in this section were acquired on the fully *n*-heptane saturated kerogen. Figure 4.9 shows the T_2 distributions that come from the projection of T_1-T_2 map (Figure 4.10(a)) for all three samples. The total porosity of "With Bitu." is 44.9 p.u., which is close to 43.3 p.u. for "Extracted A", but greater than 36.6 p.u. of "Extracted B". These porosities are consistent with the degree of swelling observed, namely, "With Bitu." and "Extracted A" have larger swelling than "Extracted B".
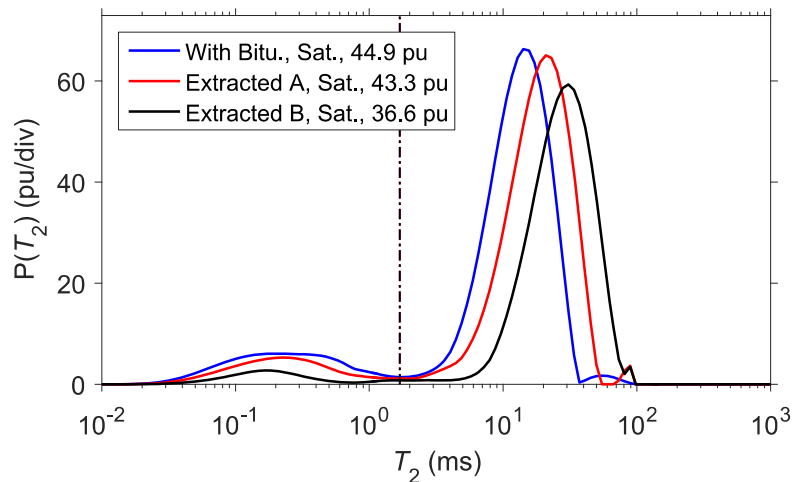
Figure 4.9 Projected 1D T_2 distribution from 2D T_1-T_2 correlation map of heptane-saturated kerogen samples. The legend indicates sample name and total porosity. The vertical dashed line is the $T_{2,\text{cutoff}}$ = 1.69 ms separating dissolved heptane signal (fast-relaxing peak) from heptane in intergranular pores (slow-relaxing peak). Note how bitumen extraction reduces the dissolved heptane porosity, and increases the intergranular relaxation time.

It is evident that all three samples have a bimodal feature. A simple way to separate these two peaks is to put a $T_{2,\text{cutoff}}$ at the local minimum of T_2 distributions. Here, $T_{2,\text{cutoff}} = 1.69$ ms (indicated by the vertical dashed line in Figure 4.9) was chosen. The fast-relaxing peak with short T_2 is interpreted as heptane dissolved in

the kerogen granule, namely in intragranular pores (labeled as "<"), while the slow-

relaxing peak with long T_2 is interpreted as heptane relaxing in kerogen

intergranular pores (labeled as ">"). Note that the intragranular (or dissolved)

pores and intergranular pores are defined in terms of the T_2's of heptane probing

each pore system, in other words, the local environment seen by the heptane

molecules. The intraganular pores may not be pre-existing, and it can be created by

the intrusion of heptane into the kerogen grains. Therefore, these pores cannot be

probed by nitrogen molecules that cannot be dissolved into the kerogen. This is the

reason why in the pore size analysis (see Section 4.5.2), the specific surface area

measured by nitrogen adsorption is assumed to only account for the intergranluar

pores.

Table 4.1 Summary of NMR porosity, T_1, T_2 and T_1/T_2 ratio log-mean values of three samples for intragranular (dissolved) heptane ("<", T_2 < 1.69 ms) and heptane in intergranular pores (">",T_2 > 1.69ms).

	With Bitu.	Extracted A	Extracted B
$\phi_<$ (p.u.)	7.1	5.1	2.1
$\phi_>$ (p.u.)	37.8	38.2	34.5
ϕ_μ (p.u.)	11.4	8.3	3.2
$T_{1LM,<}$ (ms)	10.2	5.7	5.5
$T_{1LM,>}$ (ms)	32.1	43.5	65.5
$T_{2LM,<}$ (ms)	0.23	0.22	0.20
$T_{2LM,>}$ (ms)	12.8	17.7	26.2
$(T_1/T_2)_{LM,<}$	43.6	25.3	27.3
$(T_1/T_2)_{LM,>}$	2.6	2.5	2.5

There are two main effects of bitumen extraction on the T_2 distributions: (a)

the porosity of the fast-relaxing peak, $\phi_<$, decreases from 7.1 p.u. to 5.1 p.u. for

"Extracted A" and from 7.1 p.u. to 2.1 p.u. for "Extracted B", while $T_{2,<}$ is unchanged;

(b) that relaxation time $T_{2,>}$ of the slow-relaxing peak increases by ~38 % for

"Extracted A" and ~105 % for "Extracted B", while $\phi_>$ is unchanged. All data are

summarized in Table 4.1.

Here, a measurable parameter called microporosity is defined as

intragranular pore volume divided by kerogen granule volume:

$$\phi_\mu = \frac{V_B \phi_<}{V_B(1-\phi_>)} = \frac{\phi_<}{(1-\phi_>)}, \tag{4.18}$$

where V_B is the bulk volume of kerogen pellets. Sample microporosity is also listed

in Table 4.1. These values will be used in the interpretation of apparent surface

relaxivity change of intergranular pores. All the porosities in the equations are in

dimensionless units of v/v (volume ratio), while all porosity values are reported in

p.u. (porosity units, i.e., percent) for clarity.

4.4.2.2. T_1-T_2 Correlation Map

Figure 4.10 shows the effect of bitumen extraction on the T_1-T_2 and T_1/T_2-T_2

correlation map of heptane-saturated kerogen. In addition to the two effects from

the projected T_2 distribution noted above in (a) and (b), the following additional

observations can be made: (c) bitumen extraction has no significant impact on $T_{1,<}$

for the fast-relaxing peak observed on the 2D maps (the 2D peak is broad because of

the low resolution for T_1 in the short T_2 regime); (d) $T_{1,>}$ of the slow-relaxing peak

shifts by the same amount as $T_{2,>}$, 36 % for "Extracted A" and 104 % for "Extracted

B" ; and (e) The fact that $T_{1,>}$ and $T_{2,>}$ of the slow-relaxing peak are shifted by the same amount implies the $(T_1/T_2)_>$ ratios remain constant. In addition, the unchanged $T_{1,<}$ and $T_{2,<}$ for fast-relaxing peak also implies constant $(T_1/T_2)_<$ ratio, as shown in Figure 4.10(b). To make a better comparison, all the log-mean values of T_1, T_2 and T_1/T_2 ratio are summarized in Table 4.1, along with all the porosities.

The fast-relaxing peak shows that bitumen extraction leads to a reduction of dissolved heptane porosity, resulting from less swelling of the kerogen granules. The static extraction seems to reduce the intragranular porosity and reduce the swelling more efficiently than Soxhlet extraction. In terms of the NMR measurement, "Extracted A" is intermediate between "With Bitu." and "Extracted B". Another key finding is that $T_{1,<}$ and $T_{2,<}$ for dissolved heptane has barely changed after bitumen extraction.

These findings lead to the following interpretation for the source of the fast-relaxing peak, namely: the fast-relaxing peak results from heptane dissolved in both bitumen (before extraction) and kerogen. Kerogen relaxes the dissolved heptane in the same way as bitumen since the removal of bitumen did not change the $T_{1,<}$ and $T_{2,<}$ of the fast-relaxing peak. The $(T_1/T_2)_<$ ratio for dissolved heptane is high for both kerogen and bitumen, which is reasonable since kerogen is considered as a more crosslinked bitumen. One can therefore expect the local environment experienced by a single heptane molecule to be the same whether it is dissolved in kerogen or dissolved in bitumen. The only difference is that bitumen has a higher capacity (i.e., larger porosity ϕ_μ) for heptane than kerogen.
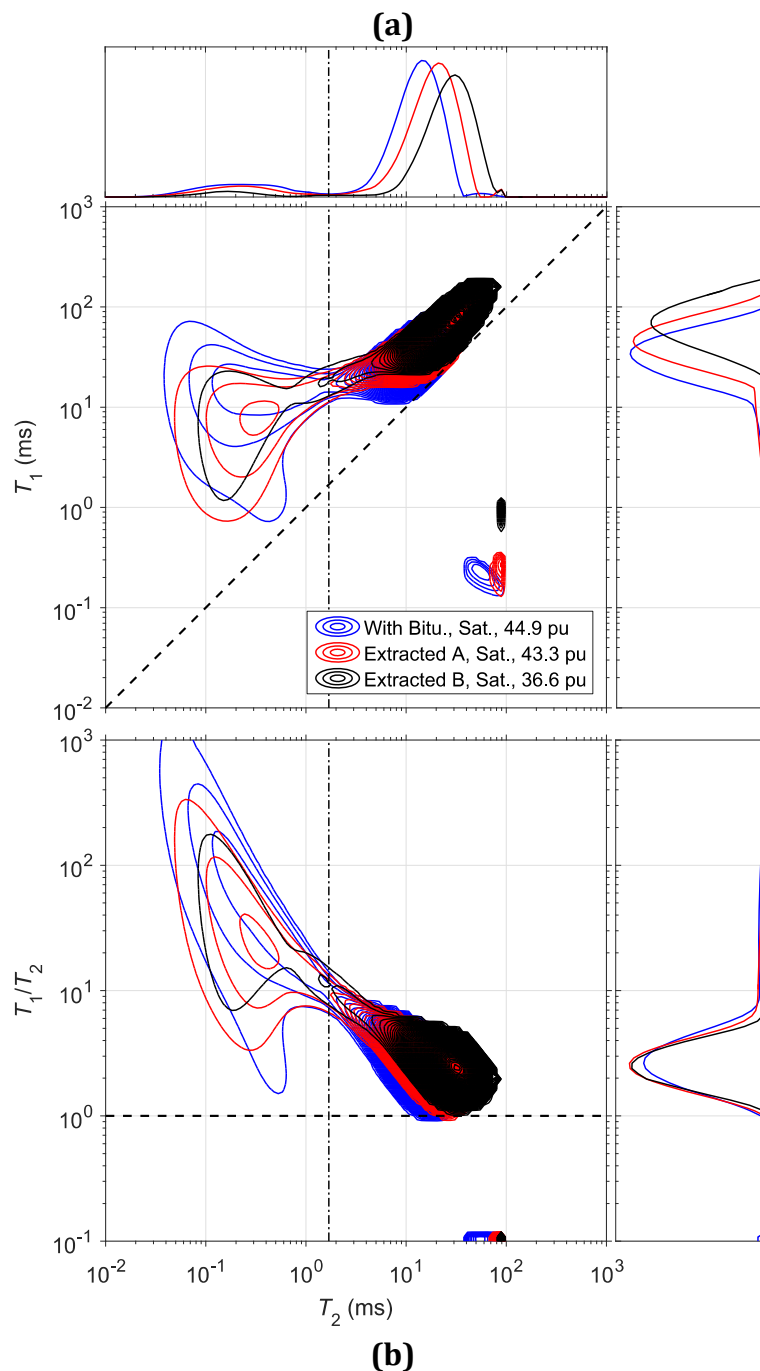
Figure 4.10 (a) A 2D correlation map of heptane saturated kerogen samples with T_1 on the y-axis, T_2 on the x-axis and porosity perpendicular to the page. The top subplot is the projected T_2 distributions shared by both (a) and (b), and the right subplot is the projected T_1 distribution. The legend indicates sample name and total porosity. The dashed diagonal line is the $T_1 = T_2$ line. The dashed vertical line is the $T_{2,\text{cutoff}}$ = 1.69 ms separating dissolved heptane (short T_2 peak) and heptane in intergranular pores (long T_2 peak), the same for (b). (b) A 2D correlation map of heptane-saturated kerogen samples with T_1/T_2 ratio on the y-axis, T_2 on the x-axis and porosity perpendicular to the page. The right subplot is the projected T_1/T_2 ratio distribution. The legend is the same as (a). The dashed horizontal line is the T_1/T_2 ratio=1 line.

The relaxation mechanism behind the high $(T_1/T_2)_<$ ratio can be qualitatively explained using a model system for crude oils made up of polymer-heptane mixtures (see section 4.6.2 for details) (Philip M Singer et al. 2017; Philip M. Singer, Chen, et al. 2018). It was shown that the relaxation mechanism of the heptane-polymer mix is dominated by [1]H-^{1}H dipole-dipole interactions, and that heptane starts to show high T_1/T_2 ratios and T_1 dispersion when its motion is highly restricted in confined space, i.e., when heptane is in the slow-motion regime. In terms of heptane dissolved in kerogen and bitumen in the present case, the heptane is dissolved in the organic materials. Thus, one expects the motion of dissolved heptane to be highly restricted as well. The restriction leads to high T_1/T_2 ratios and T_1 dispersion, similar to the viscous polymer mix with heptane (Philip M Singer et al. 2017; Philip M. Singer, Chen, et al. 2018). In summary, the high $(T_1/T_2)_<$ ratio for dissolved heptane is a result of enhanced [1]H-^{1}H dipole-dipole interactions due to nano-confinement, and a corresponding slow-motion regime.

Meanwhile, observations on the slow-relaxing peak show that the intergranular porosity is not significantly affected by bitumen extraction. This indicates that bitumen swelling does not lead to an additional increase in intergranular porosity. However, the intergranular heptane shows a uniform increase in both $T_{1,>}$ and $T_{2,>}$, which could be attributed to either an increase in pore size or a uniform decrease in surface relaxivities $\rho_{1,>}$ and $\rho_{2,>}$. The decrease in surface relaxivities after bitumen extraction is confirmed as the cause in the next sub-section.

4.4.2.3. Evaporation Test and Weak Diffusive Coupling

In additional to NMR measurements on fully saturated samples, a controlled evaporation test was done by opening the sample container to evaporate heptane from kerogen. The NMR response was measured at each step of partial desaturation. Four representative measurements of each sample were selected and plotted in Figure 4.11, Figure 4.12 and Figure 4.13.

Figure 4.11, Figure 4.12 and Figure 4.13 show similar features, namely: heptane in intergranular pores is depleted first, while dissolved heptane is unchanged. Furthermore, the persistent bimodal feature of T_2 distribution during desaturation indicates no strong diffusive coupling between dissolved heptane and intergranular heptane.

For dissolved heptane (<), the porosity, as well as T_1 and T_2 remain unchanged throughout desaturation, corroborating that heptane in the kerogen granule is strongly absorbed, and that the two pore types are only weakly diffusively coupled. As learned from experiments, a strong vacuum is needed to deplete the dissolved heptane. This indicates that the dissolved heptane within kerogen granule might not be producible, or at least, requires very long desorption time. The interpretation for the trapped heptane is the confinement effect from the absorption in kerogen particle changes the PVT properties of hydrocarbons in the kerogen (Pathak et al. 2017), which significantly reduced the volatility of the dissolved heptane.

(a)

(b)
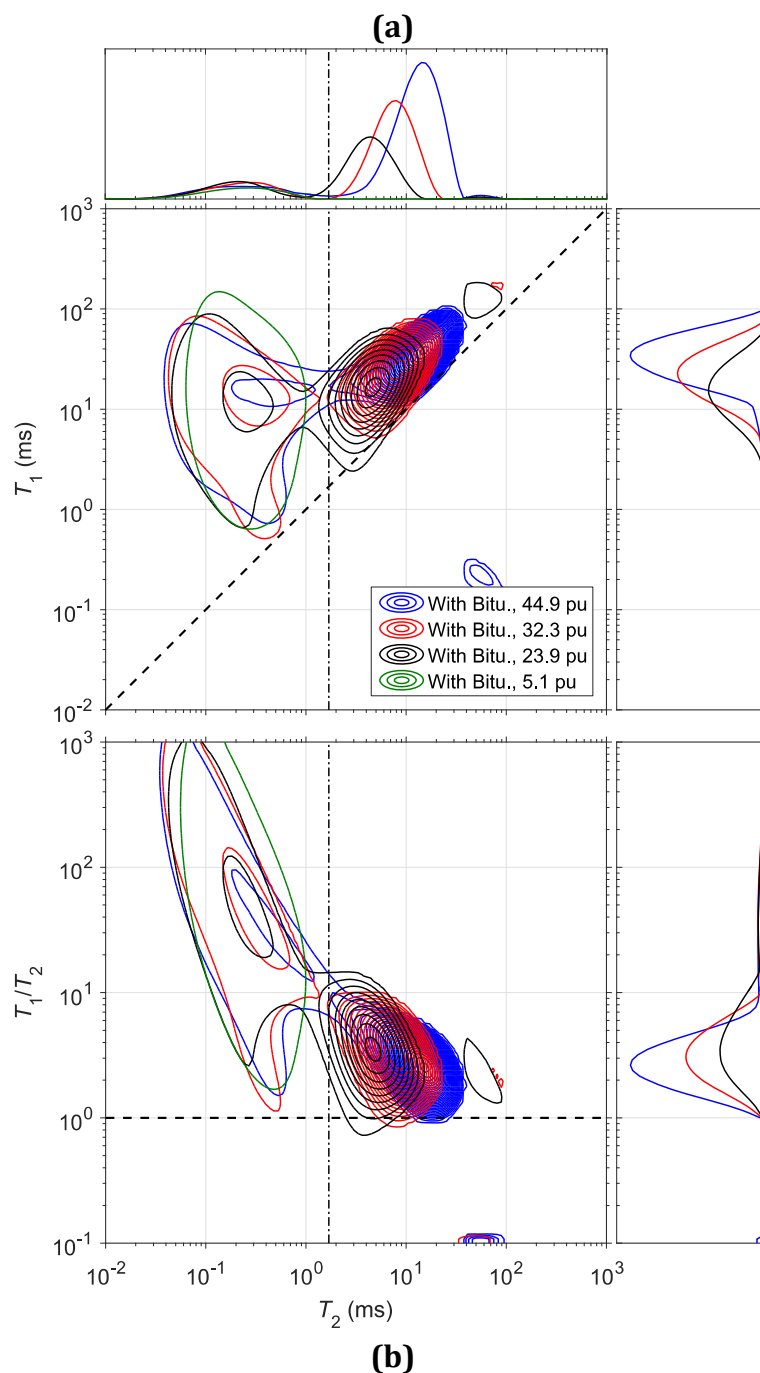
Figure 4.11 2D correlation maps of saturated "With Bitu." changing with heptane filling porosity. (a) T_1 vs. T_2 map and (b) T_1/T_2 vs. T_2 map. The legend indicates sample name and total NMR fluid porosity. The definitions of projection subplots and dashed lines are the same as Figure 4.10. Note that the persistence of the fast-relaxing peak upon desaturation indicates that the two peaks are weakly diffusively coupled.

(a)

(b)
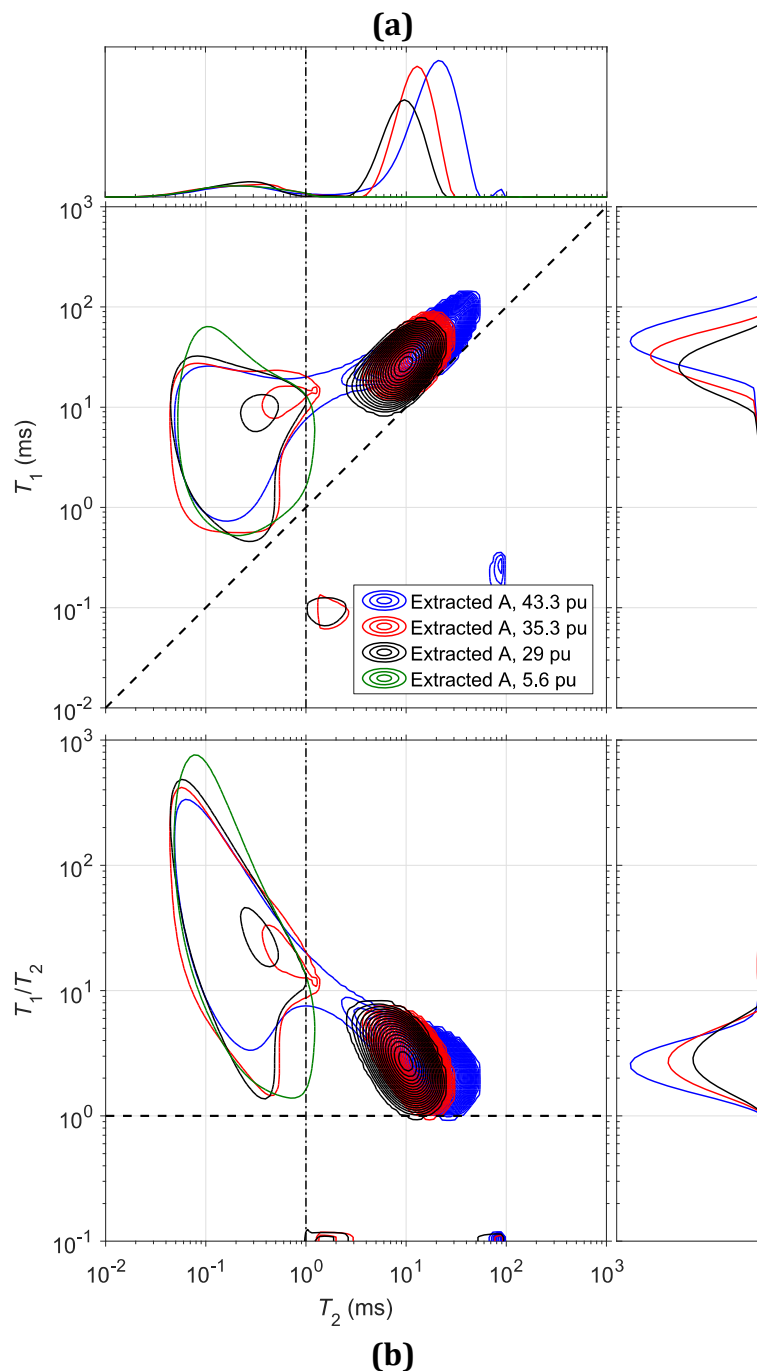
Figure 4.12 2D correlation maps of saturated "Extracted A" changing with heptane filling porosity. (a) T_1 vs. T_2 map and (b) T_1/T_2 vs. T_2 map. The legend indicates sample name and total NMR fluid porosity. The definitions of projection subplots and dashed lines are the same as Figure 4.10. Note that the persistence of the fast-relaxing peak upon desaturation indicates that the two peaks are weakly diffusively coupled.
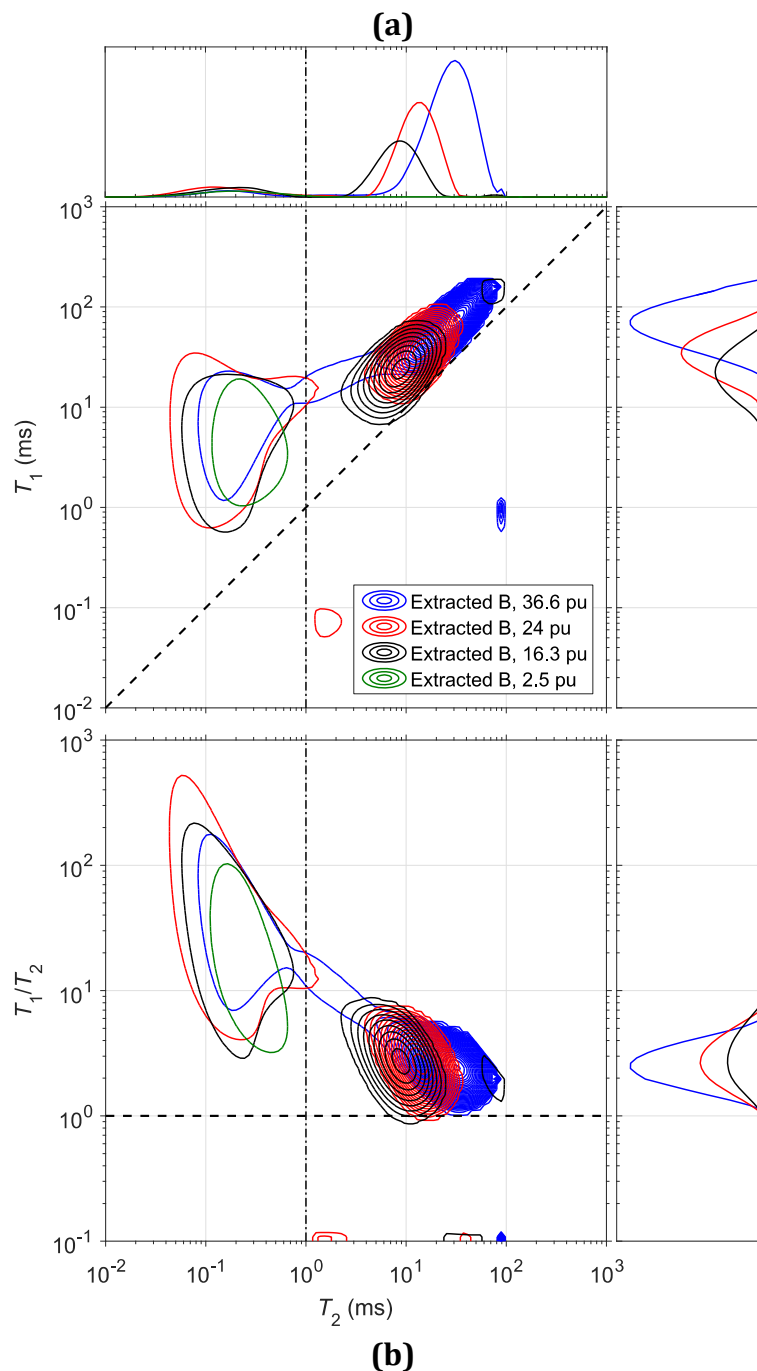
Figure 4.13 2D correlation maps of saturated "Extracted B" changing with heptane filling porosity. (a) T_1 vs. T_2 map and (b) T_1/T_2 vs. T_2 map. The legend indicates sample name and total NMR fluid porosity. The definitions of projection subplots and dashed lines are the same as Figure 4.10. Note that the persistence of the fast-relaxing peak upon desaturation indicates that the two peaks are weakly diffusively coupled.

For intergranular heptane (>), where desaturation primarily occurs, the T_1 and T_2 are continuously shortened as the heptane-filled porosity drops. During evaporation, the heptane in the middle of pores leaves first, leaving a heptane film in contact with the pore surface. This is analogous to centrifugation measurements in conventional water-saturated cores.

Moreover, the T_1/T_2 vs. T_2 maps show the T_1/T_2 ratios for both peaks are not changed during evaporation, which means for intragranular heptane, T_1 is shifted by the same factor as T_2.

The T_1 and T_2 shifts upon desaturation can be explained by Equations(2.8) and (2.9). In the case of kerogen isolates, the contribution of the internal gradient, T_{2D}, was already ruled out. For the longitudinal relaxation time of intergranular heptane, the longest $T_{1LM,>}$ is ~66 ms for "Extracted B". As for transverse relaxation, the longest $T_{2LM,>}$ is ~26 ms for "Extracted B". The log-mean relaxation times of heptane are at least 29 times less than their bulk values $T_{1B} = T_{2B} = 1{,}918$ ms. Thus, both of longitudinal and transverse relaxation are dominated by surface relaxation. Then Equations (2.8) and (2.9) can then be rewritten by incorporating Equations (2.11) and (2.12) by ignoring the negligible diffusion term, $1/T_{2D}$:

$$\frac{1}{T_1} - \frac{1}{T_{1B}} = \frac{1}{T_{1S}} = \rho_1 \frac{S}{V}, \tag{4.19}$$

$$\frac{1}{T_2} - \frac{1}{T_{2B}} = \frac{1}{T_{2S}} = \rho_2 \frac{S}{V}. \tag{4.20}$$

These expressions are valid in the fast-diffusion regime for heptane in intergranular pores, as proven to be the case in the pore-size analysis section below. Equations (4.19) and (4.20) indicate that T_{1S} and T_{2S} are proportional to the heptane filled volume, while the surface area that heptane contacts with stays the same, which explains the drift of relaxation times while evaporation occurs. Note that this drift is distinct from the relaxation time shift caused by bitumen extraction.

4.5. Interpretation of NMR Results

The results shown in the previous sub-chapter are discussed and analyzed in this sub-chapter. The first goal of this sub-chapter is to determine the surface relaxivities of intergranular pores by incorporating the BET surface area. The second goal is to derive the pore size distribution of intergranular pores using the intergranular surface relaxivities. The last goal is to interpret the changes in intergranular surface relaxivities due to bitumen extraction and then figure out the intragranular surface relaxivities and pore size.

4.5.1. Derivation of Surface Relaxivity

Equations (4.19) and (4.20) in the previous sub-chapter introduce the relationship between T_1 and T_2 with their surface-relaxivity parameters ρ_1 and ρ_2 in the fast-diffusion regime, which are applicable in the present case (see below), along with the surface-to-pore-volume ratio S/V of individual pores. The conventional approach to determine ρ_1 and ρ_2 is to take the log-mean value of both sides of Equations (4.19) and (4.20), and then integrate with the specific surface area S_{BET}

(m^2/g) acquired by BET analysis, as well as the porosity measured by NMR. This method yields single values for both ρ_1 and ρ_2.

However, even with isolated kerogen (much simpler than original Kimmeridge shale), the T_1-T_2 correlation map shows evidence of heterogeneity of pore systems, separated by $T_{2,\text{cutoff}} = 1.69$ ms (Figure 4.10). Obviously, a single value for ρ_1 or ρ_2 could not account for this heterogeneity. Thus, the simplest and most natural choice is to consider these two pore systems separately (Philip M. Singer, Chen, and Hirasaki 2016).

Here, the specific surface area S_{BET} is attributed to only the intergranular pore system, which assumes that nitrogen vapor at 77 K does not get dissolved into bitumen or kerogen. Using this assumption, Equations (4.19) and (4.20) result in:

$$\frac{1}{T_{1\text{SLM},>}} = \rho_{1,>} \left\langle \frac{S}{V} \right\rangle_> = \rho_{1,>} \frac{\rho_{\text{B}} S_{\text{BET}}}{\phi_>}, \qquad (4.21)$$

$$\frac{1}{T_{2\text{SLM},>}} = \rho_{2,>} \left\langle \frac{S}{V} \right\rangle_> = \rho_{2,>} \frac{\rho_{\text{B}} S_{\text{BET}}}{\phi_>}, \qquad (4.22)$$

where $T_{1\text{SLM},>}$ and $T_{2\text{SLM},>}$ are the log-mean surface-relaxation times of intergranular pores; $\phi_>$ is the intergranular porosity; ρ_{B} is defined as the dry-pellet mass divided by the swollen bulk-volume after heptane saturation (see Table 4.2). S_{BET} is the specific surface area measured on the dried heptane-saturated pellets.

In this study, BET was acquired at 77 K while NMR measurements were acquired on the same sample, but at 30 °C. In terms of this, it is assumed in this research that thermal-expansion effects of isolated kerogen are negligible and that

the intergranular pores seen by nitrogen and heptane are the same between BET

and NMR (Philip M. Singer, Chen, and Hirasaki 2016). As mentioned in Section 4.3.1,

an average surface-area $S_{\mathrm{BET}} = 14 \ \mathrm{m}^2/\mathrm{g}$ is adopted for all three samples.

Table 4.2 Summary of pore-size analysis for intergranular pores (>) of fully saturated samples, assuming spherical pores.

Sample	With Bitu.	Extracted A	Extracted B
ρ_{B} (g/cm³)	0.73	0.82	1.02
$\rho_{1,>}$ (μm/s)	1.1	0.7	0.4
$\rho_{2,>}$ (μm/s)	2.9	1.9	0.9
$d_{1\mathrm{LM},>}$ (nm)	223	201	146
$d_{2\mathrm{LM},>}$ (nm)	222	200	146

The surface relaxivities derived from Equations (4.21) and (4.22) are plotted

in Figure 4.14. Both $\rho_{1,>}$ and $\rho_{2,>}$ are found to be roughly constant regardless of the

decreased heptane-filled porosity, further confirming that the two distinct pore

systems are weakly diffusively coupled. The surface relaxivities of fully saturated

states are listed in Table 4.2. For fully saturated samples, the surface relaxivity $\rho_{1,>}$

decreases by 36 % by Soxhlet extraction, and by 64 % by static extraction.

Meanwhile, $\rho_{2,>}$ decreases by 34 % by Soxhlet extraction and by 69 % by static

extraction.

In this surface relaxivity analysis, the oil saturation S_{o} is assumed to be

independent of intergranular pore size, which simplifies the analysis. However,

Figure 4.15 in the following sub-chapter indicates the distributions of intragranular

pore diameter have a finite width. Thus, the apparent curvature in Figure 4.14 at

high oil saturation may be a result of pore-size dependence in oil saturation.

(a)

(b)
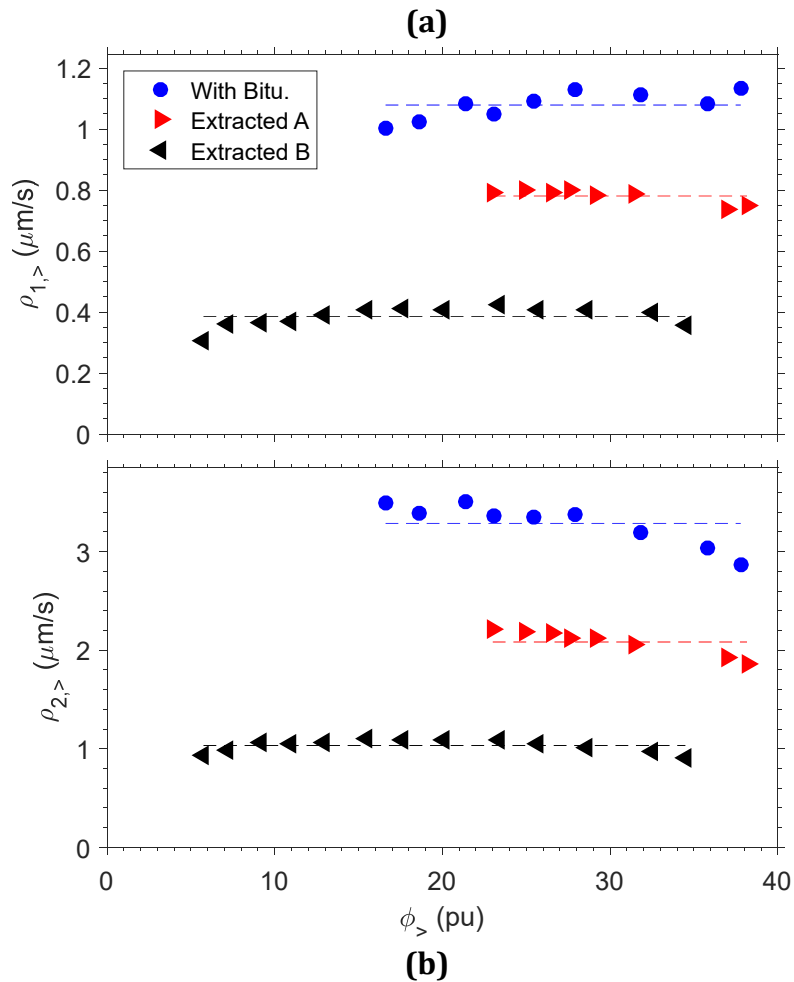
Figure 4.14 Surface relaxivity for heptane in intergranular pores of kerogen, as a function of heptane-filled porosity, decreased during controlled evaporation, for "With Bitu." (blue), "Extracted A" (red) and "Extracted B" (black). (a) is for $\rho_{1,>}$, (b) is for $\rho_{2,>}$. The average surface relaxivity of each sample is plotted as a dashed line. Note that the data indicate roughly constant surface relaxivities upon desaturation.

4.5.2. Pore-Size Analysis

Using the surface relaxivity, one can convert the relaxation times into pore diameters based on Equations (4.19) and (4.20) as follows:

$$d_{1,>} = 6\rho_{1,>}T_{1S,>}, \tag{4.23}$$

$$d_{2,>} = 6\rho_{2,>}T_{2S,>}. \tag{4.24}$$

Spherical pores have been assumed, where $S/V = 6/d$.
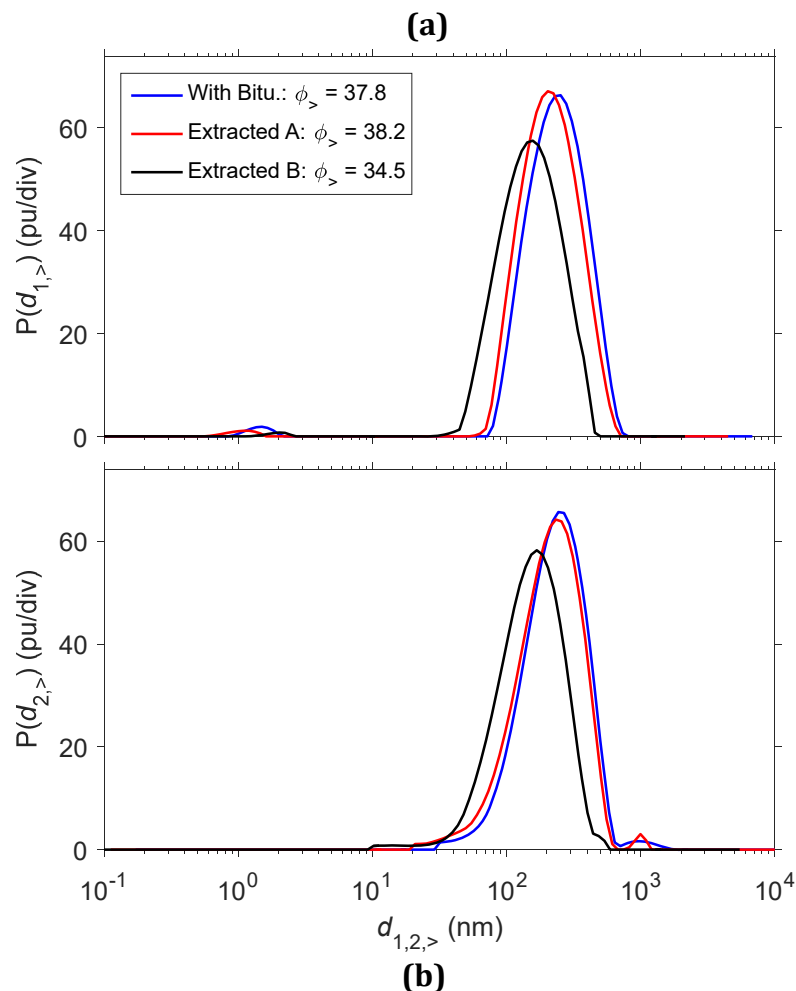
Figure 4.15 Pore diameter d distributions of heptane in intergranular pores of "With Bitu." (blue), "Extracted A" (red) and "Extracted B" with (a) d_1 and (b) d_2 derived from Equations (4.23) and (4.24), respectively, assuming spherical pores. The legend indicates the sample. Note how d_1 and d_2 agree with each other, as expected, given the above derivation.

The results plotted in Figure 4.15 show consistency between pore-size distributions derived from T_1 (Figure 4.15(a)) and T_2 (Figure 4.15(b)) for three samples. By the log-mean pore diameter (listed in Table 4.2), one finds that "With Bitu." and "Extracted A" share the same pore size. "Extracted B" shows $\sim 30~\%$ less pore diameter (146 nm) compared with the others (~ 200 nm). It is apparent that the increase in $T_{1,>}$ and $T_{2,>}$ upon bitumen extraction cannot be explained by such changes in pore size, but rather by a decrease in surface relaxivities.

The data derived in this sub-chapter are summarized in Table 4.2. It is noted that ρ_B of "With Bitu." is close to "Extracted A", but lower than "Extracted B". This observation is also consistent with the larger swelling percentage of "With Bitu." and "Extracted A". Based on the data in Table 4.2, $d_{1LM,>}\rho_{1,>}/D_0 \ll 1$ and $d_{2LM,>}\rho_{2,>}/D_0 \ll 1$ are calculated with heptane bulk diffusivity $D_0 = 3.43\ \mu m^2/ms$ for all three samples. It is apparent that the fast-diffusion regime is valid for intergranular pores since both values are much less than unity, therefore Equations (4.19) and (4.20) are valid.
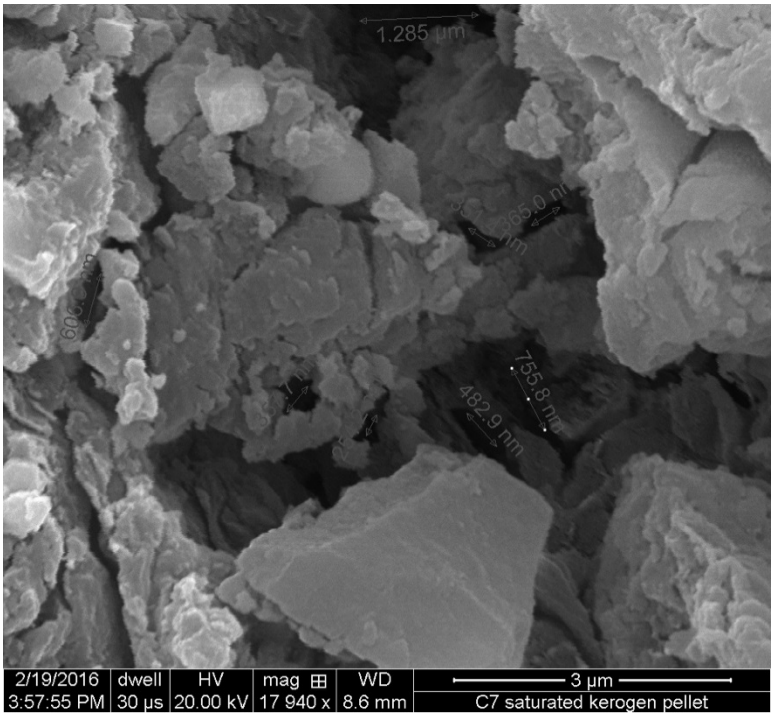
Figure 4.16 SEM image of intergranular porosity of "With Bitu." dried after heptane saturation.

Another effective way to view the NMR pore size is to use SEM. Figure 4.16 shows the kerogen grains and the intergranular pores of "With Bitu." dried after heptane saturation. The intergranular pore diameters are in the range of 200 nm to 1,000 nm. It corroborates with the NMR pore-size distributions in Figure 4.15.

4.5.3. Diffusion Length and Apparent Surface Relaxivity

In this section, the increase in intergranular $T_{1,>}$ and $T_{2,>}$ upon bitumen extraction is attributed to the reduction in surface relaxivity, instead of changes in pore size. The interpretation is the following: intergranular heptane (which is in fast-diffusion regime) travels between kerogen granules and then gets relaxed when it encounters the kerogen granules. The intergranular relaxation rate also depends on the diffusion length of heptane into the kerogen grain, which is a function of the microporosity of the granule. The diffusion length for T_1 and T_2 into the granule is discussed in Chapter 2 and Equations (4.9) and (4.10).

The diffusion length is proportional to the microporosity to the power of $(m-1)/2$. Therefore, the diffusion length is reduced by bitumen extraction as a result of a decrease in microporosity ϕ_μ. Therefore, the relaxation rate, i.e., the "apparent surface relaxivity", is reduced due to bitumen extraction.

The other way to interpret the surface relaxivity change is to implement the model by Ramakrishnan *et al.* 1999 and Dunn 2002 for the carbonate system to the kerogen system. It is shown that for carbonate systems with two pore types, the apparent surface relaxivity $\rho_{1,a}$ and $\rho_{2,a}$ can be written as a function of microporosity as in Equations (4.5) and (4.6). Since D_0, ϕ_μ, $T_{2,\mu}$ and $T_{1,\mu}$ are known, and $\rho_{1,a}$ and $\rho_{2,a}$ are $\rho_{1,>}$ and $\rho_{2,>}$ in this research, the expression for the apparent surface relaxivities from T_1 and T_2 for intergranular pores has only three unknown parameters, namely $\rho_{1,\mu}$, $\rho_{2,\mu}$ and m.

(a)

(b)
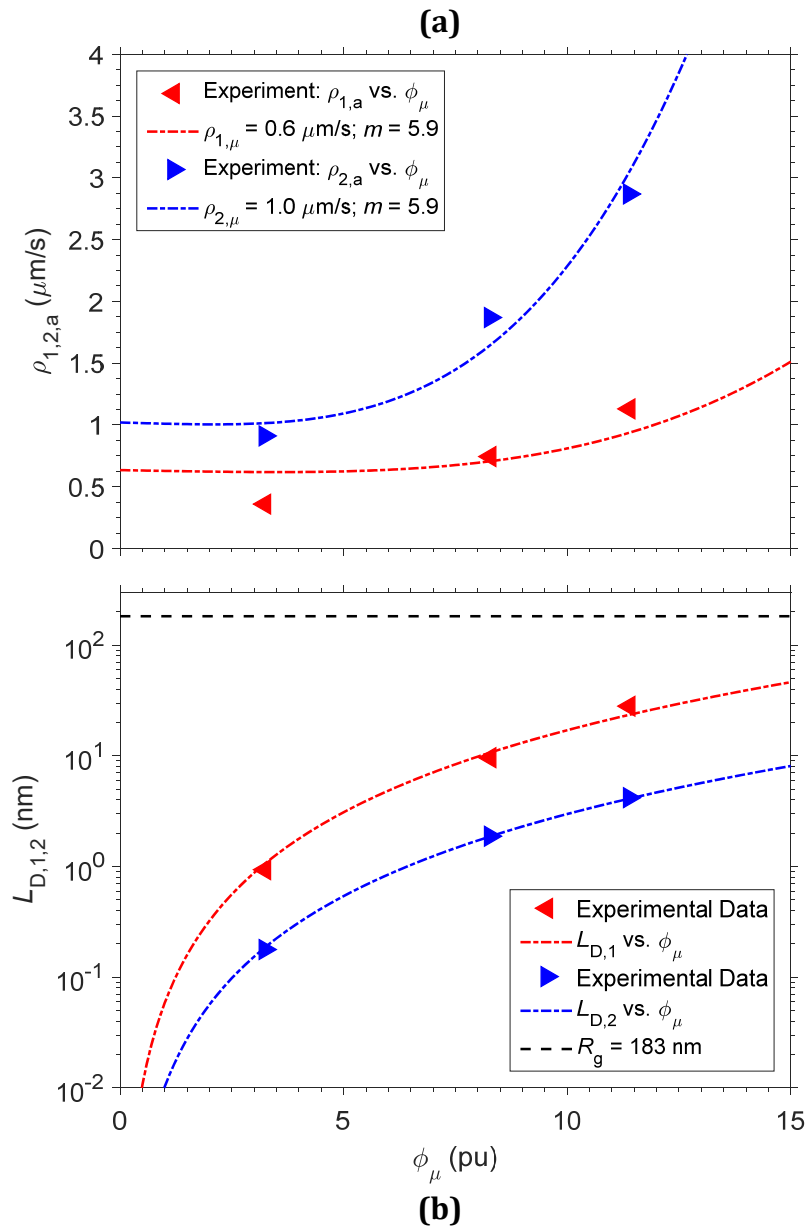
Figure 4.17 (a) Apparent surface relaxivities ($\rho_{1,a}$, $\rho_{2,a}$) for intergranular pores as a function of microporosity (ϕ_μ). Red and blue triangles represent the apparent surface relaxivity for T_1 and T_2 respectively calculated from experimental data. Red and blue lines are the nonlinear fit with fitting parameters listed in the legend for T_1 and T_2, respectively. Archie's cementation exponent m is shared by both fits. Note how increasing the microporosity increases the apparent surface relaxivity as a result of greater diffusion length within the kerogen granules. (b) Diffusion length ($L_{D,1}$, $L_{D,2}$) as a function of microporosity (ϕ_μ) with m from (a) and average $T_{1,\mu}$ and $T_{2,\mu}$. Red and blue lines show the diffusion length for T_1 and T_2 respectively. Red and blue triangles are calculated from experimental data of each sample for T_1 and T_2, respectively. Black line indicates the estimated radius of the kerogen granule.

It has already been illustrated that the bitumen extraction did not

significantly change the relaxation times for intragranular heptane. Therefore,

constant intrinsic surface relaxivities, $\rho_{1,\mu}$ and $\rho_{2,\mu}$, are assumed for all three

samples. Also, it is reasonable to have a common Archie's cementation exponent m

that is shared by all three samples for Equations (4.5) and (4.6). As a consequence,

the apparent surface relaxivities, $\rho_{1,a}$ and $\rho_{2,a}$, are functions of microporosity ϕ_μ,

along with three free parameters: $\rho_{1,\mu}$, $\rho_{2,\mu}$ and m.

Nonlinear least-square regression with three free parameters, namely $\rho_{1,\mu}$,

$\rho_{2,\mu}$ and m, is implemented to two datasets (six points), as shown in Figure 4.17(a).

Using nonlinear regression, it is found that $\rho_{1,\mu} = 0.6 \ \mu m/s$, $\rho_{2,\mu} = 1.0 \ \mu m/s$ and

$m = 5.9$ give the best fit to the experimental data. The fit captures the general

trend, namely that increasing ϕ_μ results in an increase in $\rho_{1,a}$ and $\rho_{2,a}$ as a result of

greater diffusion length within the kerogen granules. The model also indicates that

as the microporosity approaches zero (i.e., no intragranular pores), $\rho_{1,a}$ and $\rho_{2,a}$

tend towards the "intrinsic" surface relaxivities $\rho_{1,\mu}$ and $\rho_{2,\mu}$ of kerogen micropores,

respectively.

The optimized $m = 5.9$ is much higher than for most of the conventional

carbonate rocks. This may indicate much greater tortuosity in the kerogen

micropores, and/or it may indicate a limitation in the application of the carbonate

model to kerogen. One possible caveat is that the conventional Archie's formation

factor F_μ does not take surface residence time of the molecules into account. In

nanopore systems, for a given diffusion evolution time, the diffusion length L_D will

decrease due to finite surface residence time. In the conventional formulation used here, lower L_D is accounted for by larger formation factor F_μ (i.e., larger m exponent). Further investigations are required to modify the L_D and ρ_a analysis to take surface residence time into account to refine this model for kerogen.

As for the intrinsic surface relaxivities for the microporosity, $\rho_{1,\mu}$ and $\rho_{2,\mu}$ provide an opportunity to estimate the pore size of intragranular pores, namely the size of confined space for dissolved heptane:

$$d_{1,\mu} = 6\rho_{1,\mu}T_{1,\mu}, \tag{4.25}$$

$$d_{2,\mu} = 6\rho_{2,\mu}T_{2,\mu}, \tag{4.26}$$

where $d_{1,\mu}$ and $d_{2,\mu}$ are the pore diameter of intragranular pores, derived from T_1 and T_2 respectively, assuming spherical pores. By substituting the fitting parameters $\rho_{1,\mu} = 0.6\ \mu m/s$ and $\rho_{2,\mu} = 1.0\ \mu m/s$, and the average values for $T_{1,\mu} = 7.1$ ms and $T_{2,\mu} = 0.22$, one can calculate the pore diameter of intragranular pores, $d_{1,\mu} = 27$ nm and $d_{2,\mu} = 1.3$ nm, respectively. The difference between $d_{1,\mu}$ and $d_{2,\mu}$ is most likely due to uncertainties in the measurements, as well as limitations in the model; nevertheless, they provide a range of 1.3 nm to 27 nm for the diameter of the intragranular pores. In the SEM image shown as Figure 4.18, $\sim$30 nm pores were observed, which is closed to the derived intragranular pore size above. This small pore size is previously reported (Pathak et al. 2017). The extremely small pore size also confirms the expectation made in the previous section that the dissolved heptane is confined in nanopores, where the molecular motion is greatly hindered.
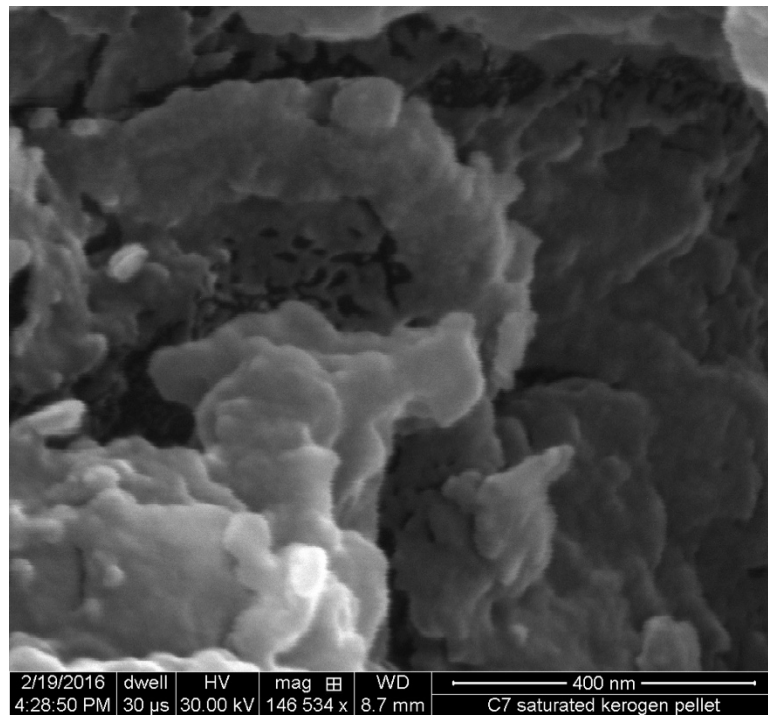
Figure 4.18 SEM image of nano-scale pores of "With Bitu." dried after heptane saturation.

The diffusion length for each sample, defined by Equations (4.7) and (4.8), can now be calculated using the fitted parameter $m = 5.9$, as shown in the Figure 4.17b. And average values $T_{1,\mu} = 7.1$ ms and $T_{2,\mu} = 0.22$ ms are used to generate the universal curves for diffusion length as a function of microporosity for all samples. It is readily shown that the diffusion length increases as the microporosity increases. The radius of the kerogen granule is also estimated (assuming spherical granules) as follows:

$$R_g = \frac{3V_g}{S_g} = \frac{3(1 - \phi_>)}{\rho_B S_{BET}}, \tag{4.27}$$

where V_g is the volume of the kerogen granule; S_g is the surface area of the kerogen granule, which is the same as the surface area of intergranular pores. The definitions for $\phi_>$, ρ_B and S_{BET} are the same as Equations (4.21) and (4.22). The calculated

radius of the kerogen granule $R_g = 183$ nm is shown as the black line in Figure 4.17(b). It is apparent that the diffusion length is an order of magnitude less than the granule radius, i.e., $L_{D,1,2} \ll R_g$, which confirms the weak diffusive coupling between intra- and intergranular pores (Anand and Hirasaki 2007).

4.5.4. Evidence of Diffusive Coupling

In the above section, we model the surface-relaxivity parameters of the inter-granular heptane using the diffusive-coupling model previously reported for carbonates, over a wide range of grain porosities. To validate the application of the diffusive-coupling model, we conduct a series of T_2-T_2 exchange experiments that can provide information about diffusion of fluid molecules that happens between neighboring pores in liquid-saturated porous media (Mitchell et al. 2014)

Figure 4.19 shows the T_2-T_2 exchange measurements on the heptane-saturated kerogen (i.e., "With Bitu,"). Four measurements with different Δ's are conducted. Two main peaks on Figure 4.19 along the diagonal line have $T_{2a}/T_{2b} = 1$. These two main peaks characterize the two environments (i.e., with different T_2 relaxation times) where heptane molecules get relaxed, namely the kerogen grains that dissolve heptane and the intergranular pore space. It is found that the off-diagonal exchange peaks exist in all measurements. The off-diagonal peaks suggest that the heptane molecules move between two environments by diffusion. It should be noted that because the storage time acts as the dead time for T_2-T_2 exchange measurements, the signal intensity of the main short T_2 peaks decreases as the storage time increases.
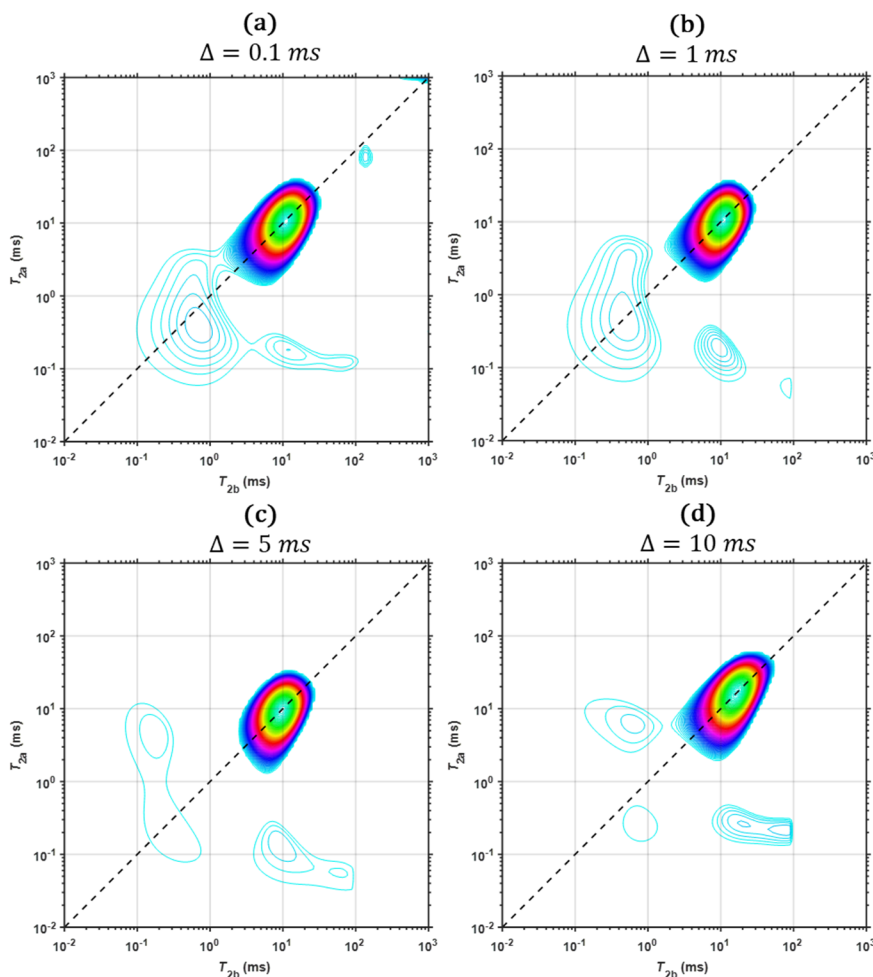
Figure 4.19 T_2-T_2 exchange correlation maps of heptane-saturated kerogen isolates with different z-storage delay duration: (a) Δ = 0.1 ms, (b) Δ = 1 ms, (c) Δ = 5 ms and (d) Δ = 10 ms. The y-axis is for the direct T_2 (i.e., T_{2a}). The x-axis is for the indirect T_2 (i.e., T_{2b}). The diagonal dashed line has T_{2a}/T_{2b} equal to 1.

The persistent off-diagonal peaks confirm the diffusive coupling between the heptane in the kerogen grains and the intergranular heptane, therefore valid the application of the diffusive-coupling model.

Note that this section is used in preparation for a peer-reviewed article.

4.6. Kerogen Surface Relaxation

4.6.1. Intra- and Intergranular ^{1}H-^{1}H Dipole-Dipole Interaction

There are many ongoing discussions about the nature of the surface-relaxations mechanism in organic shale (Kathryn E. Washburn 2014). Two mechanisms have been proposed for understanding the NMR surface-relaxivities, ρ_1 and ρ_2, in the fast-diffusion regime for organic shale (Equations (2.11) and (2.12)). The first proposition is translational 2D diffusion of fluids on the pore surface in the presence of paramagnetic sites on the surface" (J.-P. Korb et al. 2014; Nicot et al. 2016). The other proposition is enhanced ^{1}H-^{1}H dipole-dipole interactions in the presence of pore surfaces (Straley 2002; Rylander et al. 2013; Kathryn E. Washburn 2014), which does not require surface paramagnetism on the organic-pore surface. Both theories for T_1 and T_2 have some common features, namely (1) both theories have an amplitude or strength term proportional to the second moment $\langle \Delta\omega^2 \rangle$ of the interaction, (2) both theories depend on the surface residence time τ_s, which itself depends on temperature, and (3) both theories depend on resonance frequency ω under certain conditions. Assuming both mechanisms contribute yields the following relation:

$$\rho_1 = \rho_{1,\text{Dmol}} + \rho_{1,\text{Dker}} + \rho_{1,\text{P}}, \qquad (4.28)$$

$$\rho_2 = \rho_{2,\text{Dmol}} + \rho_{2,\text{Dker}} + \rho_{2,\text{P}}, \qquad (4.29)$$

where $\rho_{1,2,\text{Dmol}} + \rho_{1,2,\text{Dker}}$ is the total contribution from dipole-dipole interactions, and $\rho_{1,2,\text{P}}$ is the paramagnetic contribution.
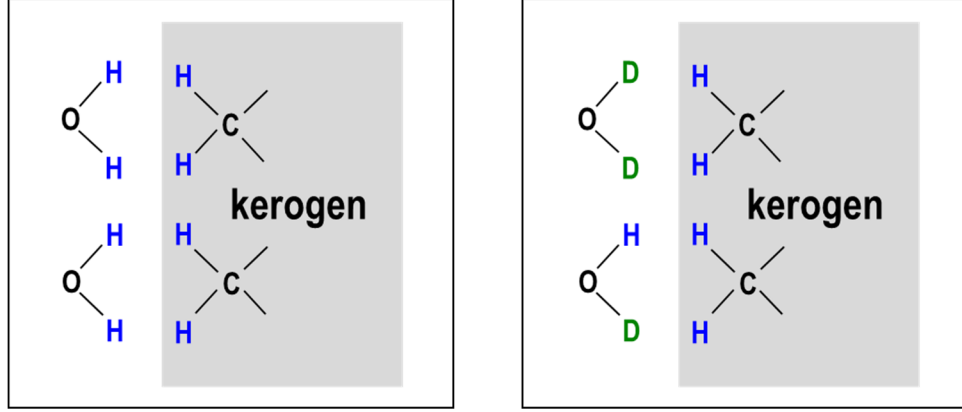
Figure 4.20 Illustration of water molecules residing on the kerogen surface (a), versus the same scenario with partial deuteration of the water molecules (b). Partial deuteration (b) removes the molecular dipole-dipole contribution to the surface relaxivity ($\rho_{1,2,\text{Dmol}}$), but not the kerogen dipole-dipole contribution ($\rho_{1,2,\text{Dker}}$). The image is a simplified snapshot of the water molecules residing on the kerogen surface for time τ_S.

An explanation of the two dipole-dipole terms in Equations (4.28) and (4.29) is shown in Figure 4.20(a) for water residing on the kerogen surface during time τ_s. The molecular dipole-dipole contribution $\rho_{1,2,\text{Dmol}}$ is defined as being between a water ¹H nucleus and its partner ¹H nucleus on the same water molecule, plus the contribution from a neighboring water molecule's ¹H nucleus also residing on the surface. The kerogen dipole-dipole contribution $\rho_{1,2,\text{Dker}}$ is defined as being between a water ¹H nucleus and a nearby ¹H nucleus bound to the solid kerogen surface. The same arguments and definitions hold for a heptane molecule residing on the kerogen surface. Put more formally, the total dipole-dipole contribution for a water molecule residing of the kerogen surface can be expressed as the sum:

$$\rho_{1,\text{D}} = \left(\rho_{1,\text{Dmol}} + \rho_{1,\text{Dker}}\right) \propto \langle \Delta\omega^2 \rangle \propto \sum_{i \neq k} \frac{\gamma_I^4}{r_{ik}^6}, \tag{4.30}$$

$$\rho_{2,\text{D}} = \left(\rho_{2,\text{Dmol}} + \rho_{2,\text{Dker}}\right) \propto \langle \Delta\omega^2 \rangle \propto \sum_{i \neq k} \frac{\gamma_I^4}{r_{ik}^6}. \tag{4.31}$$

The second moment $\langle\Delta\omega^2\rangle$ is proportional to the inverse 6th power of the ^{1}H-^{1}H

separation, r_{ik}. It is also proportional to the 4th power in the ^{1}H gyromagnetic ratio,

γ_I. For the current purposes, Equations (4.30) and (4.31) only capture the amplitude

or strength term $\langle\Delta\omega^2\rangle$, however, these equations also contain an (unknown)

dynamic term which depends on τ_s and ω. The dynamic terms remain elusive in

organic shale, just like they do for heavy crude oils where T_{1B} and T_{2B} depart from

theoretical expectations for the viscosity, i.e., the molecular correlation time, τ and

ω dependences, assuming ^{1}H-^{1}H dipole-dipole interactions dominate (Yang et al.,

2012).

The motivation for expressing Equations (4.28) and (4.29) in such a manner

is that the effect of partial deuteration of the water molecules is to significantly

reduce the $\rho_{1,2,Dmol}$ term, while keeping $\rho_{1,Dker}$ the same. This is illustrated in Figure

4.20(b), where partial deuteration of the water molecules eliminates the $\rho_{1,2,Dmol}$

(technically it is reduced by a factor of ~42, making it essentially negligible). Such a

scenario was successfully tested in carbonates (Straley 2002), where relaxation data

for 100% H_2O (equivalent to Figure 4.20(a)) were compared with a mixture (named

"D_2O" for simplicity) of 90% D_2O:10% H_2O (equivalent to Figure 4.20(b)). Figure

4.21 compares data for the water in kerogen vs. the D_2O mixture in kerogen. As

indicated in Table 3.2, T_{1LM} and T_{2LM} for D_2O in kerogen are a factor ~1.4 times

longer than for water. Given the same pore size (two saturating fluids in the sample

kerogen pellet), the ρ_1 and ρ_2 of D_2O in kerogen is less than water in kerogen, which

suggests that the $\rho_{1,2,Dmol}$ is reduced by partial deuteration. Therefore, it is

confirmed that the intramolecular [1]H-^{1}H dipole-dipole interaction contributes to ρ_1

and ρ_2.
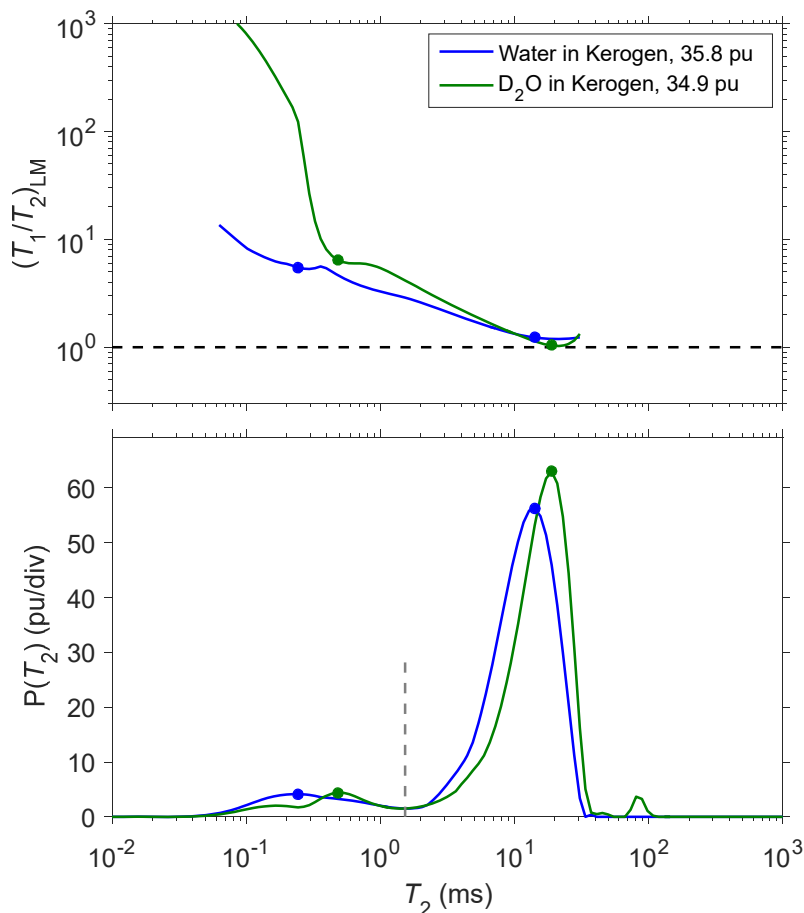
Figure 4.21 Upper figure is the log-mean $(T_1/T_2)_{LM}$ curve vs. T_2 obtained from the 2D correlation maps, and the dashed horizontal line is the $T_1/T_2=1$ line. The lower figure is the projected T_2 data from the 2D correlation maps. The legend indicates fluid name, matrix name, and total fluid porosity. The dots in upper and lower figures correspond to $T_{2,peak}$ and $(T_1/T_2)_{peak}$ listed in Table 3.1, and the dashed grey vertical line is $T_{2,cutoff}$ =1.5 ms separating dissolved fluid (<) from intergranular pores (>). The "D$_2$O" fluid consists of a 90% D$_2$O-10% H$_2$O mix.

In addition, Washburn and Cheng 2017 shows that intermolecular [1]H-[1]H

dipole-dipole interaction also contributes to the ρ_1 and ρ_2 of fluids by conducting T_2-

T_2 exchange experiments,. Extensive cross peaks are observed in the T_2-T_2 exchange

spectra between the solid and liquid constituents, indicating an exchange of

magnetization between the two phases as shown in Figure 4.22 (Kathryn E.

Washburn and Cheng 2017).
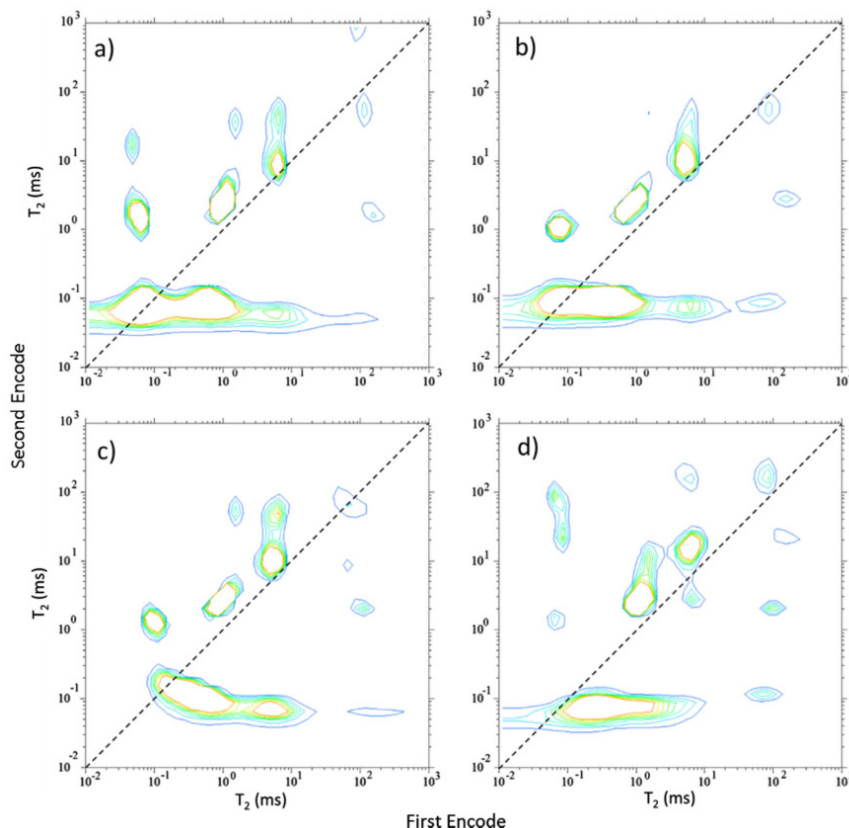
Figure 4.22 T_2-T_2 exchange plots for the re-saturated shale sample at (a) 100 μs (b) 1ms (c) 5ms (d) 10 ms mixing times (Kathryn E. Washburn and Cheng 2017).

In conclusion, even though the para-magnetism surface relaxation cannot be

completely ruled out, both of the intra- and intermolecular [1]H-^{1}H dipole-dipole

interaction contributes a non-negligible portion to the total surface relaxivity, which

has broad implications on the underlying theory of the surface-relaxation

mechanism in kerogen and organic nanopores in general.

4.6.2. A Model System: Polymer-Heptane Mixes

The results shown in the previous sub-chapter suggest that the relaxation between the dissolved heptane and kerogen is the same as heptane and bitumen. Therefore, the knowledge learned from bitumen and crude oils can be used to interpret the kerogen-heptane relaxation.

Table 4.3 Brand name, composition, viscosity η at 25 °C, density ρ at 25 °C, average molecular weight M_w, and polydispersivity index M_w/M_n for the Brookfield viscosity standards used in this study[a] (Philip M. Singer, Chen, et al. 2018)

brand name	composition	η (25 °C) (cP)	ρ (25 °C) (g/cm^3)	M_w (g/mol)	M_w/M_n
B360000	poly(isobutene)	333 400	0.885	9436	3.11
B73000	poly(isobutene)	68 070	0.888	4368	2.53
B10200	poly(isobutene)	10 650	0.875	2256	2.13
B1060	poly(1-decene)	1043	0.841	4204	1.49
B200	petroleum distillate	196	0.873		
B29	petroleum distillate	29	0.857		

[a]The polymer−heptane mixes were made using B360000 poly-(isobutene).

It is well known that the T_1/T_2 ratio of bitumen and crude oils increases with viscosity due to the dispersion of T_1 and T_2 in the slow-motion regime (a.k.a., high viscosity regime) where the viscosity is high (Yang et al. 2012). There are two main relaxation mechanisms to interpret the T_1 and T_2 dispersion. One is based on the paramagnetic sites on the asphaltene surface (J. J. Chen et al. 2014; Benamsili et al. 2014; J. P. Korb et al. 2015; Vorapalawut et al. 2015; Ordikhani-Seyedlar et al. 2016), while the other one is based on the ^{1}H-^{1}H dipole-dipole interaction, without the

need to invoke surface paramagnetism (Philip M. Singer, Chen, et al. 2018; Q. Zhang et al. 1998; Lo et al. 2002; Hirasaki, Lo, and Zhang 2003; Yang et al. 2012)

Since ^{1}H-^{1}H dipole-dipole interaction is confirmed and the main paramagnetic material, pyrite, in kerogen is highly localized, ^{1}H-^{1}H dipole-dipole interaction is most likely the dominant mechanism in the kerogen-heptane system. Therefore, this section focuses on interpretations based on the ^{1}H-^{1}H dipole-dipole interaction mechanism. It should be noted that this section is adapted from a published manuscript (Philip M. Singer, Chen, et al. 2018).

The traditional theories that are based on ^{1}H-^{1}H dipole-dipole interaction, including BPP (Bloembergen, Purcell, and Pound 1948) and Torrey theories (Torrey 1953), predict an increase in T_1 and a decrease in T_2 with increasing viscosity in the slow-motion regime (i.e., high-viscosity regime). However, the previous experiments on bitumen and heavy crude oils show that T_1 becomes independent of viscosity at high viscosities. To better understand the mechanism and interpret the experimental data, we build a model system for bitumen and crude oils using a set of pure polymers and polymer-heptane mixes spanning a wide range of viscosities (from 0.39 cP to 334,000 cP, see Table 4.3), and conduct measurement at various NMR frequencies (from 2.3 MHz to 400 MHz) at ambient conditions.

Figure 4.23 shows the T_{1LM} (i.e., log-mean of T_1) and T_{2LM} (i.e., log-mean of T_2) of the pure polymers and polymer-heptane mixes in a normalized scale. It is found that at high viscosities (i.e., in the slow-motion regime) T_{1LM} plateaus to a value $T_{1LM>} \propto \omega_0$ independent of viscosity, similar to bitumen. More specifically, on a

frequency-normalized scale, we find that $T_{1LM>} \times 2.3/f_0 \simeq 3$ ms (i.e., normalized

relative to 2.3 MHz) (Philip M. Singer, Chen, et al. 2018).
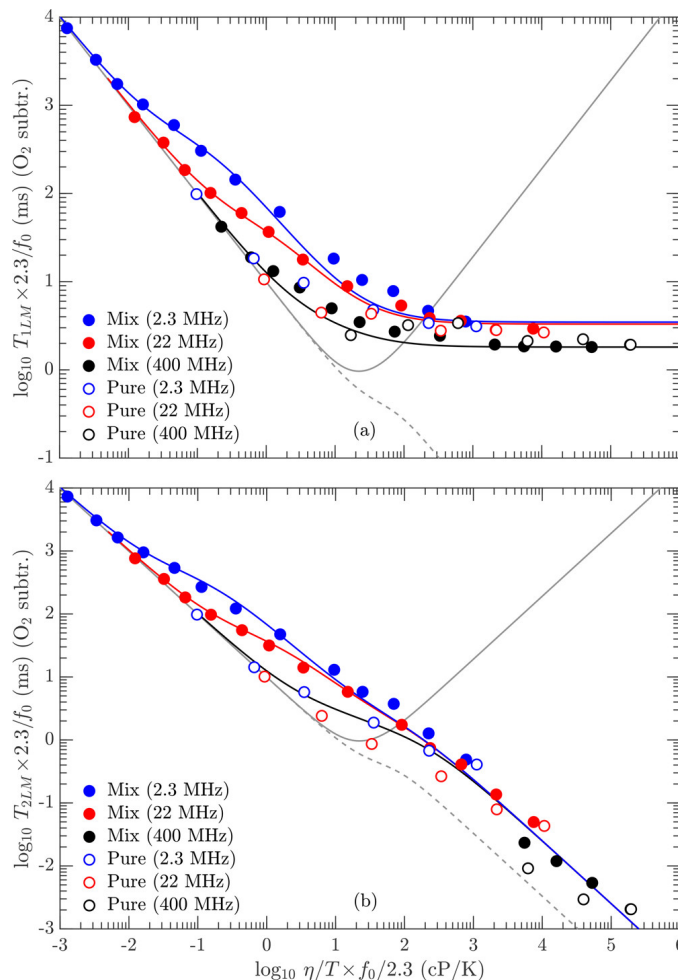
Figure 4.23 (a) T_{1LM} and (b) T_{2LM} of pure viscosity standards (open symbols) and polymer-heptane mixes (solid symbols) at different NMR frequencies versus viscosity over absolute temperature (η/T). The x-axis has been multiplied by f_0/2.3 and the y-axis has been divided by f_0/2.3, with f_0 in MHz. This plotting format is referred to as frequency normalizing relative to 2.3 MHz. Gray lines are the BPP model for T_1 (solid) and T_2 (dashed) at 2.3 MHz, while colored (solid) lines are fits using the LS model at different NMR frequencies (same colors as data). Relaxation contributions from dissolved O_2 have been subtracted from the data (Philip M. Singer, Chen, et al. 2018).

It should be noted that T_{1LM} does not follow the prediction by BPP theory,

which is presented by the solid gray line in Figure 4.23. Instead, a new model based

on LS (Lipari and Szabo 1982) theory is proposed to fit the data (Philip M. Singer,

Chen, et al. 2018). The new LS model builds on the traditional hard-sphere BPP

model of ^{1}H-^{1}H dipole-dipole interactions and adds (1) the possibility of internal motions of the nonrigid polymer branches and (2) the distribution of molecular correlation times inherent in the polymer-heptane mixes. With just two additional parameters, the new model fits T_{1LM} and T_{2LM} for pure polymer and polymer-heptane mixes across the entire viscosity and frequency range (see Figure 4.23) (Philip M. Singer, Chen, et al. 2018).
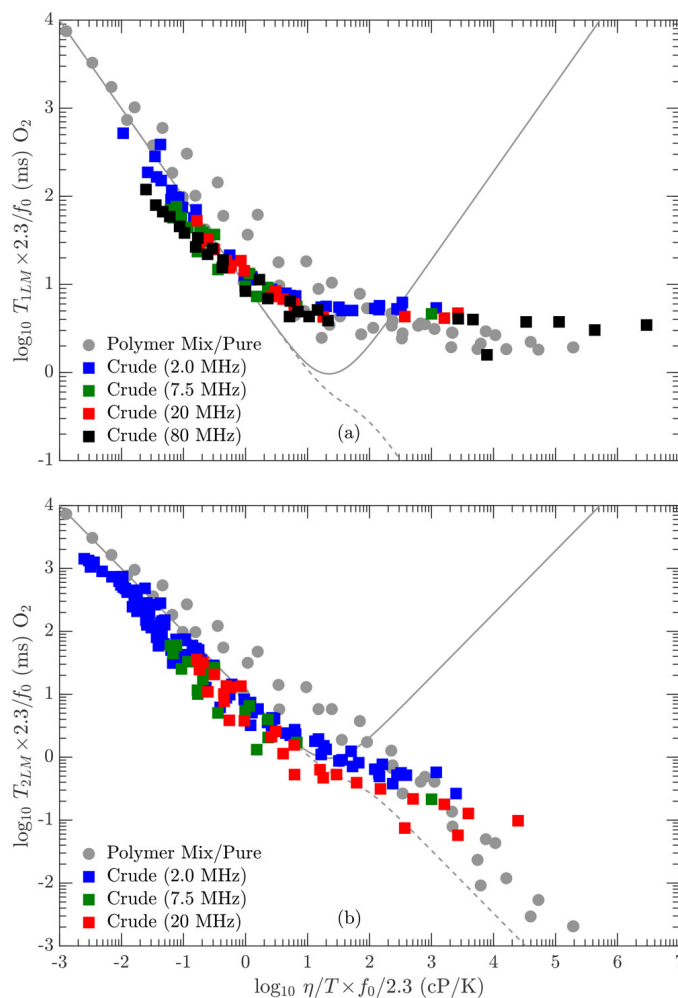
Figure 4.24 (a) T_{1LM} and (b) T_{2LM} of previously published bitumen and heavy crude oil data taken from refs (Vinegar et al. 1991; Morriss et al. 1997; Yang and Hirasaki 2008; Yang et al. 2012). All frequency normalized to 2.3 MHz as in Figure 4.23. Also shown are all the polymer data from Figure 4.23 as gray symbols (Philip M. Singer, Chen, et al. 2018).

These findings are in good agreement with bitumen and previously reported polymers (see Figure 4.24). It is clear that T_{1LM} of polymer, bitumen, and crude oils approaches to the same plateau. Likewise, in the high-viscosity limit, T_{2LM} for the polymers is found to be consistent with bitumen and heavy crude oils.

The concentration of paramagnetic impurities in the polymers under investigation is found to be at least an order of magnitude less than previously reported bitumen, which suggests that the NMR relaxation mechanisms at high viscosities for polymers, bitumen, and heavy crude oils are all dominated by ^{1}H-^{1}H dipole-dipole interactions and not surface paramagnetism (Philip M. Singer, Chen, et al. 2018).
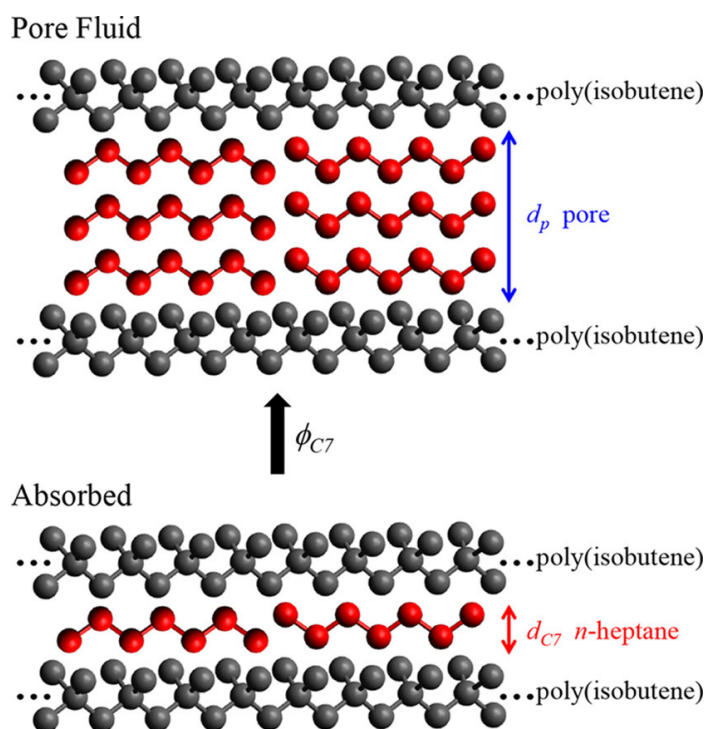
Figure 4.25 Cross-section of (locally) cylindrical transient "pores" for the two regimes in the polymer-heptane mix (only carbon atoms are shown). (Top) "Pore fluid" regime ($\phi_{C7} > 50$ vol %), where d_p is the cylindrical-pore diameter created by the polymers. (Bottom) "Dissolved" regime ($\phi_{C7} < 50$ vol %), where d_{C7} is the molecular diameter of n-heptane (Philip M. Singer, Chen, et al. 2018).

In the polymer-heptane mixes, the polymer acts as the "surface" for heptane (see Figure 4.25). The pore diameter d_p of heptane can be calculated by

$$\frac{S}{V_p} = \frac{1}{d_p} = \frac{1 - \phi_{C7}}{\phi_{C7}} \frac{S}{V_g},$$

(4.32)

where ϕ_{C7} is the heptane volume fraction in the polymer-heptane mixes, V_p is the pore volume, i.e., the volume of heptane in the polymer matrix, S/V_p is the surface to pore volume ratio of the polymer "pore", V_g is the grain volume of the polymer and S/V_g is the surface to the grain-volume ratio of the polymer. Molecular simulations indicate that S/V_g is roughly 0.859 Å^{-1} for the branched alkanes. By using Equation (4.32), the values for d_p corresponding to the specific values of ϕ_{C7} used in this study are plotted in Figure 4.26.
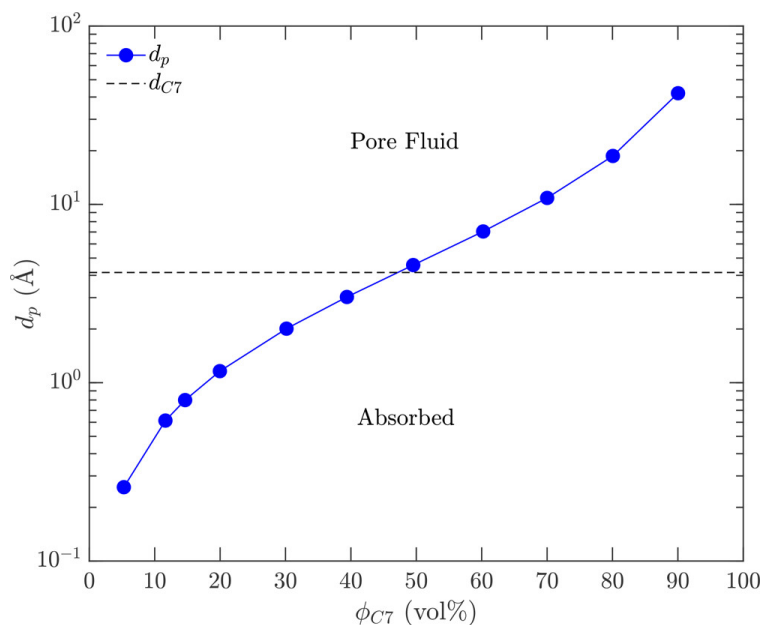
Figure 4.26 Cylindrical-pore diameter d_p for heptane in polymer-heptane mixes versus ϕ_{C7} at specific values in this study using Equation (4.32) (Philip M. Singer, Chen, et al. 2018).
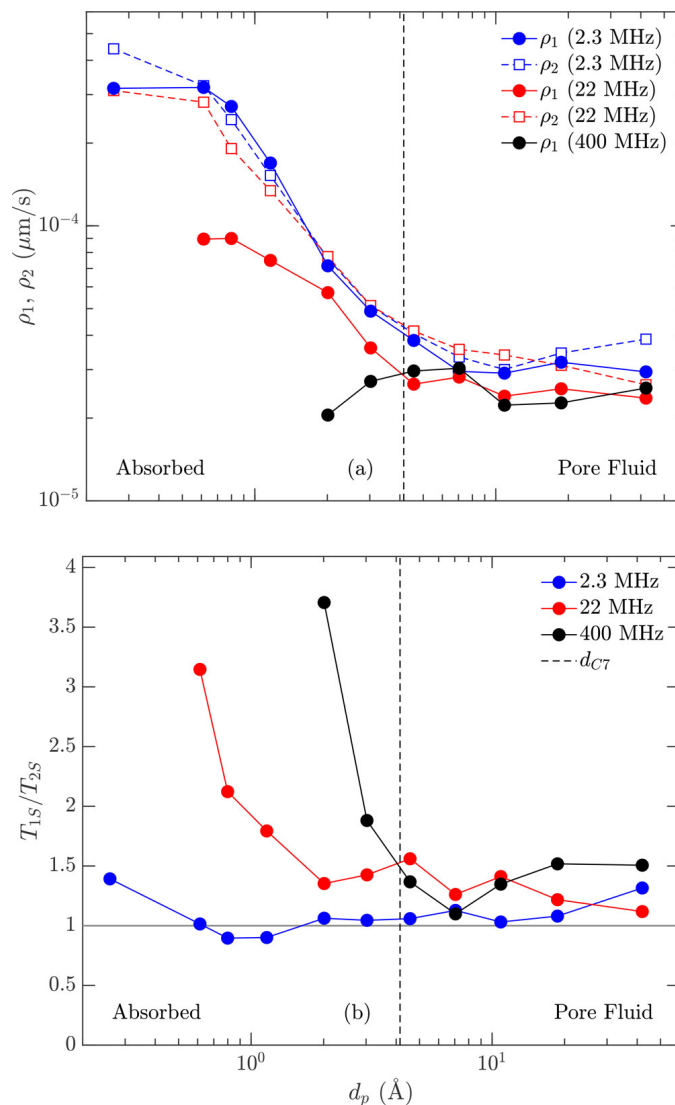
Figure 4.27 (a) Surface relaxivities ρ_1 and ρ_2 for heptane in the polymer against cylindrical pore diameter d_p taken from Figure 4.26. Dashed line separates heptane pore-fluid region ($d_p > d_{C7}$) from dissolved heptane region ($d_p < d_{C7}$). (b) Plot of T_{1S}/T_{2S} ($= \rho_2/\rho_1$) ratio versus d_p.

The surface relaxation components T_{1S} and T_{2S} of heptane in the polymer-heptane mixes are then determined by separating the heptane signal. Equation (4.32) allows for the determination of the surface relaxation ρ_1 and ρ_2 of heptane on the polymer surfaces, and for analyzing them versus pore diameter d_p. The results are shown in Figure 4.27. Two distinct regions are identified: (1) the pore-fluid region where d_p is larger than the heptane molecule d_{C7} (i.e., $d_p > d_{C7}$) and the

surface-relaxivity parameters $\rho_{1,2}$ for heptane are equal and constant versus d_p and frequency; (2) the dissolved region $d_p < d_{C7}$ where $\rho_{1,2}$ increases with decreasing d_p and ρ_1 is dispersive (i.e., frequency-dependent). Analogies can be made between heptane surface relaxation in polymers and heptane surface relaxation in bitumen and kerogen. These findings suggest that the large ratios $T_{1S}/T_{2S} \simeq 4$ and dispersion $T_{1S}(\omega_0)$ previously reported in hydrocarbon-saturated organic shales originate from ^{1}H-^{1}H dipole-dipole interactions enhanced by nanopore confinement.

4.7. Conclusions

The origin and the relaxation mechanism of the high T_1/T_2 ratio signal observed on saturating hydrocarbons in organic shales is investigated by conducting research on the kerogen isolates. Following the kerogen isolation, bitumen extraction by toluene was performed to remove bitumen from the isolated kerogen. The UV-VIS spectrum of the bitumen extract confirms that 0.6 to 0.8 wt% of Athabasca bitumen equivalent was extracted from the isolated kerogen. Soxhlet and static extraction both reduce the swelling of kerogen pellets, although the static extraction is more efficient.

Two distinct pore systems are observed on saturated kerogens (with and without bitumen extraction) by 2D T_1-T_2 correlation maps. The fast-relaxing peak has a high T_1/T_2 ratio above 20, and is interpreted as heptane dissolved within the kerogen granule. The slow-relaxing peak has relatively low T_1/T_2 ratio ~2.5, and is interpreted as heptane in intergranular pores created during pelletization.

In the case of the fast-relaxing peak, the porosity of the dissolved heptane is reduced by 28% and 70% after Soxhlet and static extraction, respectively, while their T_1 and T_2 remain unaltered. The remaining dissolved porosity after extraction indicates that heptane is still dissolved in the kerogen granule, regardless of the absence or presence of bitumen. This finding leads to the following interpretation: both bitumen and kerogen contribute to the intragranular porosity for dissolved heptane, and both cause the same relaxation. The low amount of paramagnetic impurities and clustered pyrite cubes suggests that the high T_1/T_2 ratio most likely arises from [1]H-^{1}H dipole-dipole interactions for the dissolved heptane in organic nanopores.

The T_2 shift of water in kerogen compared to partially deuterated water in kerogen, and the evidence of the movement of magnetization between the solid and liquid sample constituents indicate that both of intra- and inter-molecular [1]H-^{1}H dipole-dipole interactions contribute to ρ_1 and ρ_2. In addition, the model system by polymer-heptane mixture suggests that the high T_1/T_2 ratio of dissolve heptane results from nanopore confinement.

As for the slow-relaxing peak after bitumen extraction, both T_1 and T_2 are increased by the same factor, which leads to the same T_1/T_2 ratio. The nearly unchanged intergranular porosity indicates that bitumen swelling does not lead to additional expansion of the intergranular pore space. Surface relaxivity and pore-size analysis incorporating BET surface area demonstrate that the shift in relaxation time after bitumen extraction is due to a decrease in apparent surface relaxivity, not

the pore-size change. The diffusive-coupling model based on the carbonate system is successfully implemented to explain connections between two pore systems. The decrease in apparent surface relaxivity is attributed to the reduced diffusion length of heptane into the kerogen granule, resulting from the reduced microporosity of the granule. The apparent surface relaxivity analysis also leads to an estimate of 1.3 nm to 27 nm for the diameter for the intragranular pores. The NMR pore-size results are found to be consistent with SEM images. In addition, the T_2-T_2 exchange measurements, as well as controlled evaporation studies, confirm the existence of diffusive coupling of heptane molecules between different environments and therefore validate the application of the diffusive-coupling model.

Chapter 5

Permeability Estimation by Transient-Pressure History-Matching

Note that this chapter is based on and slightly adapted from a published conference proceeding (Z. Chen, Wang, et al. 2019), where some portion is taken word-to-word. Also note that this work is submitted to the *SPE Journal*, and potentially other journals, for consideration as a peer-reviewed article.

5.1. Introduction

Unconventional resources contribute to the majority of the oil and gas production in the U.S., making it now one of the largest producers in the world. However, the low to ultralow permeability associated with the unconventional reservoirs still imposes challenges for oil and gas production as well as the laboratory measurements. Since the permeability is a critical petrophysical

parameter to characterize the producibility of the reservoir, there are a large number of research studies conducted to improve experimental procedures and data interpretations of permeability measurements.

A review article (Sander, Pan, and Connell 2017) summarizes the pros and cons of the popular laboratory-permeability measurement methodologies that are widely accepted by the industry. The permeability-measurement approaches are divided into steady-state and unsteady-state categories. The steady-state method is a direct application of Darcy's law and is easy to implement in terms of the set-ups. However, the inaccuracy in the flow rate measurement limits the accuracy of this method on the low-permeability rocks. In addition, the differential fluid pressure between the upstream and downstream has to be limited to reduce the difference in fluid properties and the effective stress across the core. The long run time is also a bottleneck of the steady-state method. As a result, various unsteady-state methods have been invented to resolve the problems encountered by the steady-state method. The unsteady-state methods typically include the pulse-decay method, the Gas Research Institute (GRI) method, and the oscillating pressure method. The unsteady-state methods aim at improving the accuracy and shortening the run time compared to the steady-state method. However, these unsteady-state methods are much more involved in terms of the experimental setup (Bernabé, Mok, and Evans 2006; Brooks et al. 2009; Profice, Hamon, and Nicot 2016) and data interpretation (Brace, Walsh, and Frangos 1968; Kranz, Saltzman, and Blacic 1990; Cui, Bustin, and Bustin 2009; Sander, Pan, and Connell 2017). More specifically, a comprehensive understanding of the permeability measurements and prior knowledge about the

rock are required to select the best measurement approach, tune the experimental setup, and choose the proper range of data and formulation for parameter estimation (Jones 2007; Cui, Bustin, and Bustin 2009; Sander, Pan, and Connell 2017). Meanwhile, the small-differential-pressure limitation is still applied.

To resolve the issues encountered by the traditional unsteady-state approaches, an innovative unsteady-state method, named "transient-pressure method", is proposed in this study. The objective of this method is to (1) simplify the experimental set-up and procedures; (2) shorten the experimental run time; (3) reduce the complexity of the data interpretation; (4) alleviate the narrow-pressure-range constraint. This method involves both experiments and numerical simulations.

The experiment for the transient-pressure method consists of 1D core-flooding on a cylindrical core with a low-viscosity fluid (e.g., carbon dioxide). The fluid flooding can be either injection or production, which yields transient-pressure curve for history matching. Compared to the steady-state and unsteady-state methods, the transient-pressure measurement can be implemented with a simpler apparatus, thereby providing the opportunity for integration with other in-situ core analysis measurements, such as nuclear magnetic resonance (NMR) core analysis.

In conjunction with the experiment, we also simulate the transient-pressure experiments numerically in order to generate a transient-pressure history. In the case of traditional unsteady-state methods, the non-linear pressure dependence of the fluid properties is approximated by linear relationships. This approximation is

valid only when the differential pressure is small. This constraint is alleviated by our simulation, which incorporates the concept of real-gas pseudo pressure (Al-Hussainy, Ramey H. J., and Crawford 1965), and a lookup table for the fluid properties. Our simulation can deal with the nonlinear pressure dependence of the fluid properties, including the singularity during the phase transition. This capability ensures that the simulation can reproduce the entire transient-pressure history to match the experimental data over any pressure range.

This chapter is organized as follows. The experimental apparatus and procedures for the newly proposed unsteady-state method (i.e., transient-pressure method) and the standard steady-state method are presented in the "Experiments" sub-chapter. This sub-chapter is followed by the "Fluid Properties" sub-chapter that provides fluid properties inferred from the database and introduces the real-gas pseudo pressure. The next "Transient-Pressure Method" sub-chapter presents how the transient-pressure method is implemented to estimate the permeability, including the details on the rock porosity and pore-volume compressibility calculation, numerical simulation, and history matching between the experimental and simulated data. The following sub-chapter validates the transient-pressure method with the standard steady-state measurement.

5.2. Experiments

This sub-chapter presents the experimental details, including the experimental apparatus and procedures. There are two types of permeability-

measurement approaches implemented in this study. The first approach is the
transient-pressure method. The second approach is the standard steady-state
method, which is used to validate the transient-pressure method. Note that both
methods consist of 1D core flooding.

In this study, carbon dioxide (i.e., CO_2) is selected as the permeating fluid.
The investigated shale-rock sample is cored from the Eagle Ford outcrop. The
cylindrical core is 1.5 inches in diameter and 3 inches in length. During the core-
flooding experiment, the core plug is wrapped within the Teflon heat-shrink tubing,
aluminum foil, another layer of Teflon heat-shrink tubing, and rubber sleeve, then
placed in the core holder. Note that the core holder is not designed for applying tri-
axial confining stress such that only a radial confining stress (i.e., no axial stress) is
applied by the syringe pump. The end pieces of the core holder are tightened until
contacting the core plug.

5.2.1. Transient-Pressure Measurement

The proposed transient-pressure measurement consists of 1D constant-inlet-
pressure CO_2-injecting experiments with the outflow end closed. Figure 5.1 shows
the diagram of the apparatus. The upstream pump is used to regulate the CO_2
pressure during the injection, which provides constant pressure. It should be noted
that the upstream pump can also be the downstream pump if a production
measurement is performed instead (see Appendix I of this chapter).
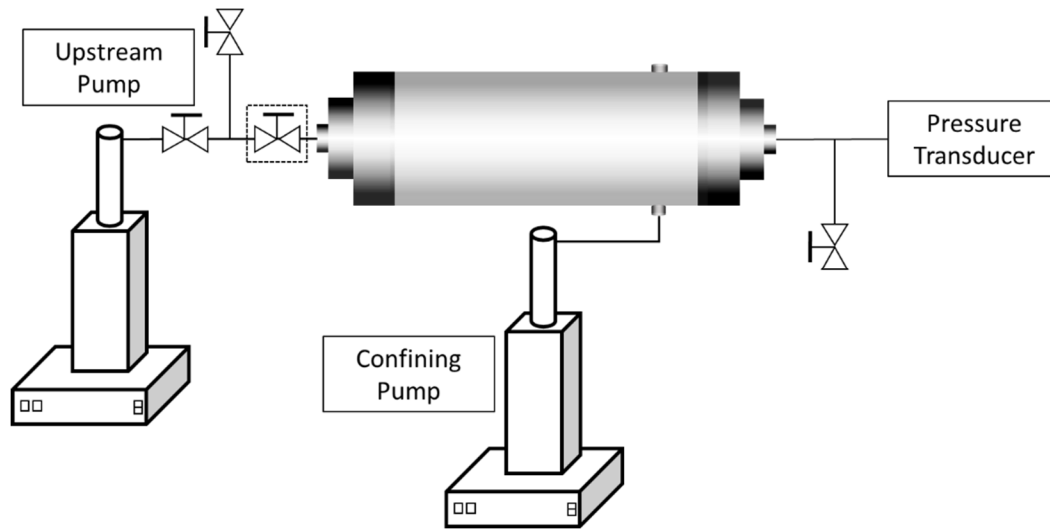
Figure 5.1 Schematic of the apparatus for the 1D transient-pressure experiment of the transient-pressure method. The valve denoted by the dashed rectangle box is the trigger of the transient-pressure experiments. The rest of the valves are bypass valves for safety purpose.

The transient-pressure experiment is implemented in two stages. Before each stage, the upstream pump pre-pressurizes the CO_2 to the target pressure up until the closest valve connected to the core holder (i.e., the trigger valve). Opening the valve triggers the transient-pressure experiment. The time of valve opening is recorded as the starting time t_0. Meanwhile, the outflow end (i.e., dead-end) of the core is connected to a pressure transducer and a valve that is closed during the experiment. The transient pressure at the dead-end versus the experimental run time (i.e., $p(t)$) is recorded by the transducer. In addition, the CO_2 volume change in the upstream pump before and after the transient-pressure experiment is also recorded for computing the rock porosity and pore-volume compressibility, the details of which are presented in the following.

The proposed transient-pressure experiment has two stages, a prefilling stage, and a testing stage. The prefilling stage is to (1) raise the pore pressure to

near reservoir conditions, and (2) provide additional mass balance information for computing the rock porosity and pore-volume compressibility. Conducting experiments at higher pressure reduces the interference from the adsorption effect and Klinkenberg effect (a.k.a. slippage effect) (Klinkenberg 1941). The testing stage produces the transient-pressure curve for history-matching with the simulation.

Table 5.1. Details of the two-stage transient-pressure CO_2-injecting experiments, including the initial and final pore pressures, the constant confining pressure and the temperature.

Stage	Initial pore pressure (psia)	Final pore pressure (psia)	Confining pressure (psia)	Temperature (°F)
Prefilling (1st stage)	15	1,181	2,015	73
Testing (2nd stage)	1,176	1,796	2,615	73

The details of the two stages are summarized in Table 5.1. The prefilling stage is conducted by injecting CO_2 to the core with an ambient pore pressure. The injecting pressure is fixed at around 1,200 psia, and the confining pressure is kept constant at roughly 2,000 psia. Note that the core is not exposed to vacuum due to the low permeability. The residual air within the rock is treated as CO_2 gas in the simulation. This approximation is valid due to the high pore pressure at the end of the prefilling stage, where the air is significantly compressed (by ~ 100 times based on the densities of the air at ambient pressure and 1,200 psia inferred from the NIST REFPROP database) such that the CO_2 is the dominant species in the pore space. Thus, the effect of the residual air on the CO_2 fluid properties during the testing stage (i.e., the second stage) is insignificant. After the prefilling stage, the confining pressure is increased to around 2,600 psia and kept constant during the testing stage. The testing stage pressurizes the pore pressure to near 1,800 psia. It should

be noted that both stages are at room temperature (i.e., 73°F), and the experiments are assumed to be isothermal, given the rock matrix and the confining fluid (i.e., water) as the heat buffer.

The dead volumes at both ends in the apparatus are measured independently. The upstream dead volume is 1.20 mL, which comes from the end piece of the core holder and the tubing to the trigger valve. The downstream dead volume is 2.60 mL, which includes the volume from the end piece, tubing, valve, and transducer. These dead volumes are considered in the calculation of the rock porosity and pore-volume compressibility, as well as in the simulation.

Note that the apparatus for the transient-pressure experiment is less complicated than that of the standard steady-state method and other unsteady-state methods (Sander, Pan, and Connell 2017). The simplified apparatus provides the opportunity for the transient-pressure method to be integrated with other core measurements. For example, the NMR core analysis may require in-situ saturation of light hydrocarbons, such as methane, ethane, and propane, at reservoir conditions (Z. Chen, Singer, et al. 2019), which is similar to the CO_2 injection. In this case, the integrated core analysis can provide permeability estimation, in addition to the NMR properties of the saturating fluids. It should be noted that the integration with NMR core analysis requires the apparatus to be changed accordingly, such as replacing the material of the core holder from metal to PEEK that is NMR silent. Also, note that the NMR measurement can be solely used to estimate the permeability (Valori et al. 2017).

5.2.2. Steady-State Measurement

Figure 5.2 shows the apparatus of the standard steady-state approach (Sander, Pan, and Connell 2017). The difference between the steady-state apparatus and the transient-pressure apparatus (shown in Figure 5.1) is (1) the outflow end of the core is connected to a downstream pump serving as a back-pressure regulator, and (2) the absolute-pressure transducer is replaced by a differential pressure sensor to monitor the pressure drop across the entire core plug.
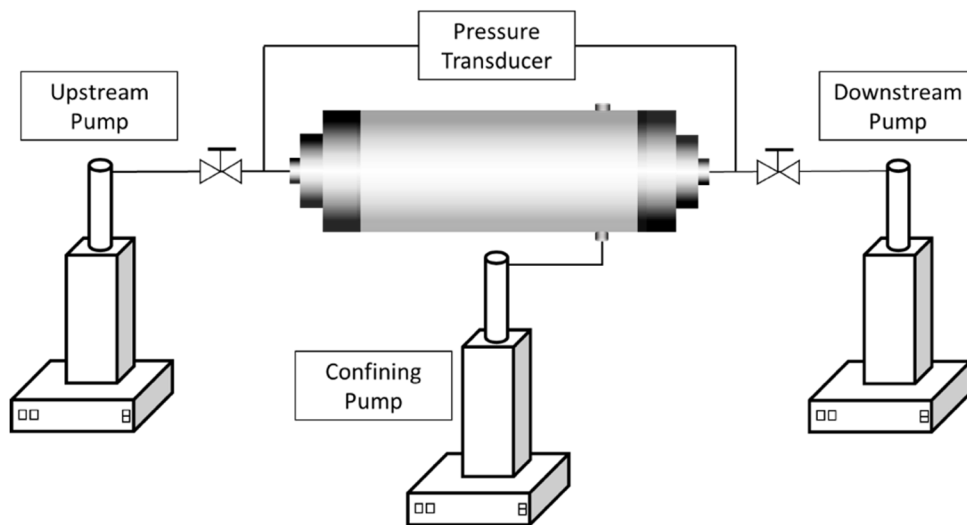
Figure 5.2. Schematic of the apparatus for the standard 1D steady-state permeability measurement.

The five-point steady-state experiment is conducted by injecting liquid-state CO_2 at constant flow rates at 0.005, 0.010, 0.015, 0.020 and 0.025 mL/min respectively. The temperature of the steady-state experiment is 73°F, which is the same as the transient-pressure experiment. The backpressure applied by the downstream pump is set at 1,727 psia during all five stages. The pressure drops across the core are recorded. The result of the steady-state permeability

measurement is presented in the following section to validate the transient-state method.

5.3. Fluid Properties

In the permeability measurements for unconventional rocks, low-viscosity fluids are preferred, such as hydrogen gas, nitrogen, and CO_2. However, the assumption of constant fluid properties, or linear pressure dependence, may not be valid, especially when the differential pressure between the upstream and downstream is substantial. The relationship between the fluid properties and pressure becomes even more complicated when the phase transition occurs. Therefore, a new approach is implemented here to obtain fluid properties by integrating table lookup and linear interpolation.

The lookup table is prepared by collecting the data of fluid properties from the REFPROP V9.1 database developed by the National Institute of Standards and Technology (NIST). The fluid properties obtained from REFPROP include the density, viscosity, compressibility factor, and isothermal compressibility.

The compressibility factor is also known as the "z" factor, or gas-law deviation factor, which is defined in the equation of state (EOS) as such:

$$\rho(p,T) = \frac{M}{RT}\left(\frac{p}{z(p,T)}\right), \tag{5.1}$$

where ρ is fluid density, M is the molar mass of fluids, R is the gas constant, T is the temperature and z is gas-law deviation factor.

The isothermal compressibility c defines the compressibility of fluids at a constant temperature as such:

$$c(p,T) = \frac{1}{\rho}\left(\frac{d\rho}{dp}\right)_T = \frac{z(p,T)}{p}\frac{d}{dp}\left(\frac{p}{z(p,T)}\right)_T.$$

(5.2)
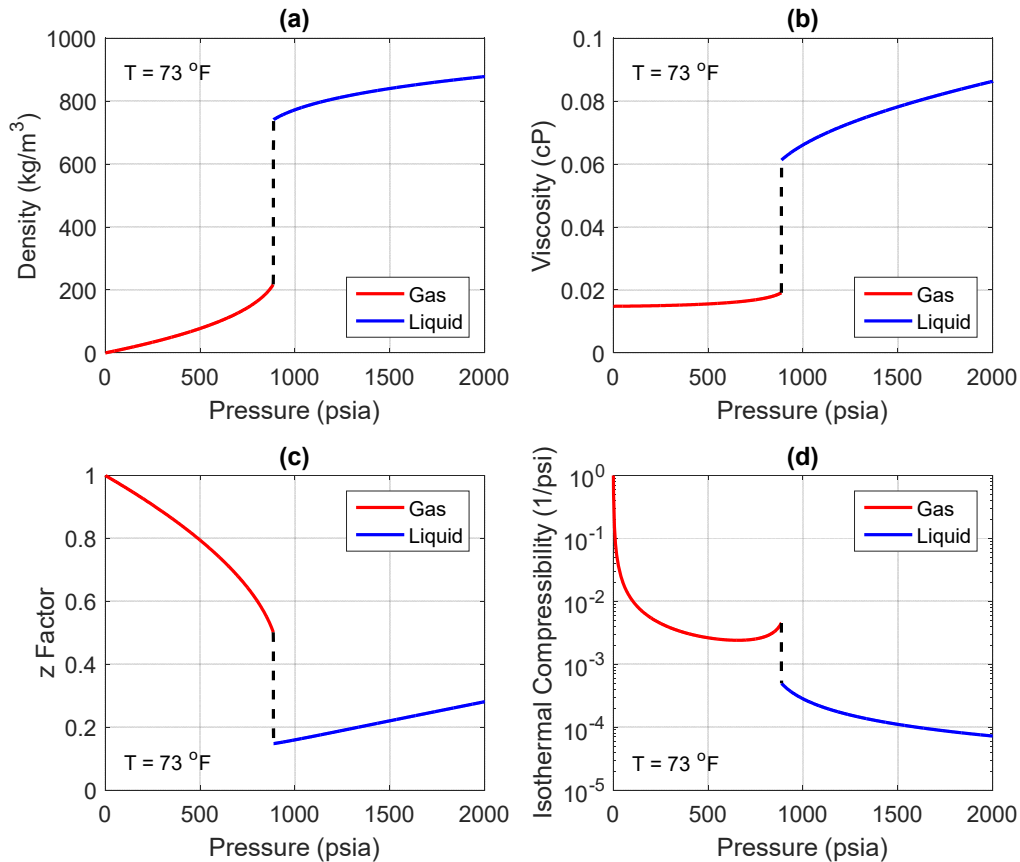
Figure 5.3. CO_2 bulk-fluid properties vs. fluid pressure at the room temperature of 73 °F, including (a) density, (b) viscosity, (c) gas-law deviation factor, and (d) isothermal compressibility. The properties of the gas-state and liquid-state CO_2 are denoted in red and blue, respectively. Dashed lines indicate the data near the phase-transition point. Note that the fluid properties are inferred from the NIST REFPROP database. Also note that the discretization of the fluid pressure is 1 psi.

The fluid properties mentioned above generally depend on both pressure and temperature. However, in the interpretation and simulation of the experiments, fluid transport is assumed to be isothermal. Therefore, no temperature effect is

considered. The temperature of CO_2 varies during the experiments, however, the temperature effect is alleviated by heat transfer to the rock matrix and the confining fluid (i.e., water), which are the heat buffer. Besides, considering the long experimental run-time scale (as a result of the low permeability), the heat can be readily dissipated (the analysis is available on request). Therefore, the isothermal assumption is made such that the fluid properties are functions of pressure only.

Figure 5.3 shows the fluid properties of CO_2 acquired at the room temperature of 73°F. The independent variable, fluid pressure, is tabulated from 1 psia to 2000 psia with a discretization of 1 psi. The fluid properties at fluid pressures between the tabulated pressures are calculated using linear interpolation. The fluid properties for the gas-state and liquid-state CO_2 are denoted in red and blue, respectively. It is clear that the CO_2 experiences a gas-liquid phase transition. The vapor pressure of CO_2 is 886.6 psia at 73°F. It should be noted that the discretized lookup table uses the assumption that a finite-slope straight line can approximate the singularity in the fluid properties at the phase transition. More specifically, the densities of liquid-state CO_2 at 887 psia and gas-state CO_2 at 886 psia are obtained from the lookup table. Based on this assumption, the density of CO_2 near the vapor pressure in between 886 to 887 psia can be computed using a linear interpolation between two endpoints. The outcome of this numerical approximation is to introduce an artificial phase without a singularity to connect the liquid phase and gas phase. This approximation is valid in the framework of this study based on the experiment-simulation comparison shown in the appendix for the one-stage approach.

Based on the viscosity and z factor, the real-gas pseudo pressure is introduced as follows (Al-Hussainy, Ramey H. J., and Crawford 1965):

$$m = 2 \int_{p_0}^{p} \frac{p'}{\mu(p')z(p')} dp', \tag{5.3}$$

where the real-gas pseudo pressure m is an integral of the fluid pressure, viscosity, and z factor. The real-gas pseudo pressure for CO_2 at 73°F is calculated and plotted in Figure 5.4. Note that the lower bound of the integration is 1 psia, and the discretization of fluid properties is 1 psi. In Figure 5.4, it is readily found that the singularity during the phase transition is smoothed.
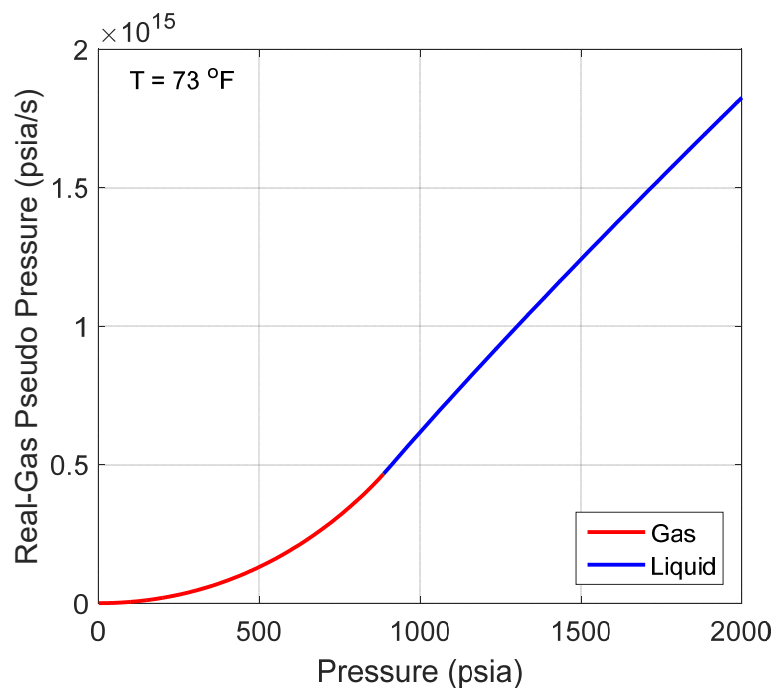
Figure 5.4. The real-gas pseudo pressure of CO_2 vs. fluid pressure computed at 73 °F. The portions for the gas-state and liquid-state CO_2 are denoted in red and blue respectively. Note that the lower bound of the integration in Equation (5.3) is 1 psia, and the discretization of the fluid properties is 1 psi.

By taking the derivative of m with respect to p, Equation (5.3) yields:

$$\frac{dm}{dp} = \frac{2p}{\mu(p)z(p)}.$$

<div align="right">(5.4)</div>

This equation is used later to simplify the mass-flow equations.

5.4. Transient-Pressure Method

5.4.1. Fundamental Equations

Sander et al. (Sander, Pan, and Connell 2017) indicate that researchers raise concerns about the validity of Darcy's law, as well as the Klinkenberg correction, on the fluid transport in low-permeability rocks, since Knudsen numbers are in the transitional flow regimes, in some cases (Javadpour 2009; Civan 2010; Fathi, Tinni, and Akkutlu 2012). As a result, quite a few modifications, such as coupling Knudsen diffusion with Darcy's law, are proposed to better interpret the measurements (Javadpour 2009; Civan 2010; Darabi et al. 2012). However, there are many studies confirm that Darcy's law and the Klinkenberg correction are valid (Rushing et al. 2004; Bertoncello and Honarpour 2013; Sinha et al. 2017; Profice, Hamon, and Nicot 2016). Therefore, Darcy's law is still widely applied in traditional steady-state and unsteady-state methods. The transient-pressure method also relies on the validity of Darcy's law.

The governing equation to describe the single-component fluid flow in porous media is the material conservation equation:

$$\frac{\partial C}{\partial t} = -\nabla \cdot (\rho \vec{u}) + q, \tag{5.5}$$

where C is the mass concentration of fluids in the porous medium, ρ is the fluid

density, $\vec{u}$ is the flux vector and q is the source term. The source term represents the

addition or reduction of fluids into the volume over a time interval due to the

sources or sinks. In this research, the core flooding is performed with a fixed

injecting pressure, such that the Dirichlet boundary condition (a.k.a. first-type

boundary condition that specifies the value of the function on a boundary) is

adopted for the inflow end. As for the downstream of the core plug, which is closed,

the no-flow boundary condition is adopted. In this case, the source term is zero

since neither source nor sink is present.

The flux vector on the right-hand side of Equation (5.5) can be expressed

using Darcy's equation:

$$\vec{u} = -\frac{k}{\mu} \nabla p, \tag{5.6}$$

where p is the pore pressure (i.e., fluid pressure), k is the permeability of the porous

medium, and μ is the viscosity of the fluid. Note that in the case of low-pressure gas

flow, the permeability is subject to Klinkenberg effect, which indicates the apparent

permeability is pressure-dependent, as such (Klinkenberg 1941):

$$k_a = k_\infty \left(1 + \frac{b}{p_m} \right), \tag{5.7}$$

where k_a is the apparent permeability, k_∞ is the Klinkenberg-corrected

permeability, b is the Klinkenberg coefficient, and p_m is the mean pore pressure.

However, in terms of the transient fluid flow, especially with high pore pressure, the

Klingenberg effect is negligible (Aronofsky 1954). An empirical correlation

established on Eagle Ford samples suggests that the Klinkenberg coefficient b for a

rock with a permeability around 1 μD is about 0.5 MPa (i.e., 73 psia) (Letham and

Bustin 2016). This estimation suggests that the Klinkenberg effect is not significant

given the high pore pressure. Hence, the permeability in Equation (5.6) refers to the

Klinkenberg-corrected permeability k_∞ in the following sections.

In addition, the permeability may vary with the net stress for specific types of

rocks (Ostermeier 1995). In this study, the permeability is assumed to be

independent of the net stress within the test pressure range.

For the right-hand side of Equation (5.5), substituting the 1D form of

Equation (5.6) yields:

$$-\nabla \cdot (\rho \vec{u}) = \frac{\partial}{\partial x}\left(\rho \frac{k}{\mu}\frac{\partial p}{\partial x}\right). \tag{5.8}$$

By substituting Equations (5.1) and (5.4) to Equation (5.8), the pore-pressure

dependent variables ρ and μ are combined into the real-gas pseudo pressure as

such:

$$\frac{\partial}{\partial x}\left(\rho\frac{k}{\mu}\frac{\partial p}{\partial x}\right) = \frac{\partial}{\partial x}\left(\frac{Mk}{RT}\frac{p}{\mu(p)z(p)}\frac{\partial p}{\partial x}\right) = \frac{M}{2RT}\frac{\partial}{\partial x}\left(k\frac{\partial m}{\partial x}\right) = \frac{Mk}{2RT}\frac{\partial^2 m}{\partial x^2}. \tag{5.9}$$

For the left-hand side of Equation (5.5), the mass concentration C is the product of the rock porosity ϕ and the fluid density ρ. The rock porosity is defined as:

$$\phi = \frac{V_p}{V_b},$$

(5.10)

where V_p is the rock pore volume and V_b is the rock bulk volume. The pore volume V_p typically varies with the net stress p_{net} defined as the difference between the confining pressure and the pore pressure (i.e., $p_{net} = p_{conf} - p$). In the experiments, the confining pressure is greater than the pore pressure such that the net stress is positive. The dependence of pore volume on the net stress can be characterized by the pore-volume compressibility c_p as such:

$$c_p = -\frac{1}{V_p}\frac{dV_p}{dp_{net}}.$$

(5.11)

The pore-volume compressibility may vary with net stress. However, in transient-pressure experiments, the maximum net stress is limited to 2,600 psi, which may not be high enough to affect the pore-volume compressibility considerably (Ostermeier 1995). As such, the pore-volume compressibility is assumed to be constant. Under this assumption, Equation (5.11) can be integrated as such:

$$V_p = V_{p0} \exp(-c_p p_{net}) = V_{p0} \exp\left(c_p(p - p_{conf})\right),$$

(5.12)

where V_{p0} is the pore volume measured at zero net-stress. Another assumption can be made that the product of pore-volume compressibility and the net stress is much less than unity, which is valid given that the pore-volume compressibility is usually small for shales, plus the net stress is limited. By conducting the Taylor expansion to first order, Equation (5.12) can be approximated by:

$$V_p = V_{p0}\left(1 + c_p(p - p_{conf})\right). \tag{5.13}$$

The pore-volume compressibility computed in the following section validates this linear approximation. It should be noted that our simulation uses the finite-volume method, where the grid size is kept constant such that the porosity used in the simulation follows the same functional form as Equation (5.13):

$$\phi = \phi_0\left(1 + c_p(p - p_{conf})\right), \tag{5.14}$$

where ϕ_0 is the porosity measured at zero net-stress.

By substituting Equations (5.2) and (5.11), and given that the confining pressure is kept constant during experiments, the left-hand side of Equation (5.5) becomes:

$$\frac{\partial C}{\partial t} = \frac{\partial(\phi\rho)}{\partial t} = \phi\rho(c_p + c)\frac{\partial p}{\partial t} = \phi\rho c_t \frac{\partial p}{\partial t}, \tag{5.15}$$

where the summation of c_p and c is defined as the total compressibility c_t. Equation (5.15) can be further simplified by substituting Equations (5.1) and (5.4) as:

$$\frac{\partial C}{\partial t} = \phi \mu c_t \frac{M}{RT} \left(\frac{p}{\mu z} \right) \frac{\partial p}{\partial t} = \phi \mu c_t \frac{M}{2RT} \frac{\partial m}{\partial t}. \tag{5.16}$$

The last step is combining Equations (5.9) and (5.16), which yields:

$$\frac{\partial m}{\partial t} = \frac{k}{\phi \mu c_t} \frac{\partial^2 m}{\partial x^2} = \eta \frac{\partial^2 m}{\partial x^2}, \tag{5.17}$$

where η is defined as the hydraulic diffusivity which is composed of the permeability, porosity, fluid viscosity, and total compressibility. The hydraulic diffusivity depends on the pore pressure under the isothermal assumption.

In Equation (5.17), the rock properties that determine the transient fluid-transport process include the permeability, porosity, and pore-volume compressibility (which is part of the total compressibility). The porosity and pore-volume compressibility are directly calculated, as shown in the next section. Hence, the permeability is the only unknown parameter and is inversely proportional to the experimental run time, such that the permeability can be estimated by history matching the experimental data with simulation results.

Note that the numerical simulation is based on Equation (5.17) with the real-gas pseudo pressure as the dependent variable. However, in the following plots, the real-gas pseudo pressure is converted to the absolute pressure using the one-to-one mapping as shown in Figure 5.4.

5.4.2. Rock Porosity and Compressibility

In the steady-state measurement, the rock porosity and pore-volume compressibility do not contribute to Darcy's equation. Instead, the rock porosity and pore-volume compressibility play essential roles in the transient-pressure measurements as suggested by Equation (5.17). These two rock properties along with the permeability directly determine the experimental run-time. As such, the porosity and pore-volume compressibility are determined before the permeability estimation.

The rock porosity and pore-volume compressibility are computed based on independent mass-balance equations. As mentioned in the Experiments section, the CO_2 injection experiments are performed in two stages (see Table 5.1). The injected volume of CO_2 recorded by the upstream pump at equilibrated states for each stage yields a mass-balance equation. The first stage is to pressurize the core with CO_2 from the ambient pressure to 1,181 psia with a constant confining pressure of 2,015 psia. The recorded volume change indicates that there is 14.33 mL of CO_2 injected at 1,181 psia. The second stage pressurizes the core from 1,176 psia to 1,796 psia, with the confining pressure fixed at 2,615 psia. At this stage, there is 1.04 mL of CO_2 injected at 1,796 psia. Based on the mass balance, the above two experiments can be materialized as:

$$\rho(1,181) \times 14.33$$

$$= \rho(1,181)\left(V_{dead} + V_0\left(1 + c_p(1,181 - 2,015)\right)\right) \quad (5.18)$$

$$- \rho(15)\left(V_{dead} + V_0\left(1 + c_p(15 - 2,015)\right)\right),$$

$$\rho(1,796) \times 1.04$$

$$= \rho(1,796)\left(V_{dead} + V_0\left(1 + c_p(1,796 - 2,615)\right)\right) \quad (5.19)$$

$$- \rho(1,176)\left(V_{dead} + V_0\left(1 + c_p(1,176 - 2,615)\right)\right).$$

In the above two equations, the density is from the lookup table. The total dead volume V_{dead} is 3.80 mL as mentioned in the Experiments sub-chapter. V_0 and c_p are the two unknown variables in this set of equations. By solving the above two equations, $V_0 = 10.63$ mL and $c_p = 7.9 \times 10^{-6}$/psi are determined. Providing the dimensions of the core, the bulk volume measured at zero net stress is 86.79 mL. Hence, the porosity at zero net-stress (i.e., ϕ_0) is 12.2 p.u. (a.k.a. porosity unit). Given the fact that the maximum net-stress is capped at 2,600 psi, the maximum change in pore volume and porosity due to the net stress is around 2.1% of the measured value of porosity, thereby validating the linear approximation in Equation (5.13).

Note that 1,800 psia is the highest fluid pressure in the experiment, thereby the lowest possible value of the isothermal compressibility for CO_2 at 73°F is 8.4×10^{-5}/psi (see Figure 5.3). Therefore, the contribution of the rock compressibility to the total compressibility is less than 10% given the lower bound

of the isothermal compressibility. This analysis indicates that the contribution from

the pore-volume compressibility to the total compressibility can be negligible if the

isothermal compressibility of the permeating fluids is an order of magnitude higher.

In such cases, the pore-volume compressibility measurement is not mandatory,

which means recording the volume change at only one stage is sufficient for the

porosity calculation.

5.4.3. Finite-Volume Simulation

The 1D simulation of the transient-pressure experiments is conducted using

the finite-volume method. Figure 5.5 presents the simulated system. The dead

volume (i.e., 2.60 mL) at the outflow end (i.e., the closed-end) is considered and

treated as an artificial "core" with a high permeability of 1,000 Darcy and a porosity

of unity. The cross-section area of the artificial "core" is the same as the investigated

core plug. The dead space at the inflow end of the core plug is ignored since the

small dead space (i.e., 1.20 mL) is equilibrated with the syringe pump within a short

time compared to the experimental run time.
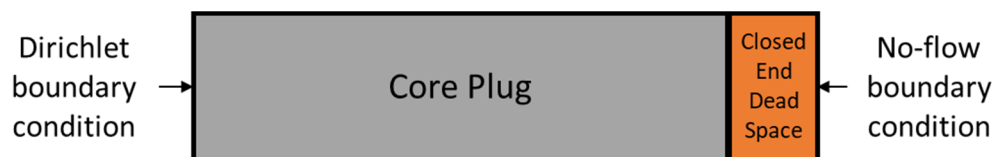
Figure 5.5. Schematic of the finite-volume simulation. Note that the outflow-end dead space is considered as an artificial "core" in the simulation.

In the simulation, the core plug is divided into 50 equal-volume (i.e., equal-

length as a result of the same cross-section area) grids. Also, one more grid is

assigned for the dead space. The length of the last grid for the dead space is

calculated by dividing the dead volume by the cross-section area of the core plug. As

mentioned in the previous sub-section, the inflow and the outflow end are subject to

Dirichlet and no-flow boundary conditions respectively.

The simulation is implemented from scratch using the implicit method,

which is also known as the backward-difference method. The implicit method

evaluates the spatial difference on the new time level (a.k.a. next time step in the

temporal discretization) using the unknown variable. The unknown variable on the

new time level is computed by matrix inversion of the linearized equations and

iterating on the pressure-dependent hydraulic diffusivity.
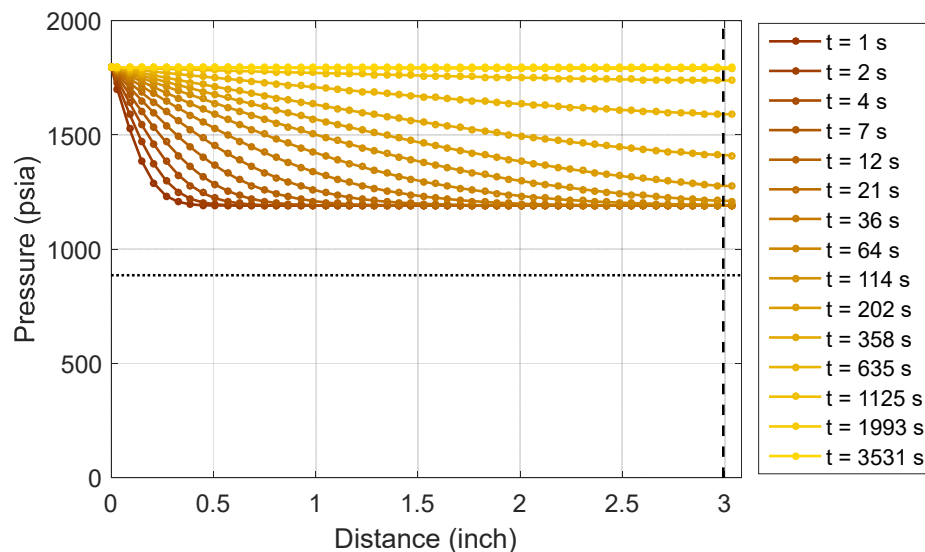
Figure 5.6. Simulated pressure-profile snapshots at different run times during the second-stage CO_2-injection experiment. The simulation uses a permeability of 1.32 µD. The colors distinguish the profile at different run times. The legend indicates the run time when the pressure profile is snapshotted. The horizontal dashed line indicates the vapor pressure of CO_2 at the experimental temperature of 73 °F. The vertical dashed line at 3 inches denotes the core boundary. Note that the last grid is for the closed-end dead volume.

Figure 5.6 illustrates the simulated pressure-profile snapshots for the

second-stage (i.e., testing stage) CO_2-injection experiments until the pore pressure

equilibrates. The plot shows how pore pressure evolves with respect to the run time. In Figure 5.6, the horizontal dashed line indicates the vapor pressure. The CO_2 at the second stage is in the liquid phase. The vertical dashed in Figure 5.6 represents the edge of the core plug. The grid beyond the edge represents the artificial "core" for the closed-end dead space, where the transducer monitors the pressure. The pressure versus the run time is plotted for history matching in the next section.

5.4.4. History Matching

The transient-pressure history at the second stage of the experiment is plotted as black dots in Figure 5.7. The second stage takes about one hour. The simulated pressure histories (i.e., the pressure history of the last grid in Figure 5.6) are also plotted in Figure 5.7 as the candidates for history matching.

The permeability is inversely proportional to the experimental run time as suggested by Equation (5.17). Therefore, the simulated data are scaled by changing the candidate permeability. The goal of the history matching is to find the best simulated-curve that fits the late-time experimental data (i.e., near the plateau where run time ≥ 0.15 hour) since the early-time data (i.e., initial data where run time < 0.15 hour) is subject to some effects (discussed below).

Instead of using algorithms to minimize the mean square error (MSE) as implemented in Chapter 2, the history matching is conducted by a bracketing approach. The bracketing approach means finding the best match between the

simulated and experimental data in the late-time stage, in which case the

experimental data are bracketed by two simulated curves with permeability value

15% away (i.e., $\pm 15\%$) from the optimal value.

The optimal history matching is shown in red in Figure 5.7. The optimal

matching yields a permeability estimate of about 1.20 μD. The clear deviation of the

two candidate curves from the experimental data at the late-time stage indicates

that the transient-pressure approach can determine the permeability within 15%

uncertainty.
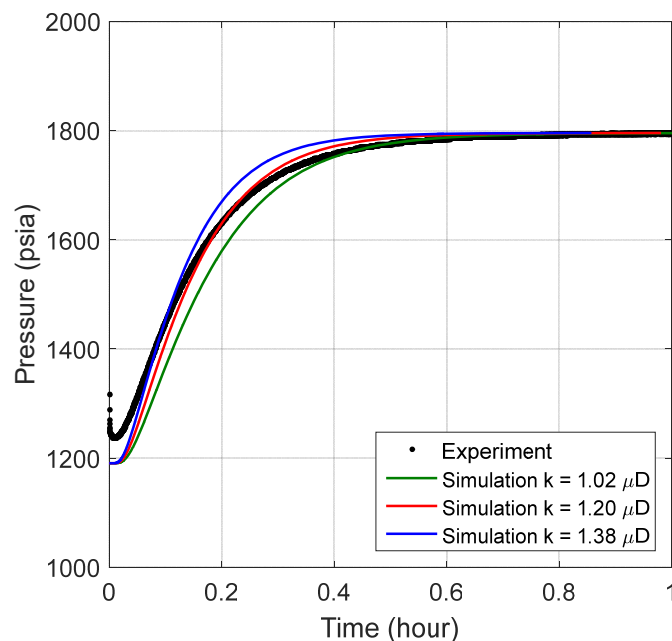
Figure 5.7. Pressure histories of the second-stage CO_2 injection from both simulation and experiment. The legend indicates the source of the pressure histories. The optimal matching is plotted in red, and the other two candidates are plotted in blue and green respectively. Note that the pressure range of the y-axis is from 1,000 to 2,000 psia.

It is readily observed that the simulation matches the experimental curve

well at the late-time stage (i.e., run time ≥ 0.15 hour), which validates the

application of Darcy's law. It is also observed that deviations appear in the early-time data in Figure 5.7.

Figure 5.7 shows a sudden pressure jump right when the experiment starts. The pressure jump is interpreted as being due to the movement of the core plug within the core holder by the initial differential pressure (around 600 psi) between upstream and downstream. Note that the core plug is confined only by the radial stress (i.e., no axial stress applied). Therefore, the dead space between the core plug and the two end pieces of the core holder initially varies. When the CO_2 injection begins, the core plug is pushed to the downstream direction by the high upstream pressure, such that the dead space between the downstream end piece and the core plug decreases. In this case, the sudden drop in the downstream dead volume increases the pore pressure, provided that the liquid-state CO_2 has relatively small compressibility. The position of the core plug is then relaxed back by the rubber sleeve surrounding the core plug, which results in the decrease in fluid pressure.

Other potential effects can lead to the deviation at the early-time stage. The effect might come from the non-Darcy flow at the early-time stage. The non-Darcy flow happens within a short time after the experiment begins. This is due to the initial large pressure-gradient which leads to a significant flow rate and thereby a large Reynolds number. Under this circumstance, Darcy's law may not be valid. The effect of non-Darcy flow is then mitigated when the flow rate decreases, namely at the late-time stage.

In addition to the above effects, temperature effects may contribute to the deviation. The temperature increase or decrease by the compression or expansion of CO_2 at the early-time stage can be significant due to high flow-rates. The temperature variation leads to changes in fluid properties, which affects fluid transport. However, at the late-time stage when the flow rate decreases, the rate of temperature variation is reduced, such that the heat conduction within the core matrix and confining fluid alleviates the temperature change. In this case, the isothermal assumption is valid. The analysis of the temperature variation is can be found in Appendix III of this chapter.

One of the main differences between our transient-pressure method and the traditional unsteady-state methods is that the former uses simulations instead of analytical solutions for data interpretation. In general, the derivation and implementation of the analytical solution are complicated and involves certain assumptions and constraints, such as constant fluid properties within the test pressure range. For the transient-pressure method, the data interpretation is more straightforward. The table lookup method to obtain fluid properties eliminates the constraint on the pressure range. It is also shown in Appendix I of this chapter that the history matching can be achieved in one-stage with a broader pressure range of around 1,800 psi, and with a phase transition.

5.5. Validation with Steady-State Measurement

This section presents the result of the standard five-point steady-state measurement. The steady-state measurement is a direct implementation of Darcy's law, of which the 1D form can be expressed as:

$$\frac{q}{A} = -\frac{k}{\mu}\frac{dp}{dx}, \tag{5.20}$$

where q is the volumetric flow rate, and A is the cross-section area of the core plug. The recorded pressures during the steady-state experiments are summarized in Table 5.2. Note that the backpressure during the experiment is kept at 1,727 psia. The inlet pressure can be calculated based on the pressure drop measured by the differential transducer.

In the steady-state measurement, the volumetric flow is not constant because of the compressibility of CO_2. On the contrary, the mass flow is invariant across the entire core plug. Therefore, the Equation (5.20) is modified by multiplying density on both sides and substituting Equation (5.1) as:

$$\rho\frac{q}{A} = -\rho\frac{k}{\mu}\frac{dp}{dx} = -\frac{Mk}{RT}\frac{p}{\mu(p)z(p)}\frac{dp}{dx}. \tag{5.21}$$

By substituting Equation (5.4), the above equation is simplified to:

$$\rho\frac{q}{A} = -\frac{Mk}{2RT}\frac{dm}{dx}. \tag{5.22}$$

Table 5.2. The measured pressure-drops and the absolute pressures at both ends of the core plug during the five-point steady-state measurements. Note that the outflow end pressure (a.k.a. backpressure) is kept at 1,727 psia.

Flow rate (mL/min)	0.005	0.010	0.015	0.020	0.025
Δp (psi)	45	94	145	199	251
p_{in} (psia)	1,772	1,821	1,872	1,926	1,978
p_{out} (psia)	1,727	1,727	1,727	1,727	1,727

In Equation (5.22), the product of ρ and q is a constant, and can be calculated using the values recorded by the upstream pump. More specifically, q is the constant volumetric flow rate injected by the upstream pump, and ρ can be inferred by table lookup using the injecting pressure. In Equation (5.22), the space variable x is the only dependent variable in m. As such, Equation (5.22) can be integrated using the "separation of variables" method as such:

$$\Delta m = m_{in} - m_{out} = \frac{2L}{kA}\frac{RT}{M}\rho q, \tag{5.23}$$

where L is the core length, m_{in} and m_{out} are the real-gas pseudo pressures at the inflow end and outflow end respectively. Note that both m_{in} and m_{out} can be determined by table lookup.

The calculated real-gas pseudo pressure drop Δm across the core plug versus the product of the density and the volumetric flow rate is plotted in Figure 5.8. Linear regression by minimizing the least-square error is applied to the data points. According to Equation (5.23), a permeability of ~ 1.40 μD is determined based on the slope of the linear fit. The linear fit also validates Darcy's law within the flow rate range.

As shown in the previous section, the permeability estimated by the two-stage CO_2-injection transient-pressure measurement is 1.20 μD, which is a < 15% deviation from the permeability estimated by the standard steady-state measurement. The standard steady-state method confirms that the transient-pressure method provides comparable results.
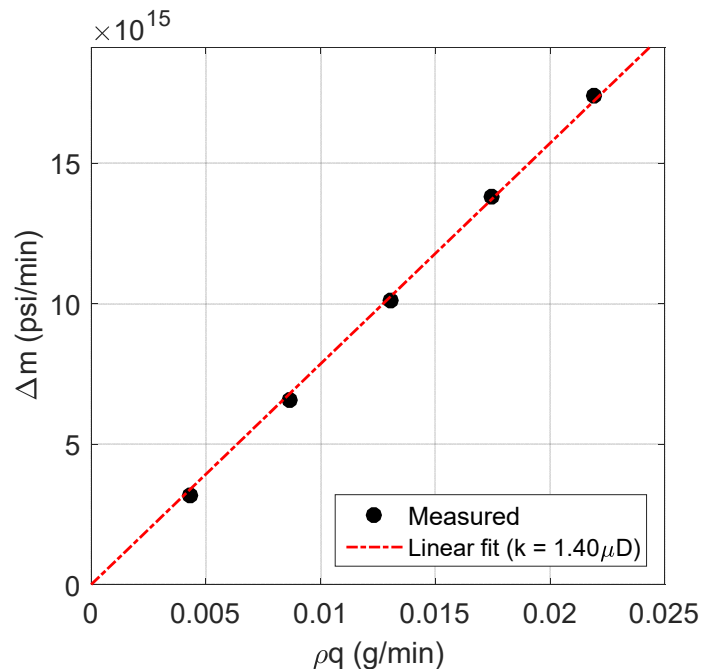
Figure 5.8. Measured real-gas pseudo pressure drops across the core versus the product of the density and the volumetric flow rate during the five-point steady-state experiment. Linear regression is applied to fit the data denoted as the red dashed straight line. The estimated permeability based on the fit is 1.40 μD.

It should be noted that each stage of the five-point steady-state measurement takes about 5 hours, which means the steady-state measurement should take 25 hours in total, not including the time for pre-pressurizing the core to the backpressure (i.e., 1,727 psia). However, the transient-pressure experiment takes only ~ 1 hour after the prefilling stage, which suggests that the time saving by using the transient-pressure measurement is a factor of ~ 25. Note that the time saving by

the transient-pressure approach can be more if the one-stage method is applicable (see Appendix I of this chapter).

5.6. Conclusions

The widely accepted permeability-estimation techniques, including both steady-state and unsteady-state methods, face various challenges. In general, the challenges include (1) elaborate experimental set-ups, (2) complicated data interpretations, (3) long run times, and/or (4) limitations on the differential pressure. A novel unsteady-state approach is proposed to resolve the challenges. The proposed transient-pressure approach is based on the transient-pressure measurement during 1D core-flooding experiments, integrated with the numerical simulation of the transient-pressure history.

For the experiment, the core plug undergoes a two-stage 1D CO_2-flooding, where the transient-pressure at the second stage is recorded for history matching. The mass balance equations at both stages are used to compute the porosity and pore-volume compressibility. For the simulation, the fluid transport during the transient-pressure experiments is simulated assuming: (1) the fluid transport is isothermal, (2) the singularity in fluid properties at the phase transition can be approximated by a finite-slope straight line, (3) the rock pore-volume compressibility is constant, and (4) the permeability does not depend on the net stress. The numerical simulation is integrated with the REFPROP database for the fluid-property table lookup. Also, the real-gas pseudo pressure is introduced to

simplify the governing equation of the simulation. The history matching between the experimental and simulated data yields permeability estimates that are in excellent agreement with the permeability measured by the standard steady-state approach.

Compared to the existing approaches, the apparatus and the procedure of the transient-pressure method is greatly simplified. The simplified apparatus and procedure provide an opportunity for the transient-pressure measurements to be integrated with other core analysis that requires in-situ measurements, such as NMR. The transient-pressure experiment saves a significant amount of run time without sacrificing accuracy. Furthermore, simulation-based history matching reduces the complexity of data interpretation compared to analytical-solution-based approaches. The numerical simulation has the capability of simulating the fluid transport over a broad pressure range, including the phase transition of the fluids; this capability alleviates the pressure constraint typically required by existing permeability-measurement approaches.

5.7. Appendix I: One-Stage Transient-Pressure Method

In the "Transient-Pressure Method" sub-chapter, a two-stage approach is proposed for permeability estimation. The primary purpose of implementing the experiment in two stages is to (1) limit the maximum net stress, and (2) conduct the permeability estimation under reservoir conditions. However, if the limitation on the net stress can be extended, and the permeability does not depend on the net

stress across a broader range, the transient-pressure experiment can be implemented in one stage using the same apparatus.

Table 5.3. Details of one-stage transient-pressure experiments and the additional stage for porosity and pore-volume compressibility calculation, including the initial and final pore pressures, the initial and final confining pressure and the temperature.

Measurement	Initial pore pressure (psia)	Final pore pressure (psia)	Initial confining pressure (psia)	Final confining pressure (psia)	Temperature (°F)
Injection	5	1,792	2,615	2,615	73
Production	1,793	15	2,615	2,615	73
Additional	1,792	1,792	2,615	3,015	73

This appendix presents one-stage injection and production experiments. The details of the experiments are summarized in Table 5.3. These experiments are also performed at 73°F. The injection experiment is conducted by injecting CO_2 to a core under partial vacuum (i.e., with a pore pressure of 5 psia). The injecting pressure is fixed at 1,792 psia, and the confining pressure is kept at roughly 2,600 psia. The volume change recorded by the upstream pump indicates that there is 14.50 mL of CO_2 injected at 1,792 psia in this experiment. On the other hand, the production experiment is done by venting the CO_2 to the atmosphere (i.e., at a constant outflow-end pressure of 15 psia) from the saturated core.

Note that there is one additional step of experimentation which involves increasing the confining pressure by 400 psi while the pore pressure is regulated at the same value by the syringe pump. As a consequence, there is 0.03 mL of CO_2 squeezed out of the core plug, which indicates the pore volume is reduced by 0.03 mL. This step provides an independent mass-balance measurement for porosity and

pore-volume compressibility. By combining the mass-balance equations from the

injection experiment and the additional step, we can infer two equations as such:

$$\rho(1{,}792) \times 14.50$$

$$= \rho(1{,}792)\left(V_{dead} + V_0\left(1 + c_p(1{,}792 - 2{,}615)\right)\right) \quad (5.24)$$

$$- \rho(5)\left(V_{dead} + V_0\left(1 + c_p(5 - 2{,}615)\right)\right),$$

$$\rho(1{,}792) \times 0.03$$

$$= \rho(1{,}792)\left(V_{dead} + V_0\left(1 + c_p(1{,}792 - 2{,}615)\right)\right) \quad (5.25)$$

$$- \rho(1{,}792)\left(V_{dead} + V_0\left(1 + c_p(1{,}792 - 3{,}015)\right)\right).$$

By solving the above two equations, $V_0 = 10.77$ mL and $c_p = 7.0 \times 10^{-6}$/psi

are determined. By knowing the bulk volume of the core plug, a porosity ϕ_0 = 12.4

p.u. is inferred. The porosity and pore-volume compressibility computed here are

close to those presented in the "Transient-Pressure Method" sub-chapter, where the

estimated porosity is 12.2 p.u. and the estimated pore-volume compressibility is

7.9×10^{-6}/psi. These two independent calculations indicate that the approach for

computing ϕ_0 and c_p is robust.

Figure 5.9 shows the simulated pressure-profile snapshots for both one-

stage injection and production experiments. It is evident that the data are divided

into two regions by the horizontal dashed line, which represents the vapor pressure.

The distinct regions arise from the difference in the fluid properties between the

liquid-state CO_2 and gas-state CO_2.

(a)

(b)
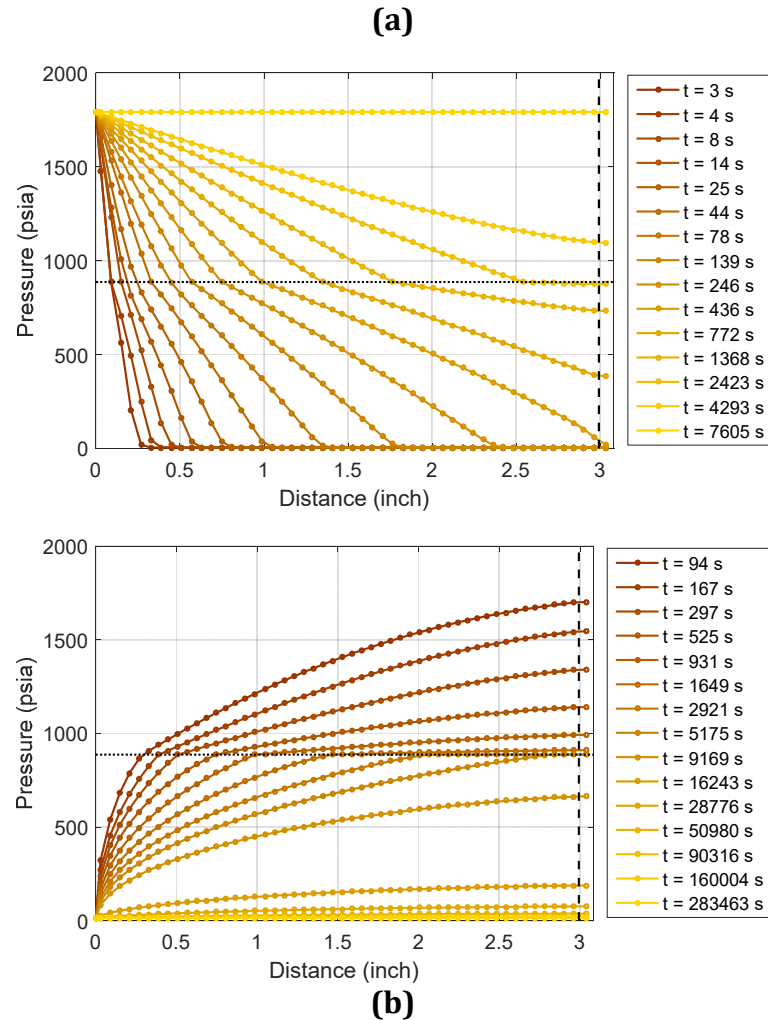
Figure 5.9. Simulated pressure-profile snapshots at different run times during one-stage transient-pressure experiments for (a) injection; (b) production. The permeability values used in the simulation are 1.32 and 1.44 μD for injection and production respectively. The profiles at different run times are distinguished by colors. The legend indicates the run time when the pressure profile is snapshotted. The horizontal dashed line indicates the vapor pressure of CO_2 at the experimental temperature 73 °F. The vertical dashed line at 3 inches denotes the core boundary. Note that the last grid block is for the closed-end dead volume.

Figure 5.10(a) presents the pressure histories for the injection measurement. The entire injection experiment takes about 2 hours. The optimal history matching shown in red yields a permeability estimate about 1.32 μD. The other two simulated curves are plotted to illustrate the sensitivity of this approach. Note that the two additional permeability values are 15% away from the optimal value.

(a)

(b)
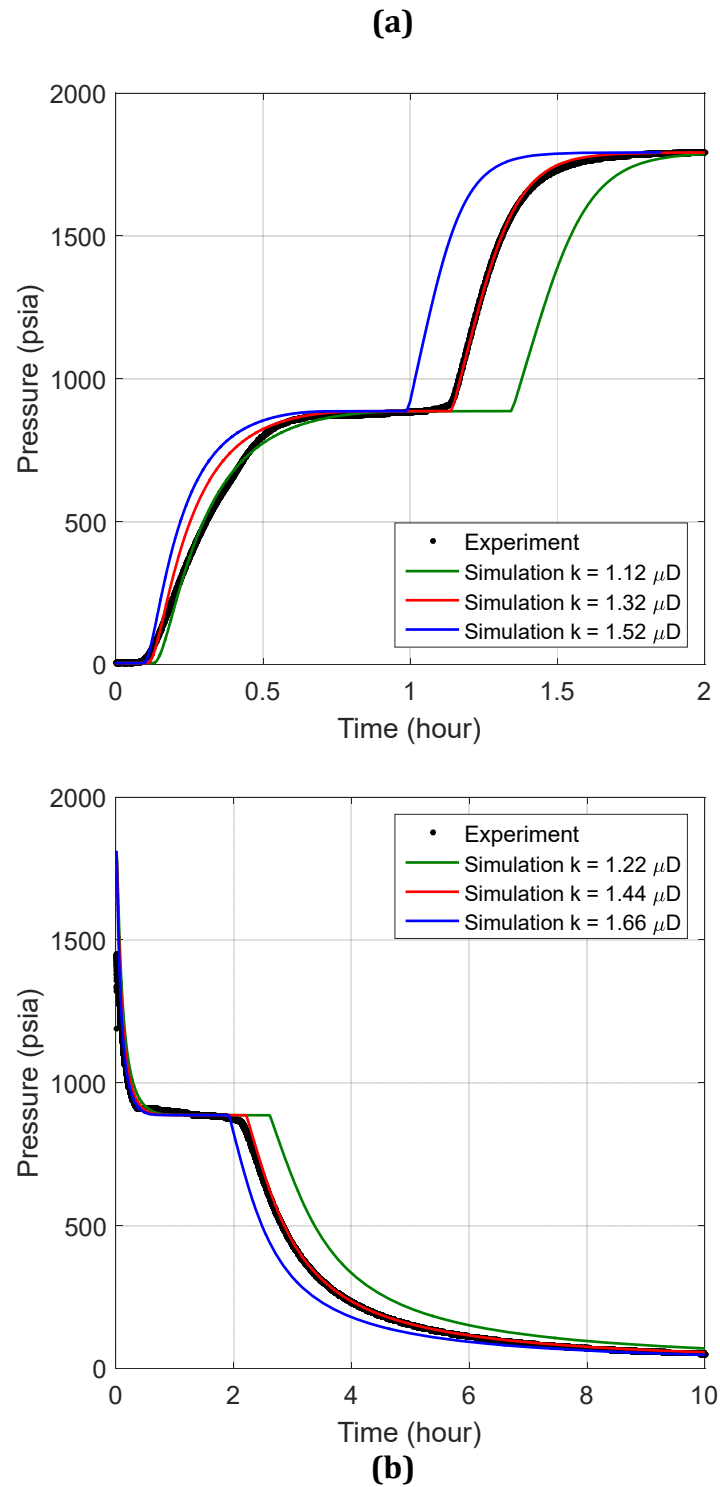
Figure 5.10. Pressure histories of the one-stage transient-pressure measurements from simulations and experiments for (a) injection and (b) production. The legend indicates the source of the pressure histories. For each subplot, the optimal matching is plotted in red, and the other two candidates are plotted in blue and green respectively.

Figure 5.10(b) presents the pressure histories for the production experiment. The production experiment takes more than 10 hours, which is significantly longer than the injection experiment. The optimal history matching yields a permeability estimate of 1.44 μD. Similar to Figure 5.10(a), two candidate simulated pressure histories with the permeability 15% away from the optimal value are to illustrate the sensitivity.

It is readily observed that the simulation captures the phase transition, namely the pressure plateaus at the vapor pressure for some time. The plateau is because the CO_2 at the closed-end dead space stays at the vapor pressure while accumulating until it is filled with liquid-state CO_2 or depleting until the liquid-state CO_2 becomes gaseous.

The permeabilities estimated by the one-stage methods (i.e., 1.32 μD by the injection method and 1.44 μD by the production method) corroborate with the two-step method (i.e., 1.20 μD) and are validated by the standard steady-state method (i.e., 1.40 μD). This suggests that the one-stage method is also capable of permeability estimation, as a faster implementation with fewer constraints. One caveat of the one-stage method is overstressing. The high net-stress may lead to irreversible change (versus elastic change) in the core plug.

Table 5.4 summarizes the results by different permeability-estimation approaches for a better comparison. Note that the one-stage injection and production approaches do not require the prefilling stage, which saves a significant

amount of experimental run time compared to the two-stage and steady-state

methods.

Table 5.4 Summary of results by different permeability-estimation approaches, including both transient-pressure and steady-state methods. Note that the transient-pressure one-stage production and steady-state methods do not provide the porosity and compressibility estimations.

Approach	Permeability (μD)	Porosity (p.u.)	Pore-volume compressibility (1/psi)	Experimental run time (hour)
Transient-pressure two-stage injection	1.20	12.2	7.9×10^{-6}	1 (after prefilling)
Transient-pressure one-stage injection	1.32	12.4	7.0×10^{-6}	2 (no prefilling)
Transient-pressure one-stage production	1.44	N.A.	N.A.	10 (no prefilling)
Steady-state	1.40	N.A.	N.A.	25 (after prefilling)

5.8. Appendix II: Numerical Simulation

As mentioned in the previous section, the numerical simulation is developed

using the implicit finite-volume method. Figure 5.11 illustrates the grid block

assignment. On the left, 50 equal-length grids denoted in grey are for the core plug.

The 51st grid denoted in orange is for the dead volume. Each grid has independent

permeability, porosity at zero net stress, and grid length.

Figure 5.11 Grid block assignment of simulation. The grey grids are for the core plug. The orange grid is for the dead volume. k represents the permeability, ϕ_0 represents the porosity measured at zero net stress, Δx represents the grid length and $\bar{k}$ represents the permeability at the boundary between grids.

The permeability at the boundary between grids is defined as $\bar{k}$. It is the harmonic mean of the permeability of adjacent grids as such:

$$\bar{k}_i = \begin{cases} k_1, & i = 1 \\ \dfrac{k_i k_{i-1}(\Delta x_i + \Delta x_{i-1})}{k_{i-1}\Delta x_i + k_i \Delta x_{i-1}}, & i = 1,2,3,\dots,NX, \\ 0, & i = NX+1 \end{cases} \qquad (5.26)$$

where i denotes the number of a grid and NX is the total number of grids, which is equal to 51 in the present case. Note that the no-flow boundary condition at the right boundary of the 51st grid (i.e., dead volume) is satisfied by setting the permeability equal to zero.

Based on the grid assignment, the mass conservation equation is re-formulated into the finite difference form by discretization. The finite difference expression for the spatial derivative in Equation (5.9) with the grid-block formulation is:

$$\frac{\partial}{\partial x}\left(k\frac{\partial m}{\partial x}\right) \cong \begin{cases} \dfrac{\bar{k}_2 \dfrac{(m_2 - m_1)}{\frac{1}{2}(\Delta x_2 + \Delta x_1)} - \bar{k}_1 \dfrac{(m_1 - m_{bd,l})}{\frac{1}{2}(\Delta x_1)}}{\Delta x_1}, & i = 1 \\[4mm] \dfrac{\bar{k}_{i+1} \dfrac{(m_{i+1} - m_i)}{\frac{1}{2}(\Delta x_{i+1} + \Delta x_i)} - \bar{k}_i \dfrac{(m_i - m_{i-1})}{\frac{1}{2}(\Delta x_i + \Delta x_{i-1})}}{\Delta x_i}, & i = 2,\dots,NX-1 \\[4mm] \dfrac{\bar{k}_{NX+1} \dfrac{(m_{bd,r} - m_{NX})}{\frac{1}{2}(\Delta x_{NX})} - \bar{k}_{NX} \dfrac{(m_{NX} - m_{NX-1})}{\frac{1}{2}(\Delta x_{NX} + \Delta x_{NX-1})}}{\Delta x_{NX}}, & i = NX \end{cases} \qquad (5.27)$$

where $m_{bd,l}$ is the real-gas pseudo pressure at the left boundary of the first grid, m_i represents the real-gas pseudo pressure of the ith grid, and $m_{bd,r}$ is the real-gas pseudo pressure at the right boundary of the last grid. Note that $m_{bd,r}$ has no impact

on the results since $\bar{k}_{NX+1}$ is zero. Therefore, $m_{bd} = m_{bd,l} = m_{bd,r}$ is adopted in the following context. The inter-block transmissibility coefficient is defined to simplify Equation (5.27):

$$T_i = \begin{cases} \dfrac{\bar{k}_1}{\frac{1}{2}(\Delta x_1)}, & i = 1 \\[3ex] \dfrac{\bar{k}_i}{\frac{1}{2}(\Delta x_i + \Delta x_{i-1})}, & i = 1, 2, \dots, NX \\[3ex] \dfrac{\bar{k}_{NX+1}}{\frac{1}{2}(\Delta x_{NX})} = 0, & i = NX + 1 \end{cases} \tag{5.28}$$

Substituting Equation (5.28) to Equation (5.27) yields:

$$\frac{\partial}{\partial x}\left(k\frac{\partial m}{\partial x}\right) \cong \begin{cases} \dfrac{T_2(m_2 - m_1) - T_1(m_1 - m_{bd})}{\Delta x_1}, & i = 1 \\[3ex] \dfrac{T_{i+1}(m_{i+1} - m_i) - T_i(m_i - m_{i-1})}{\Delta x_i}, & i = 2, \dots, NX - 1, \\[3ex] \dfrac{T_{NX+1}(m_{bd} - m_{NX}) - T_{NX}(m_{NX} - m_{NX-1})}{\Delta x_{NX}}, & i = NX \end{cases} \tag{5.29}$$

As for the left-hand side of the mass conservation equation, the finite difference expression is:

$$\frac{\partial C}{\partial t} = \frac{\partial(\phi\rho)}{\partial t} = \frac{\partial(\phi\rho)}{\partial m}\frac{\partial m}{\partial t} \cong \alpha(m_i)\frac{\Delta m_i}{\Delta t},$$

$$\alpha(m_i) = \frac{\phi(m_i + \Delta m_i)\rho(m_i + \Delta m_i) - \phi(m_i)\rho(m_i)}{\Delta m_i}, i = 1, 2, \dots, NX, \tag{5.30}$$

where Δm_i is the difference in real-gas pseudo pressure of the ith grid between the new time step and the previous time step. The reason not to use the derivative form as in Equation (5.16) is to ensure the mass balance during the simulation. It should be noted that the denominator Δm_i can not be zero. Therefore, in the simulation, Δm

is initialized with a small floating number, namely the floating-point relative

accuracy (i.e., "eps" in MATLAB).

Combining the finite-difference formulation of both sides of the mass

conservation equation, namely Equations (5.9), (5.29) and (5.30), yields:

$$\gamma(m_i)\Delta m_i = \begin{cases} T_2(m_2 - m_1) - T_1(m_1 - m_{bd}), i = 1 \\ T_{i+1}(m_{i+1} - m_i) - T_i(m_i - m_{i-1}), i = 2, \dots, NX - 1, \\ T_{NX+1}(m_{bd} - m_{NX}) - T_{NX}(m_{NX} - m_{NX-1}), i = NX \end{cases}$$

$$\gamma(m_i) = \alpha(m_i)\frac{2RT\Delta x_i}{M\Delta t}.$$

(5.31)

In Equation (5.31), the real-gas pseudo pressures on the right-hand side are

the values at the new time step as required by the implicit method. We used the

following notation to denote the changes in the real-gas pseudo pressure at different

time steps and iterations:

$$m_{n+1,i}^{k+1} = m_{n+1,i}^{k} + DMK_i = m_{n,i} + DM_i + DMK_i \,,$$

(5.32)

where the subscript n indicates the number of the time step, and the superscript k

indicates the number of the iteration. The change in real-gas pseudo pressure

between the nth and $n + 1^{th}$ time step is denoted as DM_i while the change between

the kth and $k + 1^{th}$ iteration at the new time step is denoted as DMK_i.

The goal of the simulation is to compute the real-gas pseudo pressure at the

new time step that satisfies Equation (5.31). A residual formulation of Equation

(5.31) can be introduced to reduce the effect of the computer roundoff error. By

substituting Equation (5.32) to Equation (5.31), we can derive the vectorized

residual formulation as such:

$$A \; \overrightarrow{DMK} = \overrightarrow{B_k} \,, \tag{5.33}$$

where $\overrightarrow{DMK}$ is the vector denotes the changes of m at each grid by k^{th} iteration, A is

a $NX \times NX$ matrix and $\overrightarrow{B_k}$ represents the residuals after the kth iteration. Note that

$\overrightarrow{B_k}$ will be a zero vector when m satisfies Equation (5.31). The expressions of matrix

A and vector $\overrightarrow{B_k}$ are:

$$A = \begin{bmatrix} -(T_2 + T_1) & T_2 & 0 & & & & \\ T_2 & -(T_3 + T_2) & T_3 & \cdots & & 0 & \\ 0 & T_3 & -(T_4 + T_3) & & & & \\ & \vdots & & \ddots & & & \vdots \\ & & & & -(T_{NX-1} + T_{NX-2}) & T_{NX-1} & 0 \\ & 0 & & \cdots & T_{NX-1} & -(T_{NX} + T_{NX-1}) & T_{NX} \\ & & & & 0 & T_{NX} & -(T_{NX+1} + T_{NX}) \end{bmatrix}$$

$$- \begin{bmatrix} \gamma_1 & & \\ & \ddots & \\ & & \gamma_{NX} \end{bmatrix}, \tag{5.34}$$

$$\overrightarrow{B_k} = \begin{cases} -T_2\left(m_{n+1,2}^k - m_{n+1,1}^k\right) + T_1\left(m_{n+1,1}^k - m_{bd}\right) + \gamma_1 DM_1, & i = 1 \\ -T_{i+1}\left(m_{n+1,i+1}^k - m_{n+1,i}^k\right) + T_i\left(m_{n+1,i}^k - m_{n+1,i-1}^k\right) + \gamma_i DM_i, & i = 2, \dots, NX - 1 \,, \\ -T_{NX+1}\left(m_{bd} - m_{n+1,NX}^k\right) + T_{NX}\left(m_{n+1,NX}^k - m_{n+1,NX-1}^k\right) + \gamma_{NX} DM_{NX}, & i = NX \end{cases} \tag{5.35}$$

where γ_i represents $\gamma\left(m_{n+1,i}^k\right)$ as defined in Equation (5.31). $\overrightarrow{DMK}$ is computed by

matrix inversion as:

$$\overrightarrow{DMK} = A^{-1}\overrightarrow{B_k} \,. \tag{5.36}$$

Note that after each iteration, DM_i (i.e., the real-gas pseudo pressure at new

time step) is updated by adding DMK_i. The iteration is continued until the residuals

become negligible, of which the criteria is that the summation of the absolute value

of elements in $\overrightarrow{B_k}$ is less than a threshold.

The time-step size Δt in the simulation is adjusted using an automatic time-step size selector adapted from Todd, O'Dell, and Hirasaki 1972. The new time-step size is updated based on the previous run time and time-step size as:

$$\Delta t^{n+1} = \frac{1}{2}\left(\Delta t^n + \min\left(\sqrt{t(n)}, \Delta t^n \frac{DMLIM}{DMMAX}\right)\right). \tag{5.37}$$

where Δt^{n+1} is the new time-step size, Δt^n is the previous time-step size, $t(n)$ is the previous run time, $DMLIM$ is the pre-set desired maximum changes in m, and $DMMAX = \max(\text{abs}(DM_i))$ is the maximum changes in m compute at the previous time step. The automatic time-step size selector improves the efficiency of simulation. During the simulation, the iteration on the matrix inversion may not converge due to the singularity in CO_2 density (see Figure 5.3). The iteration is repeated with the time-step size reduced by half stepwise until the iteration converges.

5.9. Appendix III: Estimated Temperature Effect

In the numerical simulation, it is assumed that the temperature of the permeating fluid is constant. Indeed, the fluid temperature can vary with the compression or expansion of the fluid. This appendix provides conservative estimates of the temperature variation and the time for dissipation under assumptions on the two transient-pressure injection experiments to justify the isothermal assumption. The conservative estimation of temperature variation is conducted in two steps consisting of 1) calculating the temperature change of CO_2

due to the compression and 2) calculating the temperature of CO_2 after equilibrating with the rock matrix.

The first step of the calculation does not consider the heat transfer with the rock matrix. The conservative temperature change is estimated by assuming CO_2 injection is adiabatic (i.e., no heat nor mass transfer) and reversible, which implies that the entropy of CO_2 is constant. The initial conditions, including the pressure, volume and temperature of CO_2 before injection, are denoted as (P_1, V_1, T_1), while the condition after CO_2 injection (i.e., the intermediate state before the heat transfer with rock) are denoted as (P_2, V_2, T_2). The temperature change in the intermediate state can be calculated using isentropic constraint and mass balance as such:

$$S(P_1, V_1, T_1) = S(P_2, V_2, T_2), \tag{5.38}$$

$$\rho(P_1, V_1, T_1)V_1 = \rho(P_2, V_2, T_2)V_2, \tag{5.39}$$

where S and ρ are the entropy and density of CO_2 at each state. Note that T_1 is room temperature, P_1 is the pressure of CO_2 before injection, and P_2 is the pressure of CO_2 after injection. In the above equations, V_1, V_2 and T_2 are unknown parameters.

The second step of the calculation focuses on the heat transfer between CO_2 and the rock matrix, which means the temperature of CO_2 equilibrates with the rock matrix. It is assumed that the time for equilibration is negligible given the large surface area of the porous media, and the temperature is re-distributed evenly in the saturated core. The fluid pressure, volume, and temperature at the equilibrated state are denoted as (P_3, V_3, T_3), where P_3 is the same as P_2, and V_3 is the pore

volume of the core. The heat transfer between the rock matrix and CO_2 and the mass balance of CO_2 yield the following two equations:

$$\int_{T_2}^{T_3} \phi \rho c_p dT + \int_{T_1}^{T_3} (1 - \phi)\rho_r c_{p,r} dT = 0, \tag{5.40}$$

$$\rho(P_2, V_2, T_2)V_2 = \rho(P_3, V_3, T_3)V_3, \tag{5.41}$$

where ϕ is the rock porosity that is reported in the previous section, ρ and ρ_r are the density of CO_2 and rock respectively, c_p and $c_{p,r}$ are the specific heat capacity of CO_2 and rock respectively. Note that the density and specific heat capacity of CO_2 varies with fluid properties and are inferred from the REFPROP database. The product of ρ_r and $c_{p,r}$ is heat capacity $C_{p,r}$ of rock that is about 2.5 J/ml/K for shale formation (Dobson and Houseworth 2014). In the above two equations, V_2, T_2 and T_3 are unknown parameters. By combining Equations from (5.38) to (5.41), the equilibrated temperature (i.e., T_3), along with three other unknown parameters (i.e., V_1, V_2, and T_2), can be determined. Figure 5.12 indicates that the initial temperature variation, namely $T_0' = T_3 - T_1$, are 10 °C and 0.6 °C for one-stage and two-stage injection, respectively.

We then estimate the time for the decay of temperature variation using the heat conduction equation. The core is cylindrical with a radius R of 0.75 inches and is assumed to be infinitely long and homogeneous such that the heat conduction happens only in the radial direction. Therefore, the heat conduction equation can be expressed as follows:

$$\frac{\partial(T')}{\partial t} = \alpha\Delta(T') = \alpha\frac{1}{r}\frac{\partial}{\partial r}\left(r\frac{\partial(T')}{\partial r}\right), \tag{5.42}$$

where T' is defined as the temperature of the saturated rock minus the room temperature (i.e., temperature variation), and $\alpha = k/C_p$ where k and C_p are the heat conductivity and heat capacity of the saturated rock. The heat conductivity k of the saturated rock is approximated by the heat conductivity of the empty rock, which is roughly 1.0 W/m/K (Dobson and Houseworth 2014), by assuming negligible heat conductivity of CO_2 (i.e., < 0.1 W/m/K). The heat capacity C_p of saturated rock is computed using a linear combination of heat capacities of rock and CO_2 as such:

$$C_p = (1 - \phi)C_{p,r} + \phi\rho c_p, \tag{5.43}$$

where ρ and c_p are the density and specific heat capacity of CO_2 computed at room temperature and final pressure.

The initial and boundary conditions for Equation (5.42) are:

$$T'(r, t = 0) = T'_0, \tag{5.44}$$

$$T(r = R, t) = 0. \tag{5.45}$$

Equation (5.44) implies that the initial temperature variation is homogeneously distributed in the saturated core. Equation (5.45) assumes the temperature at the boundary of the core is kept at room temperature, given that the core is surrounded by sleeves and a confining-water reservoir. The analytical solution of Equation (5.42) with the above initial and boundary conditions is shown as follows (Carslaw and Jaeger 1959):

$$T'(r,t) = \sum_{n=1}^{\infty} \left(\frac{2T_0'}{R} \frac{J_0(r\lambda_n)}{\lambda_n J_1(R\lambda_n)} e^{-\alpha\lambda_n^2 t} \right), \qquad (5.46)$$

where J_0 and J_1 are the Bessel functions of the first kind of order zero and one

respectively, $R\lambda_n$ is the nth positive root of J_0, and R is the core radius. Based on the

analytical solution, the decay history of the temperature variation at the center of

the core (i.e., $r = 0$), namely the highest temperature, is plotted in Figure 5.12.
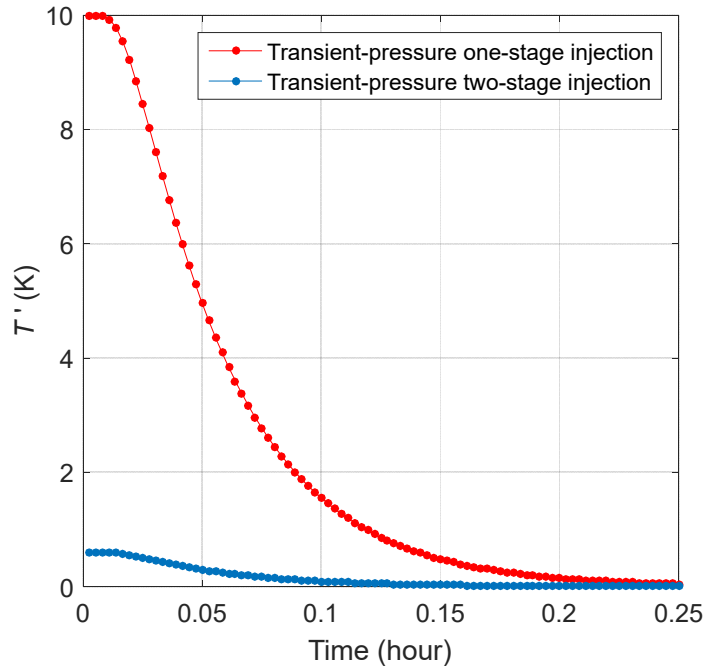
Figure 5.12 The decay history of the conservatively estimated temperature variation during two transient-pressure CO_2 injection experiments. The legend indicates the type of experiments.

Figure 5.12 indicates the temperature variation during the two-stage

injection is negligible (i.e., $< 1°C$), and the temperature variation decays to nearly

zero within 0.15 hours from the beginning of injection. Instead, the one-stage

injection yields a much higher initial temperature variation providing the pressure

during the process (i.e., from 5 psia to 1,792 psia) goes through the phase transition

of CO_2, which generates heat. However, the temperature variation during the one-stage injection decays to nearly zero within roughly 0.25 hours, which is still short compared to the total experimental run time (i.e., ~2 hours). Note that the temperature change is a conservative estimate under the adiabatic and reversible assumption such that the real temperature change can be much less. The end pieces of the core holder that are in direct contact with the core also enhance the temperature decay. Therefore, the temperature effect exists only at the very beginning of experiments and is most likely to be insignificant, which corroborates with the excellent matching between experimental and simulated data shown in previous sections.

Chapter 6

Conclusions

This thesis is based on and slightly adapted from existing publications (Philip M. Singer, Chen, and Hirasaki 2016; Z. Chen et al. 2017; Z. Chen 2018; Philip M. Singer, Chen, et al. 2018; Z. Chen, Wang, et al. 2019; Z. Chen, Singer, et al. 2019). This chapter summarized the conclusions of previous chapters, where some portion is taken word-to-word from the above publications.

In the first portion of this thesis, laboratory NMR measurements integrated with NMR logging are conducted to estimate the hydrocarbon composition in an organic-rich chalk prospect. Besides, NMR laboratory-measured restricted diffusion is used to estimate the mean pore size, heterogeneity length scale, and tortuosity of the hydrocarbon-filled porosity.

More specifically, the laboratory-measured T_2 distributions of the hydrocarbons, in saturated cores are converted to T_{2app} distributions by simulating

the effects of diffusion in the magnetic-field gradient of the NMR logging tool. The core data indicate a significant contrast in T_{2app} distributions between the different hydrocarbons due to different surface relaxivities and diffusivities. This contrast is used to estimate the downhole hydrocarbon composition by minimizing the mean square error in the T_{2app} distributions between core and log data. Meanwhile, the laboratory-measured T_1/T_2 exhibits contrast between water and light hydrocarbons. The magnetic-field gradient of NMR logging tools amplifies the contrast and makes the downhole-measured T_1/T_{2app} favorable for fluid typing. It is found that methane and natural gas liquids (NGLs) tend to yield higher T_1/T_{2app} compared to water and longer alkanes.

Also, the laboratory-measured restricted diffusivity indicates that the saturating methane can be distinguished from liquid-state hydrocarbons by the higher diffusivity. Besides, the laboratory-measured restricted diffusivities of different light hydrocarbons are fitted to the Padé approximation to estimate the mean pore size, heterogeneity length scale, and tortuosity of the light-hydrocarbon filled porosity.

The second portion of this thesis concentrates on NMR response of hydrocarbons and water in the organic-rich shale. This research validates the technique based on T_1/T_2 ratio contrast between hydrocarbons and water in organic-rich shale for fluid typing and saturation estimation. The validation is by re-saturating and measuring the responses of fluids in the organic-rich shale and its isolated components, including kerogen and clays.

The T_1/T_2 ratio for heptane-saturated kerogen (averaged $T_1/T_2 \sim 4$) is found to be consistently larger than for water-saturated kerogen (averaged $T_1/T_2 \sim 1.5$) and water-saturated clay isolates (averaged $T_1/T_2 \sim 2$), across the entire T_2 spectrum. The isolated kerogen results are compared with the re-saturated organic-shale rock, which shows a higher average $T_1/T_2 \sim 4$ for re-saturated heptane versus re-saturated water $T_1/T_2 \sim 2$, consistent with the saturated isolates data. All of the experimental findings corroborate with larger T_1/T_2 ratios for saturating hydrocarbons versus saturating water thereby validates T_1/T_2 ratio as a technique for fluid typing and saturation in organic shale.

The third portion of this paper presents a continuation of investigations into the 2D T_1-T_2 NMR response of heptane in kerogen isolates. In this study, the influence of bitumen extraction on the T_1-T_2 data of the heptane-saturated kerogen is investigated. It is found that for the fast-relaxing peak, the T_1 and T_2 values remain roughly the same after bitumen extraction, however the porosity decreases, which strongly suggests that the fast-relaxing peak is associated with dissolved heptane in bitumen and kerogen. For the slow-relaxing peak, it is found that the porosity remains roughly the same after bitumen extraction. However, the T_1 and T_2 values increase due to a decrease in apparent surface relaxivity. The diffusive-coupling model can interpret this phenomenon. The T_2-T_2 exchange experiments confirm the diffusive coupling between the dissolved and intragranular heptane. The T_2 shift of water in kerogen compared to partially deuterated water in kerogen, and the evidence of the movement of magnetization between the solid and liquid sample constituents indicate that both of intra- and inter-molecular [1]H-^{1}H dipole-dipole

interactions contribute to ρ_1 and ρ_2. A model system built with heptane and polymer mixes suggests that the large T_1/T_2 ratios reported in hydrocarbon-saturated kerogen results from nanopore confinement.

The fourth portion of this thesis presents a novel unsteady-state method to determine the permeability by transient-pressure history matching. On the experimental side, the ultralow-permeability core undergoes 1D CO_2-flooding experiments, during which the transient pressure is monitored for history matching. On the simulation side, the transient-pressure history is simulated using real-gas pseudo pressure and table lookup to deal with the non-linearity in fluid properties. The free parameter, permeability, in the simulation is adjusted for history matching to determine the rock permeability. This new unsteady-state method is validated by the standard steady-state method.

The advantages of this new unsteady-state approach are: 1) it can be implemented with simple set-ups; 2) it can be finished within a considerably short-time period; 3) the data interpretation is straightforward; 4) it can be implemented over broad pressure ranges, even with phase transitions of the permeating fluids, not limited to CO_2.

In conclusion, the technique and fundamental knowledge built in this thesis will contribute to formation evaluation.

Chapter 7

Future Work

The scope of the work presented in this thesis can be further extended.
Several potential directions for future work will be:

1. The NMR core-log integration workflow for fluid-composition estimation
   by T_2 and T_1/T_2 contrasts presented in Chapter 2 can be in principle used
   for shale-rock formations. Further study is needed to confirm the
   applicability of this new technique.

2. The research on kerogen isolates (Chapter 3 and Chapter 4) is based on
   immature type II kerogen. Efforts should be taken to expand this study to
   encompass a variety of different kerogen types and maturities.

3. The transient-pressure experiment, as part of the new permeability-
   estimation approach (Chapter 5), can be improved using bi-axial core
   holder that can apply axial confining stress onto the core, such that the
   unexpected pressure change at the early-time stage can be eliminated.

4. The transient-pressure simulation (Chapter 5) can be modified by
    including the gas adsorption and capillary condensation as functions of
    pressure. In such a case, the simulator can be used to simulate the
    depletion of methane from organic-rich shale.

References

Acholla, Francis V., and Wilson L. Orr. 1993. "Pyrite Removal from Kerogen without Altering Organic Matter: The Chromous Chloride Method." *Energy and Fuels* 7 (3): 406–10. doi:10.1021/ef00039a012.

Al-Hussainy, R., Ramey H. J., and P. B. Crawford. 1965. "The Flow of Real Gases Thorugh Porous Media." *Journal of Petroleum Technology*. doi:10.2118/1243-A-PA.

Anand, Vivek, Mansoor Rampurawala Ali, Aria Abubakar, Rahul Grover, Orlando Neto, Iain Pirie, and Jorge Gonzalez Iglesias. 2017. "Unlocking the Potential of Unconventional Reservoirs Through New Generation NMR T1/T2 Logging Measurements Integrated with Advanced Wireline Logs." *Petrophysics* 58 (2): 81–96.

Anand, Vivek, Mansoor Rampurawala Ali, Nabil Al-adani, Debby Willis, Robert Freedman, Farid Hamichi, Aria Abubakar, et al. 2015. "New Generation NMR Tool for Robust , Continuous T1 and T2 Measurements." In *SPWLA 56th Annual Logging Symposium*. Long Beach, California, USA.

Anand, Vivek, and George J Hirasaki. 2007. "Diffusional Coupling between Micro and Macroporosity for NMR Relaxation in Sandstones and Grainstones." *Petrophysics* 48 (4): 289–307.

Benamsili, Lyès, Jean Pierre Korb, Gérald Hamon, Alain Louis-Joseph, Brice Bouyssiere, Honggang Zhou, and Robert G. Bryant. 2014. "Multi-Dimensional Nuclear Magnetic Resonance Characterizations of Dynamics and Saturations of Brine/Crude Oil/Mud Filtrate Mixtures Confined in Rocks: The Role of Asphaltene." *Energy and Fuels* 28 (3): 1629–40. doi:10.1021/ef401871h.

Bernabé, Y., U. Mok, and B. Evans. 2006. "A Note on the Oscillating Flow Permeability." *International Journal of Rock Mechanics and Mining Sciences* 43 (2): 311–16. doi:10.1016/j.ijrmms.2005.04.013.

Bertoncello, A., and M.M. Honarpour. 2013. "Standards for Characterization of Rock Properties in Unconventional Reservoirs: Fluid Flow Mechanism, Quality Control, and Uncertainties." In *SPE Annual Technical Conference and Exhibition*. New Orleans, Louisiana, USA. doi:10.2118/166470-ms.

Birdwell, Justin E., and Kathryn E. Washburn. 2015. "Multivariate Analysis Relating Oil Shale Geochemical Properties to NMR Relaxometry." *Energy and Fuels* 29 (4): 2234–43. doi:10.1021/ef502828k.

Bloembergen, N., E. M. Purcell, and R. V. Pound. 1948. "Relaxation Effects in Nuclear Magnetic Resonance Absorption." *Physical Review* 73 (7): 679–712. doi:10.1103/PhysRev.73.679.

Brace, W. F., J. B. Walsh, and W. T. Frangos. 1968. "Permeability of Granite under High Pressure." *Journal of Geophysical Research* 73 (6): 2225–36. doi:http://dx.doi.org/10.1029/JB073i006p02225.

Brooks, B. R., C. L. Brooks III, Jr. A. D. Mackerell, L. Nilsson, R. J. Petrella, B. Roux, Y. Won, et al. 2009. "CHARMM: The Biomolecular Simulation Program B." *Journal of Computational Chemistry* 30 (10): 1545–1614. doi:10.1002/jcc.

Brunauer, Stephen, P. H. Emmett, and Edward Teller. 1938. "Adsorption of Gases in Multimolecular Layers." *Journal of the American Chemical Society* 60 (2): 309–19. doi:10.1021/ja01269a023.

Cao Minh, Chanh, Steven F. Crary, Lukasz Zielinski, Chengbing Liu, Sid Jones, and Scott James Jacobsen. 2012. "2D-NMR Applications in Unconventional Reservoirs." In *SPE Canadian Unconventional Resources Conference*. doi:10.2118/161578-MS.

Carslaw, H. S., and J. C. Jaeger. 1959. *Conduction of Heat in Solids*. Second Edi. Oxford : Clarendon Press.

Chen, Jin-hong, Jilin Zhang, Guodong Jin, Terrence Quinn, Elton Frost, and Jacie Chen. 2012. "Capillary Condensation and NMR Relaxation Time in Unconventional Shale Hydrocarbon Resources." In *SPWLA 53rd Annual Logging Symposium*, 1–9. Cartagena, Colombia.

Chen, Joseph J., Martin Hurlimann, Jeffrey Paulsen, Denise Freed, Soumyajit Mandal, Yi Qiao Song, Martin Hürlimann, et al. 2014. "Dispersion of T1 and T2 Nuclear Magnetic Resonance Relaxation in Crude Oils." *ChemPhysChem* 15 (13): 2676–81. doi:10.1002/cphc.201402077.

Chen, Zeliang. 2018. "NMR Characterization of Fluids in Unconventional Formations." Rice University.

Chen, Zeliang, Philip M. Singer, Kuang Jun, Francisco P. Vargas, and George J. Hirasaki. 2017. "Effects of Bitumen Extraction on the 2D NMR Response of Saturated Kerogen Isolates." *Petrophysics* 58 (5). Oklahoma City, Oklahoma, USA: 470–84.

Chen, Zeliang, Philip M. Singer, Xinglin Wang, George J. Hirasaki, and Harold J. Vinegar. 2019. "Evaluation of Light Hydrocarbon Composition, Pore Size, and Tortuosity in Organic-Rich Chalks Using NMR Core Analysis and Logging." In *SPWLA 60th Annual Logging Symposium*. Woodlands, Texas, USA. doi:10.30632/T60ALS-2019_K.

Chen, Zeliang, Xinglin Wang, Guoqing Jian, Leilei Zhang, Pengfei Dong, Philip M. Singer, and George J. Hirasaki. 2019. "Estimation of the Permeability of an Unconventional Formation Core by History-Matching the Saturation with CO2." In *URTeC*, 1–20. doi:10.15530/urtec-2019-620.

Chi, Lu, Zoya Heidari, and Artur Posenato Garcia. 2015. "Investigation of Wettability and Fluid Distribution in Organic-Rich Mudrocks Using NMR Two-Phase Simulation." In *SPE Annual Technical Conference and Exhibition*. Houston, Texas, USA.

Civan, Faruk. 2010. "Effective Correlation of Apparent Gas Permeability in Tight Porous Media." *Transport in Porous Media* 82 (2): 375–84. doi:10.1007/s11242-009-9432-z.

Cui, X., A. M. M. Bustin, and R. M. Bustin. 2009. "Measurements of Gas Permeability and Diffusivity of Tight Reservoir Rocks: Different Approaches and Their Applications." *Geofluids* 9 (3): 208–23. doi:10.1111/j.1468-8123.2009.00244.x.

Curtis, Mark Erman, Raymond Joseph Ambrose, Carl H. Sondergeld, and C.S. Rai. 2010. "Structural Characterization of Gas Shales on the Micro- and Nano-Scales." In *Canadian Unconventional Resources & International Petroleum Conference*. Calgary, Alberta, Canada. doi:10.2118/137693-MS.

Darabi, Hamed, A. Ettehad, F. Javadpour, and K. Sepehrnoori. 2012. "Gas Flow in Ultra-Tight Shale Strata." *Journal of Fluid Mechanics* 710: 641–58. doi:10.1017/jfm.2012.424.

Dobson, Patrick, and James Houseworth. 2014. "Inventory of Shale Formations in the US, Including Geologic, Geochemical, Hydrological, Mechanical, and Thermal Characteristics."

Dunn, K.-J., D.J. Bergman, and G.A. Latorraca. 2002. *Nuclear Magnetic Resonance: Petrophysical and Logging Applications*. Pergamon Press.

Durand. 1980. "Sedimentary Organic Matter and Kerogen. Definition and Quantitative Importance of Kerogen." In *Kerogen: Insoluble Organic Matter from Sedimentary Rocks*. Editions Technip.

Ertas, Deniz, Simon R. Kelemen, and Thomas C. Halsey. 2006. "Petroleum Expulsion Part 1. Theory of Kerogen Swelling in Multicomponent Solvents." *Energy and Fuels* 20 (1): 295–300. doi:10.1021/ef058024k.

Fanchi, John R. 2002. "Well Logging." In *Shared Earth Modeling*.

Fathi, Ebrahim, Ali Tinni, and I. Yucel Akkutlu. 2012. "Correction to Klinkenberg Slip Theory for Gas Flow in Nano-Capillaries." *International Journal of Coal Geology* 103. Elsevier B.V.: 51–59. doi:10.1016/j.coal.2012.06.008.

Fleury, M., E. Kohler, F. Norrant, S. Gautier, J. M'Hamdi, and L. Barré. 2013. "Characterization and Quantification of Water in Smectites with Low-Field NMR." *Journal of Physical Chemistry C* 117 (9): 4551–60. doi:10.1021/jp311006q.

Fleury, Marc, and Maria Romero-Sarmiento. 2016. "Characterization of Shales Using

T1-T2 NMR Maps." *Journal of Petroleum Science and Engineering* 137: 55–62. doi:10.1016/j.petrol.2015.11.006.

Flory, Paul J. 1942. "Thermodynamics of High-Polymer Solutions." *The Journal of Chemical Physics* 10 (1): 51–61. doi:10.1063/1.1723621.

Foley, I, S.A. Farooqui, and R.L. Kleinberg. 1996. "Effect of Paramagnetic Ions on NMR Relaxation of Fluids at Solid Surfaces." *Journal of Magnetic Resonance. Series A* 123 (1): 95–104. doi:10.1006/jmra.1996.0218.

Hirasaki, George J. 1993. "Structural Interactions in the Wetting and Spreading of van Der Waals Fluids." *Journal of Adhesion Science and Technology* 7 (3): 285–322. doi:10.1163/156856193X00718.

Hirasaki, George J., Sho-Wei Lo, and Ying Zhang. 2003. "NMR Properties of Petroleum Reservoir Fluids." *Magnetic Resonance Imaging* 21 (3–4): 269–77. doi:10.1016/S0730-725X(03)00135-8.

Hu, Yinan, Deepak Devegowda, Alberto Striolo, Anh Thi Van Phan, Tuan A. Ho, Faruk Civan, and Richard F. Sigal. 2015. "Microscopic Dynamics of Water and Hydrocarbon in Shale-Kerogen Pores of Potentially Mixed Wettability." *Society of Petroleum Engineers (SPE) Journal Journal* 20 (01): 112–24. doi:10.2118/167234-PA.

Huggins, Maurice L. 1942. "Some Properties of Solutions of Long-Chain Compounds." *Journal of Physical Chemistry* 46 (1): 151–58. doi:10.1021/j150415a018.

Hürlimann, M. D., D. E. Freed, L. J. Zielinski, Y. Q. Song, G. Leu, C. Straley, C. Cao Minh, and A. Boyd. 2009. "Hydrocarbon Composition from Nmr Diffusion and Relaxation Data." *Petrophysics* 50 (2): 116–29.

Hurlimann, M. D., K. G. Helmer, L. L. Latour, and C. H. Sotak. 1994. "Restricted Diffusion in Sedimentary Rocks. Determination of Surface-Area-to-Volume Ratio and Surface Relaxivity." *Journal of Magnetic Resonance, Series A* 111 (2): 169–78. doi:10.1006/jmra.1994.1243.

Javadpour, Farzam. 2009. "Nanopores and Apparent Permeability of Gas Flow in Mudrocks (Shales and Siltstone)." *Journal of Canadian Petroleum Technology* 48 (8): 16–21. doi:10.2118/09-08-16-DA.

Jiang, Tianmin, Erik Rylander, Philip M. Singer, Richard E. Lewis, and Steven M. Sinclair. 2013. "Integrated Petrophysical Interpretation of Eagle Ford Shale With 1-D and 2-D Nuclear Magnetic Resonance (NMR)." In *SPWLA 54th Annual Logging Symposium*. https://www.onepetro.org/conference-paper/SPWLA-2013-LL.

Jin, Zhehui, and Abbas Firoozabadi. 2016. "Thermodynamic Modeling of Phase Behavior in Shale Media." *SPE Journal*, no. February: 190–207. doi:10.2118/176015-PA.

Jones, S.C. 2007. "A Technique for Faster Pulse-Decay Permeability Measurements in Tight Rocks." *SPE Formation Evaluation* 12 (01): 19–26. doi:10.2118/28450-pa.

Kausik, Ravinath, Paul R. Craddock, Stacy Lynn Reeder, Robert L. Kleinberg, Andrew E. Pomerantz, Frank Shray, Richard E. Lewis, and Erik I. Rylander. 2015. "Novel Reservoir Quality Indices for Tight Oil Shale." *Proceedings of the 3rd Unconventional Resources Technology Conference*. doi:10.15530/urtec-2015-2154859.

Kausik, Ravinath, Kamilla Fellah, Erik Rylander, Philip M. Singer, Richard E. Lewis, and Steven M. Sinclair. 2016. "NMR Relaxometry in Shale and Implications for Logging." *Petrophysics* 57 (4): 339–50.

Kausik, Ravinath, Chanh Cao Minh, Lukasz Zielinski, Badarinadh Vissapragada, Ridvan Akkurt, Yiqiao Song, Chengbing Liu, Sid Jones, and Erika Blair. 2011. "Characterization of Gas Dynamics in Kerogen Nanopores by NMR." In *Spe 147198*, 1–16. Denver, Colorado, USA. doi:10.2118/147198-MS.

Kelemen, S. R., C. C. Walters, D. Ertas, L. M. Kwiatek, and D. J. Curry. 2006. "Petroleum Expulsion Part 2. Organic Matter Type and Maturity Effects on Kerogen Swelling by Solvents and Thermodynamic Parameters for Kerogen from Regular Solution Theory." *Energy and Fuels* 20: 301–8. doi:10.1021/ef0580220.

Kleinberg, Robert L. 1999. "Nuclear Magnetic Resonance." In *Methods in the Physics of Porous Media*, 337–85. doi:10.1016/S0076-695X(08)60420-2.

Klinkenberg, L.J. 1941. "The Permeability of Porous Media to Liquids and Gases." In *Drilling and Production Practice*, 200–213. American Petroleum Institute. doi:10.5510/OGP20120200114.

Korb, Jean-Pierre, Benjamin Nicot, A. Louis-Joseph, Salvatore Bubici, and Gianni Ferrante. 2014. "Dynamics and Wettability of Oil and Water in Oil Shales." *The Journal of Physical Chemistry C* 118 (40): 23212–18. doi:10.1021/jp508659e.

Korb, Jean Pierre, Nopparat Vorapalawut, Benjamin Nicot, and Robert G. Bryant. 2015. "Relation and Correlation between NMR Relaxation Times, Diffusion Coefficients, and Viscosity of Heavy Crude Oils." *Journal of Physical Chemistry C* 119 (43): 24439–46. doi:10.1021/acs.jpcc.5b07510.

Kranz, R. L., J. S. Saltzman, and J. D. Blacic. 1990. "Hydraulic Diffusivity Measurements on Laboratory Rock Samples Using an Oscillating Pore Pressure Method." *International Journal of Rock Mechanics and Mining Sciences And* 27 (5): 345–52. doi:10.1016/0148-9062(90)92709-N.

Krynicki, Kazimierz, Christopher D. Green, and David W. Sawyer. 1978. "Pressure and Temperature Dependence of Self-Diffusion in Water." *Faraday Discussions of the Chemical Society* 66: 199–208. doi:10.1039/DC9786600199.

Latour, L. L., P. P. Mitra, R. L. Kleinberg, and C. H. Sotak. 1993. "Time-Dependent Diffusion Coefficient of Fluids in Porous Media as a Probe of Surface-to-Volume Ratio." *Journal of Magnetic Resonance, Series A* 101 (3): 342–46. doi:10.1006/jmra.1993.1056.

Lessenger, Margaret, Dick Merkel, Rojelio Medina, Sandeep Ramakrishna, Songhua Chen, Ron Balliet, Harry Xie, et al. 2015. "Subsurface Fluid Characterization Using Downhole and Core NMR T1T2 Maps Combined With Pore-Scale Imaging Techniques." In *SPWLA 56th Annual Logging Symposium*. Long Beach, California, USA. https://www.onepetro.org/conference-paper/SPWLA-2015-UUU.

Letham, E. A., and R. M. Bustin. 2016. "Klinkenberg Gas Slippage Measurements as a Means for Shale Pore Structure Characterization." *Geofluids* 16 (2): 264–78. doi:10.1111/gfl.12147.

Levitt, Malcolm H. 2000. *Spin Dynamics: Basics of Nuclear Magnetic Resonance. John Wiley & Sons, Ltd*.

Lipari, Giovanni, and Attila Szabo. 1982. "Model-Free Approach to the Interpretation of Nuclear Magnetic Resonance Relaxation in Macromolecules. 2. Analysis of Experimental Results." *Journal of the American Chemical Society* 104 (17): 4559–70. doi:10.1021/ja00381a010.

Lo, Sho-Wei, George J. Hirasaki, Waylon V. House, and Riki Kobayashi. 2002. "Mixing Rules and Correlations of NMR Relaxation Time With Viscosity, Diffusivity, and Gas/Oil Ratio of Methane/Hydrocarbon Mixtures." *Society of Petroleum Engineers (SPE) Journal* 7 (01): 1–4. doi:10.2118/77264-PA.

Loucks, Robert G., Robert M. Reed, Stephen C. Ruppel, and Ursula Hammes. 2012. "Spectrum of Pore Types and Networks in Mudrocks and a Descriptive Classification for Matrix-Related Mudrock Pores." *AAPG Bulletin* 96 (6): 1071–98. doi:10.1306/08171111061.

Matteson, A., J.P. Tomanic, M.M. Herron, D.F. Allen, and W.E. Kenyon. 2000. "NMR Relaxation of Clay/Brine Mixtures." *SPE Reservoir Evaluation & Engineering* 3 (5): 408–13. doi:10.2118/66185-PA.

Minh, Chanh Cao, Steve Crary, Philip M. Singer, Andrea Valori, Nate Bachman, Gabor G Hursan, Shouxiang Mark Ma, Ali Belowi, and Ghazi Kraishan. 2015. "Determination of Wettability From Magnetic Resonance Relaxation and Diffusion Measurements on Fresh-State Cores." In *SPWLA 56th Anual Logging Symposium*. Long Beach, California, USA.

Mitchell, J., L. F. Gladden, T. C. Chandrasekera, and E. J. Fordham. 2014. "Low-Field Permanent Magnets for Industrial Process and Quality Control." *Progress in Nuclear Magnetic Resonance Spectroscopy* 76. Elsevier B.V.: 1–60. doi:10.1016/j.pnmrs.2013.09.001.

Mitchell, J., J. D. Griffith, J. H.P. Collins, A. J. Sederman, L. F. Gladden, and M. L. Johns. 2007. "Validation of NMR Relaxation Exchange Time Measurements in Porous Media." *Journal of Chemical Physics* 127 (23). doi:10.1063/1.2806178.

Monteilhet, L., J. P. Korb, J. Mitchell, and P. J. McDonald. 2006. "Observation of Exchange of Micropore Water in Cement Pastes by Two-Dimensional T2-T2 Nuclear Magnetic Resonance Relaxometry." *Physical Review E* 74 (6): 1–9. doi:10.1103/PhysRevE.74.061404.

Morriss, C. E., R. Freedman, C. Straley, M. Johnston, H. J. Vinegar, and P. N. Tutunjian. 1997. "Hydrocarbon Saturation and Viscosity Estimation from NMR Logging in the Belridge Diatomite." *The Log Analyst* 38 (2): 44–59. http://www.scopus.com/inward/record.url?eid=2-s2.0-0031095613&partnerID=40&md5=65589577bb0c206ec221e6ea3817ce54.

Nicot, Benjamin, Nopparat Vorapalawut, Berengere Rousseau, F. Madariaga Luis, Gerald Hamon, Jean-Pierre Korb, Luis F Madariaga, et al. 2016. "Estimating Saturations in Organic Shales Using 2D NMR." *Petrophysics* 57 (1): 19–29. https://www.onepetro.org/download/journal-paper/SPWLA-2016-v57n1a2?id=journal-paper/SPWLA-2016-v57n1a2.

Odusina, Elijah, Carl Sondergeld, and Chandra Rai. 2011. "An NMR Study on Shale Wettability." *Canadian Unconventional Resources Conference*, 1–15. doi:10.2118/147371-MS.

Oosting, P. H., and N. J. Trappeniers. 1971. "Proton-Spin-Lattice Relaxation and Self-Diffusion in Methanes. I. Spin-Echo Spectrometer and Preparation of the Methane Samples." *Physica* 51 (3): 395–417. doi:10.1016/0031-8914(71)90047-4.

Ordikhani-Seyedlar, Amin, Oliver Neudert, Siegfried Stapf, Carlos Mattea, Ravinath Kausik, Denise E. Freed, Yi Qiao Song, and Martin D. Hürlimann. 2016. "Evidence of Aromaticity-Specific Maltene NMR Relaxation Enhancement Promoted by Semi-Immobilized Radicals." *Energy and Fuels* 30 (5): 3886–93. doi:10.1021/acs.energyfuels.6b00273.

Ostermeier, R.M. 1995. "Deepwater Gulf of Mexico Turbidites - Compaction Effects on Porosity and Permeability." *SPE Formation Evaluation* 10 (02): 79–85. doi:10.2118/26468-pa.

Ottiger, Stefan, Ronny Pini, Giuseppe Storti, and Marco Mazzotti. 2008. "Competitive Adsorption Equilibria of CO2 and CH4 on a Dry Coal." *Adsorption* 14: 539–56. doi:10.1007/s10450-008-9114-0.

Ozen, Ayse E., and Richard F. Sigal. 2013. "T1/T2 NMR Surface Relaxation Ratio for Hydrocarbons and Brines in Contact with Mature Organic-Shale Reservoir Rocks." *Petrophysics* 54 (1): 11–19.

Pathak, Manas, Hyukmin Kweon, Milind Deo, and Hai Huang. 2017. "Kerogen Swelling and Confinement: Its Implication on Fluid Thermodynamic Properties in Shales." *Scientific Reports* 7 (12530). Springer US: 1–14. doi:10.1038/s41598-017-12982-4.

Profice, Sandra, Gérald Hamon, and Benjamin Nicot. 2016. "Low-Permeability Measurements : Insights." *Petrophysics* 57 (1): 30–40.

Ramakrishnan, T. S., E. J. Fordham, L. Venkataramanan, M. Flaum, and L. M. Schwartz. 1999. "New Interpretation Methodology Based on Forward Models for Magnetic Resonance in Carbonates." In *SPWLA 40th Annual Logging Symposium*. http://www.onepetro.org/mslib/servlet/onepetropreview?id=SPWLA-1999-MMM&soc=SPWLA&speAppNameCookie=ONEPETRO.

Ramirez, T., J. Klein, R. Bonnie, and J. Howard. 2011. "Comparative Study of Formation Evaluation Methods for Unconventional Shale Gas Reservoirs: Application to the Haynesville Shale (Texas)." In *SPE North American Unconventional Gas Conference and Exhibition*. The Woodlands, Texas, USA. doi:10.2118/144062-MS.

Reeder, Stacy Lynn, Paul R. Craddock, Erik Rylander, Iain Pirie, Richard E. Lewis, Ravinath Kausik, Robert L. Kleinberg, Jing Yang, and Andrew E. Pomerantz. 2016. "The Reservoir Producibility Index : A Metric to Assess Reservoir Quality in Tight-Oil Plays from Logs." *Petrophysics* 57 (2): 83–95.

Restuccia, Francesco, Nicolas Ptak, and Guillermo Rein. 2017. "Self-Heating Behavior and Ignition of Shale Rock." *Combustion and Flame* 176: 213–19. doi:10.1016/j.combustflame.2016.09.025.

Rushing, J. A., K. E. Newsham, P. M. Lasswell, J. C. Cox, and T. A. Blasingame. 2004. "Klinkenberg-Corrected Permeability Measurements in Tight Gas Sands: Steady-State Versus Unsteady-State Techniques." In *SPE Annual Technical Conference and Exhibition*. Houston, Texas, USA. doi:10.2118/89867-MS.

Rylander, Erik, Philip M. Singer, Tianmin Jiang, Rick Lewis, Ryan McLin, and Steve Sinclair. 2013. "NMR T2 Distributions in the Eagle Ford Shale: Reflections on Pore Size." In *Unconventional Resources Conference*. The Woodlands, Texas, USA. doi:10.2118/164554-MS.

Sander, Regina, Zhejun Pan, and Luke D. Connell. 2017. "Laboratory Measurement of Low Permeability Unconventional Gas Reservoir Rocks: A Review of Experimental Methods." *Journal of Natural Gas Science and Engineering* 37. Elsevier B.V: 248–79. doi:10.1016/j.jngse.2016.11.041.

Sigal, R.F., and E. Odusina. 2011. "Laboratory NMR Measurements on Methane Saturated Barnett Shale Samples." *Petrophysics* 52 (1): 32–49.

Sigal, Richard Frederick. 2015. "Pore-Size Distributions for Organic-Shale-Reservoir Rocks From Nuclear-Magnetic-Resonance Spectra Combined With Adsorption Measurements." *SPE Journal*, no. August: 824–30. doi:10.2118/174546-PA.

Singer, P. M., D. Asthagiri, Z. Chen, A. Valiya Parambathu, G. J. Hirasaki, and W. G. Chapman. 2018. "Role of Internal Motions and Molecular Geometry on the NMR Relaxation of Hydrocarbons." *Journal of Chemical Physics* 148 (16). doi:10.1063/1.5023240.

Singer, Philip M., D. Asthagiri, Walter G. Chapman, and George J. Hirasaki. 2018. "NMR Spin-Rotation Relaxation and Diffusion of Methane." *The Journal of Chemical Physics* 148 (204504). doi:arXiv:1802.10191v1.

Singer, Philip M., Dilip Asthagiri, Walter G. Chapman, and George J. Hirasaki. 2017. "Molecular Dynamics Simulations of NMR Relaxation and Diffusion of Bulk Hydrocarbons and Water." *Journal of Magnetic Resonance* 277: 15–24. doi:10.1016/j.jmr.2017.02.001.

Singer, Philip M., Zeliang Chen, Lawrence B. Alemany, George J. Hirasaki, Kairan Zhu, Z. Harry Xie, and Tuan D. Vo. 2018. "Interpretation of NMR Relaxation in Bitumen and Organic Shale Using Polymer–Heptane Mixes." *Energy and Fuels* 32 (2): 1534–49. doi:10.1021/acs.energyfuels.7b03603.

Singer, Philip M., Zeliang Chen, and George J. Hirasaki. 2016. "Fluid Typing and Pore Size in Organic Shale Using 2D NMR in Saturated Kerogen." *Petrophysics* 57 (6): 604–19.

Singer, Philip M., Erik Rylander, Tianmin Jiang, Ryan McLin, Richard E. Lewis, and Steven M. Sinclair. 2013. "1D and 2D NMR Core-Log Integration in Organic Shale." In *International Symposium of the Society of Core Analysts*. Napa Valley, California, USA. http://www.scaweb.org/assets/papers/2013_papers/SCA2013-018.pdf.

Singer, Philip M, Zeliang Chen, Lawrence B. Alemany, George J. Hirasaki, Kairan Zhu, Zonghai Harry Xie, and Tuan D. Vo. 2017. "NMR Relaxation of Polymer - Alkane Mixes, A Model System for Crude Oils." In *SPWLA 58th Annual Logging Symposium*. Oklahoma City, Oklahoma, USA.

Sinha, Ankita, Son Dang, Carl Sondergeld, and Chandra Rai. 2017. "Impact of Solvent Extraction on Surface Area Measurements in Organic-Rich Shales Using Nitrogen Adsorption." In *Unconventional Resources Technology Conference (URTeC)*. Austin, Texas, USA.

Straley, Christian. 2002. "A Mechanism for the Temperature Dependence of the Surface Relaxation Rate." In *SCA*.

Tandon, Saurabh, Zoya Heidari, and Hugh Daigle. 2017. "Pore-Scale Evaluation of Nuclear Magnetic Resonance Measurements in Organic-Rich Mudrocks Using

Numerical Modeling." In *Unconventional Resources Technology Conference (URTeC)*. Austin, Texas, USA. doi:10.15530/urtec-2017-2674057.

Thern, Holger, Carsten Horch, Frank Stallmach, Baoyan Li, Alberto Mezzatesta, Hao Zhang, and Roberto Arro. 2018. "Low-Field NMR Laboratory Measurements of Hydrocarbons Confined in Organic Nanoporous Media at Various Pressures." *Microporous and Mesoporous Materials* 269: 21–25. doi:10.1016/j.micromeso.2017.11.047.

Tinni, A., E. Odusina, I. Sulucarnain, C. Sondergeld, and C. Rai. 2014. "NMR Response of Brine, Oil, and Methane in Organic Rich Shales." In *SPE Unconventional Resources Conference*, 1–9. The Woodlands, Texas, USA. doi:10.2118/168971-MS.

Tinni, Ali, Carl Sondergeld, and Chandra Rai. 2018. "New Perspectives on the Effects of Gas Adsorption on Storage and Production of Natural Gas From Shale Formations." *Pertrophysics* 59 (1): 99–104.

Todd, M. R., P. M. O'Dell, and G. J. Hirasaki. 1972. "Methods for Increased Accuracy in Numerical Reservoir Simulation." *Society of Petroleum Engineers (SPE) Journal* 253: 515–30.

Torrey, H. C. 1953. "Nuclear Spin Relaxation by Translational Diffusion." *Physical Review* 92 (4): 962–69. doi:10.1103/PhysRev.92.962.

U.S. Energy Information Administration. 2018. "Annual Energy Outlook 2018 with Projections to 2050." doi:DOE/EIA-0383(2017).

Ungerer, Philippe, Julien Collell, and Marianna Yiannourakou. 2015. "Molecular Modeling of the Volumetric and Thermodynamic Properties of Kerogen: Influence of Organic Type and Maturity." *Energy and Fuels* 29 (1): 91–105. doi:10.1021/ef502154k.

Valori, Andrea, Sidney Van Den Berg, Farhan Ali, and Wael Abdallah. 2017. "Permeability Estimation from NMR Time Dependent Methane Saturation Monitoring in Shales." *Energy and Fuels* 31 (6): 5913–25. doi:10.1021/acs.energyfuels.7b00433.

Venkataramanan, Lalitha, Yi-qiao Song, and Martin D Hürlimann. 2002. "Solving Fredholm Integrals of the First Kind With Tensor Product Structure in 2 and 2.5 Dimensions." *IEEE Transaction on Signal Processing* 50 (5): 1017–26.

Vinegar, H.J., P.M. Tutunjlan, W.A. Edelstein, and P.B. Roemer. 1991. "Whole-Core Analysis by 13C NMR." *SPE Formation Evaluation*, no. June: 183–89.

Vorapalawut, Nopparat, Benjamin Nicot, Alain Louis-Joseph, and Jean Pierre Korb. 2015. "Probing Dynamics and Interaction of Maltenes with Asphaltene Aggregates in Crude Oils by Multiscale NMR." *Energy and Fuels*. doi:10.1021/acs.energyfuels.5b01142.

Wang, Hai-Jing, Albina Mutina, and Ravinath Kausik. 2014. "High-Field Nuclear Magnetic Resonance Observation of Gas Shale Fracturing by Methane Gas." *Energy and Fuels* 28 (6): 3638–44. doi:10.1021/ef5002937.

Washburn, K. E., and P. T. Callaghan. 2006. "Tracking Pore to Pore Exchange Using Relaxation Exchange Spectroscopy." *Physical Review Letters* 97 (17): 25–28. doi:10.1103/PhysRevLett.97.175502.

Washburn, Kathryn E. 2014. "Relaxation Mechanisms and Shales." *Magnetic Resonance Part A* 43A (3): 57–78. doi:10.1002/cmr.a.21302.

Washburn, Kathryn E., and Yuesheng Cheng. 2017. "Detection of Intermolecular Homonuclear Dipolar Coupling in Organic Rich Shale by Transverse Relaxation Exchange." *Journal of Magnetic Resonance* 278: 18–24. doi:10.1016/j.jmr.2017.02.022.

Xiao, Lizhi, Guangzhi Liao, Feng Deng, Huabing Liu, Gongpu Song, and Mengchun Li. 2015. "Development of an NMR System for Down-Hole Porous Rocks." *Microporous and Mesoporous Materials* 205. Elsevier Inc.: 16–20. doi:10.1016/j.micromeso.2014.09.024.

Yang, Zheng, and George J. Hirasaki. 2008. "NMR Measurement of Bitumen at Different Temperatures." *Journal of Magnetic Resonance* 192 (2): 280–93. doi:10.1016/j.jmr.2008.03.007.

Yang, Zheng, George J. Hirasaki, Matthias Appel, and Daniel A. Reed. 2012. "Viscosity Evaluation for NMR Well Logging of Live Heavy Oils." *Petrophysics* 53 (1): 22–37.

Zhang, Boyang, and Hugh Daigle. 2017. "NMR Surface Relaxation Mechanisms of Kerogen." *Geophysics* 82 (6): 1–38. doi:10.1190/geo2016-0350.1.

Zhang, Q., S.-W. Lo, C.C. Huang, G.J. Hirasaki, R. Kobayashi, and W.V. House. 1998. "Some Exceptions to Default NMR Rock and Fluid Properties." In *SPWLA 39th Annual Logging Symposium*. https://www.onepetro.org/conference-paper/SPWLA-1998-FF.